

MONASH UNIVERSITY

Harnessing particle mechanics in a liquid medium

by

Murat Muradoglu

A thesis submitted in partial fulfillment for the
degree of Doctor of Philosophy

in the
Faculty of Engineering
Department of Mechanical and Aerospace Engineering

July 2014

Declaration of Authorship

I, Murat Muradoglu, declare that this thesis titled, ‘Harnessing particle mechanics in a liquid medium’ and the work presented in it are my own. I confirm that:

- This work was done wholly or mainly while in candidature for a research degree at this University.
- It contains no material which has been accepted for award of any other degree in any university
- Where I have quoted from the work of others, the source is always given. With the exception of such quotations, this thesis is entirely my own work.
- I have acknowledged all main sources of help.

Copyright notice

Under the Copyright Act 1968, this thesis must be used only under the normal conditions of scholarly fair dealing. In particular no results or conclusions should be extracted from it, nor should it be copied or closely paraphrased in whole or in part without the written consent of the author. Proper written acknowledgement should be made for any assistance obtained from this thesis.

I certify that I have made all reasonable efforts to secure copyright permissions for third-party content included in this thesis and have not knowingly added copyright content to my work without the owner’s permission.

Signed:

Date:

“Yesterday I was clever, so I wanted to change the world. Today I am wise, so I am changing myself”

“Your task is not to seek for love, but merely to seek and find all the barriers within yourself that you have built against it.”

Rumi

MONASH UNIVERSITY

Abstract

Faculty of Engineering

Department of Mechanical and Aerospace Engineering

Doctor of Philosophy

by Murat Muradoglu

The manipulation of bioparticles ranging from nano to micrometers in diameter has become a fundamental tenet to much of biochemical and biomedical applications. Integral to these experiments is the need to precisely manipulate particle locations, separate and/or organize them whilst limiting the possibility of damage to the specimens that are, by nature, required to be suspended in a liquid medium. A crucial aspect in any such form of particle manipulation is the ability to reliably and repeatedly sense and distinguish their presence. To achieve these goals, their small nature and typically large number warrant the use of up and coming nanotechnologies- for example nano-optics- to achieve practicable and effective results. Yet, there remains major challenges in such technologies, including but not limited to: (a) better sorting (size, density, etc), (b) assembly, (c) concentration, (d) dilution, (e) fictionalization and finally most importantly (f) a better understanding of the interdisciplinary coupling with digital microfluidics. Further to this, the implications of working with such small particles is the inherent random jiggling of said particles in a liquid medium, i.e. Brownian dynamics. Not only are the dynamics of the liquid medium necessary in evaluation, but they also create an impetus to harness it for useful applications in itself. Therefore, the primary focus of this thesis is to study various particle manipulation mechanisms with secondary support areas in Brownian dynamics and discrete liquid mechanics.

Acknowledgements

I'd like to thank my supervisor A/Prof. Tuck W. NG for his endless support and most importantly, for giving me a chance at a PhD.

A warm thank you to my family and friends for their ongoing support throughout my candidature.

I can, without doubt, claim that most of my research ideas have come to me whilst riding a motorcycle. It is truly a little known form of meditation. Hail motorcycles!

Contents

Declaration of Authorship	iii
0.1 Copyright notice	iii
Abstract	v
Acknowledgements	vi
List of Figures	xi
List of Tables	xxi
1 Introduction	1
1.1 Introduction	1
1.2 Rationale	1
1.3 Thesis Outline	2
2 Literature Review	5
2.1 Manipulating with Optics	5
2.1.1 Optical Tweezers	6
2.1.2 Plasmonics	10
2.2 Brownian Dynamics	11
2.3 Discrete Liquid Mechanics	14
2.3.1 Microplates	16
3 Background Theory	19
3.1 Electromagnetics Preliminaries	19
3.2 Scattering Problem	23
3.2.1 Gaussian Beam	26
3.2.2 Point Matching	28
3.2.3 Translation and Rotation	30
3.2.4 Force Calculation	31
3.3 Plasmonics	32
3.3.1 Simulation Technique and Normalization	33
3.3.2 Plasmonic Resonance	34
3.4 Conclusion	36

4	Optical Forces on Particles	37
4.1	Introduction	37
4.2	Optical Tweezers	38
4.2.1	Lateral Push/Pull	42
4.2.2	Bioreactor	45
4.2.3	Optical Trapping Map	48
4.2.4	Selective Sorting and Swelling Particles	57
4.3	Plasmonics	59
4.3.1	Design	61
4.3.2	Results and Discussion	63
4.4	Chapter Summary	66
5	Brownian Dynamics	69
5.1	Introduction	69
5.2	Sorting of Brownian rods by the use of an asymmetric potential	70
5.2.1	Stage one	74
5.2.2	Stage two	76
5.2.3	Results and Discussion	77
5.2.4	Conclusion	80
5.3	Nano scale environment sensing scheme with Brownian nanorod and plasmon resonator	80
5.3.1	Modeling	82
5.3.2	Results	83
5.3.3	Conclusion	88
5.4	Chapter Summary	90
6	Discrete Liquid Mechanics	91
6.1	Introduction	91
6.2	Precise drop dispensation	92
6.2.1	Materials and Methods	94
6.2.2	Results and Discussion	95
6.2.3	Analysis of aerosol formation	101
6.2.4	Conclusion	104
6.3	Contact angle and volume retention effects from capillary bridge evaporation in biochemical microplating	105
6.3.1	Theoretical considerations	106
6.3.2	Materials and methods	110
6.3.3	Results and discussion	113
6.3.4	Conclusion	120
6.4	Scale-like cantilever cell traps	121
6.4.1	Materials and Methods	121
6.4.2	Results and Discussion	124
6.4.3	Conclusion	134
6.5	Chapter Summary	135
7	Conclusions	137

A Formulas	141
A.1 Translation Addition Theorem	141
B Peer reviewed Publications	143
B.1 Publication List	143
B.2 Tailored leaky plasmon waves from a subwavelength aperture for optical particle trapping on a chip	146
B.3 Sorting of Brownian rods by use of an asymmetric potential	151
B.4 Optical force lateral push-pulling using focus positioning	157
B.5 Optical stirring in a droplet cell bioreactor	164
B.6 Precise drop dispensation on superhydrophobic surfaces using acoustic nebulization	170
B.7 Optical trapping map of dielectric spheres	179
B.8 Contact angle and volume retention effects from capillary bridge evaporation in biochemical microplating	189
B.9 Scale-like cantilever cell traps	198
B.10 Nanoscale environment sensing scheme with Brownian nanorod and plasmon resonator	207
 Bibliography	 215

List of Figures

2.1	Effective wavelength versus particle size domains of the various scattering regimes. The domain of interest here is the Mie scattering region, where $r \approx \lambda$.	8
3.1	Efficiency in trapping a spherical particle using a focusing laser beam is dependent on its radius r and refractive index n_1 , the refractive index of the medium n_2 , and the NA of the light beam, which is a function of the half-angle.	23
3.2	Scattering of a coated sphere. The inner and outer core refractive indices are given by n_0 and n_1 .	25
3.3	Three field components $ E_x $, $ E_y $ and $ E_z $ of an x -polarized Gaussian beam with $NA = 1.0$ when recovered by expanding its beam coefficients with VSWF in the focal plane $x - y$. The fields are normalized to the maximum of $ E_x $ and lengths are in units of wavelength, λ .	29
3.4	Translation and Rotation of the incident beam as described in Eq. (3.40). Steps are (i) rotate the system by θ , (ii) translate in z'' , and finally (iii) rotate back by $-\theta$. The construction of the rotation and translation matrices become costly as $ d $ gets bigger thus the computational time is spent in the matrix multiplication.	30
3.5	Real and Imaginary components of the dielectric function for gold (left) and silver (right) at the wavelength range of $300\text{nm} \leq \lambda \leq 900\text{nm}$.	34
3.6	Geometry of simple plasmonic waveguide with wave propagation along the x direction and homogeneity in y such that $\partial/\partial y \equiv 0$.	35
4.1	Contour plots of the optical force efficiency on a $3\mu\text{m}$ polystyrene particle shown separated into its (a) x component Q_x and (b) z component Q_z . By combining these two components, the net force efficiency $\mathbf{Q} = Q_x + Q_z$, together with the E_x component of the beam, is shown in (c). The dotted circle is provided as an indication of the intercepted area of the particle relative to the beam.	40
4.2	Contour plots of the optical force efficiency on a $3\mu\text{m}$ polystyrene particle shown separated into its (a) x component Q_x and (b) z component Q_z , at points 4 to $18\mu\text{m}$ above the focal point. The overlaid arrows indicate the direction of force for the respective components. When $z > 13\mu\text{m}$ a transition is observed in (a) whereby the optical forces in the x direction switch polarity, i.e. from pulling to pushing.	41

4.3	(a) Contour plot of the optical force efficiency, Q_x , in the $x - z$ plane beyond the transition line. (b) Plot of optical force efficiency, Q_x , along $z = 16\mu\text{m}$ and $z = 17\mu\text{m}$ as indicated by the solid and dashed lines in (a), respectively. The optical force efficiency drops off rapidly after $3.5\mu\text{m}$. Based on this observation we safely neglect optical force calculations beyond $8\mu\text{m}$ to lessen computational demands.	41
4.4	Plots of distance to transition line, z_T , versus particle refractive index. Each line corresponds to a different particle size.	42
4.5	Contour plots of the optical force efficiency on a $3\mu\text{m}$ polystyrene particle shown separated into its (a) x component Q_x and (b) z component Q_z , at points 4 to $13\mu\text{m}$ below the focal point.	43
4.6	Proposed scheme where locating the beam focus below or above the sphere moves it laterally predominantly while a beam in the opposite direction restores the sphere axially.	43
4.7	Schematic description of the optical push-pull setup used, BS, beam splitter, M mirror	44
4.8	Images of laser beam focus located axially (a) above and (b) below particles. The former pulls and the latter pushes particles laterally with respect to the beam axis (cursor)	44
4.9	The setup to accomplish optical stirring involves focusing the laser beam close to the bottom surface of the droplet and using the microscope stage to move the slide and droplet in the $x - y$ plane.	46
4.10	Plot of local displacements of particles on microscope stage for $z = 16\mu\text{m}$ at various power levels starting from the right to left, 10mW (blue), 20mW (red), 25mW (green), 40mW (blue-dotted), 100mW (red-dotted) and 200mW (green-dotted). The optical stirring effect can be controlled by changing laser power. Inset: The plot of the global particle trajectories at optical powers 10mW (black), 15mW (green), 20mW (red) and 35mW (blue).	47
4.11	With the laser beam located axially below the polystyrene beads and having sufficient power, the image sequence (a) before and (b) after shows the particles numbered 1 and 2 laterally pushed away from the beam center. With the laser beam located axially below the polystyrene beads but having insufficient power, the image sequence (c) before and (d) after shows the cluster of particles circled in red unaffected by the beam. The arrow shows the general direction of travel of the particles.	48
4.12	With the laser beam located axially below the particles and having sufficient power, the image sequence (a) before and (b) after shows the red blood cells numbered 1 and 2 laterally pushed away by the beam. The arrow shows the general direction of travel of the cells.	49
4.13	Iso-surface of $Q_{z,RFmin} = -1 \times 10^{-10}$ representing the ability to conduct optical trapping calculated in relation to NA, particle refractive index n_1 , and radius r values. The volume space above the distribution represents those parameters that do not lead to optical trapping.	49
4.14	Example slice plots from Fig. (4.13) obtained by keeping the (a) refractive index, (b) normalized radius, and (c) NA fixed. Finger landscapes are observed in all three cases. The white areas correspond to $Q_{z,RFmin} = 0$, which indicates a non-trap condition.	51

4.15	Optical force efficiency, Q_z calculated for particles trapped under parameter conditions p_A and p_B placed at positions along the beam axis z . For both particles, the radiation patterns at different locations corresponding to the maximum forward restoration force, equilibrium point and maximum reverse restoration force are also shown.	52
4.16	Optical force efficiency, Q_z calculated for particles trapped under parameter conditions p_C and p_D placed at positions along the beam axis z . For both particles, the radiation patterns at different locations corresponding to the maximum forward restoration force, focal point and $z = 1.0\mu\text{m}$ are also shown.	53
4.17	Zoomed-in region for Fig. (4.14), ($2.0\mu\text{m} \leq r \leq 2.5\mu\text{m}$ and $2.5 \leq n_1 \leq 3.0$), with smaller parameter value intervals, which show that the fingers form smoothly before they are thinned out and eventually vanish. Two lines, L_1 and L_2 , indicate that particles with a radius ratio between 2.115 and 2.135 would be selectively trapped, which illustrates the ability for sorting.	54
4.18	Potential energy wells corresponding to a particle located in the trapping finger and safe region, depicted under conditions p_B (left) and p_E (right), respectively.	54
4.19	Trapping strength and its gradient along the lines (a) L_1 and (b) L_2 as depicted in Fig. (4.17)	56
4.20	Selective sorting can be achieved by scanning a line of particles in a plane. Here, the red particles have parameter combinations that reside on the trapping region, e.g. the trapping fingers, and the green particles do not. At the end of the scan, only the red particles will remain in the plane while the green are scattered off plane.	57
4.21	Schematic description of situation where a spherical of volume V_0 of refractive index n_1 undergoes swelling by absorbing material from the surrounding media of refractive index n_2 such that its volume increases by δV	58
4.22	Trajectory of a swelling dielectric sphere with an original radius $r_0 = 2.095\mu\text{m}$ and refractive index $n_1 = 2.506$, placed in a medium with refractive index $n_2 = 1.33$ for (a) $NA = 1.2248$ and (b) $NA = 1.33$. The growth rate, α , was linearly increased from 0.0 to 2.0.	59
4.23	Dispersion relation for silver (left) and gold (right)	59
4.24	(a) Optical scheme of illuminating metallic structures in a whole-field manner to create localized plasmon field for trapping. (b) Envisaged approach of having illumination delivered from individually addressable waveguides within a substrate to subwavelength apertures in the metallic layer to create switchable surface plasmon sites for trapping; which in the process will facilitate many lab-on-a-chip procedures	61
4.25	(a) Simulation geometry with a lattice constant, groove height, and width of p , h , and w , respectively. The Gaussian source, located to the left, has a center wavelength of $\lambda = 1.5\mu\text{m}$ and a pulse width of $\lambda = 1\mu\text{m}$. (b) Simulation geometry with a subwavelength aperture and tailored surface corrugations on a silver substrate. Throughout this study the subwavelength aperture width s , and slab thickness, t , are fixed at 140 and 1000 nm, respectively.	62

4.26	Transmission spectra for a grating period of (a) 400, (b) 500 and (c) 600 nm, respectively, at different h and w configurations. (d) Combined transmission spectra outlines the input Gaussian spectra. The strongest resonance is observed when $h = 150\text{nm}$, $w = 250\text{nm}$, and $p = 500\text{nm}$	63
4.27	Snapshots of the electric field intensity, $\ \mathbf{E}\ ^2$, shown as a contour plot along the metallic structure for (a) $p = 500\text{nm}$, $\lambda = 1380\text{nm}$, $h = 150\text{nm}$, and $w = 250\text{nm}$; (b) $p = 500\text{nm}$, $\lambda = 1464\text{nm}$, $h = 150\text{nm}$, and $w = 250\text{nm}$; (c) $p = 600\text{nm}$, $\lambda = 1587\text{nm}$, $h = 150\text{nm}$, and $w = 200\text{nm}$; (d) $p = 600\text{nm}$, $\lambda = 1715\text{nm}$, $h = 150\text{nm}$, and $w = 200\text{nm}$	64
4.28	Snapshots of the electric field intensity, $\ \mathbf{E}\ ^2$, shown as a contour plot along the metallic structure where $p = 500\text{nm}$, $\lambda = 1380\text{nm}$, $h = 150\text{nm}$, $w = 250\text{nm}$, $p' = 500\text{nm}$, $h' = 125\text{nm}$, $w' = 300\text{nm}$, and (a) $q = 0$; (b) $q = 105\text{nm}$; (c) $q = 155\text{nm}$; (d) $q = 205\text{nm}$	65
4.29	Optical trapping force developed on a spherical polystyrene particle with a radius of 80nm and refractive index of 2.5 in water inserted into the design producing the electric intensity field of Fig. (4.28b).	65
5.1	(a) Directions of diffusion coefficients superimposed on a typical rod under consideration, with the static laboratory frame in the top left. (b) PDFs for small and large spheres at a given time t . The greatest difference in probability between the small and big spheres occurs at the intersections of the PDFs (marked as b). (c) Diagrammatic representation of the position and alignment of rods near the end of the on period from both top and side views	71
5.2	Plot of D_{yy} (upper curves) and D_{xx} (lower curves) vs time for two different rods with dimensions $595.2 \times 168 \times 168\text{nm}^3$ (black, dashed) and $864 \times 72 \times 72\text{nm}^3$ (red, solid). Horizontal lines represent \bar{D} and vertical lines represent τ_θ	73
5.3	Contour plots of diffusion coefficient in the laboratory x direction over a range of rod sizes taken at time (a) 30 and (b) $400\mu\text{s}$. The percentage difference in length (L) and diameter (D) are taken from a $960 \times 120 \times 120\text{nm}^3$ base rod. The circles on the plot indicate the rod sizes used in simulations, with the blue coloured circles indicating the rods that were taken to the second stage of sorting. The red and black circles are rod sizes on adjacent contours at $30\mu\text{s}$, and are overlaid in (b) to emphasize the change in diffusion coefficient over time. The largest diffusion coefficients correspond to the smallest particle sizes in the lower left corner of the plot (red contours) and decrease toward the top right (blue contours). The colours of dots used correspond to the curves in Fig. (5.5).	74
5.4	Separation time (blue squares) and number of cycles for separation (green squares) vs off time for three different rod sizes taken to stage 2 of sorting. Rod sizes used were $595.2 \times 168 \times 168$, $710.4 \times 120 \times 120$, and $864 \times 72 \times 72\text{nm}^3$. Separation time has been defined as number of cycles for separation multiplied by the off time, and is shown as it is a more meaningful performance characteristic than number of cycles required to separate rod populations.	76

5.5	[(a) and (c)] Plots of 10th and 90th percentiles of expected rod populations vs cycles, and [(b) and (d)] expected number of particles in each potential well at 20,000 cycles using an initial population of 10,000 particles. These were determined for [(a) and (b)] first stage sorting using $30\mu s$ off time with nine different rod dimensions (as shown in Table 5.1) along three contours (overlaid dots in Fig. 5.3), and [(c) and (d)] second stage sorting using 400 ms off time with the blue population from the first stage (curve colours correspond to circles in Fig. 5.3).	79
5.6	Schematic of a microenvironment sensing scheme in which a micron scale rod is drawn to a cylindrical pillar using an attractive force as viewed three dimensionally (a) and from the top (b). If motion is assumed to be exclusively in the x-y plane the Brownian rod motion can be monitored by a camera placed in the z-axis.	81
5.7	Schematic of the proposed nano environment sensing scheme in which a nano scale rod is drawn to a cylindrical pillar using an attractive force as viewed three dimensionally (a) and from the top (b). The cylindrical pillar serves as a plasmonic optical resonator sensor with light input and output through the optical fiber. The contact of the Brownian nano rod with the cylinder causes changes to the optical signal. Under this scheme, no imaging of the nano rod is required.	82
5.8	Transmission spectra of a nano-rod placed a distance, $d = 0$ (contact), $d = 2.5nm$ and $d = 10nm$, indicated by the blue, green and red lines respectively. The orientation of the particle is either vertical, $\theta = 0^\circ$, or horizontal $\theta = 90^\circ$ indicated by the non-marked and marked lines, respectively.	84
5.9	Transmission spectra for gap values $d = 0, 2.5 \text{ nm}, 5 \text{ nm}, 7.5 \text{ nm}, 10 \text{ nm}$ over a continuous range of angle from 0° to 90° . The absolute value of the transmission spectra is given here to better illustrate the surface curvature.	84
5.10	Aggregated differences of the transmission spectra over all angles between all contact and non-contact combinations, i.e. $W(0, q)(\lambda)$ were $q = 1, 2, 3, 4$. The plot shows that between contact and non-contact cases there is a distinguished difference of transmission at 600nm. This feature allows for unique detection of contact between nanorod and cylindrical pillar.	85
5.11	Transmission readings at 600nm showing distinct perceptibility when gap value $d = 0$. The orientation angle does affect the distinct perceptibility.	86
5.12	Plots of f (the fraction of time in state I) against the normalized charge product calculated from 18,000 samples at 0, 25, and $100^\circ C$. All simulations started with the rod touching the edge of the pillar. Increasing the magnitude of the charges such that the force is attractive reduces the proportion of time spent in state I	87
5.13	Plots of f (the fraction of time in state I) against temperature calculated from 18,000 samples at various normalized charge products. All simulations started with the rod touching the edge of the pillar. It can be seen that all the trends are approximately linear	88

5.14	Plot of the approximated values of df/dT (taken between 273 K to 373 K) against the normalized charge product. Higher values of df/dT indicate higher sensitivity. A normalized charge of -200 gave a maximal value of df/dT	89
6.1	Schematic description of the scheme to obtain precise volumes of drops on superhydrophobic surfaces. A surface acoustic wave nebulizer delivers a spray of aerosol droplets onto the receptacle in which the exact volume is determined using an accurate weighing scale. By covering with a superhydrophobic lid and gentle shaking, a single drop is created.	93
6.2	Scanning electron micrographs obtained from immersing the copper coupons into the silver nitrate solution for different lengths of time followed by air drying. It can be seen that granular structures developed with short period immersion, whilst dendritic structures formed with longer period immersion.	96
6.3	Scanning electron micrographs at higher magnifications that provide a clearer picture of the (a) granular and (b) dendritic structures developed.	97
6.4	Plots of the readings from the weighing scale against the operation time of the nebulizer. The trends from each run are highly linear, albeit the slope variation indicates that pre-calibrated operation without the weighing scale was not feasible.	98
6.5	Images of (a) multiple nebulized droplets formed on the surface of the receptacle and (b) a single drop that results after shaking the receptacle.	98
6.6	Illustrations depicting predominantly high (a) Cassie and (b) Wenzel wetting states of relatively larger drops and aerosols residing respectively on superhydrophobic surfaces. (c) When further aerosols arrive at the surface, they merge with existing aerosols on the surface to create larger volumes that coalesce with other surface bound aerosols. Due to the lack of a sufficiently large perturbation, the predominant Wenzel states cannot convert to Cassie states, allowing the liquid body to stay on the inclined surface with larger volumes.	100
6.7	Illustrations depicting predominantly high (a) Wenzel wetting state of a drop on the surface in which with sufficient momentum developed (in the direction of the arrow) will (b) cause the drop to dislodge and leave behind a thin film of liquid. The very small volume of the latter renders it easily evaporable while the former now functions as a drop in the Cassie state.	101
6.8	The residence of the aerosol droplet on the surface can be described using a model comprising two spheres that intersect with each other. The relevant parameters can be related, through the equations that can be solved, to the solid angle.	102
6.9	Plots of the solid angle Ω subtended by an aerosol droplet that arrives as a sphere with radius r' on a semi-spherical surface of radius R for various equilibrium three-phase contact angles θ . The residence of the aerosol droplet on the surface can be described using a model comprising two spheres that intersect with each other. The relevant parameters can be related, through the equations that can be solved, to the solid angle.	104
6.10	Schematic description of a sessile drop where its shape is semi-spherical. The volume can be determined using the measurable parameters of θ and a	106

6.11	Schematic description of the half height and width of a symmetrical capillary bridge between two flat surfaces when (a) $\theta < \pi/2$, and (b) $\theta > \pi/2$. The volume can be calculated using the parameters θ , h and a	107
6.12	Schematic description of (a) the cross-section of three rods of equal diameter located with equal distance z to each other. The contacts of capillary bridge (at points A and C) with the rod, shown in (b) subtend an angle of 2Φ on it. The areas computer of OO'A in (c), O'AB and the semicircle AB in (d), and OAC in (b) permit the volume of the capillary bridge to be determined	109
6.13	Schematic depiction of the experimental setup used for recording the liquid bridge between two flat surfaces, with (a) providing a front view of the setup where the dotted lines show the axes of symmetry and where the main imaging axis is through the center marked point. The side view (b) of the setup shows the imaging axis with the light source being opposite to the microscope camera and the illumination axis along the imaging axis.	111
6.14	Schematic depiction of the experimental setup used for recording the liquid bridge between two flat surfaces, with (a) providing a front view of the setup where the dotted lines show the axes of symmetry and where the main imaging axis is through the center marked point. The side view (b) of the setup shows the imaging axis with the light source being opposite to the microscope camera and the illumination axis along the imaging axes.	111
6.15	Schematic depiction (a) of the experimental setup for creating a liquid bridge (darkened areas) between glass rods in which the front view comprise dotted lines showing the position of the axial centers of the rods at the vertices of an equilateral triangle. In recording (b) the main imaging axis is through the center marked point is recorded using one camera, and another camera records perpendicular to this axis.	112
6.16	Trace of the contact angle progression with time as a $3\mu\text{L}$ sessile drop (see inset) is evaporated on the flat surfaces made of glass, silanized glass, and silicone. The contact angle is taken as the average of the angles marked 1 and 2 in the picture.	114
6.17	Trace of the remnant volume against time of a $3\mu\text{L}$ sessile drop as it is evaporated on the flat surfaces made of glass, silanized glass, and silicone.	114
6.18	Trace of the contact angle progression with time as a $3\mu\text{L}$ capillary bridge (see inset) is evaporated between two flat surfaces made of glass, silanized glass, and silicone. The contact angle is taken as the average of the angles marked 1-4 in the picture.	115
6.19	Trace of the remnant volume against time of a $3\mu\text{L}$ capillary bridge as it is evaporated between two flat surfaces made of glass, silanized glass, and silicone.	116
6.20	Trace of the contact angle progression with time as a $3\mu\text{L}$ capillary bridge (see inset) is evaporated between three rods (A-C) made of glass. The contact angle is taken as the average of the angles marked 1-6 in the picture.	118
6.21	Breakdown trace of the contact angles developed on the three glass rods in Fig. (6.20) with time as a $3\mu\text{L}$ capillary bridge is evaporated between them. Significant fluctuations (in the order of 20°) can be observed.	118

6.22	Breakdown trace of the contact angles developed on the top and bottom of the two glass flat surfaces in Fig. (6.18) with time as a $3\mu\text{L}$ capillary bridge is evaporated between them. The fluctuations are noticable much smaller ($< 5^\circ$).	119
6.23	Map of the cross sectional area of the capillary bridge held between three liquid rods calculated for various values of θ and Φ . The units are in m^2 and area based on $z = 3.733\text{mm}$ and $r = 1\text{mm}$ in Fig. (6.12).	119
6.24	Schematic description of the ability to use a moving tip to trap particles in a liquid bridge on a structured substrate. A light microscope is useable to observe the trapping of the particles as they are still in the liquid medium. For higher resolution imaging, the sample is dried and placed in an SEM	122
6.25	Precision ion beam machining with the right parameters which creates a well structured scale-like cantilever in (a). The use of a too large diameter ion beam can produce warping in the cantilever as shown in (b)	125
6.26	SRIM simulation of 1000 Ga ion against Si ₃ N ₄ monolayer. The pattern of ion ablation is nearly circular. Due to this the ends of the cut were smooth despite the kerf size being 200nm.	125
6.27	Optical profilometry (a) map of the fabricated cantilever which shows good topographic control in the manufacture. Taking a (b) central horizontal section of the created cantilever shows a tilt of angle 6°	126
6.28	FEA stress analysis results of (a) rectangular cantilever with inverse aspect ratio 1.618:1; (b) scale-like cantilever with 315° central angle; (c) square cantilever; (d) rectangular cantilever with aspect ratio 1:1.618. The effective lengths are kept at $10\mu\text{m}$ in all cases. The corners of the fixed end are clearly areas of high stress concentration from a similar force imposed on all nodes.	127
6.29	The probability density function of stress distributions for the four different types of cantilevers modeled. These curves indicate a goodness of fit value (also often referred to as the p-value) of larger than 0.98. They indicate that the majority data of circular and square cantilever stress values range between 0 and 3MPa.	128
6.30	(a) Box plots of the stress distribution for the edge of cuts with 1kPa normal pressure for the four different types of cantilevers simulated. The box includes the data points between first quartile and third quartile of the data set, while the asterisks are values larger than 1.5 times of third quartile. With the (b) box plots of deflection of points around cantilever edges with 1kPa normal pressure the number of data points larger than 1.5 times of third quartile was substantially lower	129
6.31	Distributions of the maximum stress and tip deflection change with the central angle of the circular cantilever under 1kPa normal pressure. The trends show that control of deflection through the right ion beam delivery should also be considered in relation to the maximum stress developed.	130

-
- 6.32 Snapshots (top) of the simulation of the piling process in progress which leads to a triangular collection. The piling characteristic is described by the height of the pile h , in relation to the radius of the obstacle R , and the repose angle θ . The results from simulated piling indicate that the equilibrium triangular shape was dependent on the ability of each point to remain in relation to the slope condition that can be withstood. The plot (below) shows a normalized parameter of height of the pile h against obstacle radius R , to follow an increasing trend with the repose angle θ 131
- 6.33 Experimental record of the trapping of $1\mu\text{m}$ polystyrene beads using the scale-like cantilever in (a) which shows piling with particle aggregation. The trapping of bacterial cells in (b) shows capacity to slip into the gap of the cantilever despite the size of the bacteria being larger. The directions of the flow in all cases are indicated by arrows. When the direction of flow was reversed with the $1\mu\text{m}$ polystyrene beads (c) and bacterial cells (d), there was diminished trapping ability. This demonstrates a directional trapping capacity. 132
- 6.34 Typical optical microscopy images recorded of the $1\mu\text{m}$ polystyrene beads in liquid interacting with the scale-like cantilever where flow in one direction traps them (a) while flow in the opposite direction clears them off (b). For the flow causing the particles to be trapped, the distribution of the number of beads at each run, indicated in (c), has an average of 67 beads trapped with a standard deviation of 17. 133

List of Tables

3.1	Coefficients for Gold and Silver.	33
5.1	Actual rod dimensions used in simulations, along with percentage differences compared to a $960 \times 120 \times 120 \text{nm}^3$ base rod and diffusion coefficients in the laboratory x direction at both early and late off times. Entries are arranged in the same way as Fig. (5.3), with the top set corresponding to the red circles, center set to blue circles and bottom set to black circles	78
5.2	Scale factors used to adjust the theoretical diffusion coefficients in the three degrees of freedom considered.	78

Dedicated to my family. . . .

Chapter 1

Introduction

1.1 Introduction

Nanotechnology is the newest of evolutionary science technology- broadly speaking it refers to the science of anything within the nanometer scale (10^{-9}m). One aspect of nanotechnology is all about building working mechanisms using components with nanoscale dimensions. This corresponds closely with the manipulation of materials at the molecular level. The ability to carry out such manipulation, for the most of us, is initially very difficult to fathom, however, the realization of such a goal brings forward a plethora of cutting edge applications. In the quest to conquer the nano-world, a number of physical phenomena, defying our intuitive common-sense, become more pronounced as we diverge from the physical laws of the big, such as gravity, to the physical laws of the small- the quantum realm. In the same way the creation of dedicated hunting and carving tools were the cornerstone of early man, a set of dedicated nano-tools is of paramount importance in the future of nanotechnology and indeed mankind. And so, forth, must mankind go, into the arduous process of investigation and refinement of his tools as he has relentlessly done so in the past.

1.2 Rationale

The manipulation of bioparticles ranging from nano to micrometers in diameter has become a fundamental tenet to much of biochemical and biomedical applications. Integral to these experiments is the need to precisely manipulate particle locations, separate and/or organize them whilst limiting the possibility of damage to the specimens that are, by nature, required to be suspended in a liquid medium. A crucial aspect in any such form of particle manipulation is the ability to reliably and repeatedly sense and

distinguish their presence. To achieve these goals, their small nature and typically large number warrant the use of up and coming nanotechnologies- for example nano-optics- to achieve practicable and effective results. To this end, optical tweezers, acoustics, electrical forces and surface modification have been used to provide a whole host of different forces, including translation, rotation and stretching.

Yet, there remains major challenges in such technologies, including but not limited to: (a) better sorting (size, density, etc), (b) assembly, (c) concentration, (d) dilution, (e) functionalisation and finally most importantly (f) a better understanding of the interdisciplinary coupling with digital microfluidics. While these challenges remain true for particle manipulation it is impertinent to consider the system in its entirety, where particle manipulation is only one component of the overall biochemical and/or biomedical system. This motivation, in the broader sense, imposes the requirement that these tiny particles be contained in a liquid medium. Naturally, it then becomes necessary to develop an understanding, not only of the manipulative forces, but also the operation and dynamics of the liquid medium. The recent trends towards the development of so-called “lab-on-a-chip” devices, which essentially are self-contained laboratories at the chip scale, further drives the need to consider the interdisciplinary aspects of particle manipulation.

Typically, lab-on-chip systems have microscale flows of fluid which in itself encompasses a discipline alone that is capable of a diverse array of applications that varies from drug delivery, organic synthesis and microreactors. In particular, the application of digital microfluidics, i.e. the use of discrete volumes of fluid (droplets), provides a means to individually control each volume and offers greater potential for increased throughput and scalability than continuous-flow systems.

Perhaps more elusively, another implications of working with such small particles in a liquid medium is the inherent random jiggling of said particles, i.e. Brownian dynamics. In addition to evaluating the contribution of these dynamics to any particle manipulation scheme, an opportunity exists to understand and harness them for useful applications. In summary, the primary focus of this thesis is to study various particle manipulation mechanisms based on nano-optic technologies, along with two support studies into Brownian dynamics and discrete liquid mechanics.

1.3 Thesis Outline

The thesis is organized into the following chapters:

- Chapter (2): A review of existing literature on the major focus of this thesis, that being optical particle manipulation technologies, in particular optical tweezers and plasmonics is given. In line with the minor area of study, a review of sorting and sensing of Brownian particles and discrete liquid mechanics is also provided.
- Chapter (3): A description of the background theoretical methods used for the simulation and design of optical devices is provided.
- Chapter (4): In this chapter we simulate and apply optical tweezers and plasmonic structures to achieve a variety of particle manipulation mechanisms. Using an optical tweezer we show that: (a) a focused beam can be used to pull and push particles in a predominantly lateral sense by altering the focal plane relative the particles; (b) particles can be gently and tunably stirred allowing for a bioreactor that limits photodamage. Further to this, a comprehensive computation of the optical tweezer revealed parametric optical trapping blind spots as well as resonance conditions that allowed for trapping of high refractive index particles.

Finally, a corrugated structure has been designed to efficiently couple light from a subwavelength aperture to surface plasmonic modes on the structured surface. By carefully placing a secondary grated structure some distance from the original structure, we were able to produce strong reflection, which, with the coherent nature of light used, created strong optical standing wave fields that could be harnessed for particle trapping.

- Chapter (5): A scheme to sense Brownian nanorods using a plasmonic whispering gallery is developed that is further shown to have great perceptibility of contact conditions. We further examine the possibility of using stochastic ratchets to sort populations of Brownian rods, investigating, in particular, the role that the crossover time from anisotropic to isotropic motion takes in this process.
- Chapter (6): In this chapter we address the need to deliver drops of specific volumes on superhydrophobic surfaces from cost effective storage media such as paper. In the process, we will show the nature of how small aerosols form on these surfaces before evolving into single drops. We investigate the feasibility of using the capillary bridges developed between solid bodies (rods) to interrogate the contact angle development under the effect of evaporation. In addition, we also seek to ascertain the progress of volume change. These findings will help to provide insights on the ability to relate wetting to analyte characteristics and mitigate evaporation in biochemical microplating schemes developed for use in resource-limited laboratories. And finally, using biomimicry, we show a unique way to anchor and trap particles.

Chapter 2

Literature Review

2.1 Manipulating with Optics

It is well known that light carries both linear and angular momentum that can exert observable force and torque on small matter. The force exerted on earth-bound objects by the sun was found by P. N. Lebedev in 1901 [1] to be $10\mu\text{N}/\text{m}^2$; a remarkable feat at the time. Reflecting objects such as a cup of coffee would by this measure experience a force of approximately 30nN , which is far from the required force to move it. However, at smaller scales such as in the nanometers (10^{-9}m), this force is more pronounced and provides an exceptional means to control particles. Moving small-scale matter in a prescribed fashion with optical forces is attractive in many areas of inquiry. The phenomena known as photophoresis has been known for a long time in which the studies of Hettner [2] have shed much understanding. Direct photophoresis is caused by the transfer of photon momentum to a particle by refraction and reflection [3], allowing particle movement when the particle is transparent and has a refractive index larger than its surrounding medium. On the contrary, indirect photophoresis occurs as a result of an increase in the kinetic energy of molecules when particles absorb incident light only on the irradiated side, thus creating a temperature gradient within the particle [4, 5]. Direct photophoresis has been used to accomplish manipulation operations [6, 7]. When the light beam is sufficiently focused, the forces developed are strong enough to detach cells from the adherent surfaces in a technique known as laser catapulting [8, 9].

The challenge, then, is to engineer photonic devices that produce novel light fields that can reliably exert desirable forces onto particles. Such forces may include, the trapping of particles, spinning, stretching, pulling, pushing and so forth. To this end, we shall discuss two main technologies (a) Optical Tweezers and (b) Plasmonics.

2.1.1 Optical Tweezers

In 1970 Ashkin demonstrated that particles can be accelerated and trapped by light [10]. The principle behind the physics is relatively simple and was mathematically well described by James Clerk Maxwell [11] in 1873 as radiation pressure. A particle that is hit by a photon either loses or gains momentum and, in accordance with Newton's laws, experiences a net force. Sometime later, Ashkin demonstrated that the three-dimensional trapping of dielectric particles was possible using a single, highly focused laser beam [12]. Now, not only was light shown to *push* particles in its propagation direction, but it could also *pull* particles to regions of high intensity gradient. This can be visualized as a damped Hooke spring which exhibits a restoring force to the region of high intensity. This device, the optical tweezer, has become a cardinal tool for manipulating small particles. Ashkin's work broadened into a very active research field comprising two Nobel prizes for the laser cooling of atoms [13] and the creation of Bose-Einstein condensates in cold atomic gases [14]. In the biological sciences the optical tweezer is a favoured tool due to its non-mechanical nature of manipulation which dramatically reduces the chances of damaging biological specimens. For example it is used to study kinesin molecular movement [15], drug screening, [16], cell/particle sorting [17] and DNA mechanics [18]. Particles such as spheres, viruses, bacteria [19], living cells [20] and even strands of DNA [21] have been optically trapped and manipulated. Furthermore, the ability to transport and modify cells precisely has led to clinical applications such as in-vitro fertilization [22]. However, the trapping of biological particles near the focal point, which also happens to be the location of highest intensity of the beam, presents a problem in manipulating cells, where there have been reports of photodamage [23–25]. The damage is primarily caused by the lossy dielectric nature of the particle, i.e. the dielectric constant has an imaginary component causing it to absorb some of the incident energy thereby causing localized heating and thus *cooking* the cell.

Optical tweezers can trap objects as small as 5 nm [26, 27] and can exert forces exceeding 100 pN [28–30] with resolutions as fine as 100 aN [31, 32]. Their precise nature allows the selecting of individual microbes from heterogeneous populations. Using an optical tweezer to scan through multiple particles, dwelling briefly on each one, and then moving on can be used to trap multiple particles [33, 34]. This can be extremely useful for organizing planar assemblies of colloidal particles [35], for testing new ideas in statistical mechanics [36], and for measuring macromolecular interactions [37]. In such applications as those mentioned, where selectivity is required, it is crucial to ask: which particles can be trapped? To answer this, an appropriate model that can closely represent the physical problem is required to calculate the optical forces.

Due to its high symmetry, the numerical description of the optical trapping of spheres has been widely investigated [38–41]. In the traditional modeling of such scattering problems, such as in the work by Ashkin [41], the particle size is assumed to be typically a few micrometers. Together with the more convenient paraxial representation of a Gaussian beam (i.e., where the beam angle θ is relatively small and can be approximated by plane waves at different angles), means that the Ray Optics approximation is relatively successful at obtaining the scattered field and resultant optical force. While this approach is sufficient for most cases, the Ray Optics approximation is not a full solution to Maxwell’s equation and is limited to particle sizes such that $r \gg \lambda$, where r is the radius of the particle and λ is the wavelength of incident light. Alternatively, the scattering of smaller particles ($r \ll \lambda$) in an optical tweezer can be modeled with the Rayleigh approximation which represents the particles as single oscillating dipoles such that the scattered energy is much less than the energy intercepted by the particle.

Both these approaches are sufficient in their relative domains, however, they both lack any real ability to represent the rich near-field diffraction effects that can occur as the wavelength approaches the radius of the particle. A good example that is well known in literature is the extinction paradox. The paradox arises from the rather counterintuitive finding that the particle scatters twice the intercepted power, i.e. $\sigma_s = 2\sigma_g$, where σ_g denotes the amount of incident power, in terms of area, that is intercepted by a particle and σ_s denotes the scattered power, in terms of area. Among the most common explanations is that from van de Hulst [42] that relies on diffraction effects around the spherical particle. In fact the explanations of the extinction paradox is ongoing [43, 44].

The effective domains of these scattering regimes is depicted in Fig. (2.1). The Mie scattering regime was originally developed to solve the scattering of spherical particles with an incident plane wave [45]. This has since been extended to include arbitrary particles using the T-matrix [46, 47]. Soon after, a framework that could support arbitrary particles with arbitrary incident beams was developed. This is known as the *Generalized Lorenz-Mie Theory* (GLMT) that continues as an active field of research [48].

In recent years, perhaps the most well known method of modeling optical tweezers, is by using the Optical Tweezer Toolbox [39]. Based on the GLMT, the toolbox provides a framework to obtain the Gaussian beam coefficients, solve electromagnetic scattering and calculate the optical forces on spherical particles. Addressing the toolbox, a later work by Sun et. al has pointed out that the force predictions made with particle radii much smaller than the wavelength of light can be erroneous [49]. This, as was pointed out, was due to errors (by up to a factor of 10) generated by the Bessel function routines with small input arguments when the inbuilt recursive algorithm in MATLAB was used.

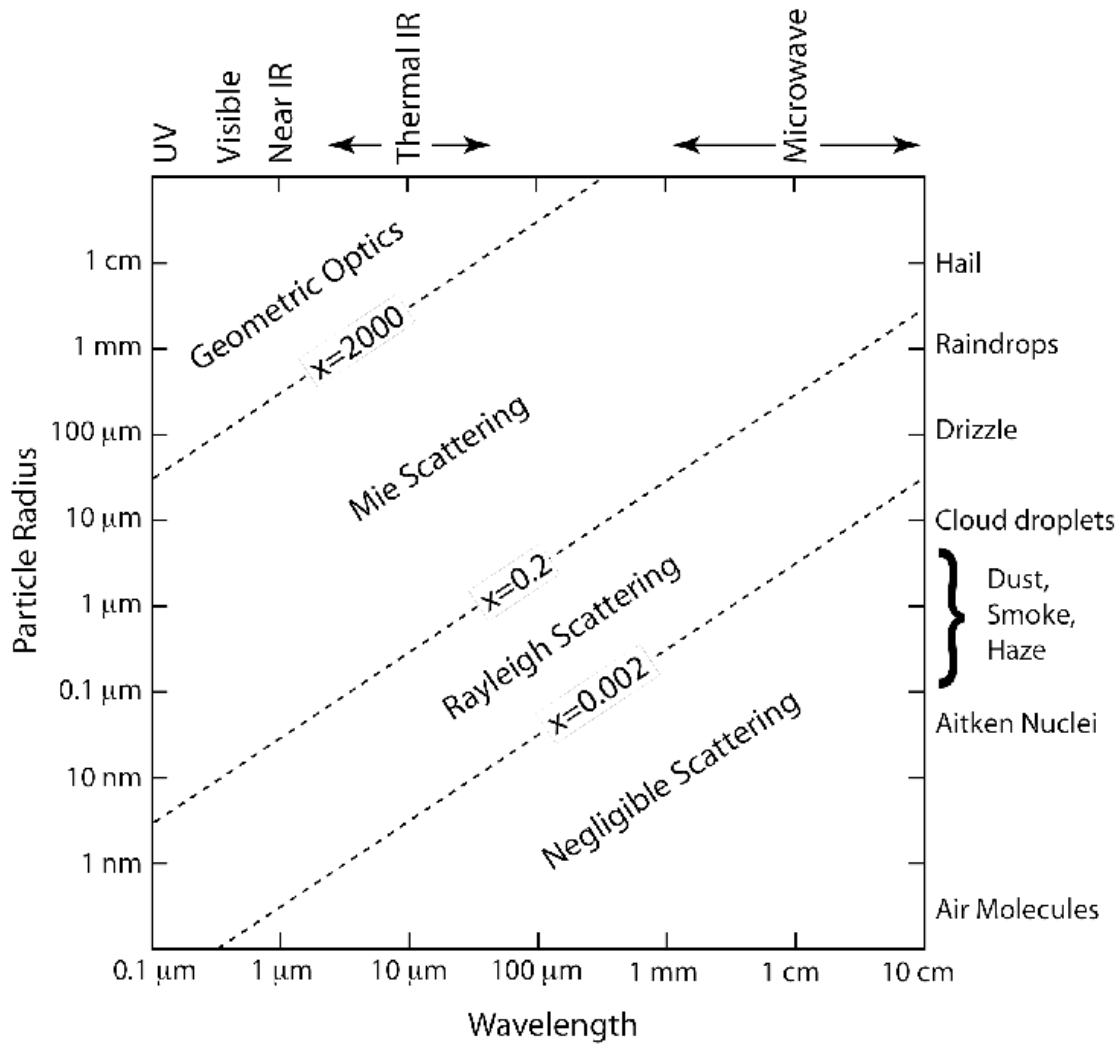


FIGURE 2.1: Effective wavelength versus particle size domains of the various scattering regimes. The domain of interest here is the Mie scattering region, where $r \approx \lambda$.

Here, small input arguments translate to mean small particles. In particular, the domain of inaccuracy pointed out was typically in the Rayleigh domain.

Utilizing this toolbox, some erstwhile studies have been conducted where it was briefly shown that certain interference and diffraction effects [50] could allow the trapping of high refractive index particles [51], i.e. $n_1 > 1.5n_2$, where n_1 and n_2 are refractive indices of the particle and surrounding medium, respectively. The effects of these extremely narrow band forward scattering modes allowed the formation of optical trapping “fingers”, i.e. areas in the parameter space of $(r, n_1/n_2)$ that traditional models of optical tweezers suggested that trapping was not possible. The rationalization of these structures was based on the correlation of peaks in the extinction coefficients with trapping. This basis is applicable only to lower Numerical Aperture (NA) Gaussian beams where the plane wave representation is closer. To the best of our knowledge, no map has been created

to date that fully depicts the trapping efficiency with respect to the three parameters, r , n_1/n_2 and NA, presumably due to the intensive computational demands of such an endeavor. The existence of such a map will be invaluable not only to establish the operational ranges of allowing the selecting of individual particles from heterogeneous populations with specificity, but also to exploit novel applications. For example, the ability to trap high refractive index microspheres (made from materials such as silicon, which have $n_1 = 3.5$) that typically have good optical confinement properties, makes them ideal for use in creating microcavities with very high Q-factor resonances [52, 53].

Other applications of optical tweezers have been in Photonic Force Microscopy (PFM), wherein the ability to detect very small position changes of the trapped particle is used as a probe to scan the local environment forces [54]. Photonic force microscopy relies on the collection of the scattered and unscattered light by means of a quadrant photo-diode, where a phase shift is detected and used to calculate the position. Furthermore, engineered laser beam profiles such as a self-restoring Airy beam [55] and a non-diffracting Bessel beam [56] have been used to enable particle transport along curved paths [57], trap particles [58] and construct conveyor belts [59]. These applications suggest that particle manipulation mechanisms can be achieved by designing novel light fields, which can be modularly integrated into lab-on-chip environments.

In the pursuit of lab-on-chip solutions, the diffraction limit is perhaps the most restricting principle in optics. One of its consequences is that light of wavelength λ exiting from a region much smaller than $\lambda/2$ undergoes a strong angular spread and fills out the whole 2π solid angle. In fact this principle can be considered a specialization of Heisenberg's uncertainty principle with respect to position (δx) and momentum ($p = \hbar\lambda$) [60]. The typical range of wavelengths used for particle manipulation are anywhere from $\lambda = 300\text{nm}$ to $\lambda = 1500\text{nm}$. Couple this with the ongoing improvement of fabrication techniques that allow for smaller and smaller feature sizes in chips (45nm is commercially available) and the diffraction limit immediately becomes discernible. For the purpose of particle manipulation, the diffraction limit is detrimental since light cannot be well localized to permit the transfer of momentum to particles. The diffraction limit becomes less of a deterrent if the concept of free wave propagation is abandoned and evanescent waves are used, which are classified as optical near-fields [61]. In recent years, various experiments based on near-field trapping and manipulation have emerged. In these experiments, the near-field was generated in the form of an evanescent wave at the interface between two different media [62–66]. Compared to a conventional optical tweezer, trapping based on near-field provides a significant improvement in that it does not require complicated optics to create the optical trapping landscape. For this reason they can be easily integrated into lab-on-a-chip applications in order to produce novel chips with increased functionality. The two most practical candidates for addressing

these lab-on-chip requirements are Photonic Crystals (PC) and Plasmonics. A review of Plasmonics is found in the next section 2.1.2. To progress on to feasible lab-on-a-chip applications, nevertheless, it will be necessary to attain the ability to carry out trapping at selected spatial locations at prescribed time sequences.

2.1.2 Plasmonics

The term plasmonics refers to the science and technology dealing with the manipulation of electromagnetic signals by coherent coupling of photons to free electron oscillation at an interface between a metal and a dielectric. At this interface a strongly enhanced optical near-field confined to the metal surface can be excited. This confined near-field is known as a Surface Plasmon Polariton (SPP). To obtain a surface bound solution from Maxwell's equations, it is required that the normal components of the wave-vector be purely imaginary in both media giving rise to evanescent solutions. Propagation in the direction parallel to the interface is also required.

The surface plasmon modes have greater momentum than a free space photon of the same frequency which therefore means that *free* light cannot be directly coupled to the surface plasmon mode on a flat metal surface. For this reason, various geometries are used to match the wave-vector and simultaneously conserve energy and momentum (wave-vector). One such geometry is the Kretschmann geometry using a prism [67]. This method requires the integration of an additional excitation structure within the device to excite the surface modes, thus rendering it inefficient for lab-on-chip purposes.

Another geometry utilizes a metal surface with corrugated grooves. The periodic nature of the corrugated grooves can *boost* the incident wave-vector by $2\pi n/a$ and thus a surface plasmon mode can be excited. The gratings on the metal substrate need to be designed so as to match the impinging light with the resonance condition. Considering this point, in the first respect, it would be readily expected that these surface gratings on a metal substrate not only act as a passage for impinging light to become an SPP, but also are able to serve as an outlet for an SPP to radiate light. This property is the key concept behind generating collimated beaming from subwavelength apertures [68].

The use of evanescent fields, in particular plasmon fields, emanating from a subwavelength aperture or from a probe, have been shown to be effective for sometime in addressing the need for strong optical trapping at the subwavelength scale and in a coplanar geometry. A single subwavelength aperture is compact, amenable to integration and insensitive to the incident angle of light whilst providing the necessary matching wave-vectors to excite surface modes [69]. Recent advances reported have begun to tackle the need to have optical trapping at specific and selective locations over the chip as well;

which holds great promise for lab-on-a-chip purposes. A seminal scheme reported for this involved creating plasmonic standing waves from the interference of laser beams [70]; which essentially translated the known ability of standing waves to trap effectively at multiple sites in the axial sense [71] to a lateral geometry. Yet, the alternative approach of tailoring metallic surfaces to create multiple trapping sites from whole-field illumination [72–74] has been shown to be more convenient and practical. As mentioned, it will be necessary to attain the ability to carry out trapping at selected spatial locations at prescribed time sequences. This will be conceivably difficult to accomplish using schemes that depend on the whole field light stimulation of plasmons unless the onerous challenge of creating fine and high intensity probe beams is met.

The strong beaming of light from subwavelength aperture surrounded by surface corrugations on a thin metal film was first demonstrated by Lezel et. al. [68]. Since then, there have been substantial efforts made to understand the underlying physics of the phenomena [75] with the interest of facilitating directional light beaming at the chip level [76]. An interesting discovery has been the contribution of leaky plasmon waves in affecting the characteristics of light beaming [77]. There has been no reporting of efforts to harness these leaky waves to create tailored optical trapping sites on the metallic surface. The ability to do this opens up the avenue of having multiple apertures on the surface addressable using waveguides within the chip in order to maintain close control of optical trapping at specific and selective locations over the entire chip.

Another need in particle manipulation is the ability to trap particles into rings which is typically achieved using an axicon [78]. Some efforts have been reported to utilize phase matching with photonic structures to permit subwavelength fields [79]. The availability of optical forces on a chip allows for the assembly of nanoparticles beyond the use of means such as evaporation where a degree of randomness can be expected. Once held in place, tailored patches within the nanoparticle will be able to hold such assemblies in place when optical forces are switched off [80]. Surface plasmons are an excellent candidate for such purposes since the fields are inherently subwavelength with strong plasmon intensity fields.

2.2 Brownian Dynamics

Mobile particles immersed in an ambient medium undergo an incessant and irregular motion. Robert Brown in 1827 [81], while examining grains of pollen of the plant *Clarika pulchella* suspended in water observed, under a microscope, that they had a continuous jittery motion. By further observing the same motion in particles of inorganic matter

he had ruled out that the effect was life-related. This phenomena is now known as Brownian motion.

For a particle of radius 1 mm in water the motion can hardly be noticed, while for particles on the edge of microscopic visibility the motion is marked. There is a definite dependence on the nature of the fluid medium, and especially on its viscosity. Another characteristic of Brownian motion is its stability in time. The motion persists as long as the particles remain suspended in the fluid. This has been observed in preparations allowed to stand for over a year. A final very characteristic property is independence of most external influences. Electric fields, light (as long as it is not absorbed and does not heat the system), gravity (as long as the particles do not settle out) and similar disturbances from the outside seem to have no effect. Temperature has a marked effect, however. This could be expected from the observation that the motion depends on the viscosity of the medium; as is well known, the viscosity of fluids is appreciably temperature dependent.

The Brownian motion of spherical particles in an unbounded fluid volume was first established by Einstein [82, 83] and Smoluchowski [84]. In confined spaces, there is an interaction between the particles and the surrounding walls, and considerable advances have been made into understanding the ensuing motion under such conditions [85–87]. When considering Brownian rods, it is necessary to consider the various rotational and translational frictions [88, 89]. In two-dimensions, this leads to differential diffusion equations based on a rotational constant and translation constant parallel and perpendicular to the particle’s long axis. The result is that the anisotropic behaviour ensues in the short term and crosses over to isotropic behaviour in the longer term (when considered from a static axis system) as shown recently experimentally [90]. As for spheres, when the proximity of a wall is considered, hydrodynamic interactions occur. In the case of a rod this has been shown to significantly reduce the diffusion constants, the effect being the strongest on the translational diffusion coefficient along the rod when compared with that perpendicular to the length of rod [91]. A description of the mechanics for this was furnished via experiments using different chamber thicknesses, and thus, degrees of constraining [92]. It was found that when an ellipsoidal Brownian particle is approximately neutrally buoyant, it is most likely to reside close to the central plane of a thin fluid chamber, [90] this being an entropic effect: the number of possible orientations is reduced when the center-of-mass of an elongated particle is close to a wall [93]. Such hydrodynamic interactions affecting rods have also been modeled recently [94].

An account of how Brownian rods are able to end-tether naturally to surfaces [95] underlines a rotational-translational coupling. While this tethering behavior may allow

information on the micro-environment to be interrogated, it is hampered by opportunistic ventures of the free end towards the surface to cause the motion to cease altogether. A recent scheme has been reported to overcome these limitations wherein a Brownian rod is drawn in by a tunable attractive force from a cylindrical pillar [96]. This approach requires the rotational diffusion to be derived from image sequences of the rod's movement, which is possible when the rod dimensions are diffraction resolvable optically but, crucially, not when a nano scale rod is used.

Brownian motion is often detrimental to sorting as a consequence of fluctuating forces that lead to distributions spreading [97]. Despite this, considerable work has been conducted to exploit the size based variations in diffusion as a sorting metric in itself. Asymmetric periodic potentials have been actively investigated to rectify the symmetric fluctuations in Brownian particles [98–104]. A convenient scheme to accomplish this is via the switching on and off (conveniently described as cycling) of a periodic but spatially anisotropic potential [99, 100]. Such stochastic ratchets have been demonstrated as capable of sorting spherical Brownian particles [101]. It is vital to therefore examine the possibility of using such stochastic ratchets to sort populations of Brownian rods, investigating, in particular, the role that the crossover time from anisotropic to isotropic motion takes in this process.

Further to sorting, the nature of Brownian motion can be exploited by tracking the motion of particles as a means to sense the local environment [105]. Arguably, the first experiment to physically demonstrate this was based on measuring the milli-Kelvin temperatures in electrical circuits [106]. Deriving information of parameters such as temperature and viscosity from the liquid micro-environment is crucial for processes that involve electrochemistry and biology. Tracking a single Brownian particle's motion offers an attractive means of measuring the localized parameters at its immediate vicinity. The merits of such a sensor include its minimal disturbance to the evolution of the measured quantity around the localized environment and an absence of any input energy to drive the probe [107]. Some recent adaptations have been reported to ascertain parameters such as magnetic susceptibility and surface forces [108–110]. While fluctuations in Brownian motion using freely translating particles should provide inexhaustible amounts of information, there is the problem of these particles drifting away from the venue of measurement as well as colliding with other particles. The former causes the problem of lapses in measurement continuity. This can be mitigated somewhat by use of external forces to restrict the particle to a specific location (e.g., optical traps) [97]. Nevertheless, this and the latter issue of collisions tend to introduce additional complexity in interpreting the underlying mechanics [111].

One means of tracking nano-scale objects with an optical microscope is by using fluorescence labeling. A major drawback of this is the limited observation time due to photo-bleaching (organic dyes) and the erratic signal due to blinking. Alternatively, gold and silver nano-particles show strong light scattering at the plasmon resonance wavelength due to the collective oscillation of their conduction electrons. By imaging only the scattered light from a sample [112], it has been claimed that the detection of particles down to 20 nm in size is possible. That the scattered light is strongly polarized along the long axis makes gold nano-rods in principle an ideal orientation probe. The use of a birefringent crystal to create twin images of a nano-rod at orthogonal polarizations had been reported as a means to track its rotational and translation venture [113]. This approach is limited by the accuracy of correlating the rotational state of the rod to the intensity variations associated to the two polarization states in the image. More robust information can be gleaned from interrogating the surface plasmon interaction instead. Surface plasmon resonance (SPR) is well understood as the collective oscillation of electrons in a solid or liquid stimulated by incident light. SPR is the basis of many standard tools for measuring adsorption of material onto planar metal surfaces, giving rise to the fundamental principle behind many bio-sensor applications and different lab-on-a-chip sensors [114]. Optical resonators, by virtue of their confinement properties, have been proposed to provide higher sensitivity measurements of fluctuations in scattering and/or absorption of nearby particles [115–117]. By combining the benefits of highly sensitive optical resonators with plasmonic nano-rods there exists an opportunity to develop an enhanced sensing and tracking scheme of Brownian motion.

2.3 Discrete Liquid Mechanics

Since the advent of technology able to create structures at the micron and smaller length scales, there has been a wide range of scientific investigations into, as well as the development of devices to transport and manipulate fluids at the micron scale [118]. These types of investigations involving fluids, aptly known as microfluidics, have rekindled research interest in fluid dynamics where the Reynolds number is low [119]. The multi-disciplinary nature of microfluidics involves fundamental concepts from a broad range of fields from biology to electrical engineering. Thus, it generates an equally diverse array of applications that includes, genetic analysis of influenza [120], miniaturized systems for biological analysis [121] and bioreactions [122], clinical diagnostics [123, 124], organic synthesis [125], microreactors [126, 127] and immunoassays [128].

Using only a fraction of the volume of reagents typically used in laboratory operations, microfluidics holds great promise. Reducing reagent use from milliliters and microliters

to nano or even femtoliters allows for the reduction of reaction times to mere seconds or less. Alternatively, droplet based microfluidics, also known as discrete or digital microfluidics, is a subcategory of microfluidics unlike the typical continuous flow systems, where a discrete volume of liquid is created with the use of immiscible phases [129]. This is not unlike the chemical and biological operations that are typically carried out in nature, for example in cells and their organelles. Inherent at these scales is the high surface area to volume ratios, heat and mass transfer times and shorter diffusion distances, which again allows for faster reaction times. The independent control of each droplet allows for individually transported, mixed and analyzed microreactors. Furthermore, the highly monodisperse nature of the droplets permits parallel processing and experimentation, thereby enhancing throughput and scalability. A wealth of technologies for improved droplet generation, intra-droplet content manipulation, and methods for controlled trafficking, all enabled a wide range of appealing applications [130, 131] from chemical kinetics [132] and crystallization [133, 134] to material synthesis [135] and single cell analysis [136].

The power, and critical factor, of droplet based microfluidic systems lies in the formation of uniform droplets and particles. Since biological and chemical properties of microparticles are strongly affected by both the size and morphology, it is essential to be able to generate these structures at well-defined volumes and composition. Obtaining fine control over size, shape, and monodispersity of droplets is of utmost importance in droplet microfluidics. A number of techniques have been developed, many of which share the same basic principles. The first is in the form of an emulsion created using two immiscible fluids such as water and oil [137]. Alternatively, air-liquid systems have also been shown to be feasible [138].

It is often useful to look to nature for inspiration to a solution of such problems. Nature provides an inexhaustible source of functional surfaces. Plants and animals have developed surfaces with special wettability ranging from highly slippery to highly sticky surfaces. The surface wettability is measured by the contact angle which a droplet forms when it is put on the surface. Well known examples include the lotus leaves and the legs of water striders [139, 140]. On a slippery surface, the droplets do not penetrate the unevenness of the surface, and thus the interactions with the surface are lowered. The means to develop superhydrophobic surfaces has been a hot research topic. A common theme amongst these methods is to artificially mimic superhydrophobic surfaces found in nature [141–145].

Initially superhydrophobicity provided a means of engineering self-cleaning, anti-contamination and anti-sticking surfaces. Now, there is substantial effort aimed at harnessing it for biochemical applications [146–151]. In the context of discrete droplets mentioned, the

ability of superhydrophobic surfaces to provide a means to transport analytes or samples is a crucial component. Typically, the adhesion forces of liquid drops on superhydrophobic surfaces are in the nano-Newton range [152]. This presents a real problem in the dispensation of liquid drops from pipettes. The use of flexible pipette tips [148] permits drop volumes down to around $10\mu\text{L}$ to be deposited, albeit this requires careful execution in order for them not to contact the surface which could damage the nano and micro features that enable superhydrophobicity.

The quest to develop bioanalysis tools based on superhydrophobicity is also founded on the issues of availability and cost. Many researchers in resource-limited developing countries, or field workers in remote locations far from modern conveniences, have been unable to take advantage of modern bioanalytical techniques due to a lack of infrastructure. Not surprisingly, there have been recent efforts expended to use alternative materials such as paper to serve as the analyte handling media [153]. This approach, while useful for methods based on electrochemical detection, is not as effective for methods that are based on optical detection, that arguably offers the highest versatility and sensitivity. Alternative cost effective approaches have since been reported [154, 155]. Despite this, paper remains indispensable as a relatively cheap, compact and robust reservoir for test samples and biochemical analytes. The ability to deliver drops of specific volumes, that can be developed into a cost effective device permitting transport, is a crucial necessity in remote laboratory environments that needs to be addressed.

2.3.1 Microplates

The microplate (multiwell plate or microtiter plate) has become a standard tool in analytical research and clinical diagnostic testing laboratories. In microplate instrumentation, the trend is moving towards testing increasingly smaller liquid volumes [156–159]. Smaller test volumes (i) increase the number of assays that can be conducted per plate thereby increasing throughput, and (ii) reduce sample quantity needed per assay which is crucial when the test samples/reagents are scarce or expensive. In dealing with miniaturized assays, alternative approaches have been developed to handle small liquid volumes, their preparation and testing without the need for complex or precise machinery [156, 159] or limitations from wetting [160]. Yet, there is also impetus to create microplates that are cost effective enough to be available for use in resource-limited laboratories so that diagnostic outcomes can be achieved in a more timely fashion. Two approaches that have been advanced recently to address this without affecting the efficacy in optical diagnosis are through the use of samples on transparencies [154, 155] and between rods [161].

It is sometimes necessary to incubate samples for prolonged periods in microplates. In such situations, the influence of evaporation cannot be overlooked. One aspect that needs to be considered is the effect on wetting. The contact angle (CA) of a liquid on a solid surface is widely considered to be a key parameter that characterizes wetting behavior. The CA is most universally defined as the angle between the liquid-vapor and the solid-liquid interfaces, at the point where the three phases (solid, liquid, and gas) meet.

Some treated surfaces are high-energy and permit liquids to spread spontaneously on them [162, 163]. Most surfaces, however, do not exhibit this property, resulting in the formation of a drop. Surfaces that cause the CA to be smaller than 90° are defined as hydrophilic while those that engender a CA larger than 90° are classified as hydrophobic. By using chemical treatments to develop nano-scale structures on surfaces, it is possible to achieve contact angles that are close to 180° , which are increasingly harnessed for use in applications that require high degrees of non-wetting [148, 164]. Arguably, the most widely used method to determine the CA of a sessile drop is by direct imaging of its side-profile [165–167]. In another method called the Wilhelmy balance, the contact angle is deduced from the force exerted by the liquid on a small plate or ring, which is advanced to and/or receded from the liquid [168]. The use of contact between a spherical lens and liquid bath has been advanced as yet another means of determining the contact angle [169], which apparently is suited for characterizing surfaces with very low contact angle hysteresis.

The sessile drop method is prone to the problem of evaporation due to the large proportion of liquid surface area exposed to air. From the outset, it has been established that the process involves stages where the drop is either pinned at the contact line, or that the contact line undergoes slipping. Efforts to characterize the evaporation of drops can arguably be traced to the analysis of Picknett and Bexon [170]. Since then, other models have appeared in an attempt to better account for evaporation flux distribution [171]. In all these models, the underlying basis of a sessile drop situated on a solid surface is that the adjacent air becomes saturated with vapor due to the rapid interchange of the molecules between the liquid and its vapor. The vapor is essentially then a thin saturated region that diffuses outward into the surrounding unsaturated air. Assuming a quasi-equilibrium process for slow evaporation in still air, the evaporation rate of the vapor Q can be taken to be represented by Fick's law such that

$$Q = \rho \frac{dV}{dt} = 4\pi DR(C_s - C_\infty)f(\theta) \quad (2.1)$$

where D is the vapor diffusivity in still air, R radius of drop surface curvature, C_s the saturated vapor concentration at drop surface, C_∞ the ambient vapor concentration

determined by the relative humidity, and $f(\theta)$ is the dependence of evaporation rate on the contact angle. The models to describe the temporal evolution of a drop volume require the functional form of $f(\theta)$ and the temporal variations of R and θ to be known a priori. Recent studies have shown $f(\theta)$ to be dependent on the nature of the surface since porous types can cause the liquid to imbibe in them such that it enters into a strongly Wenzel wetting state [172]. However, the determination of $f(\theta)$ may be side stepped if the objective is to trace the progression of the contact angle due to pinning and slipping. In addition, the volume trace may also be determined via computations based on the geometrical shape of the liquid body to sufficiently depict the mechanics.

In contrast to the sessile drop, an approach based on determining the height of a laser lighted meniscus in capillaries offers an alternative means to trace the contact angle progression with time [173]. The heightened level of liquid confinement offered there is helpful in reducing the extent of evaporation. Nevertheless, this approach is suited more to interrogating the wetting behavior of different liquids than variations in the surface itself as (i) modifying treatments and (ii) microscopic examination, will generally be difficult to carry out on the inner surfaces of the capillary. Clearly, surfaces that offer improved resistance to evaporation and are yet easily accessible will be beneficial.

Liquid bodies that are placed between surfaces will develop capillary bridges. The compression of this body between two flat parallel plates creates the condition for growth of the menisci in which its stability can be established [174]. This has also been studied in the case of tension, leading to important application implications in colloidal microstructure formation [175], biological system attachment [176] and flow generation and transfer [177]. Capillary bridges too form when the liquid body is placed between circular rods [178] and this has been recently applied to serve as a biochemical microplating device with the ability for mixing [161]. The feasibility of using the capillary bridges developed between solid bodies as well as the contact angle developed under evaporation need to be investigated. These findings will help to provide insights on the ability to relate wetting to analyte characteristics and mitigate evaporation in biochemical microplating schemes developed for use in resource-limited laboratories.

Chapter 3

Background Theory

In this chapter we cover the background theory of the simulation techniques used in the following chapters. In particular, optical scattering and basis of plasmonics is discussed.

3.1 Electromagnetics Preliminaries

In differential form and in SI units the macroscopic Maxwell's equations have the form

$$\nabla \times \mathbf{E}(\mathbf{r}, t) = -\frac{\partial \mathbf{B}(\mathbf{r}, t)}{\partial t} \quad (3.1a)$$

$$\nabla \times \mathbf{H}(\mathbf{r}, t) = -\frac{\partial \mathbf{D}(\mathbf{r}, t)}{\partial t} + \mathbf{J}(\mathbf{r}, t) \quad (3.1b)$$

$$\nabla \cdot \mathbf{D}(\mathbf{r}, t) = \rho(\mathbf{r}, t) \quad (3.1c)$$

$$\nabla \cdot \mathbf{B}(\mathbf{r}, t) = 0 \quad (3.1d)$$

where \mathbf{E} denotes the electric field, \mathbf{D} the electric displacement, \mathbf{H} the magnetic field, \mathbf{B} the magnetic induction, \mathbf{J} the current density, and ρ the charge density. The components of these vector and scalar fields constitute a set of 16 unknowns. The electromagnetic properties of the medium are most commonly discussed in terms of macroscopic polarization \mathbf{P} and magnetization \mathbf{M} according to

$$\mathbf{D}(\mathbf{r}, t) = \epsilon_0 \mathbf{E}(\mathbf{r}, t) + \mathbf{P}(\mathbf{r}, t) \quad (3.2a)$$

$$\mathbf{H}(\mathbf{r}, t) = \frac{1}{\mu_0} \mathbf{B}(\mathbf{r}, t) - \mathbf{M}(\mathbf{r}, t) \quad (3.2b)$$

where ϵ_0 and μ_0 are the permittivity and permeability of vacuum, respectively. Substituting the fields \mathbf{D} and \mathbf{B} in Eq. (3.1a) and (3.1b) using the expressions Eq. (3.2a) and

(3.2b) we obtain two resulting equations

$$\nabla \times \nabla \times \mathbf{E} + \frac{1}{c^2} \frac{\partial^2 \mathbf{E}}{\partial t^2} = -\mu_0 \frac{\partial}{\partial t} \left(\mathbf{J} + \frac{\partial \mathbf{P}}{\partial t} + \nabla \times \mathbf{M} \right) \quad (3.3a)$$

$$\nabla \times \nabla \times \mathbf{H} + \frac{1}{c^2} \frac{\partial^2 \mathbf{H}}{\partial t^2} = \nabla \times \mathbf{J} + \nabla \times \frac{\partial \mathbf{P}}{\partial t} + \mu_0 \frac{\partial \mathbf{M}}{\partial t}. \quad (3.3b)$$

The constant c is known as the speed of light and is given in terms of the vacuum permittivity and permeability as $c = (\epsilon_0 \mu_0)^{-1/2}$. Maxwell's equations define the fields that are generated by currents and charges in matter. However, they do not describe how these currents and charges are generated. For this we require the material equations known as the constitutive relations. In a non-dispersive and isotropic medium they have the form

$$\mathbf{D} = \epsilon_0 \epsilon \mathbf{E} \quad (\mathbf{P} = \epsilon_0 \chi_e \mathbf{E}) \quad (3.4a)$$

$$\mathbf{B} = \mu_0 \mu \mathbf{H} \quad (\mathbf{M} = \chi_m \mathbf{H}) \quad (3.4b)$$

$$\mathbf{J}_c = \sigma \mathbf{E} \quad (3.4c)$$

where χ_e and χ_m denote the electric and magnetic susceptibility, ϵ and μ denote the relative permittivity (dielectric constant) and permeability, and σ denotes the conductivity, respectively. The total current density \mathbf{J}_t is a sum of free and bound currents, \mathbf{J}_b and \mathbf{J}_f , written as

$$\mathbf{J}_t = \mathbf{J}_f + \mathbf{J}_b \quad (3.5a)$$

$$\mathbf{J}_f = \mathbf{J}_s + \mathbf{J}_c = \mathbf{J}_s + \sigma \mathbf{E} \quad (3.5b)$$

$$\mathbf{J}_b = \left(\frac{\partial \mathbf{P}}{\partial t} + \nabla \times \mathbf{M} \right) \quad (3.5c)$$

where \mathbf{J}_s , \mathbf{J}_c , $\frac{\partial \mathbf{P}}{\partial t}$ and $\nabla \times \mathbf{M}$ are the source, induced (Eq. 3.4c), polarization and magnetization currents, respectively. We have assumed a linearity of the material so that both \mathbf{P} and \mathbf{M} contain only linear terms. In the above notation the variables ϵ and μ can be represented as functions of frequency, ω , and/or position, \mathbf{r} . Furthermore, they can be represented as 3×3 tensors for anisotropic material. At an interface between two different material, denoted i and j , the boundary conditions for Maxwell's equations can be split into those relating to the tangential components

$$\begin{aligned} \mathbf{n} \times (\mathbf{E}_i - \mathbf{E}_j) &= 0 \\ \mathbf{n} \times (\mathbf{H}_i - \mathbf{H}_j) &= \mathbf{K} \end{aligned} \quad (3.6)$$

where \mathbf{n} is the unit normal vector on the boundary and \mathbf{K} is the surface current density. If the fields are considered to be homogenous on both sides and if a surface charge

density σ is assumed, the boundary conditions for the normal field components become

$$\begin{aligned}\mathbf{n} \cdot (\mathbf{D}_i - \mathbf{D}_j) &= \sigma \\ \mathbf{n} \cdot (\mathbf{B}_i - \mathbf{B}_j) &= 0\end{aligned}\tag{3.7}$$

In most practical situations there are no sources in the individual domains, and therefore \mathbf{K} and σ consequently vanish. The time dependence of a non-harmonic electromagnetic field can be Fourier transformed and every spectral component can be treated separately as a monochromatic field. The general time dependence is obtain from the inverse transform. The time dependence in the wave equations can be easily separated to obtain a harmonic differential equation. A monochromatic field can then be written as

$$\mathbf{E}(\mathbf{r}, t) = \text{Re}\{\mathbf{E}(\mathbf{r})e^{-i\omega t}\} = \frac{1}{2} [\mathbf{E}(\mathbf{r})e^{-i\omega t} + \mathbf{E}^*(\mathbf{r})e^{i\omega t}],\tag{3.8}$$

that allows Maxwell's equations to then be written as

$$\nabla \times \mathbf{E}(\mathbf{r}) = i\omega\mathbf{B}(\mathbf{r})\tag{3.9a}$$

$$\nabla \times \mathbf{H}(\mathbf{r}) = -i\omega\mathbf{D}(\mathbf{r}) + \mathbf{J}(\mathbf{r})\tag{3.9b}$$

$$\nabla \cdot \mathbf{D}(\mathbf{r}) = \rho(\mathbf{r})\tag{3.9c}$$

$$\nabla \cdot \mathbf{B}(\mathbf{r}) = 0\tag{3.9d}$$

which is equivalent to Maxwell's equations Eq. (3.1) for the spectra of arbitrary time-dependent fields. Using Eqs. (3.4) and (3.5) in Eq. (3.9a) and Eq. (3.9b) we obtain

$$\nabla \times \mathbf{E} = i\omega\mu_0\mu\mathbf{H}\tag{3.10a}$$

$$\nabla \times \mathbf{H} = -i\omega\epsilon_0\varepsilon\mathbf{E} + (\mathbf{J}_s + \sigma\mathbf{E})\tag{3.10b}$$

which can, after applying the curl to Eq. (3.10a) and substituting Eq. (3.10b), be arranged to obtain

$$\begin{aligned}\nabla \times \frac{1}{\mu}\nabla \times \mathbf{E} &= i\omega\mu\nabla \times \mathbf{H} \\ &= \omega^2\mu_0\epsilon_0\varepsilon\mathbf{E} + i\omega\mu_0\sigma\mathbf{E} + i\omega\mu_0\mathbf{J}_s \\ &= \frac{\omega^2}{c^2}(\varepsilon + i\sigma/(\omega\epsilon_0))\mathbf{E} + i\omega\mu_0\mathbf{J}_s.\end{aligned}\tag{3.11}$$

The first term on the right hand side of Eq. (3.11) can be used to define the complex dielectric function that is dispersive (i.e. depends on ω),

$$\varepsilon(\omega) + i\sigma(\omega)/(\omega\epsilon_0) \rightarrow \varepsilon(\omega)\tag{3.12}$$

Utilizing the vector identity $\nabla \times \nabla \times = -\nabla^2 + \nabla \nabla \cdot$, and defining the wavenumber $k = (\omega/c)\sqrt{\mu\epsilon}$ we obtain the inhomogenous vector Helmholtz equation:

$$(\nabla^2 - k^2) \mathbf{E} = -i\omega\mu_0\mu\mathbf{J}_s \quad (3.13)$$

If we assume a homogenous (source free) problem then one of the equations in Eq. (3.13) can be written in spherical coordinates as a scalar equation

$$\left[\frac{1}{r^2} \frac{\partial}{\partial r} \left(r^2 \frac{\partial}{\partial r} \right) + \frac{1}{r^2 \sin\theta} \frac{\partial}{\partial \theta} \left(\sin\theta \frac{\partial}{\partial \theta} \right) + \frac{1}{r^2 \sin^2\theta} \frac{\partial^2}{\partial \phi^2} + k^2 \right] \psi(\mathbf{r}) = 0. \quad (3.14)$$

where $\psi(\mathbf{r})$ can be any one of the three components of \mathbf{E} . The general outgoing wave solution to Eq. (3.14) is known and has the form

$$\psi_{mn}(kr, \theta, \phi) = h_n^{(p)}(kr) P_n^m(\cos\theta) e^{im\phi} \quad (3.15)$$

with $n = 0, 1, 2, \dots$ and $m = 0, \pm 1, \dots, \pm n$. In Eq. (3.15) the function $h_n^{(1)}$ is the spherical Hankel function of the first kind and P_n^m is the associated Legendre function. The RHS terms, sans the spherical Hankel function, is also known as the spherical harmonic given by

$$Y_n^m = P_n^m(\cos\theta) e^{im\phi} \quad (3.16)$$

The scalar solution in Eq. (3.14) is not a vector solution to Helmholtz equation. For this, we require the vector spherical harmonics, defined by [179] [180]

$$\mathbf{B}_{nm}(\theta, \phi) = \mathbf{r} \nabla Y_n^m(\theta, \phi) \quad (3.17a)$$

$$\mathbf{C}_{nm}(\theta, \phi) = \nabla \times (\mathbf{r} Y_n^m(\theta, \phi)) \quad (3.17b)$$

$$\mathbf{P}_{nm}(\theta, \phi) = \hat{\mathbf{r}} Y_n^m(\theta, \phi) \quad (3.17c)$$

The vector spherical wavefunctions (VSWFs) are thus defined as

$$\begin{aligned} \mathbf{M}_{mn}^{(1,2)}(k\mathbf{r}) &= N_n h_n^{(1,2)}(kr) \mathbf{C}_{nm}(\theta, \phi) \\ \mathbf{N}_{mn}^{(1,2)}(k\mathbf{r}) &= \frac{h_n^{(1,2)}(kr)}{kr N_n} \mathbf{P}_{nm}(\theta, \phi) + N_n \left(h_{n-1}^{(1,2)}(kr) - \frac{nh_n^{(1,2)}(kr)}{kr} \right) \\ &\quad \times \mathbf{B}_{nm}(\theta, \phi) \end{aligned} \quad (3.18)$$

where $N_n = 1/\sqrt{n(n+1)}$ are normalization constants and the operator \mathbf{Rg} represents the regularization operator such that $\mathbf{RgM}(kr) = \frac{1}{2} [\mathbf{M}_{mn}^{(1)}(kr) + \mathbf{M}_{mn}^{(2)}(kr)]$. This corresponds to a singularity-free representation of the incoming and outgoing VSWFs. They

both satisfy the vector Helmholtz equation:

$$\nabla \times \nabla \times Rg\mathbf{M}_{mn} - k^2 Rg\mathbf{M}_{mn} = 0 \quad (3.19a)$$

$$\nabla \times \nabla \times Rg\mathbf{N}_{mn} - k^2 Rg\mathbf{N}_{mn} = 0 \quad (3.19b)$$

so that a linear expansion over m and n are solutions to Eq. (3.13). The VSWFs in Eq. (3.18) when taken to the large r limit lose their radial components, becoming

$$\lim_{kr \gg n^2} \mathbf{M}_{mn}^{(1,2)}(kr) \simeq \frac{N_n}{kr} (\mp i)^{n+1} e^{\pm ikr} \mathbf{C}_{mn}(\theta, \phi) \quad (3.20a)$$

$$\lim_{kr \gg n^2} \mathbf{N}_{mn}^{(1,2)}(kr) \simeq \frac{N_n}{kr} (\mp i)^n e^{\pm ikr} \mathbf{B}_{mn}(\theta, \phi) \quad (3.20b)$$

3.2 Scattering Problem

Consider an electromagnetic wave focussed at \mathbf{r}_f impinging upon a spherical particle of radius r with a refractive index of n_1 located at \mathbf{r}_p that is suspended in a liquid with refractive index of n_2 , (Fig. 3.1). The particle scatters a quantity of the incident wave in all directions that can be characterized by its full scattering matrix (S-Matrix). We pick the origin of the scattering system so that $\mathbf{r}_p = (0, 0, 0)$.

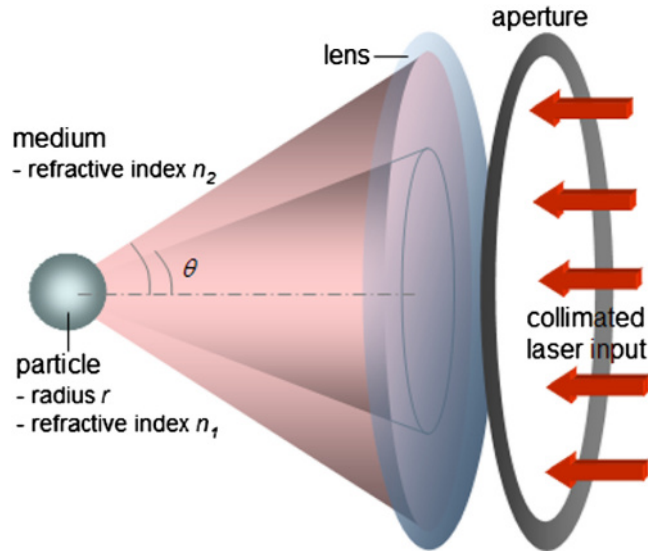


FIGURE 3.1: Efficiency in trapping a spherical particle using a focusing laser beam is dependent on its radius r and refractive index n_1 , the refractive index of the medium n_2 , and the NA of the light beam, which is a function of the half-angle.

With GLMT, the incident and scattered fields can be expanded using Eq. (3.19) so that we have

$$\mathbf{E}_{inc}(\mathbf{r}) = \sum_{n=1}^{\infty} \sum_{m=-n}^n a_{nm} \mathbf{RgM}_{mn}(k\mathbf{r}) + b_{nm} \mathbf{RgN}_{nm}(k\mathbf{r}) \quad (3.21a)$$

$$\mathbf{E}_{sca}(\mathbf{r}) = \sum_{n=1}^{\infty} \sum_{m=-n}^n p_{nm} \mathbf{M}_{mn}^{(1)}(k\mathbf{r}) + q_{nm} \mathbf{N}_{nm}^{(1)}(k\mathbf{r}) \quad (3.21b)$$

For an ordinary plane wave propagating in the (θ, ϕ) direction with a polarization $\vec{E}_p = [E_r, E_\theta, E_\phi]$ where $E_r = 0$ the beam coefficients a_{nm} and b_{nm} are analytically known to be

$$a_{nm} = \frac{(2n+1)}{n(n+1)} i^n \frac{\vec{E}_p \cdot \mathbf{C}_{nm}(\theta, \phi)}{\xi_{mn}} \quad (3.22a)$$

$$b_{nm} = \frac{(2n+1)}{n(n+1)} i^{n-1} \frac{\vec{E}_p \cdot \mathbf{B}_{nm}(\theta, \phi)}{\xi_{mn}} \quad (3.22b)$$

where $\xi_{mn} = n(n+1)$ and for only $m = \pm 1$. Using the beam coefficients in Eq. (3.22) the GLMT problem reduces to the original Mie scattering formulation. The scattering coefficients p_{nm} and q_{nm} remain unknown. To determine them, the following steps are required: (a) represent the total field as a summation of the incident and scattered fields, i.e. $\mathbf{E}_{tot}(\mathbf{r}) = \mathbf{E}_{inc} + \mathbf{E}_{sca}$ and (b) apply the electromagnetic boundary conditions (Eq. 3.6 and 3.7) at the interface between the spherical particle and the surrounding material to obtain a relationship between the incident and scattered coefficients. Step (b) is also known as the Extended Boundary Method (EBM), which produces the system transfer operator (T-matrix) that operates on the incident beam coefficients as follows:

$$\begin{aligned} p_{mn} &= \sum_{m'n'} \left[T_{mn,m'n'}^{(11)} a_{m'n'} + T_{mn,m'n'}^{(12)} b_{m'n'} \right] \\ q_{mn} &= \sum_{m'n'} \left[T_{mn,m'n'}^{(21)} a_{m'n'} + T_{mn,m'n'}^{(22)} b_{m'n'} \right] \end{aligned} \quad (3.23)$$

To put the representation in a more compact form a combined index, l of n and m is introduced. Suppose the truncation of the infinite summation is at multipole $n = N_{max}$. Then the number of terms in, for example, a_{nm} is $L_{max} = N_{max}(N_{max} + 2)$. The combined index l can be used to represent the two indices n and m as follows

$$l = n(n+1) + m \quad (3.24)$$

Utilizing this combined index the beam and scattering coefficients can be reduced to a vector allowing the representation of Eq. (3.23) as a matrix relation

$$\begin{bmatrix} \vec{p} \\ \vec{q} \end{bmatrix} = \begin{bmatrix} T^{(11)} & T^{(12)} \\ T^{(21)} & T^{(22)} \end{bmatrix} \begin{bmatrix} \vec{a} \\ \vec{b} \end{bmatrix} \quad (3.25)$$

For the case of dielectric spheres with a relative refractive index of $n_r = n_1/n_2$ the T-matrix reduces to the Mie-scattering coefficients [181], and as such is diagonal, so that

$$\begin{aligned} T_{mn,m'n'}^{(11)} &= \delta_{mm'}\delta_{nn'}T_n^{(M)} \\ T_{mn,m'n'}^{(22)} &= \delta_{mm'}\delta_{nn'}T_n^{(N)} \end{aligned} \quad (3.26)$$

where

$$\begin{aligned} T_n^{(M)} &= -\frac{j_n(k_s r) [ka j_n(kr)]' - j_n(kr) [k_s r j_n(k_s r)]'}{j_n(k_s r) [ka h_n(kr)]' - h_n(kr) [k_s r j_n(k_s r)]'} \\ T_n^{(N)} &= -\frac{k_s^2 r^2 j_n(k_s r) [ka j_n(kr)]' - k^2 r^2 j_n(kr) [k_s r j_n(k_s r)]'}{k_s^2 r^2 j_n(k_s r) [ka h_n(kr)]' - k^2 r^2 h_n(kr) [k_s r j_n(k_s r)]'} \end{aligned} \quad (3.27)$$

producing a diagonal matrix where only $m = \pm 1$ elements are non-zero. The terms j_n , h_n , k_s , k and the superscript $'$ define the spherical bessel and hankel function of n^{th} order, wave number in sphere $2\pi/\lambda n_r$, wave number in surrounding medium $2\pi/\lambda$ and the derivative, respectively.

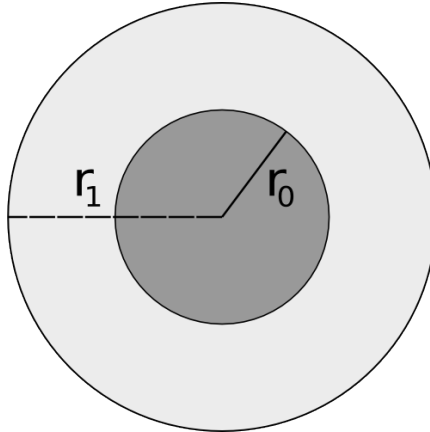


FIGURE 3.2: Scattering of a coated sphere. The inner and outer core refractive indices are given by n_0 and n_1 .

Similarly, the coefficients $T_n^{(M)}$ and $T_n^{(N)}$ for the coated sphere shown in Fig. (3.2) are given as

$$\begin{aligned} T_n^{(M)} &= \frac{[\rho j_n(\rho)]' [j_n(\zeta) + B_n y_n(\zeta)] - \{[\zeta j_n(\zeta)]' + B_n [\zeta y_n(\zeta)]'\} j_n(\rho)}{[\rho h_n(\rho)]' [j_n(\zeta) + B_n y_n(\zeta)] - \{[\zeta j_n(\zeta)]' + B_n [\zeta y_n(\zeta)]'\} h_n(\rho)} \\ T_n^{(N)} &= -\frac{[\rho j_n(\rho)]' \zeta^2 [j_n(\zeta) + A_n y_n(\zeta)] - \{[\zeta j_n(\zeta)]' + A_n [\zeta y_n(\zeta)]'\} \rho^2 j_n(\rho)}{[\rho h_n(\rho)]' \zeta^2 [j_n(\zeta) + A_n y_n(\zeta)] - \{[\zeta j_n(\zeta)]' + A_n [\zeta y_n(\zeta)]'\} \rho^2 h_n(\rho)} \end{aligned} \quad (3.28)$$

where

$$\begin{aligned} B_n &= -\frac{[\xi j_n(\xi)]' j_n(\eta) - [\eta j_n(\eta)]' j_n(\xi)}{[\xi y_n(\xi)]' j_n(\eta) - [\eta j_n(\eta)]' y_n(\xi)} \\ A_n &= -\frac{[\xi j_n(\xi)]' \eta^2 j_n(\eta) - [\eta j_n(\eta)]' \xi^2 j_n(\xi)}{[\xi y_n(\xi)]' \eta^2 j_n(\eta) - [\eta j_n(\eta)]' \xi^2 y_n(\xi)} \end{aligned} \quad (3.29)$$

and $\rho = kr$, $\xi = k_1 r_0$, $\zeta = k_1 r_1$, $\eta = k_0 r_0$ and y_n is the spherical bessel function of the second kind. With the plane wave coefficients given in Eq. (3.22), the T-matrix in Eq. (3.27) and the matrix equation in Eq. (3.25), the scattering problem can now be solved. To address slightly more complicated incident beams, i.e. a focused Gaussian beams, a different approach is necessary as an analytical expression for the beam coefficients is unavailable. This is discussed in the next section.

3.2.1 Gaussian Beam

Consider a fundamental laser beam with a linearly polarized, Gaussian field distribution in the beam waist

$$\mathbf{E}(r, z) = \mathbf{E}_0 \frac{w_0}{w(z)} e^{-\frac{r^2}{w^2(z)}} e^{i(kz - \eta(z) + kr^2/2R(z))} \quad (3.30)$$

where w_0 is the beam waist width, $r^2 = x^2 + y^2$, $z_0 = kw_0^2/2$ the rayleigh length, and

$$w(z) = w_0 \sqrt{1 + z^2/z_0^2} \quad (3.31a)$$

$$R(z) = z(1 + z_0^2/z^2) \quad (3.31b)$$

$$\eta(z) = \arctan(z/z_0). \quad (3.31c)$$

Here $w(z)$, $R(z)$ and $\eta(z)$ represent the beam radius, wavefront radius and phase correction, respectively. The 180° phase change that happens gradually as the beam propagates through its focus, known as the Guoy phase shift, is described by the factor $\eta(z)$. The Gaussian field distribution given in Eq. (3.30) is obtained using the paraxial approximation. The polarization can be set using the $\mathbf{E}_0 = [E_x \ E_y \ E_z]$. The far-field spherical wave limit of Eq. (3.30) is found by converting to spherical coordinates and

taking the large r limit, giving the scalar amplitude

$$\mathbf{E}(\theta, \phi) = \mathbf{E}_0 e^{-k^2 w_0^2 \tan^2 \theta / 4} \quad (3.32)$$

where we have set $\eta(z) = 0$ and $w(z) = 0$. To represent the Gaussian beam more accurately we utilize the perturbation method to solve the vector Helmholtz equation for the fundamental Gaussian beam (TEM₀₀) with higher-order corrections. The electric field components of a Gaussian beam that is linearly polarized in the x direction, propagating in the z direction, focused at the origin $\mathbf{r}_f = (0, 0, 0)$ and corrected up to the ninth-order are expressed as [182]:

$$\begin{aligned} E_x &= E_0 \Psi_0 e^{i\zeta/s^2} \{1 + s^2(-\rho^2 Q^2 + i\rho^4 Q^3 - 2Q^2 \xi^2) \\ &\quad + s^4 [2\rho^4 Q^4 - 3i\rho Q^5 - 0.5\rho^8 Q^6 + (8\rho^2 Q^4 - 2i\rho^4 Q^5)\xi^2] \\ &\quad + s^6 [-5\rho^6 Q^6 + 9i\rho^8 Q^7 + 2.5i\rho^{10} Q^8 - (1/6)i\rho^{12} Q^9 \\ &\quad + -\xi^2(30\rho^4 Q^6 - 12i\rho^6 Q^7 - \rho^8 Q^8)] \\ &\quad + s^8 [(112Q^8 \rho^6 - 56iQ^9 \rho^8 - 8Q^{10} \rho^{10} + (1/3)iQ^{11} \rho^{12})\xi^2 \\ &\quad + 14Q^8 \rho^8 - 28iQ^9 \rho^{10} - 10Q^{10} \rho^{12} + (7/6)iQ^{11} \rho^{14} \\ &\quad + (1/24)Q^{12} \rho^{16}] \} \\ E_y &= E_0 \Psi_0 e^{i\zeta/s^2} \{-2s^2 Q^2 \xi \eta + s^4 [(8\rho^2 Q^4 - 2i\rho^4 Q^5)\xi \eta] \\ &\quad + s^6 [-\xi \eta (30\rho^4 Q^6 - 12i\rho^6 Q^7 - \rho^8 Q^8) \\ &\quad + s^8 (112Q^8 \rho^6 - 56iQ^9 \rho^8 - 8Q^{10} \rho^{10} + iQ^{11} \rho^{12}/3)] \} \\ E_z &= E_0 \Psi_0 e^{i\zeta/s^2} \{-2sQ\xi + s^3 [(6\rho^2 Q^3 - 2i\rho^4 Q^4)\xi] \\ &\quad + s^5 [(-20\rho^4 Q^5 + 10i\rho^6 Q^6 + \rho^8 Q^7)\xi] \\ &\quad + s^7 (70\rho^6 Q^7 - 42i\rho^8 Q^8 - 7\rho^{10} Q^9 + i\rho^{12} Q^{10}/3)\xi \\ &\quad + s^9 (-252Q^9 \rho^8 + 168iQ^{10} \rho^{10} + 36Q^{11} \rho^{12} \\ &\quad - 3iQ^{12} \rho^{14} + (1/12)Q^{13} \rho^{16})\xi \} \end{aligned} \quad (3.33)$$

where $\xi = x/w_0$, $\eta = y/w_0$ and $\zeta = z/l$ with the Rayleigh length $l = kw_0^2$ and beam waist radius w_0 corresponding to that of the Airy diffraction pattern

$$w_0 = \frac{1.22\lambda_0}{n} \sqrt{\left(\frac{n_2}{\text{NA}}\right)^2 - 1}, \quad (3.34)$$

and $s = w_0/l = 1/kw_0 = \lambda/2\pi w_0$. The unperturbed solution is the paraxial Gaussian beam given as $\Psi_0 = iQe^{iQ\rho^2}$ with $\rho^2 = \xi^2 + \eta^2$ and $Q = 1/(i + 2\zeta)$. The electric field components are normalized by

$$E_0 = \sqrt{\left(\frac{4P}{c\epsilon_n \pi w_0^2 (1 + s^2 + 1.5s^4 + 3s^6 + 7.5s^8)}\right)} \quad (3.35)$$

where P is the beam power, c the speed of light, and $\epsilon_n = \epsilon_0 n_2^2$. A comparison between the paraxial Gaussian beam and perturbed Gaussian with 7th and 9th order corrections is given in [182], where it can be seen that at higher numerical apertures, i.e. tighter focus, the paraxial representation becomes less accurate.

3.2.2 Point Matching

The expansion of the incident beam into the VSWFs presents a difficulty because the paraxial Gaussian beam is a scalar field, while the VSWFs are a complete and orthogonal vectorial function basis for the solutions of the vector Helmholtz equation. Inserting Eq. (3.20) into Eq. (3.21) we obtain

$$\begin{aligned} \mathbf{E}_{inc}(\theta, \phi) &= \sum_{n=1}^{\infty} \sum_{m=-n}^n a_{nm} \frac{N_n}{kr} (\mp i)^{n+1} e^{\pm ikr} \mathbf{C}_{mn}(\theta, \phi) \\ &+ b_{nm} \frac{N_n}{kr} (\mp i)^n e^{\pm ikr} \mathbf{B}_{mn}(\theta, \phi) \end{aligned} \quad (3.36)$$

where $\mathbf{E}_{inc}(\theta, \phi) = [E_{inc,r} \ E_{inc,\theta} \ E_{inc,\phi}]$. Obviously $E_{inc,r} = 0$ when taking a farfield limit. The spherical domain can now be discretized into a set for the θ component, $q_\theta = \{0 < \theta < \pi\}$ and for the ϕ component, $q_\phi = \{0 < \phi < 2\pi\}$. The zero, π and 2π ends are carefully avoided to dodge computational problems. From here we obtain an ordered coordinate pair (q_θ, q_ϕ) . Conveniently we may set the cardinality of both sets so that $|q_\theta| = |q_\phi| = Q$. We have for Eq. (3.36) after separation of components and utilizing the combined index l ,

$$\hat{\theta} \cdot \mathbf{E}_{inc}(\theta_q, \phi_q) = \sum_{l=1}^{N_{max}} a_l \alpha_l \hat{\theta} \cdot \mathbf{C}_l(\theta_q, \phi_q) + b_l \alpha_l \hat{\theta} \cdot \mathbf{B}_l(\theta_q, \phi_q) \quad (3.37a)$$

$$\hat{\phi} \cdot \mathbf{E}_{inc}(\theta_q, \phi_q) = \sum_{l=1}^{N_{max}} a_l \alpha_l \hat{\phi} \cdot \mathbf{C}_l(\theta_q, \phi_q) + b_l \alpha_l \hat{\phi} \cdot \mathbf{B}_l(\theta_q, \phi_q) \quad (3.37b)$$

where $\alpha_l = \frac{N_n}{kr} (\mp i)^{n+1}$. Picking only the θ component in Eq. (3.37a) to simplify our discussion we introduce the following notations

$$\begin{aligned} E_{\theta,q} &= \hat{\theta} \cdot \mathbf{E}_{inc}(\theta_q, \phi_q) \\ \mu_{q,p} &= \hat{\theta} \cdot \alpha_p \mathbf{C}_p(\theta_q, \phi_q) \\ \nu_{q,p} &= \hat{\theta} \cdot \beta_p \mathbf{B}_p(\theta_q, \phi_q) \end{aligned} \quad (3.38)$$

In matrix form Eq. (3.37a) can be represented as

$$\begin{bmatrix} E_{\theta,1} \\ E_{\theta,2} \\ \vdots \\ E_{\theta,Q} \end{bmatrix} = \begin{bmatrix} \mu_{1,1} & \mu_{1,2} & \cdots & \mu_{1,N_{max}} & \nu_{1,1} & \nu_{1,2} & \cdots & \nu_{1,N_{max}} \\ & \ddots & & & & & \ddots & \\ & & \ddots & & & & & \ddots \\ \mu_{Q,1} & & & \mu_{Q,N_{max}} & \nu_{Q,1} & & & \nu_{Q,N_{max}} \end{bmatrix} \begin{bmatrix} a_1 \\ a_2 \\ \vdots \\ a_{N_{max}} \\ b_1 \\ b_2 \\ \vdots \\ b_{N_{max}} \end{bmatrix} \quad (3.39)$$

A similar process is required for the ϕ component. The number of matched points is set to be larger than the number of unknown coefficients so that an overdetermined system of equations is obtained. They are then solved by minimizing the root mean square error.

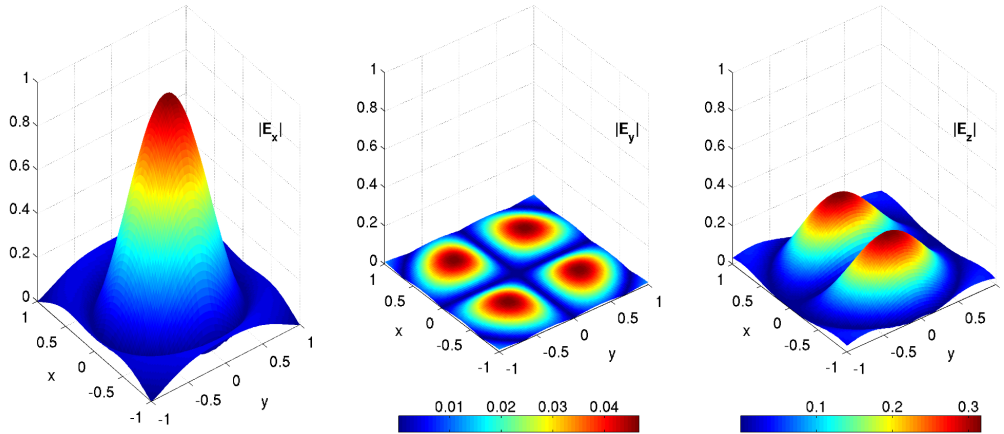


FIGURE 3.3: Three field components $|E_x|$, $|E_y|$ and $|E_z|$ of an x -polarized Gaussian beam with $NA = 1.0$ when recovered by expanding its beam coefficients with VSWF in the focal plane $x - y$. The fields are normalized to the maximum of $|E_x|$ and lengths are in units of wavelength, λ .

The three field components $|E_x|$, $|E_y|$, and $|E_z|$ of an x -polarized Gaussian beam constructed by Eq. (3.30) were recovered by expanding with vector spherical wave functions (VSWF) in the focal plane $x - y$ (Fig. 3.3). The fields are normalized to the maximum of $|E_x|$ and lengths are scaled to the wavelength λ . It is important to note that the x -polarized beam has significant components in y and z , although there are no y and z components in Eq. (3.30).

3.2.3 Translation and Rotation

The expansions for the incident and scattered beams, thus far, have all been considered about the origin, i.e. $\mathbf{r}_p = \mathbf{r}_f = (0, 0, 0)$. It will be necessary to solve scattering problems where the Gaussian beam is focused in an off-axis position, i.e. when $\mathbf{r}_p \neq \mathbf{r}_f$. To achieve this, it is convenient to rotate and translate the coordinates so that the scatterer is always at the origin, i.e. $\mathbf{r}_p = (0, 0, 0)$. The concept is depicted in Fig. (3.4). Inherently, the off-axis focal point creates asymmetry about the origin that is contrary to the nature of the VSWFs which are spherically symmetric about the origin.

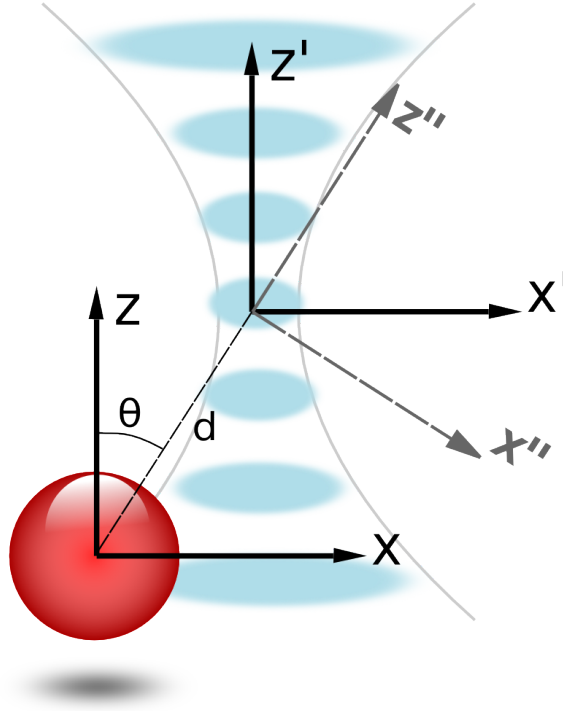


FIGURE 3.4: Translation and Rotation of the incident beam as described in Eq. (3.40). Steps are (i) rotate the system by θ , (ii) translate in z'' , and finally (iii) rotate back by $-\theta$. The construction of the rotation and translation matrices become costly as $|d|$ gets bigger thus the computational time is spent in the matrix multiplication.

Utilizing the VSWF Translation Addition and the Wigner D matrices provides an effective translation in the z -direction and a rotation about the y or x axis respectively. The construction of these matrices is based on a recursive seed algorithm that is shown in Appendix (A). The matrix operation to translate the beam coefficients \vec{a} and \vec{b} , a magnitude d at an angle θ is denoted as

$$\begin{aligned}\vec{a}' &= \mathbf{D}_{-\theta} \mathbf{A}_d \mathbf{D}_{\theta} \vec{a} + \mathbf{D}_{-\theta} \mathbf{B}_d \mathbf{D}_{\theta} \vec{b} \\ \vec{b}' &= \mathbf{D}_{-\theta} \mathbf{B}_d \mathbf{D}_{\theta} \vec{a} + \mathbf{D}_{-\theta} \mathbf{A}_d \mathbf{D}_{\theta} \vec{b}\end{aligned}\tag{3.40}$$

where \mathbf{A} and \mathbf{B} are the translation matrices, \mathbf{D} is the wigner rotation matrix about the y -axis, \vec{a} and \vec{b} are the vectorized beam coefficients of a_{nm} and b_{nm} using the l combined index, respectively. To accurately apply this translation and rotation scheme we found a good approximation of the required N_{max} is given by $(ka + 2\pi|d|) + 3(ka + 2\pi|d|)^{1/3}$, where d represents the distance of the translation. The number of terms required grows substationally as d grows which adds up to a rather challenging computational task even when sparse matrices are used.

3.2.4 Force Calculation

Once the electromagnetic scattering problem is solved, the optical force, \mathbf{F} , on a particle can be determined by evaluating Maxwell's Stress tensor around that object as

$$\mathbf{F} = \int_S \langle \mathbf{T}(\mathbf{r}, t) \rangle \cdot \mathbf{n}(\mathbf{r}) dS \quad (3.41)$$

where $\langle \cdot \rangle$, S and \mathbf{T} represent the time-average operator, surface enclosing the particle and Maxwell's stress tensor, respectively. Since the dynamics of the particle is much slower than the speed of light, a quasi-static approach can be applied by taking the time averaged force in Eq. (3.41). The construction of Maxwell's stress tensor is given by

$$\mathbf{T} = \left[\varepsilon_0 \mathbf{E}\mathbf{E} - \mu_0 \mathbf{H}\mathbf{H} - \frac{1}{2}(\varepsilon_0 E^2 + \mu_0 H^2) \mathbf{I} \right], \quad (3.42)$$

where it is evident that the full vectorial solution to Maxwell's equation is required. The evaluation of Eq. (3.41) and (3.42) in the GLMT framework reduces to a convenient arithmetic of the scattered and incident coefficients [183]. The axial force efficiency along the z -axis, Q_z , is given as

$$\begin{aligned} Q_z = & \frac{2}{P} \sum_{n=1}^{\infty} \sum_{m=-n}^n \frac{m}{n(n+1)} \text{Re} (a_{nm}^* b_{nm} - p_{nm}^* q_{nm}) \\ & - \frac{1}{n+1} \left[\frac{n(n+2)(n-m+1)(n+m+1)}{(2n+1)(2n+3)} \right]^{\frac{1}{2}} \\ & \times \text{Re} (a_{nm} a_{n+1,m}^* + b_{nm} b_{n+1,m}^* \\ & - p_{nm} p_{n+1,m}^* - q_{nm} q_{n+1,m}^*) \end{aligned} \quad (3.43)$$

in units of $n_2 \hbar k$ per photon. This can be converted to SI units by multiplying by $n_2 P/c$. The force efficiency in the x direction can be obtained using the rotation matrix, \mathbf{D}_{90} and an identity translation so that $\mathbf{A}_0 = \mathbf{B}_0 \equiv \mathbf{I}$ in Eq. (3.40) sans the corrective \mathbf{D}_{-90} .

3.3 Plasmonics

The interaction of metals with electromagnetic fields can be firmly understood in a classical framework based on Maxwell's equations. For frequencies up to the visible part of the spectrum metals are highly reflective and do not allow electromagnetic waves to propagate through them.

The optical properties of metals can be explained by the plasma mode, where a gas of free electrons of number density n moves against a fixed background of positive ion cores. For alkali metals, this range extends up to the ultraviolet, while for noble metals interband transitions occur at visible frequencies, limiting the validity of this approach. In the picture we adopt here, the presence of an electric field leads to a displacement \mathbf{r} of an electron, which is associated with a dipole moment $\mathbf{u} = e\mathbf{r}$. The cumulative effect of all individual dipole moments of all free electrons result in a macroscopic polarization per unit volume $\mathbf{P} = n\mathbf{u}$, where n is the number of electrons per unit volume. As in the Drude model, valence electrons are assumed to be completely detached from their ions (forming an electron gas). As in an ideal gas, electron-electron interactions are completely neglected. The electrostatic fields in metals are weak because of the screening effect. The displacement of free electrons, $\mathbf{r}^{(f)}$, derived from the Drude-Sommerfeld model and that for bound electrons, $\mathbf{r}^{(b)}$ are given as

$$m_e \frac{\partial^2 \mathbf{r}^{(f)}}{\partial t^2} + m\Gamma \frac{\partial \mathbf{r}^{(f)}}{\partial t} = e\mathbf{E}_0 e^{i\omega t} \quad (3.44a)$$

$$m \frac{\partial^2 \mathbf{r}^{(b)}}{\partial t^2} + m\gamma \frac{\partial \mathbf{r}^{(b)}}{\partial t} + m\omega_0^2 \mathbf{r}^{(b)} = e\mathbf{E}_0 e^{i\omega t} \quad (3.44b)$$

where e , m_e , m is the electron charge, the effective mass of the free electrons and the effective mass of bound electrons, respectively. \mathbf{E}_0 and ω are the amplitude and the frequency of the applied electric field. Note that in Eq. (3.44a) there is no restoring force since free electrons are considered whilst in Eq. (3.44b) there is a restoring force with a spring constant ω_0^2 . The damping term $\Gamma = v_F/l$ where v_F is the Fermi velocity and l is the electron mean free path between scattering events. The damping term γ describes the radiative damping of bound electrons. The solution ansatz $\mathbf{r}(t) = \mathbf{r}_0 e^{-i\omega t}$ can be used on both Eq. (3.44) to find

$$\begin{aligned} \mathbf{r}_0^{(f)} &= \frac{(e/m)\mathbf{E}_0}{-\omega - i\gamma\omega} \\ \mathbf{r}_0^{(b)} &= \frac{(e/m)\mathbf{E}_0}{\omega_0^2 - \omega - i\gamma\omega} \end{aligned} \quad (3.45)$$

The solution \mathbf{r}_0 represents the displacement of the electron or dipole moment, such that polarization can be defined as $\mathbf{P} = \eta\mathbf{r}_0 e$, where η can be either the number of free

TABLE 3.1: Coefficients for Gold and Silver.

Silver (Ag)	i=1	2	3	4	5	6
ω_P	$9.01e/\hbar$					
f_i	0.845	0.065	0.124	0.011	0.840	5.646
$\Gamma_i\hbar/e$	0.048	3.886	0.452	0.065	0.916	2.419
$\omega_i\hbar/e$	0.000	0.816	4.481	8.185	9.083	20.29
Gold (Au)	i=1	2	3	4	5	6
ω_P	$9.03e/\hbar$					
f_i	0.760	0.024	0.010	0.071	0.601	4.384
$\Gamma_i\hbar/e$	0.053	0.241	0.345	0.870	2.494	2.214
$\omega_i\hbar/e$	0.000	0.415	0.830	2.969	4.304	13.32

electrons per unit volume \tilde{N} , or alternatively the number of bound electrons per unit volume N . Utilizing the definition of polarization in Eq. (3.4a) in complex notation, i.e. $\mathbf{P}(\omega) = \varepsilon\chi_e(\omega)\mathbf{E}(\omega)$ we find the complex susceptibility becomes

$$\chi_e^{(f)}(\omega) = \frac{\omega_f^2}{-\omega - i\gamma\omega} \quad (3.46a)$$

$$\chi_e^{(b)}(\omega) = \frac{\omega_b^2}{\omega_0^2 - \omega - i\gamma\omega} \quad (3.46b)$$

where $\omega_b = \sqrt{Ne^2/\varepsilon_0m}$ and $\omega_f = \sqrt{\tilde{N}e^2/\varepsilon_0m}$ are both referred to as the volume plasma frequency. These two equations represent the behaviour of the free electrons and bound electrons when excited by an external electric field. In noble metals, such as Gold and Silver, both these terms contribute to the dielectric function. To accommodate for K damped harmonic oscillators to describe the small resonances observed in the metal's frequency response we may generalize the dielectric function as

$$\varepsilon(\omega) = \varepsilon_\infty + \sum_{k=0}^K \frac{f_k\omega_P^2}{\omega_k^2 - \omega - i\gamma_k\omega} \quad (3.47)$$

where f_k represents the strength of the k^{th} damped oscillator. The values of the constants for gold and silver are given in Table 3.1. These values have been obtained via experiments described in [184].

3.3.1 Simulation Technique and Normalization

To simulate a plasmonic device we utilize an opensource finite-difference time-domain code called MEEP [185]. For numerical simulations it is generally good practice to utilize the scaling properties of the governing equations. In this case, Maxwell's equations, are

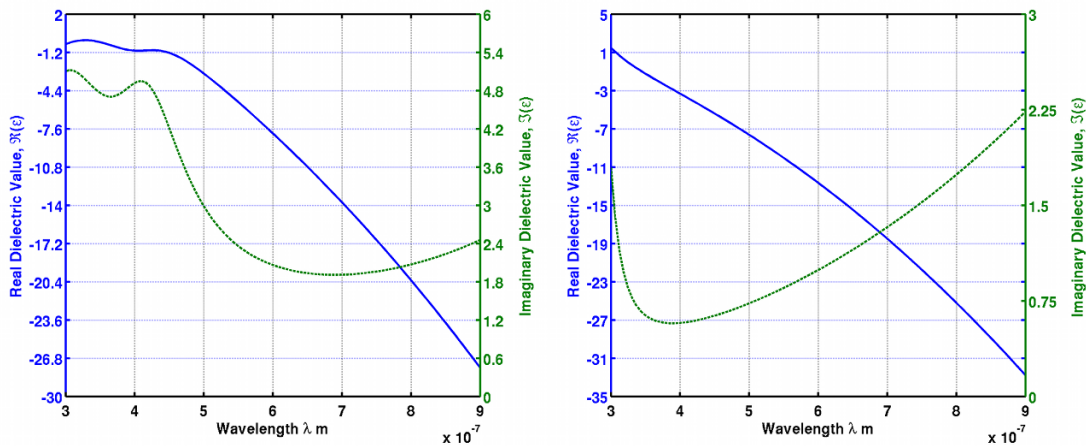


FIGURE 3.5: Real and Imaginary components of the dielectric function for gold (left) and silver (right) at the wavelength range of $300\text{nm} \leq \lambda \leq 900\text{nm}$.

scale invariant meaning we can conveniently normalize all parameters to a unit length of a . The normalized parameters, \hat{f} , $\hat{\lambda}$, $\hat{\omega}$, \hat{c} , corresponding to the frequency, wavelength, angular frequency and speed of light are related to the non-normalized parameters by $(a/c)f$, $(1/a)\lambda$, $(a/c)\omega$ and $(1/c)c = 1$, respectively. In particular, MEEP supports any material dispersion of the form of a sum of harmonic resonances, plus a term from the frequency-independent electric conductivity:

$$\varepsilon_m(\hat{\omega}, \hat{\mathbf{x}}) = \left(1 + \frac{i\hat{\sigma}_D(\hat{\mathbf{x}})}{\hat{\omega}} \right) \left[\varepsilon_\infty(\mathbf{x}) + \sum_k \frac{\hat{\sigma}_k \hat{k}_P^2}{\hat{k}_k^2 - \hat{\omega}^2 - i\hat{\omega}\hat{\gamma}_k} \right] \quad (3.48)$$

A scaling factor of $s_f = 2\pi c/a$ is introduced, so that ω_P , γ_k and ω_k in Eq. (3.47) when normalized for Eq. (3.48) become $\hat{k}_P = \omega_P/s_f$, $\hat{\gamma}_k = \gamma_k/s_f$ and $\hat{\omega}_k = \omega_k/s_f$, respectively. The oscillator strength $\hat{\sigma}_k$ is scaled as

$$\hat{\sigma}_k = f_k \left(\frac{\hat{\omega}_P}{\hat{\omega}_k} \right)^2 \quad (3.49)$$

It is important to note that while the $\sigma_D(\mathbf{x})$ term in Eq. (3.48) corresponds to the electrical conductivity, we have set this to zero, i.e. $\sigma_D = 0$, to match our material model.

3.3.2 Plasmonic Resonance

A simple geometry that can produce Surface Plasmon Polaritons (SPPs) is a single flat interface between a dielectric, ε_2 , occupying the $z > 0$ half-space and a conducting material in $z < 0$ described by the dielectric function $\varepsilon_1(\omega)$. We therefore can assume a source free system, i.e. \mathbf{J}_s and $\sigma = 0$, propagating along the metal-air interface shown

in Fig. (3.6). The structure is assumed to be homogenous in the \hat{y} direction, so that $\partial/\partial y \equiv 0$ and propagation is restricted to the \hat{x} direction so that $\partial/\partial x = ik_x$. The curl operator in Eq. (3.10) can be explicitly written to obtain two decoupled equations. The transverse magnetic mode equations are given as

$$\begin{bmatrix} 0 & 0 & i(\omega\varepsilon_0\varepsilon)^{-1}\partial/\partial y \\ 0 & 0 & (\omega\varepsilon_0\varepsilon)^{-1}k_x \\ i(\omega\mu_0\mu)^{-1}\partial/\partial y & (\omega\varepsilon_0\varepsilon)^{-1}k_x & 0 \end{bmatrix} \begin{bmatrix} E_x \\ E_y \\ H_z \end{bmatrix} = \begin{bmatrix} E_x \\ E_y \\ H_z \end{bmatrix} \quad (3.50)$$

for which the wave equation is

$$\frac{\partial^2 H_y}{\partial z^2} + (k_0^2\varepsilon - k_x^2) H_y = 0 \quad (3.51)$$

The SPPs are those solutions to Eq. (3.51) that propagate in the \hat{x} direction and are



FIGURE 3.6: Geometry of simple plasmonic waveguide with wave propagation along the x direction and homogeneity in y such that $\partial/\partial y \equiv 0$.

confined to the interface with an evanescent decay in the \hat{z} direction, i.e. they should have the form $\alpha e^{ik_x x} e^{-k_z z}$ in $z > 0$ and $\beta e^{ik_x x} e^{k_z z}$ in $z < 0$. The excitation of such modes are known to only occur in transverse magnetic (TM) modes which is why we have limited our discussion to only the TM equations [67]. Applying the Maxwellian boundary conditions and using the solution ansatz in Eq. (3.51) the well known dispersion relation of SPPs propagating at the interface between the two half spaces is

$$k_x(\omega) = \frac{\omega}{c} \sqrt{\frac{\varepsilon_1(\omega)\varepsilon_2(\omega)}{\varepsilon_1(\omega) + \varepsilon_2(\omega)}}. \quad (3.52)$$

For the SPP wavelength we obtain

$$\lambda_{spp} = \frac{2\pi}{\text{Re}(k_x)} \quad (3.53)$$

where the decay length of SPP fields away from the interface into the metal and insulator are given, respectively, as

$$\begin{aligned} k_{1,z} &= \frac{\omega}{c} \sqrt{\frac{\text{Re}(\varepsilon_1^2)}{\text{Re}(\varepsilon_1) + \text{Re}(\varepsilon_2)}} \left[1 + i \frac{\text{Im}(\varepsilon_1)}{2\text{Re}(\varepsilon_1)} \right], \\ k_{2,z} &= \frac{\omega}{c} \sqrt{\frac{\text{Re}(\varepsilon_2^2)}{\text{Re}(\varepsilon_1) + \text{Re}(\varepsilon_2)}} \left[1 - i \frac{\text{Im}(\varepsilon_1)}{2(\text{Re}(\varepsilon_1) + \text{Re}(\varepsilon_2))} \right] \end{aligned} \quad (3.54)$$

3.4 Conclusion

In conclusion, the techniques to solve (a) Maxwell's equations for a scattering object illuminated by a focused Gaussian beam and (b) Maxwell's time dependent equations for dispersive plasmonic structures, have been shown.

tion. (

Chapter 4

Optical Forces on Particles

4.1 Introduction

The ability to move small-scale matter in a prescribed fashion optically is attractive in many areas of inquiry. Light manipulation of matter advanced significantly with the work of Ashkin et al. in which a single small piece of matter could be held in place using a method commonly known as laser tweezing or optical tweezing. The ensuing efforts to harness this capability have been wide. The ability to hold single matter in place has traditionally been explained by the interplay of the scattering and gradient force components of a focused beam of light.

Major challenges remain in acquiring the ability to attain strong optical trapping (i) at the subwavelength scale, (ii) in a coplanar geometry, and (iii) at specific and selective locations over the entire chip. The use of evanescent fields, in particular plasmon fields emanating from a subwavelength aperture or from a probe, have been shown to be effective for some time in addressing issues (i) and (ii). Experiments to manipulate matter are often done in a fluid chamber that is limited in the axial dimension and as such involves matter moving more significantly in the lateral sense. It is essentially not necessary to use tweezing to do this, although it is difficult to introduce a photophoretic force due to the constraints of applying illumination in the lateral sense. Airy beams offer a means of applying a light beam axially while obtaining accentuated matter motion in the lateral sense, albeit more in a ballistic manner.

The near-field localization of light in surface plasmonic presents a possible solution in which tailored leaky waves using surface corrugations from a subwavelength aperture offer the opportunity for flexible design. Nevertheless, this is currently limited to matter manipulation at the surface and not in the medium. Since the discovery of the contribution of leaky plasmon waves in affecting the characteristics of plasmonic beaming

structures, there has been no report of effort, to the best of our knowledge, to harness these leaky waves for optical trapping. The ability to do this opens up the avenue of having multiple apertures on the surface with light addressable waveguides within the chip in order to maintain close control of optical trapping at specific and selective locations over the entire chip.

Regardless of the underlying physics used to obtain the light field, the primary indicator of its practicality is depicted by its optical force field. In a real sense, this requires the mapping, either by accurate simulative or experimental methods, of the optical force field. In this chapter, we explore two photonic technologies; The Optical Tweezer and Plasmonics. In doing so, we have established and experimentally tested, new practical methods of manipulating particles. Furthermore, we present in this chapter what we believe is the first complete optical trapping map of dielectric spheres. From this map, we seek to elucidate the basis of the ridge region trapping characteristics with high refractive index material more clearly and outline a feasible way to harness it for applications.

4.2 Optical Tweezers

An x -polarized TEM₀₀ Gaussian beam propagating along the optical axis z with a numerical aperture (NA) of 0.98 and wavelength of $1.06\mu\text{m}$ impinges on a scatterer. The surrounding medium is assumed to be water with a refractive index of $n_2 = 1.33$, resulting in a beam angle of approximately 47° . The scatterer is considered to be a polystyrene particle with a refractive index of $n_1 = 1.59$ and $r = 3\mu\text{m}$ radius.

Before any optical force calculations can be made, a solution to the aforementioned scattering problem is required. The simulation technique in Section (3.2) is implemented. In carrying out the simulation, we found that we had to significantly limit the grid size due to the rapidly growing number of expansion terms required at points far from the focal point. Such an approach will suffice in the context of our analysis. Execution times and memory requirements depended significantly on the translation distance from the focal point. The results are expressed in units of force efficiency \mathbf{Q} , where the optical force is given by $\mathbf{F} = nP\mathbf{Q}/c$, in which P is the beam power at the focus and c is the speed of light in free space.

In order to approach this more systematically, we demarcate three beam axis distance regions relative to the beam center: (i) the focal point region ($-6\mu\text{m} \leq z \leq 6\mu\text{m}$), (ii) the post-focal-point region ($4\mu\text{m} \leq z \leq 18\mu\text{m}$) and (iii) the pre-focal-point region ($-13\mu\text{m} \leq z \leq -4\mu\text{m}$). For the focal-point region, we have the optical force profiles for the x - (Fig. 4.1a) and z - (Fig. 4.1b) axes components calculated. This is the

region that is most reported. In relation to the x -axis component, one finds an island of maximal efficiency of approximately $Q_x = 0.5$, located away from the z axis a distance of $3\mu\text{m}$. The nature of this force distribution indicates that pulling in particles from radial distances further away is rather improbable. With the z axis component, one finds a region of zero force (located about $1.2\mu\text{m}$ from the focal point) that corresponds to z_e , the “sweet spot” of conventional single beam trapping wherein the so called gradient and scattering forces are in equilibrium. Combining the two components Q_x and Q_z into a vector plot over the E_x field expansion of the beam, an articulate representation of the optical tweezer force field is obtained in Fig. 4.1c. The dotted circle is provided as a reference of the geometrically intercepted power of the particle ($r = 3\mu\text{m}$), which serves to explain why the island of maximal efficiency is located approximately r from the z axis.

If we shift our attention to the post-focal-point region, we find the x -axis force component undergoing a crossover (Fig. 4.2a) from an inward pulling force towards the z axis to an outward pushing force away from the z axis. From this we note the transition line, z_T , defined as the distance up the z axis from the focal point of the laser, after which the x -component of the force, Q_x , switches polarity.

Such a situation confirms that, as long as the z -axis position is above the crossover, the particle should never be able to enter the beam axis as long as the laser is on. This seems to be counter intuitive for a focused laser beam. No force changeover, however, exists for the z component of the force, which remains positive throughout (Fig. 4.2b). It is noteworthy that the magnitude of force efficiency in the x direction is 6×10^{-4} , which is almost 3 orders lower than in the central region. The calculated optical force efficiency, Q_x , in the $x - y$ plane is shown in Fig. (4.3). As can be seen, the optical force efficiency is highest at around $z = 16.5\mu\text{m}$ at a lateral distance of about $2.5\mu\text{m}$ away. Beyond a lateral distance of $3\mu\text{m}$, the order of Q_x drops rapidly as is shown in Fig. (4.3b). This limits the region of influence of the laser. Based on this observation, we can safely approximate the optical force at points beyond $8\mu\text{m}$ as zero. The distance from the focal point to the transition line, z_T , primarily depends on the particle refractive index n_1 . Simulating for a range of refractive indices in the range $1.5 \leq n_1 \leq 1.8$ and particle sizes $a = \{0.5\mu\text{m}, 1.0\mu\text{m}, \dots, 3.0\mu\text{m}\}$ a search for z_T is conducted. The results in Fig. (4.4) indicate that a lower refractive index pushes the transition line higher and a smaller particle size pushes the transition line lower. The relationship between these parameters is not linear. As the particle refractive index approaches that of water ($n_2 = 1.33$), due to a non-trapping condition, an asymptote is expected and therefore there is no transition line. In the case of red blood cells, which have a refractive index of 1.4 [186], and radius $3\mu\text{m}$, the transition line occurs much further upward at $z_T = 34\mu\text{m}$.

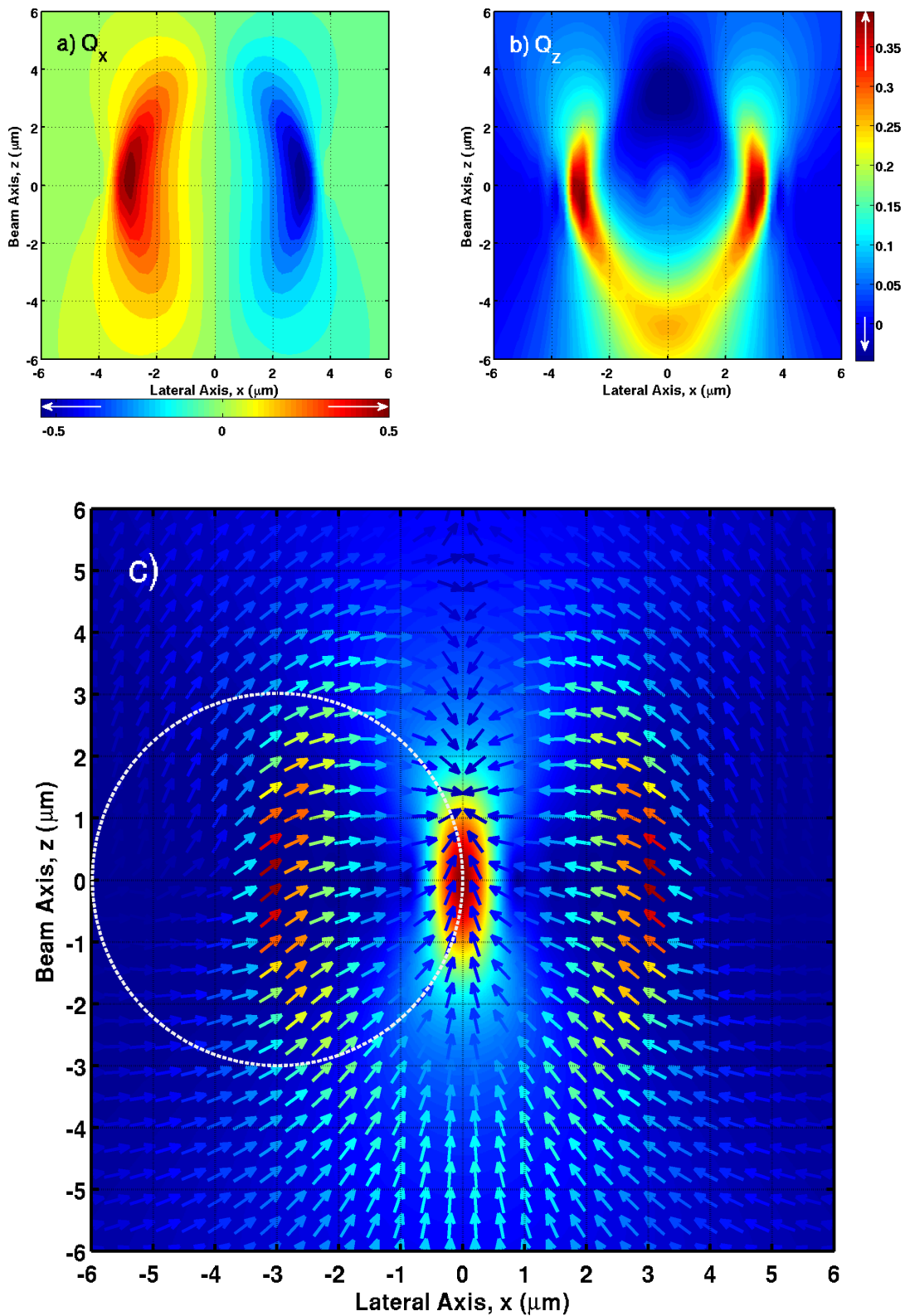


FIGURE 4.1: Contour plots of the optical force efficiency on a $3\mu\text{m}$ polystyrene particle shown separated into its (a) x component Q_x and (b) z component Q_z . By combining these two components, the net force efficiency $\mathbf{Q} = Q_x + Q_z$, together with the E_x component of the beam, is shown in (c). The dotted circle is provided as an indication of the intercepted area of the particle relative to the beam.

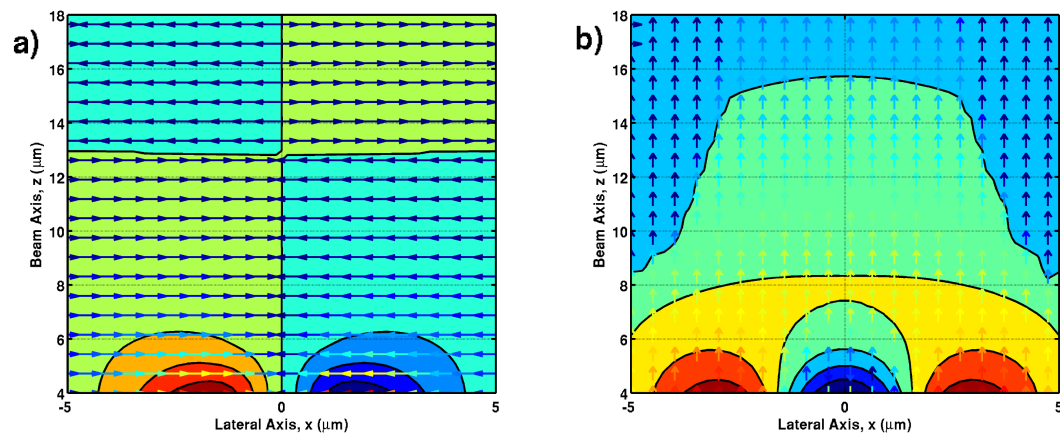


FIGURE 4.2: Contour plots of the optical force efficiency on a $3\mu\text{m}$ polystyrene particle shown separated into its (a) x component Q_x and (b) z component Q_z , at points 4 to $18\mu\text{m}$ above the focal point. The overlaid arrows indicate the direction of force for the respective components. When $z > 13\mu\text{m}$ a transition is observed in (a) whereby the optical forces in the x direction switch polarity, i.e. from pulling to pushing.

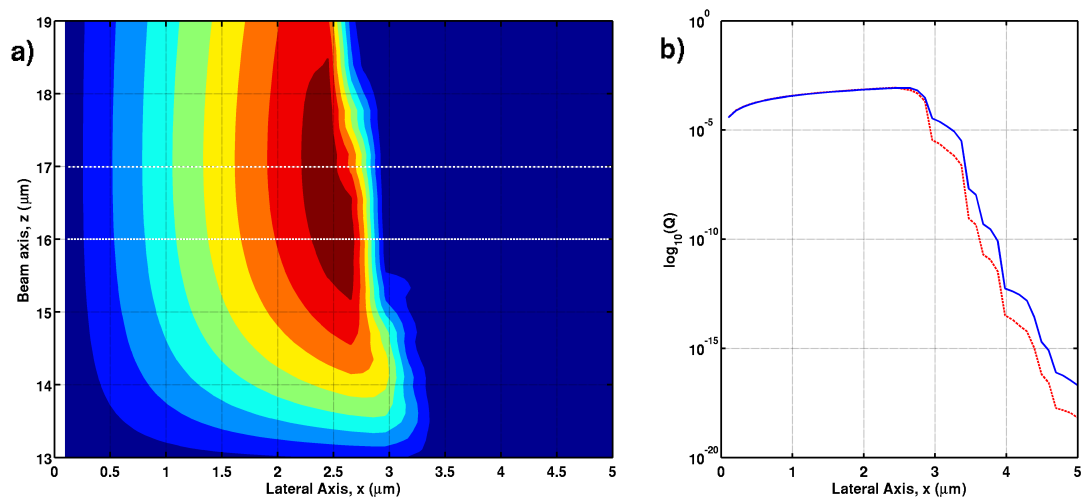


FIGURE 4.3: (a) Contour plot of the optical force efficiency, Q_x , in the $x-z$ plane beyond the transition line. (b) Plot of optical force efficiency, Q_x , along $z = 16\mu\text{m}$ and $z = 17\mu\text{m}$ as indicated by the solid and dashed lines in (a), respectively. The optical force efficiency drops off rapidly after $3.5\mu\text{m}$. Based on this observation we safely neglect optical force calculations beyond $8\mu\text{m}$ to lessen computational demands.

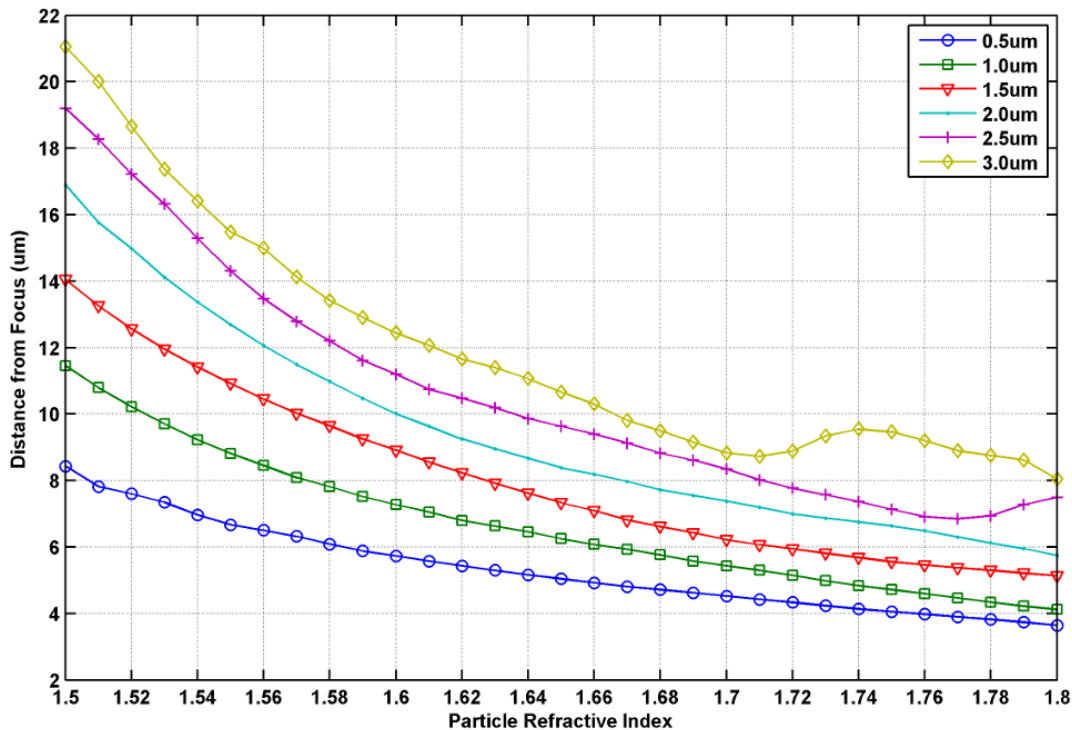


FIGURE 4.4: Plots of distance to transition line, z_T , versus particle refractive index. Each line corresponds to a different particle size.

In the case of the pre-focal-point region, one finds the x component force and z component force maps (Fig. 4.5) that draw particles toward the beam axis and upward. Here we find a more significant drop off in the z - component force when further away from the beam axis. This translates to particles being drawn in toward the beam axis. Such a trend conforms with the envelope of the light beam. It will appear then that the use of a larger NA lens should increase the propensity of movement towards the beam axis.

4.2.1 Lateral Push/Pull

We thus propose a switching system between two light sources to accomplish lateral positioning with light irradiation on a spherical particle, depicted in Fig. (4.6). We propose to achieve this by controlling (x_f, z_f) , i.e., the location of the beam focal point. With the laser arriving from the objective lens, and the particle located at (x_p, z_p) , locating the focal point above the sphere so that $z_f > z_p$, the particle can be moved toward the beam axis and upward. Alternatively, locating the focal point below the sphere so that $z_T < z_p$, the particle can be moved away from the beam axis and upward. At this point, it is important to point out the possible action of buoyancy and sedimentation. If the particle is denser than the medium, sedimentation will limit movement of the particle

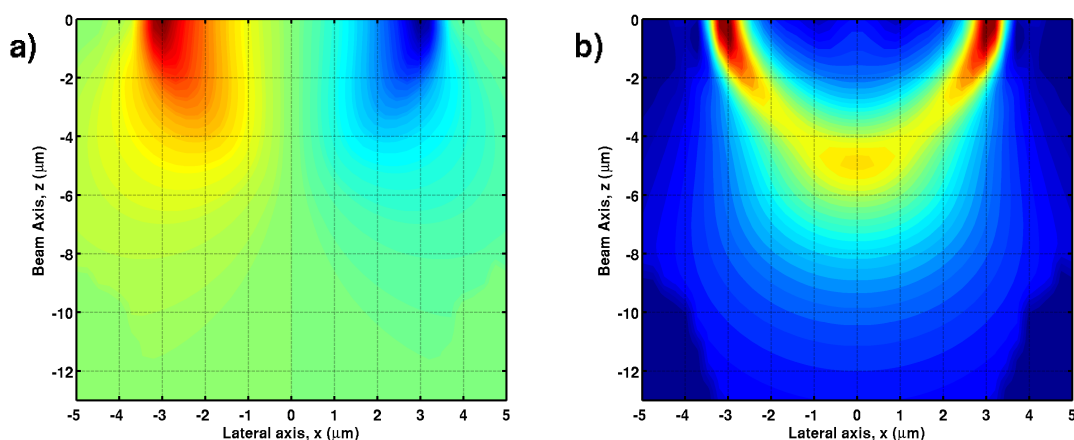


FIGURE 4.5: Contour plots of the optical force efficiency on a $3\mu\text{m}$ polystyrene particle shown separated into its (a) x component Q_x and (b) z component Q_z , at points 4 to $13\mu\text{m}$ below the focal point.

upward, and one then will have motion almost exclusively in the lateral sense. However, if the particle is of equal or lower density than the medium, there will be a movement of particle axially upward as well as laterally. In this case, switching the laser to one that arrives from the opposite direction applies the basic photophoretic force to restore the sphere's axial position. As particle position is accomplished without it entering the beam focus, the propensity for photodamage is reduced.

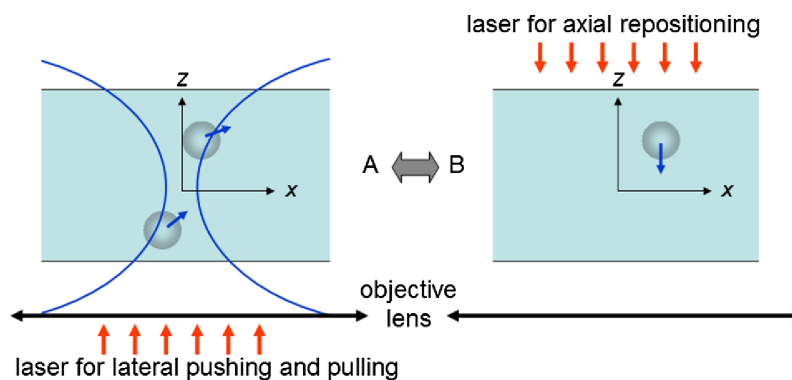


FIGURE 4.6: Proposed scheme where locating the beam focus below or above the sphere moves it laterally predominantly while a beam in the opposite direction restores the sphere axially.

In order to verify this scheme, experimentation was done on a conventional laser single beam trapping system (Cell Robotics, Inc.) operating at a wavelength of $1.06\mu\text{m}$ and maximum power of 5 watts. The setup of the system that was applied on an inverted microscope configuration is given in Fig. (4.7). Video sequences were captured using a video camera (Moticam 2000) and digitized for image analysis. Polystyrene beads of $3\mu\text{m}$ radius (Bangs Laboratories) were used. In order to reduce sticking to surfaces,

Triton-X100 reagent (Sigma Aldrich) was added to the bead suspension. The bead solution was then placed in a chamber created by sealing two cover slips. The laser trap was then placed in a chamber created by sealing two cover slips. The laser trap was operated using a $60\times$ objective having an NA of 0.98. The positioning of the bead relative to the beam center was done by visual estimation and tracking the movement of the stage in the x , y and z direction. The experimental results shown in

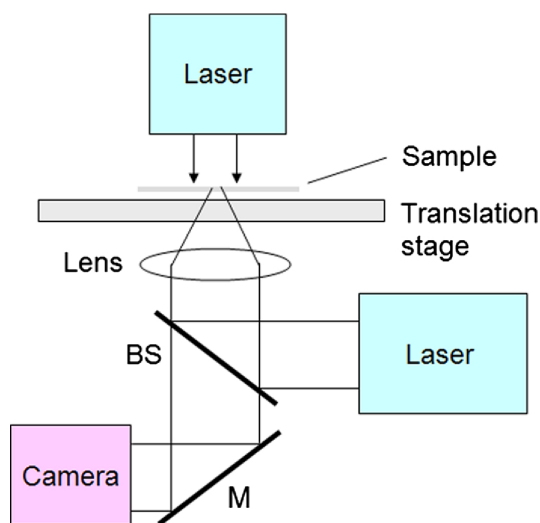


FIGURE 4.7: Schematic description of the optical push-pull setup used, BS, beam splitter, M mirror

Fig (4.8a) gives an example image recorded with the beam focus located axially above some surrounding particles. The particles were found to be drawn toward the beam axis (denoted by cursor). Fig (4.8b), alternatively, is an example image in which the beam focus is axially placed below a surrounding particle. In this case, the particle was seen to be nudged away from the beam axis. The particles are observed to be slightly blurry as the laser beam focus corresponds with the imaging focus.

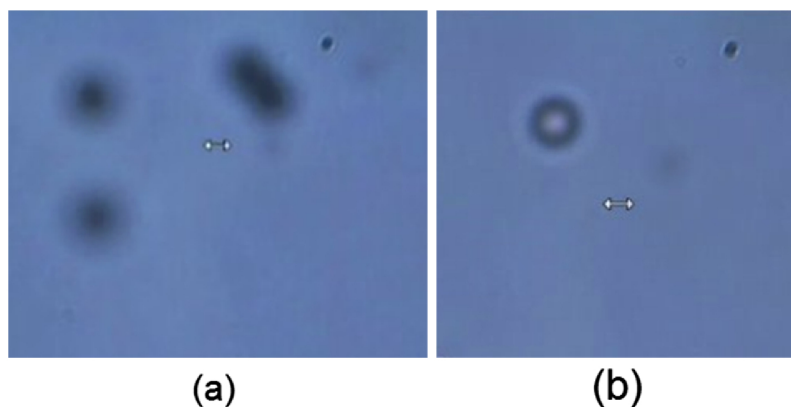


FIGURE 4.8: Images of laser beam focus located axially (a) above and (b) below particles. The former pulls and the latter pushes particles laterally with respect to the beam axis (cursor)

4.2.2 Bioreactor

A bioreactor, in the context of cell culture, refers to a device or system meant to grow cells or tissues. Traditionally, cell cultivation processes required the screening of large number of cell lines in shake flask cultures. The need to carry out a vast number of development cultivations has led to the increasing widespread deployment of small-scale bioreactor systems that offer miniaturized and high throughput solutions. This has led to efforts in incorporating microfluidics [187–189], which has resulted in arguably the smallest bioreactor possible using optical tweezers [190]. In the realm of microfluidics, there is a trend towards the use of discrete volume systems that offer flexible and scalable system architectures as well as high fault tolerance capabilities [191–193]. Moreover, because sample volumes can be controlled independently, such systems have greater ability for reconfiguration whereby groups of unit parts in an array can be altered to change their functionality.

Cells are often sensitive to their microenvironment in which cues from other cells, and mechanical stimuli from movement are crucial [194, 195]. The ability to provide the latter in a discrete fluidic system presents a significant challenge. Intuitively, the capacity to provide mechanical stimuli will benefit from a gentle *stirring* of the contents within as little photodamage as possible. Whilst it is conceivable that direct photophoresis may provide the means of doing this, such a system will generally be difficult to fabricate. Utilizing the findings in Section (4.2.1) an approach is investigated that offers the ability for generating a gentle and tunable stirring effect.

In being able to stir effectively without the particle ever falling into the beam focus (where photodamage may occur) it would be necessary for the particle to only reside in the upper region. We thus propose a system described in Fig (4.9), whereby the laser beam is focused within the liquid medium but close to the bottom surface of the droplet. Coincidentally, this is also the region where the particles (if they are large enough) will settle by gravitational sedimentation. For sedimentation to be facilitated or hastened, an auxiliary light source from above can be used to create a photophoretic force downwards. Stirring is accomplished simply by moving the slide and droplet around in the $x - y$ plane using the microscope stage. One strategy will be to perform a line scan along the x direction followed by step movements in the y direction or vice-versa. The degree with which a particle *bounces off* the laser beam center will depend on the relative position between the particle and beam center, the translator's speed, the laser beam power for a specific particle's refractive index and size, and hydrodynamic effects.

Due to the inherent rotational symmetry about the z -axis, we limit our calculations to only the $x - z$ plane. Utilizing the map of force efficiency over the $x - z$ plane,

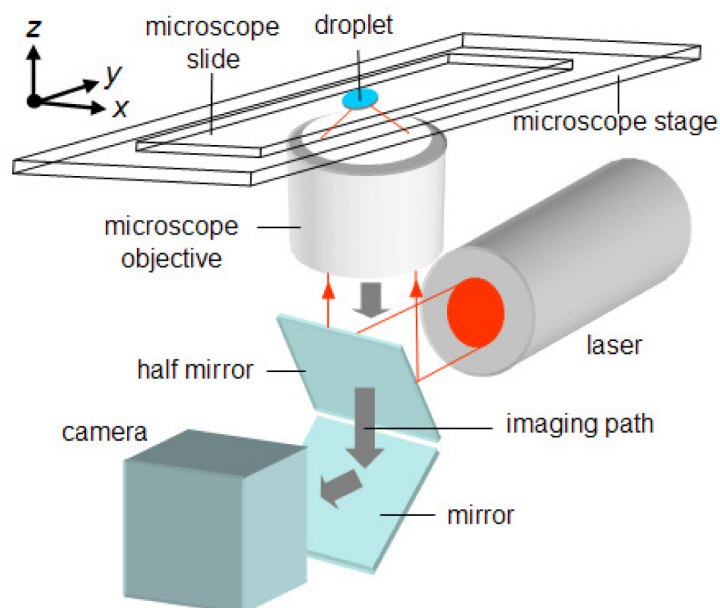


FIGURE 4.9: The setup to accomplish optical stirring involves focusing the laser beam close to the bottom surface of the droplet and using the microscope stage to move the slide and droplet in the $x - y$ plane.

the dynamic equations of motion were applied to an inertial frame, i.e. the microscope stage moving at a constant speed, v_P , over the fixed laser beam. In this model, the very low Reynolds number (much less than 1), dictates that the Stokes drag term is linearly dependent on velocity. Hydrodynamics effects associated with the relative position of the particle to the cover slip walls were neglected.

Experimentation was done on a conventional laser single beam trapping system (Cell Robotics Inc.) operating at a wavelength of $1.06\mu\text{m}$ and having a rated full power of 5W. Video sequences were captured using a video camera (Moticam 2000) and digitized for image analysis. Polystyrene beads of $3\mu\text{m}$ radius (Bangs Laboratoies) were used. In order to reduce sticking to surfaces, Triton-X100 reagent (Sigma Aldrich) was added to the bead suspension. The bead solution was then placed as droplet in a circular shallow chamber created by varnish or silicone tape. The laser trap was operated using a 60X objective having a numerical aperture of 0.98. Similar experiments were also conducted with red blood cells from sheep (R3378 Sigma Aldrich). These samples, originally in dry powder form and glutaraldehyde treated, were rehydrated using 0.9% sodium chloride solution.

The displacement of the particle at various laser powers with respect to the stationary laser and moving stage are shown in Fig. (4.10). The results show that the extent of stirring of the particles can be controlled by varying the applied power. The stirring

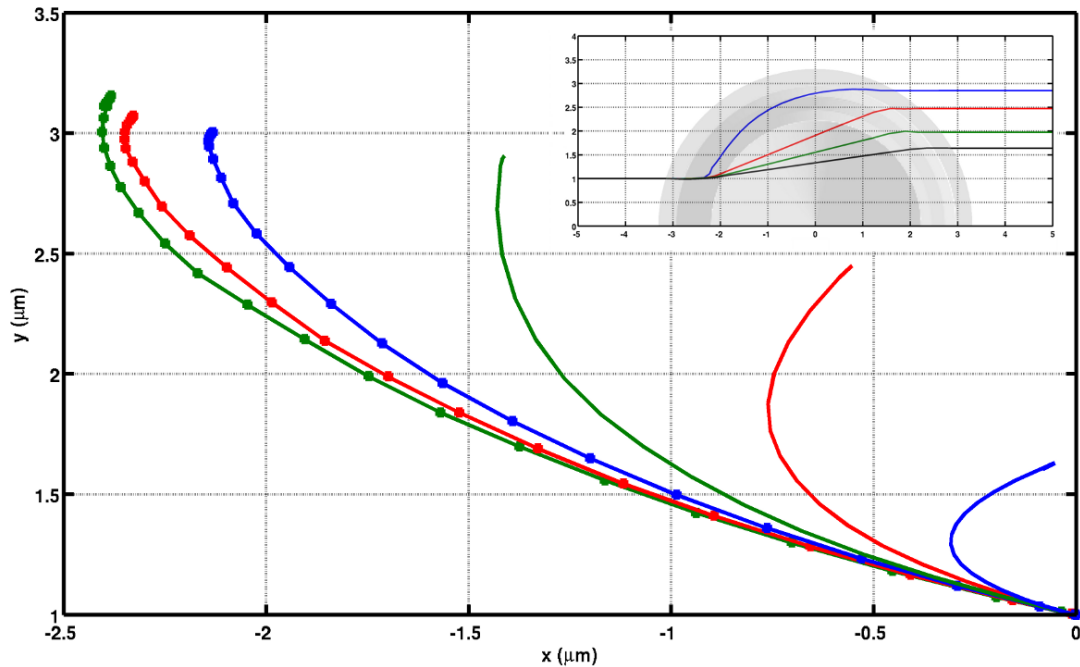


FIGURE 4.10: Plot of local displacements of particles on microscope stage for $z = 16 \mu\text{m}$ at various power levels starting from the right to left, 10mW (blue), 20mW (red), 25mW (green), 40mW (blue-dotted), 100mW (red-dotted) and 200mW (green-dotted). The optical stirring effect can be controlled by changing laser power. Inset: The plot of the global particle trajectories at optical powers 10mW (black), 15mW (green), 20mW (red) and 35mW (blue).

effect saturates at higher laser powers since the order of the optical force efficiency drops rapidly after $3 \mu\text{m}$, as was shown in Fig. (4.3).

The experimentation results shown in Fig. (4.11, 4.12) comply with the modeling results. With 40% power, the polystyrene particles identified as 1 and 2 in Fig. (4.11a - 4.11b) can be seen to depart from their general motion paths such that they are pushed away from the laser beam center. The manner of the pushing is strongly lateral rather than axial, thus limiting the possibility of photothermal or phototoxicity damage. When the laser beam power was reduced to 10%, one finds the cluster of particles identified in Fig. (4.11c- 4.11d) being able to move past the laser beam center almost without being affected. Hence, the optical stirring effect requires a certain threshold for operation. This is consistent with the modeling results.

The optical stirring effect was found to be operational with red blood cells as well, as indicated in Fig. (4.12). This illustrates the viability of the method applied to living organisms. A modeling of the forces will be more involved due to the shape complexity of these cells over simple shapes such as spheres and rods. The experimental results, however, indicate that a simple scaling effect, as far as the optical stirring effect is concerned, may be in operation.

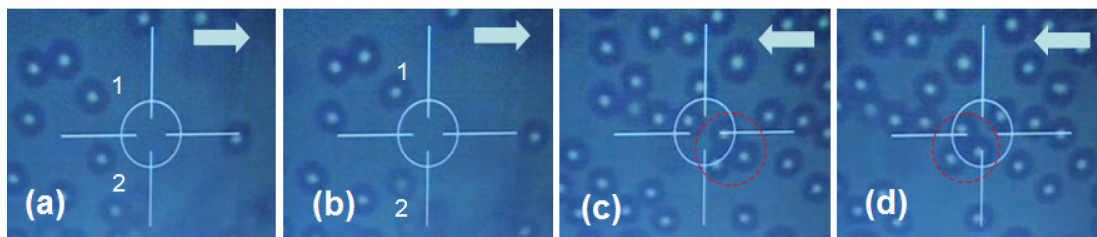


FIGURE 4.11: With the laser beam located axially below the polystyrene beads and having sufficient power, the image sequence (a) before and (b) after shows the particles numbered 1 and 2 laterally pushed away from the beam center. With the laser beam located axially below the polystyrene beads but having insufficient power, the image sequence (c) before and (d) after shows the cluster of particles circled in red unaffected by the beam. The arrow shows the general direction of travel of the particles.

At this juncture, we should mention that acoustic [196, 197], magnetic [198], and dielectrophoretic [199] devices are also able to create a swirling motion that is able to move particles and cells around. The strong motion of material within the liquid medium associated with the effect will generally not be amenable for cells or to guide cells towards desired differentiation or biological response pathways. In both bioreactor and micro-bioreactor scale culture, a delicate balance or trade-off has to be reached in terms of the need to provide a perfusion or mixing function and controlling hydrodynamic shear stress. While perfusion and mixing provides a more homogenous environment by maintaining dissolved oxygen and nutrient concentrations and serves to reduce media cytotoxicity via recirculation effects, the consequent hydrodynamic shear forces, if on a high magnitude, are generally considered to have an adverse impact on cell survival and proliferation [200]. This is especially the case for shear sensitive cell types [201]. Evidences from studies also show that shear stress can have a significant influence on cellular morphology, growth patterns, and biological responses [202, 203]. Different magnitudes of hydrodynamic shear stress evoke differential gene expression in signaling pathways in human bone marrow derived mesenchymal stem cells [204] and human endothelial progenitor cells [205], induce important changes in secretion and assembly of glycoproteins in mammalian cell cultures [206] as well as influence proliferation and osteoblastic differentiation [207]. Hence, in the setting of a static discrete droplet format, the gentle stirring afforded by our approach provides advantages of preserving cellular integrity and viability apart from promoting fidelity of biochemical and differentiation responses during cell culture and/or when performing cell-based assays.

4.2.3 Optical Trapping Map

The performance of an optical tweezer depends mostly on three crucial parameters, the radius and refractive index of the particles you wish to trap, and the numerical aperture.

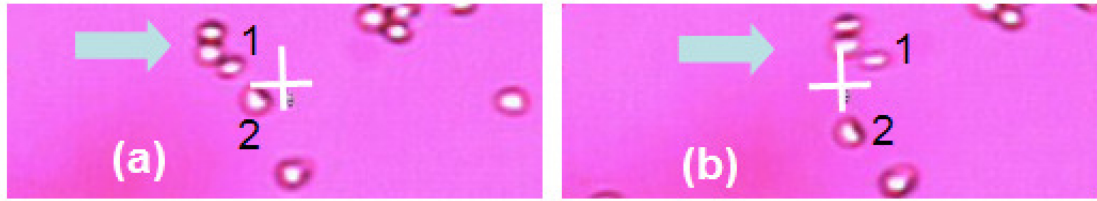


FIGURE 4.12: With the laser beam located axially below the particles and having sufficient power, the image sequence (a) before and (b) after shows the red blood cells numbered 1 and 2 laterally pushed away by the beam. The arrow shows the general direction of travel of the cells.

These three parameters form the dimensions of our optical trapping map.

We swept a three-dimensional (3D) parameter set, comprising (i) $1.3 \leq n_1 \leq 4.0$, (ii) $0.3 \leq NA \leq 1.2$, and (iii) $0.5\lambda \leq r \leq 4.0\lambda$. For each set of parameters, we conducted two trap searches. The first was a search in the axial sense; i.e., trapping along the beam axis, z (i.e., $-5\mu\text{m} \leq z \leq 5\mu\text{m}$) and $x = 0$. The second was a search for trapping in the radial sense; i.e., trapping in the $x - y$ plane, where $-5\mu\text{m} \leq z \leq 5\mu\text{m}$ and $z = 0$. In both cases, when a zero crossing was found, we recorded the peak restoration force, $Q_{i,RFmin}$; if not found, we assumed that it was a non-trapping condition that set $Q_{i,RFmin} = 0$, where i was either x or y for radial trapping and z for axial trapping.

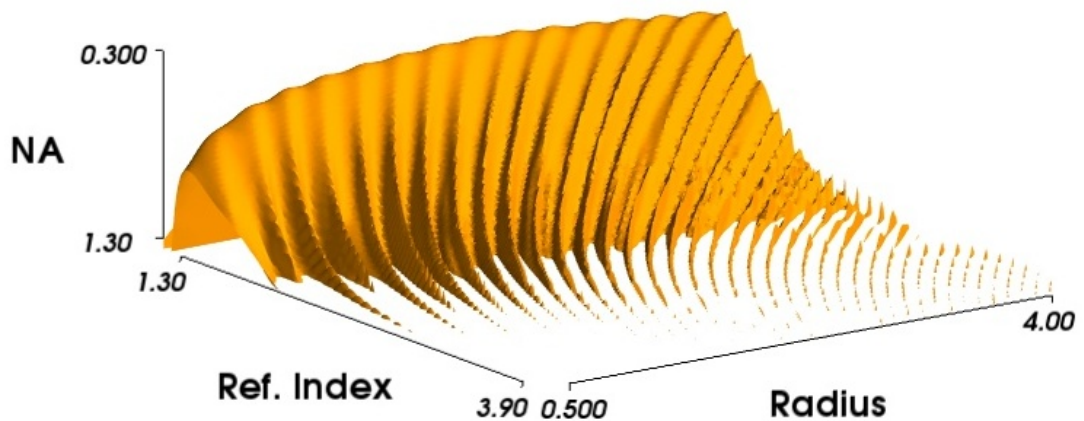


FIGURE 4.13: Iso-surface of $Q_{z,RFmin} = -1 \times 10^{-10}$ representing the ability to conduct optical trapping calculated in relation to NA, particle refractive index n_1 , and radius r values. The volume space above the distribution represents those parameters that do not lead to optical trapping.

Since the computations were highly serial, we have reduced the order of some calculations from $\mathcal{O}(n^3)$ to $\mathcal{O}(n^2)$ and greatly increased performance through the use of batch parallelization. The code was compiled to run on a high-performance computing facility

ideally suited to data-intensive tasks, comprised of up to 201 nodes, 1408 CPU cores, 4376 GB RAM space, and operating at up to 12410 gigaflops per second. The total parameter grid consisted of 9,800,000 points. As mentioned, for each grid point a scan in the x or y for radial and z for axial trapping was conducted. Roughly, each scan used 200 grid points, making for an estimated total of 1,960,000,000 scattering problems. The computational difficulty of each grid point depended strongly on $d = \text{abs}(\mathbf{r}_f - \mathbf{r}_P)$, i.e. the translated distance of particle center from the focal point. This relates to the work involved in calculating the recursive translation and rotation algorithms for larger and larger N_{max} to satisfy $N_{max} = (ka + 2\pi|d|) + 3(ka + 2\pi|d|)^{1/3}$ as discussed in Section (3.2). We obtained a computation speed of approximately 12 s per parameter combination per thread.

Figure (4.13) shows a 3D iso-surface of $Q_{z,RFmin} = -1 \times 10^{-10}$ (i.e. the axial optical trapping landscape), where the x, y and z axis represent the particle radius ratio (r/λ), refractive index ratio (n_1/n_2), and NA, respectively. Interestingly, the iso-surface follows a clam-shell-like contour with ridges, providing a means to engineer applications by controlling the parameters, as will be discussed later. The volume space above the distribution represents the parameter combinations that do not lead to optical trapping. We refer to these combinations as optical trapping *blind spots*. Technically, however, the input laser is not blind to the particle and is still able to move the particle through scattering forces.

Figure (4.13) provides a more comprehensive overview of the optical trapping process, albeit more information can be gleaned by appropriate dissections. For instance, it appears that increases in the NA, as opposed to the refractive index or the radius, are solely responsible for creating the ridge structures that extend into the optical trapping space. When slice plots are made by keeping either the refractive index or radius constant, they manifest as finger landscapes, examples of which are depicted in Fig. (4.14). However, in the example slice plot in Fig. (4.14), obtained by keeping the NA fixed, the finger landscapes are also present.

Suppose that we select two parameter points from Fig. (4.14c), $A = (2.1927, 1.2632)$ and $B = (2.1927, 1.4123)$, which lie on the finger region and another two, $C = (2.1927, 1.2105)$ and $D = (2.1927, 1.3509)$, which lie just outside the finger region. To simplify the discussion, we reference the parameter points as p_N where $N = A, B, C$ or D . At these points, we then calculate the force efficiency along the beam axis z , and provide the radiation patterns of the particles at different beam axis locations as shown in Fig. (4.15) and Fig. (4.16).

When comparing the radiation patterns of p_A and p_B against p_C and p_D at the positive peak before the equilibrium point (referred to as maximum forward restoration,

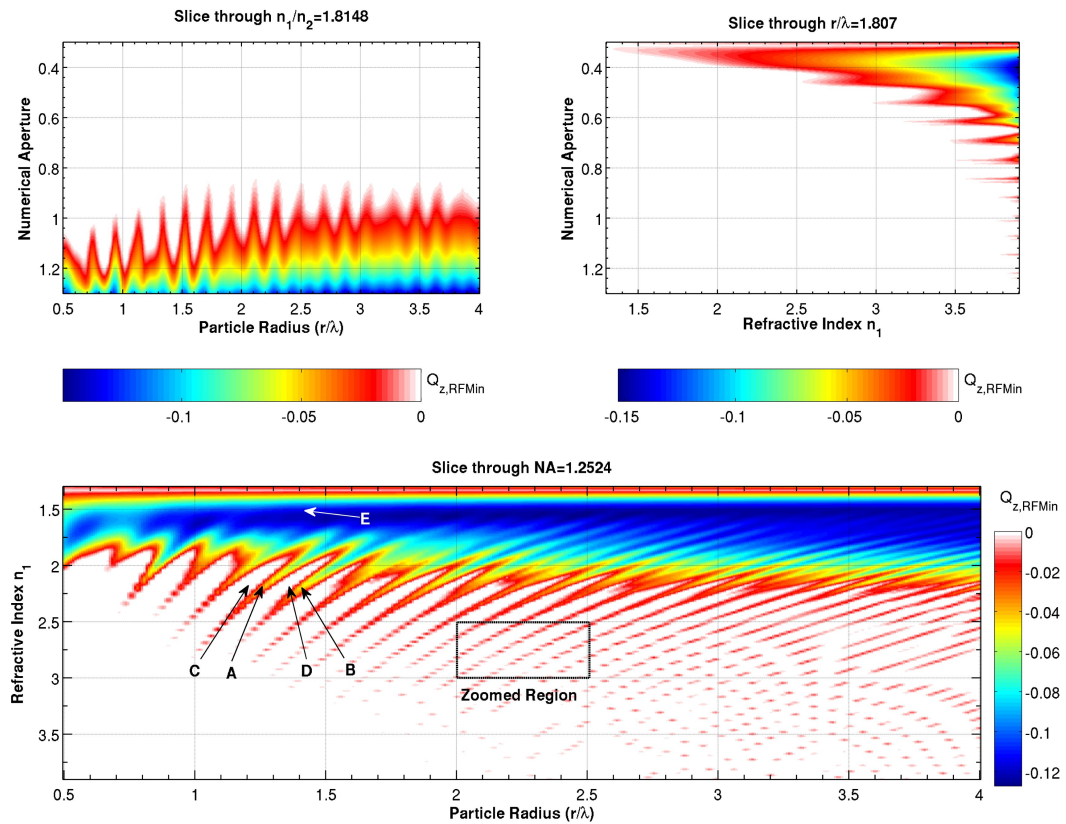


FIGURE 4.14: Example slice plots from Fig. (4.13) obtained by keeping the (a) refractive index, (b) normalized radius, and (c) NA fixed. Finger landscapes are observed in all three cases. The white areas correspond to $Q_{z,RFmin} = 0$, which indicates a non-trap condition.

$Q_{z,RFmax}$), we observe strong backscattering mode effects in all cases. As the particle approaches the focal point, the trapped particles at p_A and p_B should experience a faster change from strong backscattering to forward scattering. However, at the point of peak restoration force ($Q_{z,RFmin}$), the radiation patterns reveal that there is a smaller backscattering component for p_A and p_B as opposed to for p_C and p_D . These findings indicate the role played by scattering. Clearly, particles that backscatter too much cannot be trapped. However, this is a necessary condition. The sufficient condition for trapping also requires a forward-scattering component.

At first glance, Fig. (4.14) appears to have small islands where optical trapping occurs at locations just off the ridges. We zoomed into an example region ($2.0\mu\text{m} \leq r \leq 2.5\mu\text{m}$ and $2.5 \leq n_1 \leq 3.0$) by computing with smaller parameter value intervals for closer examination. The zoomed region, shown in Fig. (4.17), confirms that the fingers form smoothly before thinning out and vanishing eventually. Hence, the trapping islands observed in Fig (4.14) were merely artifacts of using too low a sampling rate.

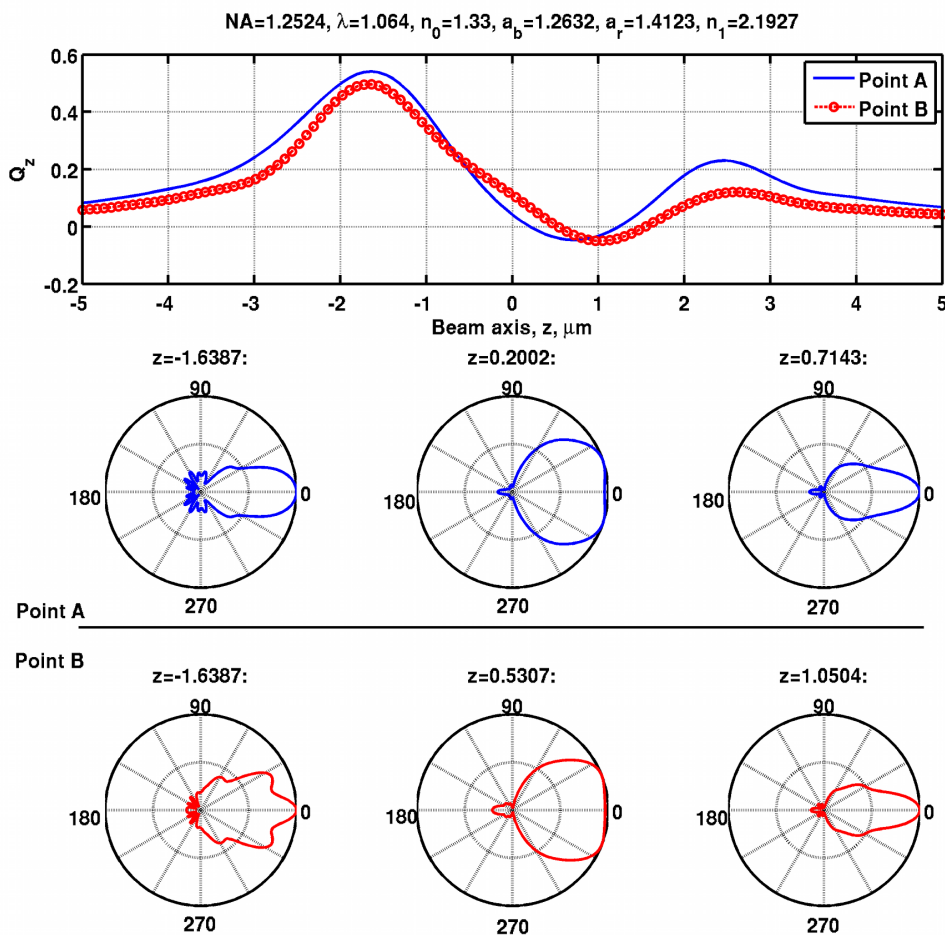


FIGURE 4.15: Optical force efficiency, Q_z calculated for particles trapped under parameter conditions p_A and p_B placed at positions along the beam axis z . For both particles, the radiation patterns at different locations corresponding to the maximum forward restoration force, equilibrium point and maximum reverse restoration force are also shown.

The next issue is defining how well particles are drawn into and held in the trap. The former is often deduced from the magnitude of the trapping efficiency $Q_{z,RFmin}$ whilst the latter is determined from the stiffness. Both of these metrics are taken to be corresponding (i.e. high Q automatically should mean high stiffness). Such an assumption can be especially problematic at the ridge regions associated with trapping. The stiffness metric also assumes a linear relationship between force and displacement. Larger particles can show considerable deviation from linearity, rendering problems in using stiffness as a descriptor.

In Fig. (4.14), the parameter points p_B and p_E , where $E = (1.5, 1.4123)$, both permit trapping. Nevertheless, their respective stiffness values of $0.198Q/\mu\text{m}$ and $0.0636Q/\mu\text{m}$

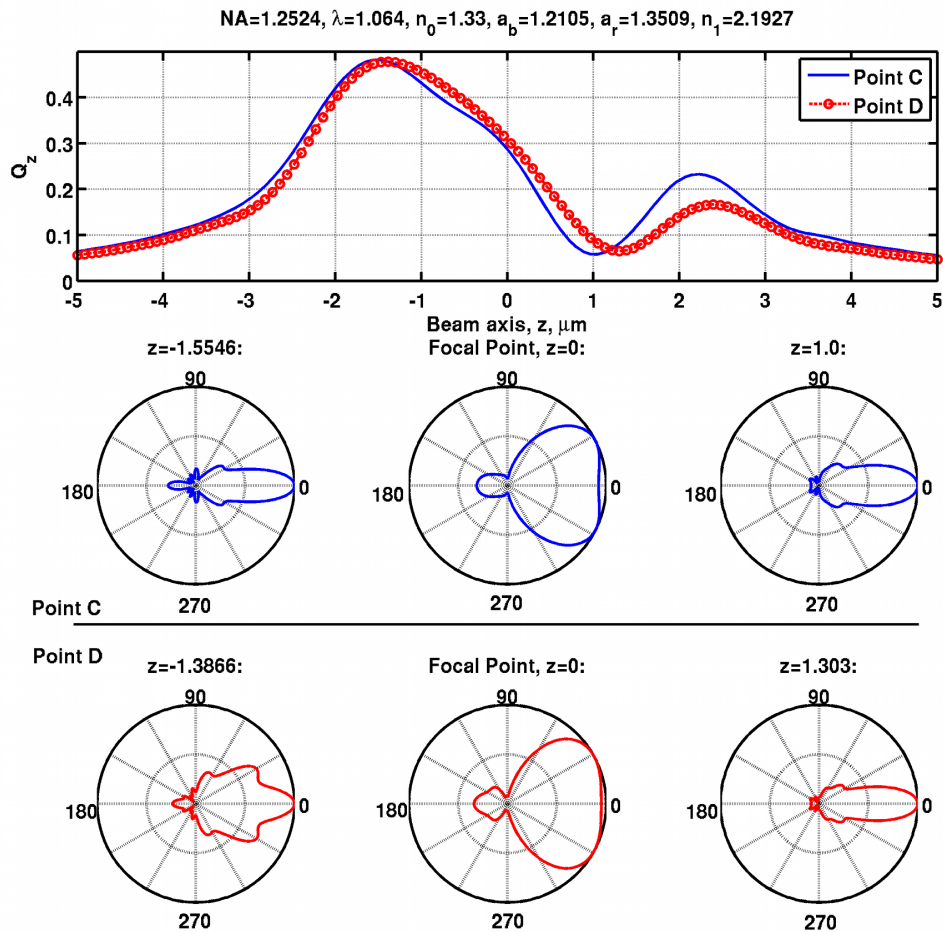


FIGURE 4.16: Optical force efficiency, Q_z calculated for particles trapped under parameter conditions p_C and p_D placed at positions along the beam axis z . For both particles, the radiation patterns at different locations corresponding to the maximum forward restoration force, focal point and $z = 1.0\mu\text{m}$ are also shown.

are significantly different, indicating that once trapped it should be harder to displace a particle p_B . However, is this really the case? Is it also reasonable to assume that a particle will be drawn in with equal likelihood at conditions B and E ?

The potential energy distributions in relation to axial position for both parameter conditions are depicted in Fig. (4.18). Both particle parameters result in a zero-crossing and a restoration force. Nevertheless, it is intuitive that a particle should be more easily trapped in E than in B due to the creation of a deeper well-like potential.

This argument is also reasonable because particles are always brought in from a free position to a trapped position, rather than appearing at the trap position instantaneously. In other words, the momentum carried by a particle when it descends into the trap

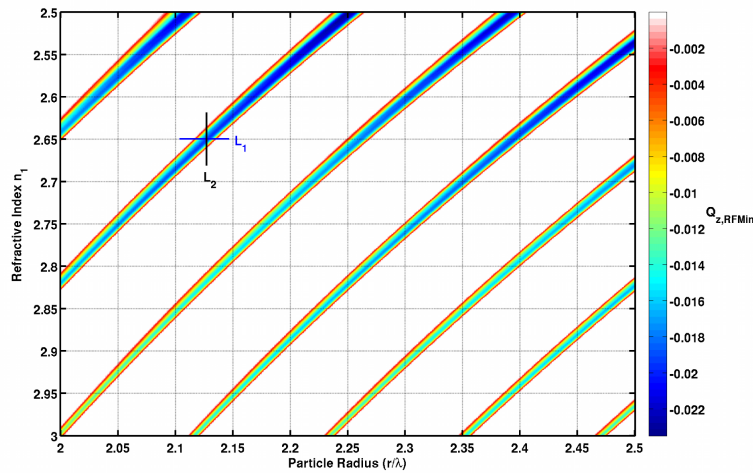


FIGURE 4.17: Zoomed-in region for Fig. (4.14), ($2.0\mu\text{m} \leq r \leq 2.5\mu\text{m}$ and $2.5 \leq n_1 \leq 3.0$), with smaller parameter value intervals, which show that the fingers form smoothly before they are thinned out and eventually vanish. Two lines, L_1 and L_2 , indicate that particles with a radius ratio between 2.115 and 2.135 would be selectively trapped, which illustrates the ability for sorting.

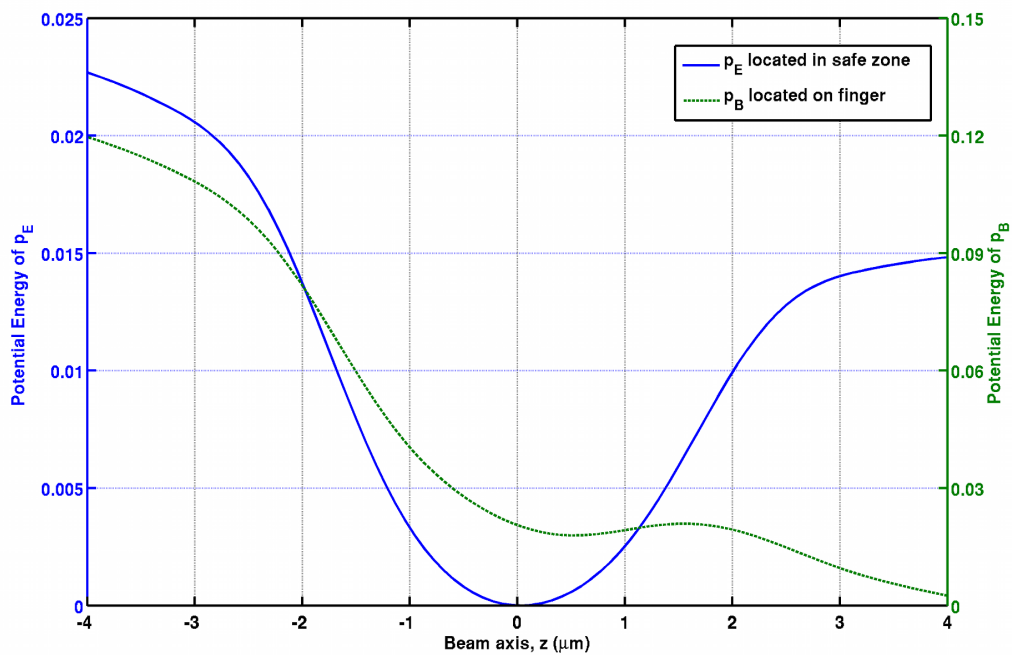


FIGURE 4.18: Potential energy wells corresponding to a particle located in the trapping finger and safe region, depicted under conditions p_B (left) and p_E (right), respectively.

location, provided that it is not overdamped, will cause it to be more readily sustained in the case of p_E . Based on this information, it also is pertinent to note that the premise of a stiffer trap is only reasonable when comparing distributions that are strongly symmetrical (e.g. p_E) and not when they are highly asymmetrical (e.g. p_B). This is because the latter provides a lower energy obstacle path for the particle to depart from the trap.

It is not uncommon in particle motion simulations for the condition of overdamping to be applied, which, in turn, implies an inability of the particle to possess any inertia force. It is important to note, however, that the overdamped assumption is valid only for sufficiently large evolution time intervals. Furthermore, a particle that has descended into a potential well will not remain stationary there, since Brownian perturbations continue to exist.

Even under the assumption of overdamping, it has been shown that Brownian perturbations can cause particles to exit potential wells [208]. Clearly, any description that does not take into consideration the asymmetry of the well is problematic. Despite these definition difficulties, it will be desirable to have at least some indication of the relative asymmetry of the trap. We content that a more apt representation to use should be what we call the trapping quality, which is described by

$$TQ = \begin{cases} 0 & Q_{z,RFmin} \geq 0 \\ \frac{Q_{z,RFmin}}{Q_{z,RFmax}} & Q_{z,RFmin} \leq 0 \end{cases} \quad (4.1)$$

This metric is reasonable because the forward restoration will always be higher due to the scattering and gradient components complementing each other in the forward direction. In contrast, they oppose each other during the reverse restoration process. In other words, we will always have $TQ < 1$, in which a value closer to 1 indicates a higher symmetry in the trap. Based on this metric, we computed that $TQ_B = 0.1$ and $TQ_E = 0.69$, which logically depicts the situation in which trapping should be more likely at p_E than in p_B (based on their potential distributions).

Note here that radial trapping behaves considerably different than axial trapping. Trapping is often taken to mean that the axial and radial trapping events are mutually exclusive (i.e. radial trapping cannot occur unless there is axial trapping and vice versa). However, calculations with radial trapping will not reveal the landscapes in Fig (4.14), meaning that there are no radial optical trapping blind spot structures in the parameter space. Determining whether particles are trapped or not, consequently, should not be based on the axial condition alone. This argument is supported by the experiment findings from previous work, where a transition from radial pulling to trapping or release was uncovered. More specifically, a particle that is sucked up from the bottom of the

beam focus will head upward along the beam axis until it reaches the focus point wherein it will be either trapped or released upward and outward in a trajectory not unlike a water fountain spray.

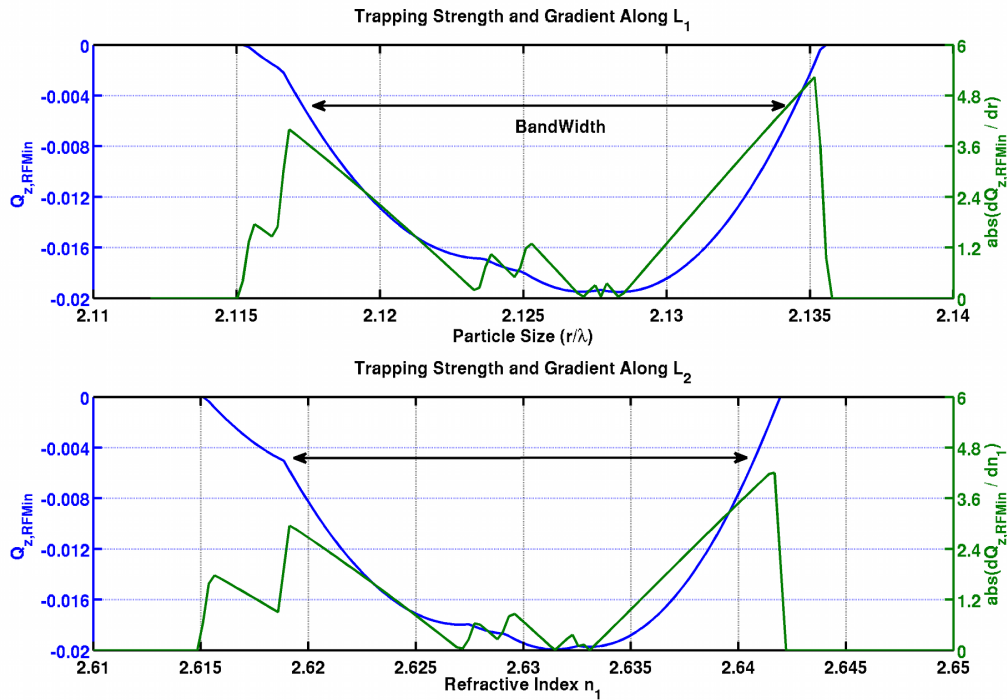


FIGURE 4.19: Trapping strength and its gradient along the lines (a) L_1 and (b) L_2 as depicted in Fig. (4.17)

The narrowing fingertips in the trapping map provide a highly selective and precise set of trapping parameters. Any small variation of the radius or refractive index would cause the particle to be set free. The trapping strength distribution along the two lines L_1 and L_2 in Fig. (4.17), and its derivative, are shown in Fig. (4.19a), which indicates that particles with radius ratio between 2.115 and 2.135 would be selectively trapped. In Fig (4.19b), alternatively, we find that particles with refractive index between 2.615 and 2.642 would be trapped. Clearly, the selection of any line across the finger landscape permits the process to operate somewhat like a tuneable bandpass filter; i.e., the ranges can be controlled by choosing a narrower or wider section of the finger. The narrower the finger is, the smaller the bandwidth will be and vice versa. That the gradient is steepest at the edges of the finger helps to enhance its selectivity. However, it is the width of the finger that determines the range of tolerances of particle radius or refractive index that can be trapped. Because these factors can be independent of each other, as seen in Fig (4.14), this imbues the capacity for effective sorting.

4.2.4 Selective Sorting and Swelling Particles

While sorting approaches with fluid flow offer apparent higher throughput, they are prone to channel effects [209, 210]. The situation becomes more complicated when non-Newtonian fluids are involved [211]. Let's consider an alternative approach based on our findings. Suppose we have an optical trap that scans a population of different sized particles of two distinct refractive indices in a plane (Fig. 4.20). Through the right wavelength selection, it will be possible to trap particles of one refractive index while allowing those of another refractive index to be scattered (note that while the gradient force is not strong enough to hold the particle, it does not mean that the scattering force is absent). At the end of the scan, only particles of one refractive index will remain in the plane. With recent developments using tailored optics, it should be possible to develop multiple trapping (and removal) sites to increase the throughput of such a process [212], albeit this may reduce the optical power at each trapping site. That the perturbation to remove selected particles is based on the optical scattering force makes this an all-optical sorting approach. This has potentially strong advantages over approaches that rely on coupled optical and Brownian forces [7], since the latter is a strongly stochastic process. At this point, we highlight interesting parallels between the effect of interference leading to parameter spaces that permit trapping based sorting here and the use spatial interference fields itself to accomplish sorting [210, 213].

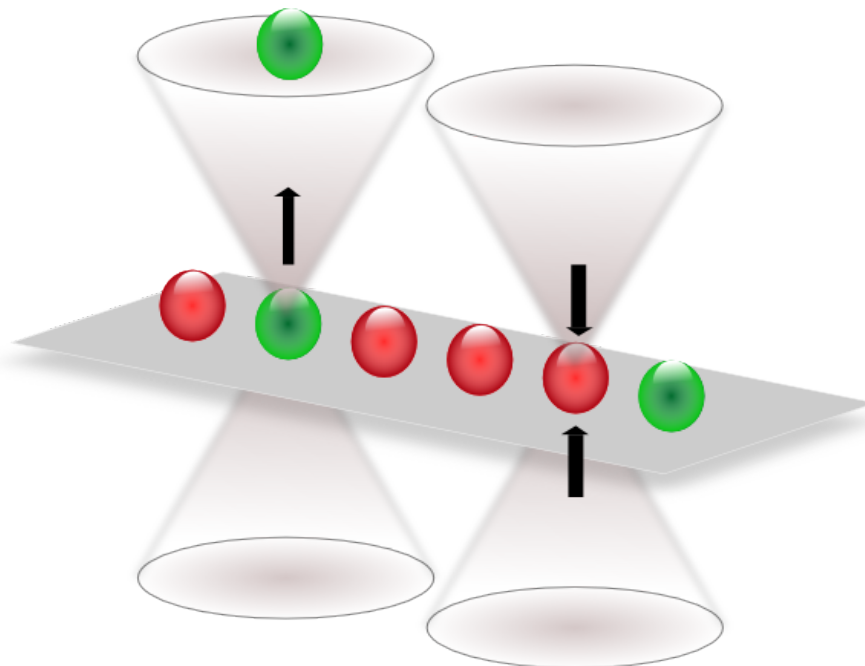


FIGURE 4.20: Selective sorting can be achieved by scanning a line of particles in a plane. Here, the red particles have parameter combinations that reside on the trapping region, e.g. the trapping fingers, and the green particles do not. At the end of the scan, only the red particles will remain in the plane while the green are scattered off plane.

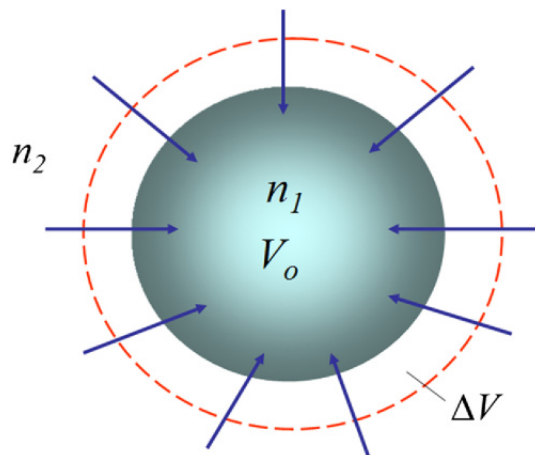


FIGURE 4.21: Schematic description of situation where a spherical of volume V_0 of refractive index n_1 undergoes swelling by absorbing material from the surrounding media of refractive index n_2 such that its volume increases by δV .

Arguably, the most potent use of the trapping map lies in situations where multiparameter variations are involved. Returning to the topic of targeted drug delivery, a popular mode of release involves swelling of the micro beads [214]. Suppose that we adopt a simple model in which a dielectric sphere of original radius $r_0 = 2.095\mu\text{m}$ and refractive index $n_1 = 2.506$ is placed in a medium with refractive index $n_2 = 1.33$. Under the assumption that the medium material fills into the bead uniformly and the bead maintains a spherical shape throughout swelling, the original volume V_0 can be taken to undergo a volume increase δV under the relationship $\delta V = \alpha V_0$, where α depicts the progress of the swelling (i.e. $\alpha = 0$ when no swelling occurs) Fig. (4.21). The refractive index of the bead can now be indicated by:

$$n'_1 = \frac{V_0 n_1 + \delta n_2}{V_0 + \delta V} = \frac{V_0 n_1 + \alpha V_0 n_2}{V_0 + \alpha V_0} = \frac{n_1 + \alpha n_2}{1 + \alpha} \quad (4.2)$$

The radius can also be described using α as

$$r = r_0 (\sqrt[3]{1 + \alpha}) \quad (4.3)$$

On the parameter map using $NA = 1.2248$ Fig (4.22), this will result in a trajectory where the particle is first trapped but strays into the condition of non-trapping with swelling increase of the sphere. That the trapping state is encountered again later is irrelevant since the particle would have been released from the hold of the potential well. If the NA is increased to $NA = 1.3$, particle trapping will be maintained throughout.

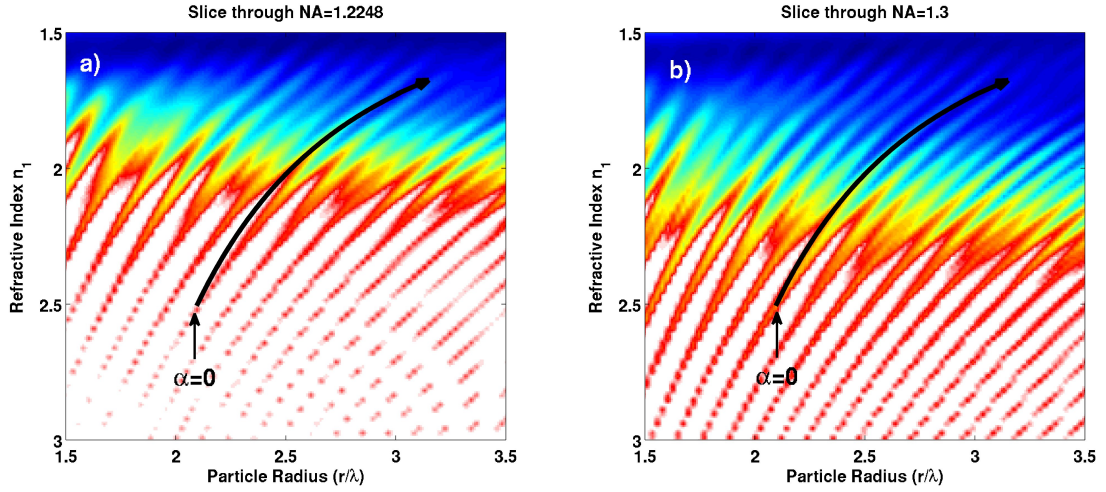


FIGURE 4.22: Trajectory of a swelling dielectric sphere with an original radius $r_0 = 2.095\mu\text{m}$ and refractive index $n_1 = 2.506$, placed in a medium with refractive index $n_2 = 1.33$ for :(a) $NA = 1.2248$ and (b) $NA = 1.33$. The growth rate, α , was linearly increased from 0.0 to 2.0.

4.3 Plasmonics

Assuming the geometry in Fig. (3.6), where $\varepsilon_2 = 1$ (air) and $\varepsilon_1(\omega)$ as given by expansion in Eq. (3.47) and coefficients in Table (3.1) for silver and gold, respectively, the dispersion relation is shown in Fig. (4.23).

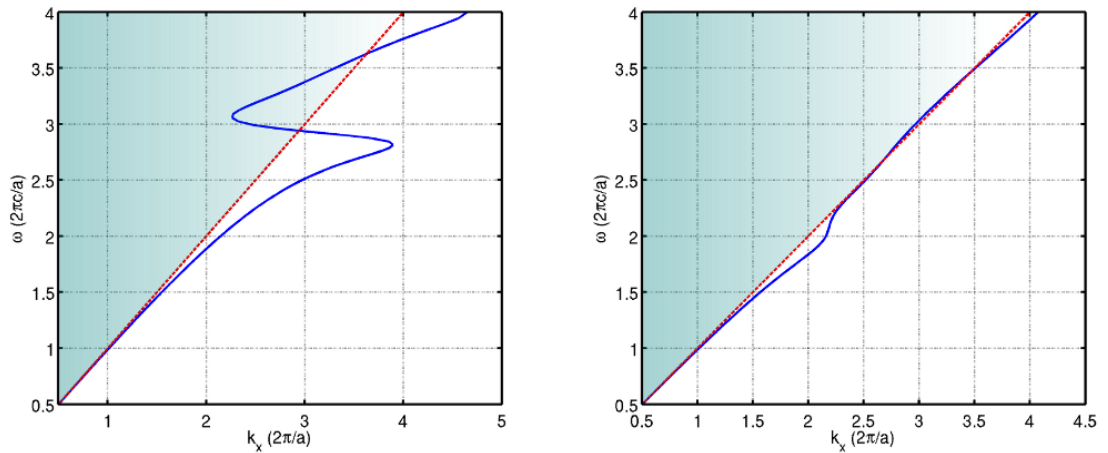


FIGURE 4.23: Dispersion relation for silver (left) and gold (right)

The dispersion characteristics of the surface plasmons in Fig. (4.23) show plasmon modes that lay below the light line, i.e. the unshaded area. Unlike most typical studies the surface plasmonic mode does not asymptote due to the interband damping terms in the complex dielectric function. The light line corresponds to the momentum that a free space photon carries at different frequencies. The region above the light line, indicated

by the shaded region, are said to be in the *light cone*. This means they can be excited by free space light. The modes that lay outside of the light cone, or below the light line if you wish, can not be excited by free space light. This is because these modes have higher momentum than what the free space light can provide.

When $\omega \lesssim 3$ the evanescent SPP modes for silver are observed, approaching the light line at short wave vectors but terminating at finite wave vector on resonance. The fairly large SPP wave vectors (and hence small SPP wavelength) achieved near resonance compete with the largely reduced group velocity in this frequency range. A similar process is observed for gold, albeit less pronounced and at a lower frequency, i.e. $\omega \lesssim 2.25$. Above $\omega \gtrsim 3$ the Radiative (RPP) mode is noticeably observed for silver, which corresponds to wavelengths satisfying the relation $\text{Im}(\varepsilon_1) > |\text{Re}(\varepsilon_1)|$.

Matching the wave vector of an incident beam of free light to simultaneously conserve energy/momentum and excite an SPP mode is a known challenge. To this end, various geometries have been used. One such geometry is the Kretschmann geometry using a prism [215]. Another geometry, which we will utilize here, consists of a metal surface with corrugated grooves with a lattice constant, groove height and width of p , h and w respectively. The periodic structure contributes a reciprocal wave vector of $2\pi n/p$ and thus the mismatch in the wave vector with incident light $k_x = k\sin(\theta)$ and k_{spp} is overcome when

$$k_{spp} = k\sin\theta \pm \frac{2\pi n}{p} \quad (4.4)$$

where $n = (1, 2, 3)$ and $k \approx 2\pi/\lambda_0$ in air. Both the methods mentioned require excitation using light incident at an angle. The geometry that we submit here overcomes this requirement by utilizing a periodic corrugated (grating) structure on the metal with a subwavelength aperture providing the necessary parallel components of the wave vector through its confined optical near fields. Once the near field along the surface is defined, the optical forces and potentials can be calculated as per Eq. (3.41).

There has been substantial efforts made to understand the underlying physics of light transmission through subwavelength apertures and aperture arrays [216], with the interest of facilitating directional light beaming at the chip level. There have been no reports of efforts, to the best of our knowledge, to harness these structures to create tailored optical trapping sites on the metallic surface. The ability to do this opens up the avenue of having multiple apertures on the surface with light addressable wavelength within the chip in order to maintain close control of optical trapping at specific and selective locations over the entire chip (see Fig. 4.24).

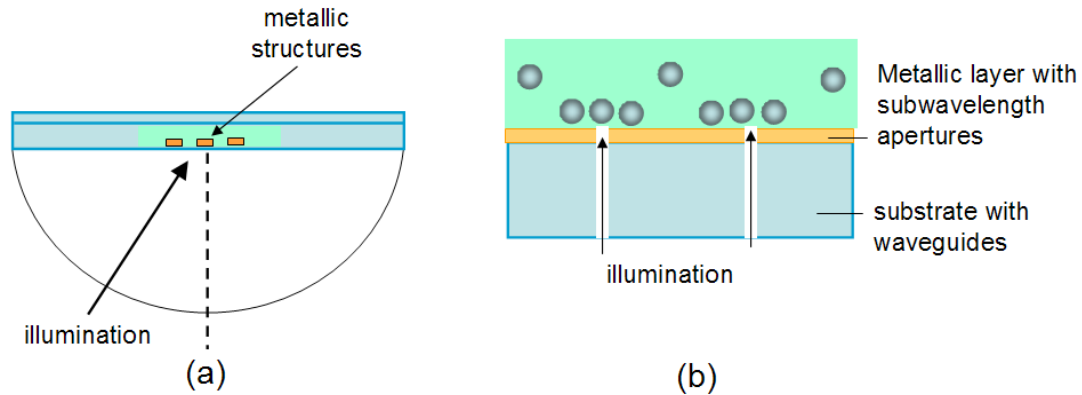


FIGURE 4.24: (a) Optical scheme of illuminating metallic structures in a whole-field manner to create localized plasmon field for trapping. (b) Envisaged approach of having illumination delivered from individually addressable waveguides within a substrate to subwavelength apertures in the metallic layer to create switchable surface plasmon sites for trapping; which in the process will facilitate many lab-on-a-chip procedures

4.3.1 Design

To design the height and width of the corrugations, we study the transmission spectra of a silver film by varying h and w corrugations on its surface at three lattice periodicities: $p = 400, 500, 600\text{nm}$ (Fig. 4.25). We do this by assuming the excitation source as a temporal Gaussian source located along the left boundary of the domain with a central wavelength of $\lambda = 1.5\mu\text{m}$ and a pulse width of $\lambda = 1\mu\text{m}$. We place a virtual line detector along the right boundary of the domain and conduct a frequency response analysis. To perform all simulations, we used the fully vectorial FDTD method described in Section (3.3).

Following this, we conducted a two-dimensional (2D) simulation along the surface of a silver film, surrounded by air, with a subwavelength slit through it and a set of tailored corrugations, with a height h and width w , of which the basic form is shown in Fig. (4.25b). Throughout this study the subwavelength aperture width s and slab thickness t are fixed at 140 and 1000 nm, respectively. The simulation grid size was a $20\mu\text{m}$ by $8\mu\text{m}$ rectangle with a pixel size of 20nm, accounting for a total of 400,000 pixels per time step. We applied a perfectly matched layer with approximately 60 pixel thickness as the boundary to simulate an open boundary while truncating the computational domain. The input light source was assumed to be H_z polarized and continuous. The parameter q refers to the offset distance between the slit edge and the start of the periodic corrugations. This permits for small adjustments to the phase matching between the slit and the corrugations. We initially considered $q = w' = h' = p' = 0$. Running the

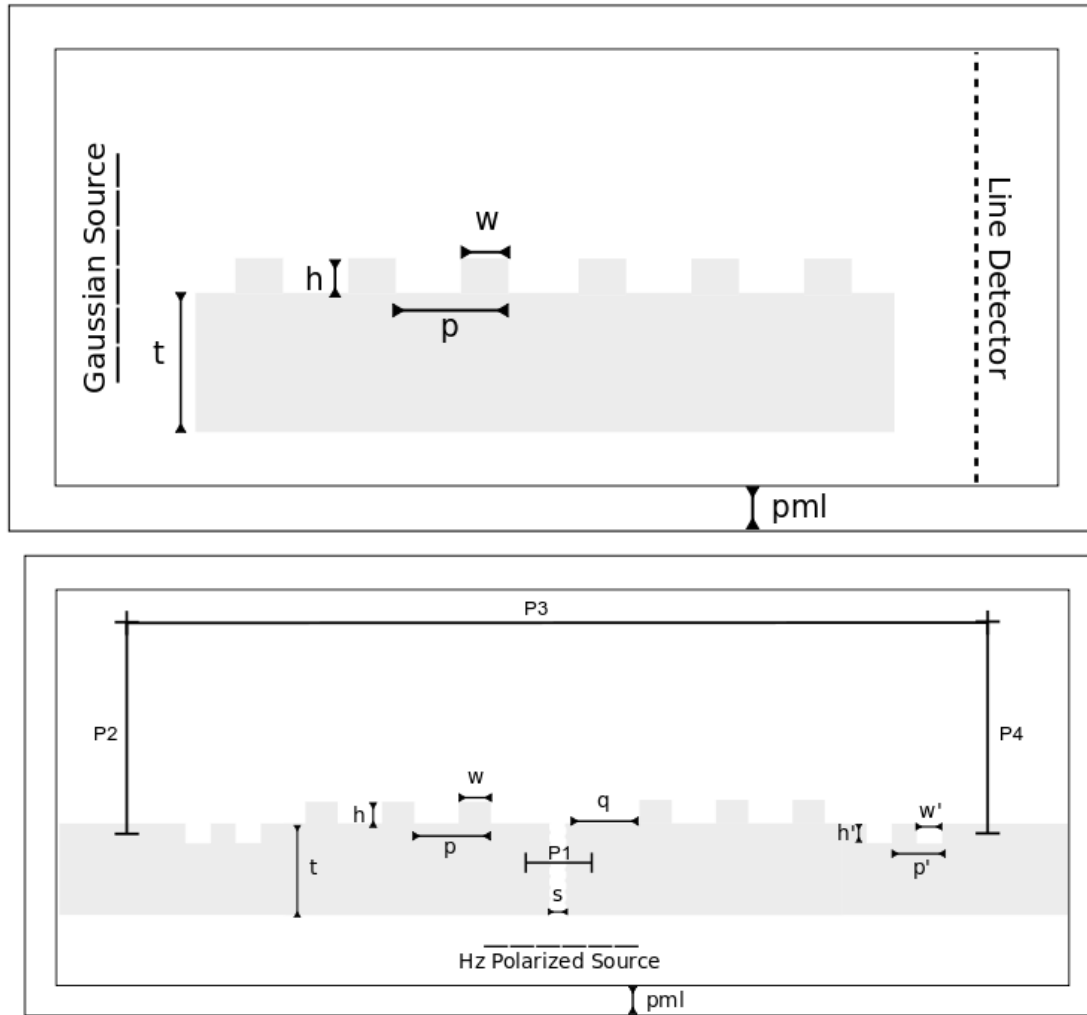


FIGURE 4.25: (a) Simulation geometry with a lattice constant, groove height, and width of p , h , and w , respectively. The Gaussian source, located to the left, has a center wavelength of $\lambda = 1.5\mu\text{m}$ and a pulse width of $\lambda = 1\mu\text{m}$. (b) Simulation geometry with a subwavelength aperture and tailored surface corrugations on a silver substrate. Throughout this study the subwavelength aperture width s , and slab thickness, t , are fixed at 140 and 1000 nm, respectively.

simulation on an Intel I7-920 CPU, we attained an average 2D simulation time of 3 min (in single core operation).

From the simulated field vectors, we were able to obtain the optical trapping forces developed on a spherical polystyrene particle having radius of 80 nm and refractive index of $n_1 = 1.59$. The media is assumed to be water having a refractive index of $n_2 = 1.33$. The particle is placed at each location of interest and the forces, using Eq. (3.41) are calculated.

4.3.2 Results and Discussion

The resulting transmission spectra for different h and w combinations is shown in Fig. (4.26) for each value of p in Fig. (4.25a). From all three transmission plots we notice in general the occurrence of two sharp resonance peaks. This resonance behaviour is most obvious for the system where $p = 500\text{nm}$ and $p = 600\text{nm}$ (Figs. 4.26b,c). The two strongest resonant peaks seen in Fig. (4.26b) occur for parameters $h = 150\text{nm}$, $w = 250\text{nm}$, and $p = 500\text{nm}$ at the two encircled locations A and B. The wavelength at A is approximately near the center wavelength at $\lambda = 1.464\mu\text{m}$ and at B it is approximately near $\lambda = 1.38\mu\text{m}$. However, for a larger periodicity of $p = 600\text{nm}$, the strongest resonant peaks occur for parameters $h = 150\text{nm}$ and $w = 200\text{nm}$ at the two encircled locations, A and B. The wavelength at A is near $\lambda = 1.715\mu\text{m}$ and the second, B, is near $\lambda = 1.587\mu\text{m}$.

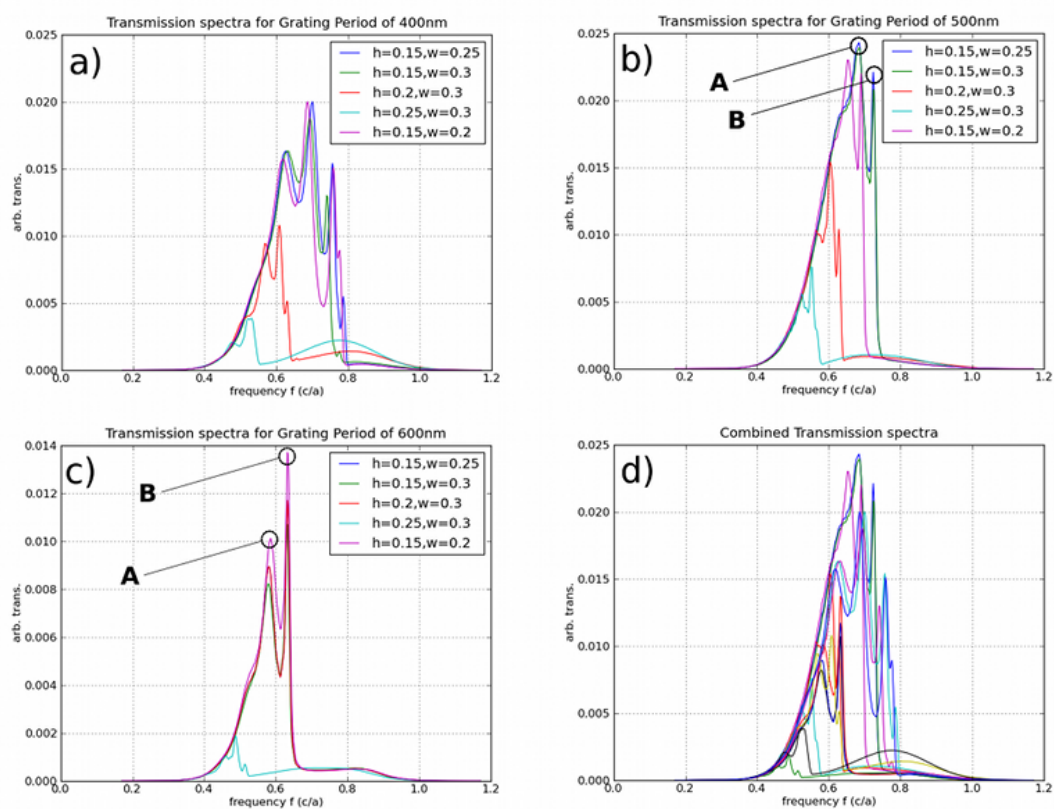


FIGURE 4.26: Transmission spectra for a grating period of (a) 400, (b) 500 and (c) 600 nm, respectively, at different h and w configurations. (d) Combined transmission spectra outlines the input Gaussian spectra. The strongest resonance is observed when $h = 150\text{nm}$, $w = 250\text{nm}$, and $p = 500\text{nm}$.

We present in Fig. (4.27) a snapshot and animation as a contour plot of the electric field intensity ($\|E\|^2$) mode profiles of the two points A and B in Figs. (4.26b,c). For a periodicity of $p = 500\text{nm}$, we have used the configuration $h = 150\text{nm}$ and $w = 250\text{nm}$ (corresponds to the blue curve in Fig. 4.26) and for a periodicity of $p = 600\text{nm}$ we have

used the configuration $h = 150\text{nm}$ and $w = 200\text{nm}$ (corresponds to the pink curve in Fig. (4.26c)).

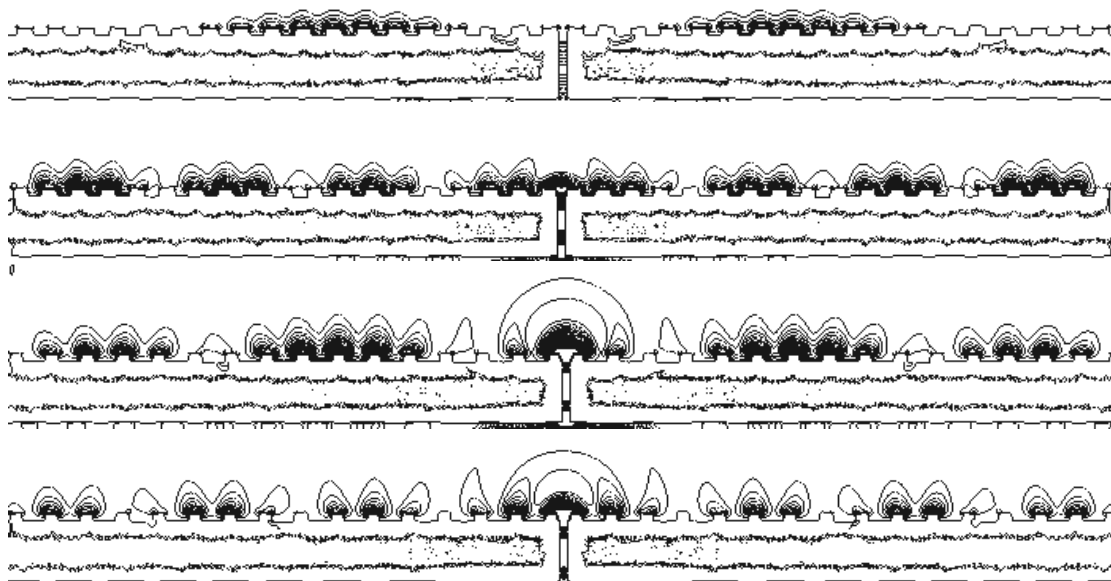


FIGURE 4.27: Snapshots of the electric field intensity, $\|\mathbf{E}\|^2$, shown as a contour plot along the metallic structure for (a) $p = 500\text{nm}$, $\lambda = 1380\text{nm}$, $h = 150\text{nm}$, and $w = 250\text{nm}$; (b) $p = 500\text{nm}$, $\lambda = 1464\text{nm}$, $h = 150\text{nm}$, and $w = 250\text{nm}$; (c) $p = 600\text{nm}$, $\lambda = 1587\text{nm}$, $h = 150\text{nm}$, and $w = 200\text{nm}$; (d) $p = 600\text{nm}$, $\lambda = 1715\text{nm}$, $h = 150\text{nm}$, and $w = 200\text{nm}$

Noticeable differences between the designs include the wavelength of the surface plasmon modes and the decay length into air. While the results indicate a possibility of channeling light power onto the surface, the manner of its propagation, in packets at the speed of light, per se, will not permit particle trapping. To facilitate this, the optical field has to be in the form of a standing wave. We achieved this by introducing structures at the distal ends away from the slit, shown in Fig. (4.26) with parameters w', h' and p' . The structures are designed using the transmission spectra obtained previously such that the transmission across its surface at the wavelength of interest is highly suppressed. This has the effect of causing the traveling packets of leaky waves to be reflected back. Since coherence is preserved, careful design will enable standing waves to develop.

Utilizing the design that produces the outcome of Fig. (4.27a), we calculate the time-averaged electric field intensity, as shown in Figs. (4.28) for different offset values of $q = 0, 105, 155, 205\text{nm}$. The chosen parameters for the reflective corrugations at the ends are $p' = 500\text{nm}$, $h' = 125\text{nm}$, and $w' = 300\text{nm}$. For larger values of q , the structures begin to exhibit beaming behaviour similar to those reported previously.

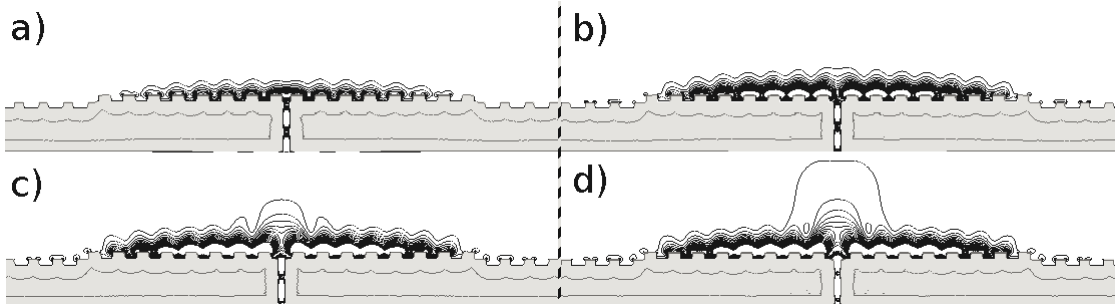


FIGURE 4.28: Snapshots of the electric field intensity, $\|\mathbf{E}\|^2$, shown as a contour plot along the metallic structure where $p = 500\text{nm}$, $\lambda = 1380\text{nm}$, $h = 150\text{nm}$, $w = 250\text{nm}$, $p' = 500\text{nm}$, $h' = 125\text{nm}$, $w' = 300\text{nm}$, and (a) $q = 0$; (b) $q = 105\text{nm}$; (c) $q = 155\text{nm}$; (d) $q = 205\text{nm}$.

Using the design that produces the outcome in Fig. (4.28b) we inserted into the simulation domain a spherical polystyrene particle with a radius of 80 nm. The particle is placed at each location of interest and the forces are calculated. The resulting force field is shown in Fig. (4.29).

It is noteworthy that, at this length scale, Brownian perturbations will serve to disperse the trapped nanoparticle from its intended trapped location. The trapping potential extends to approximately 350 nm above the surface of the device, which again indicates that this scheme is feasible to trap nanoparticles. It should be noted that, by modifying the number of corrugations on either side of the slit, the width of the trapping site can be modified. Furthermore, the decay into air can be somewhat increased by using a different mode profile. For example, it is obvious that the decay lengths of the modes in Fig. (4.27c) are longer even though the mode profiles are more complex. This approach, however, would require the careful design of the reflective defects to preserve coherence.

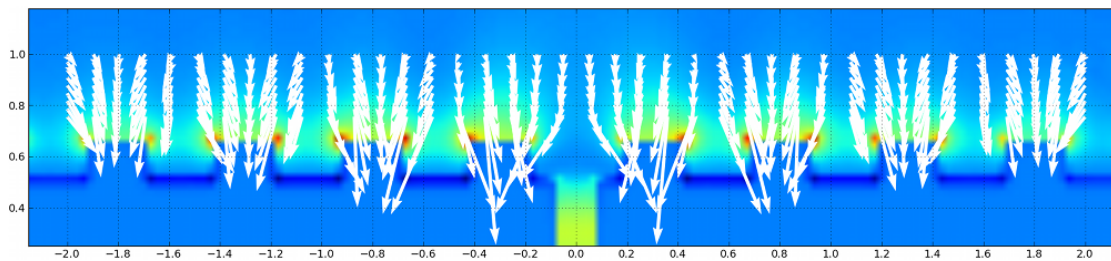


FIGURE 4.29: Optical trapping force developed on a spherical polystyrene particle with a radius of 80nm and refractive index of 2.5 in water inserted into the design producing the electric intensity field of Fig. (4.28b).

While the method is demonstrated here with the situation of slit apertures on the surface, we envisage that the progression from 2D to an axis-symmetric three-dimensional optical trap should not be difficult. The optical trapping of particles into rings is typically achieved using an axicon [78]. As in the case of conventional traps, the resolution of the

optical fields is limited by diffraction. Some efforts have been reported to utilize phase matching using photonic structures to permit subwavelength fields [217]. In our case, these rings will be inherently subwavelength with strong plasmon intensity fields. The availability of optical forces on a chip allows for the assembly of nanoparticles beyond the use of means such as evaporation, where a degree of randomness can be expected. Once held in place, tailored patches within the nanoparticle will be able to hold such assemblies in place when the optical forces are switched off [218]. It is also conceivable that metallic nanoparticles instead of corrugations may be placed at the output of waveguides to create the optical trapping fields via a plasmon generating effect as well. Means to ensure that the nanoparticles stay at the site without the presence of light, where Brownian forces are significant, will however, be needed for this.

4.4 Chapter Summary

We have proposed a scheme that locates the focus of the beam either above or below the matter to pull and push it relative to the beam axis in a predominant lateral sense using the resultant action of scattering and gradient forces. Numerical simulation and experimental results confirm this approach. This simple approach offers remedy to photodamage of living matter held using conventional optical tweezers. Furthermore, by moving a medium containing particles past a laser beam arranged in this manner, we have been able to develop an approach that creates a gentle and tunable stirring effect of particles. The computer simulations performed, enabled us to trace the expected deflection trajectories of the particles. Since the deflection effect is not enhanced beyond a certain laser power, this can be used as a basis to find optimal powers for stirring. Experiments using polystyrene micro-beads and red blood cells confirm the optical stirring effect. This approach portends the capability to execute mechanical stimuli of cells in a small liquid volume bioreactor that is free of flow, leading to better realization of lab-on-a-chip systems.

A comprehensive computation was successfully conducted to ascertain the axial trapping efficiency, which is limiting, of spherical dielectric particles using a focused Gaussian laser beam based on (i) the particle radius r , (ii) the ratio of the refractive index of particle over the medium, and (iii) the NA of the delivered light beam. It yielded an iso-surface that follows a clam-shell-like contour with ridges that offer a way to engineer applications by controlling the parameters used.

It also was found that a volume space exists based on specific parameter combinations that do not lead to optical trapping. By examining specific points in the computed parameter volume space, we uncovered difficulties using the trapping efficiency and stiffness

metrics in defining how well particles are drawn into and held in the trap. An alternative calculation based on the maximum forward and restoration values of the trapping efficiency in the axial sense, which we called the trapping quality, provided a more practical metric. The ridge regions of trapping offer high specificity on whether trapping can occur or not based on small parameter changes. Consequently, this may be harnessed for effective particle sorting. Finally we discussed how the optical trapping blind spots can be advantageous in applications that use optical forces for particle translation in which photothermal damage is eschewed. We also highlighted the use of the map to guide multiparameter changes during trapping.

Finally, we have designed a corrugated structure and a subwavelength aperture to demonstrate the possibility of guiding light from the aperture along the surface via an appropriate corrugation geometry with silver. By carefully placing a secondary grated structure some distance from the original structure, we were able to produce strong reflection, which, with the coherent nature of light used, created strong optical standing wave fields that could be harnessed for particle trapping. We demonstrated this concept in the form of linear field traps. With careful design, we envisage the ability to create optical traps of various geometries without difficulty via the same principles as outlined.

The findings described in this chapter have been reported in the following publications:

1. M. Muradoglu, T.W. Ng, A. Neild, I. Gralinski, Tailored leaky plasmon waves from a subwavelength aperture for optical particle trapping on a chip. *Journal of the Optical Society of America B*. 28 (2011), enclosed in Appendix (B.2).
2. M. Muradoglu, T. Le, C.Y. Lau, O.W. Liew, T.W. Ng. Optical stirring in a droplet cell bioreactor. *Biomedical Optics Express*. 3 (2012) 2465-2470, enclosed in Appendix (B.5).
3. M. Muradoglu, W.S.-Y. Chiu, T.W. Ng Optical force lateral push-pulling using focus positioning. *Journal of the Optical Society of America B*. 29 (2012) 874-880, enclosed in Appendix (B.4).
4. M. Muradoglu, T.W. Ng, Optical trapping map of dielectric spheres. *Applied Optics*. 52 (2013) 3500-3509. Featured in June 2013 Issue of *Laser Focus World*, enclosed in Appendix (B.7).

Chapter 5

Brownian Dynamics

5.1 Introduction

Tracking a Brownian particle's motion allows localized parameters at its immediate vicinity to be measured. Such parameters include the temperature and viscosity from the liquid microenvironment which are crucial for processes that involve electrochemistry and biology. Critical to such a sensor is its minimal disturbance to the evolution of the measured quantity around the localized environment and an absence of any input energy to drive the probe. While fluctuations in the Brownian motion using freely translating particles should provide inexhaustible amounts of information, there is the problem of these particles drifting away from the venue of measurement as well as colliding with other particles. The former causes the problem of lapses in measurement continuity. This and the latter issue of collisions tend to introduce additional complexity in interpreting the underlying mechanics.

On the other hand, Brownian motion is often detrimental to sorting as a consequence of fluctuating forces that lead to distributions spreading. Asymmetric periodic potentials have been actively investigated to rectify the symmetric fluctuations in Brownian particles. A convenient scheme to accomplish this is via the switching on and off (conveniently described as cycling) of a periodic but spatially anisotropic potential. Such stochastic ratchets have been demonstrated as capable of sorting spherical Brownian particles.

In Section (5.2), we theoretically examine the possibility of using stochastic ratchets to sort populations of Brownian rods, investigating, in particular, the role that the crossover time from anisotropic to isotropic motion takes in this process.

In Section (5.3) we present a rod that is drawn by a tunable attractive force to a cylindrical pillar that overcomes the aforementioned problems of the particle drifting away from the venue of measurement as well as colliding with other particles. The rod is assumed to be a Gold nanorod that allows for strong light scattering at the plasmon resonance wavelength. That the scattered light is strongly polarized along the long axis makes gold nanorods in principle an ideal orientation probe. We contend that more robust information can be gleaned from interrogating the surface plasmon interaction between the Brownian rod and a plasmonic whispering gallery.

5.2 Sorting of Brownian rods by the use of an asymmetric potential

Consider the case where the motion of Brownian particle is confined to a plane in a fluidic chamber wherein an asymmetric potential can be imposed. Suppose the asymmetric potential can be switched with a prescribed duty cycle. During the on cycle of the potential, the potential will collect particles at the force potential minima. Typically, this would correspond to lines within the plane of interest. It can be reasonably assumed that the rods will align along these lines. During the off phase the motion of the particles are due to free diffusion Brownian effects. The Brownian motion of a rod can be described by the Langevin equations

$$\begin{bmatrix} \dot{x} \\ \dot{y} \\ \dot{\theta} \end{bmatrix} = \begin{bmatrix} \sqrt{2D_a}\cos^2\theta + \sqrt{2D_b}\sin^2\theta & (\sqrt{2D_a} - \sqrt{2D_b})\cos\theta\sin\theta & 0 \\ (\sqrt{2D_a} - \sqrt{2D_b})\cos\theta\sin\theta & \sqrt{2D_a}\sin^2\theta + \sqrt{2D_b}\cos^2\theta & 0 \\ 0 & 0 & \sqrt{2D_\theta} \end{bmatrix} \begin{bmatrix} \xi_x \\ \xi_y \\ \xi_\theta \end{bmatrix}, \quad (5.1)$$

where a dot indicates a time derivative and $\xi_{x,y,\theta}$ are the time derivatives of a delta-correlated random Weiner process, such that $\langle \xi_i(t)\xi_j(t') \rangle = \delta(t-t')\delta_{ij}$ with $i, j = x, y, \theta$. In other words, ξ_x , ξ_y , and ξ_θ are statistically independent noise sources. As shown in Fig. (5.1a), the x and y axes are static laboratory frames. The translational and rotational motion is characterized by the diffusion coefficients, D_a , D_b and D_θ , which describe the translation parallel to the length of the rod, the translation perpendicular to the length of the rod, and the rotation of the rod, respectively.

The directions of D_a and D_b can be seen in Fig. (5.1a). When considering motion in a bulk fluid volume, the values for these diffusion coefficients are given approximately by

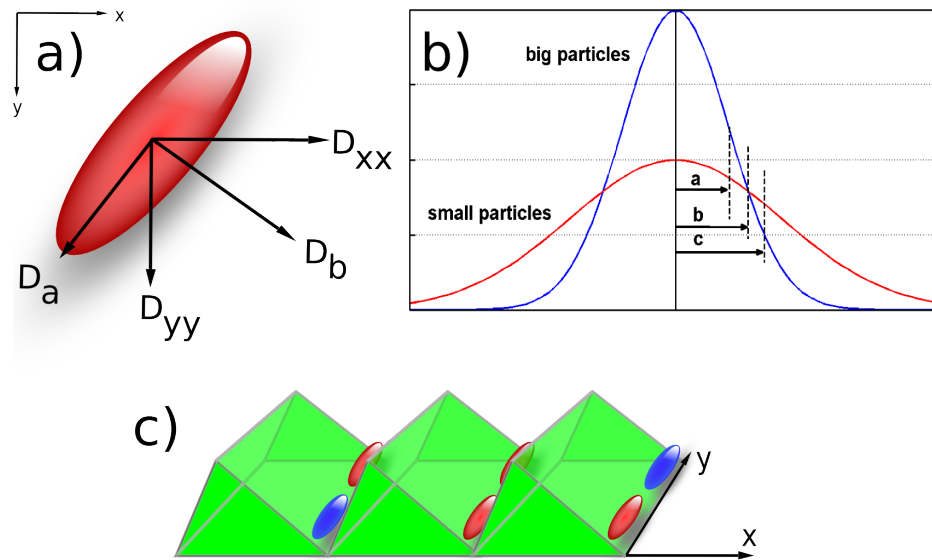


FIGURE 5.1: (a) Directions of diffusion coefficients superimposed on a typical rod under consideration, with the static laboratory frame in the top left. (b) PDFs for small and large spheres at a given time t . The greatest difference in probability between the small and big spheres occurs at the intersections of the PDFs (marked as b). (c) Diagrammatic representation of the position and alignment of rods near the end of the on period from both top and side views

[219]

$$D_a = \frac{k_B T [\ln(2r) - 0.5]}{2\pi\eta_s L} \quad (5.2a)$$

$$D_b = \frac{k_B T [\ln(2r) + 0.5]}{4\pi\eta_s L} \quad (5.2b)$$

$$D_\theta = \frac{3k_B T [\ln(2r) - 0.5]}{\pi\eta_s L^3} \quad (5.2c)$$

where k_B is the Boltzmann's constant, T is the temperature in Kelvin, $r = L/d$ is the aspect ratio (L and d are the length and the diameter of the fiber, respectively), and η_s is the viscosity of water at T . A system that is highly confined in the third dimension (i.e., with a small height component) can be treated approximately as a 2D system. Thus the actual values of the diffusion coefficients are considerably lower than these bulk values due to hydrodynamic interactions with the walls [91]. The diffusion coefficients are thus scaled in our simulations based on the experimental results obtained by Han et al [90].

The Brownian motion of a particle during the off cycle dictates the potential minimum location that it will converge to once the asymmetric potential is switched on. For spherical particles, the probability density function (PDF) is based on a single diffusion constant D which depends on the radius of the particle. This PDF is normally

distributed and is given by [220]

$$PDF(x) = \frac{1}{\sqrt{4\pi Dt}} e^{-\frac{x^2}{4Dt}} \quad (5.3)$$

where D is the diffusion coefficient at time t and x is the distance moved, such that for two particles of different sizes starting at the same minima at the start of the off cycle, one will see the smaller particle having a higher probability of moving further before the on cycle starts. The relative probabilities are shown with respect to the force potential in Fig. (5.1b). Once the force field resumes, those particles which have passed the nearest maxima will move one step further along the chamber. The asymmetry of the potential will skew the probability of progression in one direction. A relationship between the off cycle duration and the barrier length can be determined so that an optimized sorting scheme can be designed [7].

When examining the motion of Brownian rods, it is necessary to consider it in the fixed laboratory frame, x - y . At the end of an on cycle, the particles are aligned parallel to the y -axis and within wells spaced along the x direction as depicted in Fig. (5.1c). Upon release from effects of the potential the particles move according to Eq. (5.1) based on the three diffusion parameters linked to the rod geometry. However, when this motion is described by a diffusion coefficient in the laboratory frame, the value changes over time. Over short time periods, the particle aligned with its long axis, approximately along the y -axis, will diffuse preferentially along the y -axis. However, over longer periods of time, that initial rotational alignment with the y -axis is washed out by the ensuing random motion. The diffusion coefficients in the laboratory frame can be expressed as

$$D_{xx}(t) = \bar{D} - \frac{\delta D \tau_4(t)}{2t}, \quad (5.4a)$$

$$D_{yy}(t) = \bar{D} + \frac{\delta D \tau_4(t)}{2t} \quad (5.4b)$$

where D_{xx} and D_{yy} are the diffusion coefficients in the x and y directions, respectively, and $\bar{D} = (D_a + D_b)/2$, $\delta D = D_a - D_b$, and $\tau_4(t) = (1 - e^{-4D_\theta t})/4D_\theta$. These values are plotted in Fig. (5.2) for two rod sizes. It can be seen that there is an initial maximum difference in D_{xx} and D_{yy} .

After a period of time, this anisotropy is lost and the motion in both directions is equally likely. This period is characterized by the crossover time as expressed by

$$\tau_\theta = \frac{1}{2D_\theta} \quad (5.5)$$

where τ_θ is the crossover time and D_θ is as defined earlier.

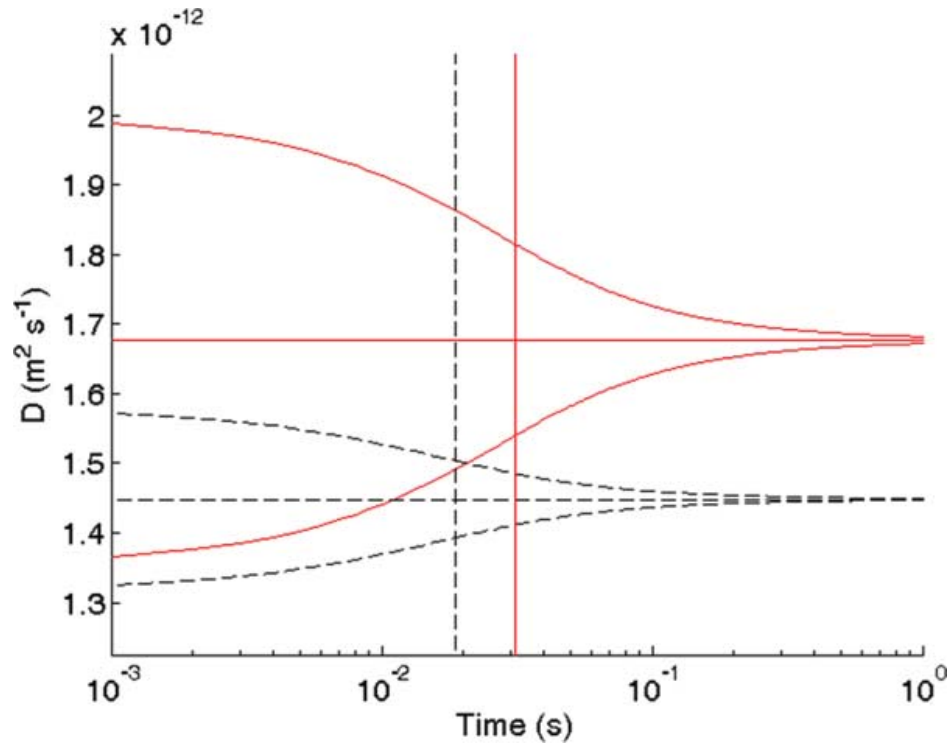


FIGURE 5.2: Plot of D_{yy} (upper curves) and D_{xx} (lower curves) vs time for two different rods with dimensions $595.2 \times 168 \times 168 \text{nm}^3$ (black, dashed) and $864 \times 72 \times 72 \text{nm}^3$ (red, solid). Horizontal lines represent \bar{D} and vertical lines represent τ_θ .

The dependence of a rod's diffusion coefficient (in a certain fixed direction) with time differs greatly from a sphere. In the case of the spheres the diffusion coefficient is independent of time; in addition [with reference to Fig. 5.1b] it is clear that the separation of particles is based on them having different diffusion values. Hence, a direct link is available between the optimal barrier length and the off time, with the sorting capability limited only by the smallness of the minimal barrier length that can be created.

However, for a rod with the diffusion coefficients in the x direction varying over time, the relationship becomes time dependent. The x direction is of importance as it dictates whether the rods will cross from one minimum to the next. Furthermore, different time periods can be used to separate different sets of rod sizes. The effect is depicted in Fig. (5.3), which shows a map of D_{xx} for a grid of particle sizes after two different periods of time have elapsed. Within these plots, rods on the same contour lines have the same D_{xx} value and cannot be sorted. Rods on different contour lines can be sorted. Thus, it can be seen that different clusters of rod sizes (diameter and length combinations) can form depending on the off time chosen. This is seen visually by the change of the angle of the contour lines, which occurs when comparing between the two plots. This means that a degree of sorting by length and diameter should be possible if a two stage process is used, one using an off time much lower than the crossover time, and the other using a

value larger or close to the crossover time. We now examine the design of this two stage process in more detail.

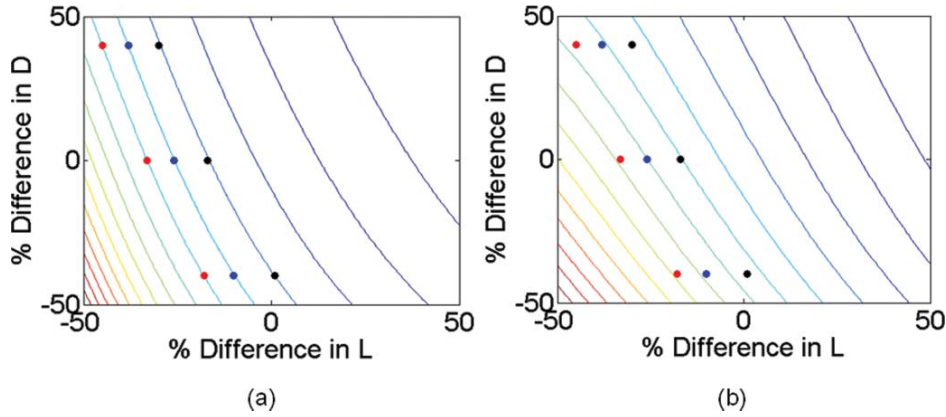


FIGURE 5.3: Contour plots of diffusion coefficient in the laboratory x direction over a range of rod sizes taken at time (a) $30\mu\text{s}$ and (b) $400\mu\text{s}$. The percentage difference in length (L) and diameter (D) are taken from a $960 \times 120 \times 120\text{nm}^3$ base rod. The circles on the plot indicate the rod sizes used in simulations, with the blue coloured circles indicating the rods that were taken to the second stage of sorting. The red and black circles are rod sizes on adjacent contours at $30\mu\text{s}$, and are overlaid in (b) to emphasize the change in diffusion coefficient over time. The largest diffusion coefficients correspond to the smallest particle sizes in the lower left corner of the plot (red contours) and decrease toward the top right (blue contours). The colours of dots used correspond to the curves in Fig. (5.5).

5.2.1 Stage one

At very short and very long off times, the orientations of the equal diffusion contour lines in plots such as those shown in Fig. (5.3) do not change significantly. For a given off time, the choice of the barrier length has a direct impact on the amount of sorting that can be achieved per cycle. With reference to Fig. (5.1b), the barrier length determines where the PDFs are cut, i.e., what proportion of rods progress to the next potential well and the proportion that remains in the current well. This allows the optimal barrier lengths for sorting particles with similar diffusion coefficients to be calculated. The barrier length used is the optimal length for the pair of particles with the least amount of sorting achieved. This ensures that the particles that are the hardest to separate have their optimal barrier lengths chosen. Take two particles with different diffusion coefficients D_1 and D_2 at an off time t . These are normally distributed as described by the following PDFs:

$$\begin{aligned} X_1 &\sim N(0, \sqrt{2D_1t}) \\ X_2 &\sim N(0, \sqrt{2D_2t}) \end{aligned} \tag{5.6}$$

The greatest difference between two normally distributed cumulative density functions occurs when their PDFs intersect, so we are interested in the points where $X_1 = X_2$. This is also the point at which we wish to put our barrier. Equating PDFs leads to

$$\begin{aligned}
\frac{1}{\sqrt{4\pi D_1 t}} e^{-\frac{x_1^2}{4D_1 t}} &= \frac{1}{\sqrt{4\pi D_2 t}} e^{-\frac{x_2^2}{4D_2 t}} \\
\sqrt{\frac{D_2}{D_1}} &= e^{\left(\frac{x_1^2}{4D_1 t} - \frac{x_2^2}{4D_2 t}\right)} \\
\frac{1}{2} \ln\left(\frac{D_2}{D_1}\right) &= \frac{X_1^2}{4t} \left(\frac{1}{D_1} - \frac{1}{D_2}\right) \\
2t \ln\left(\frac{D_2}{D_1}\right) &= X_1^2 \left(\frac{D_2 - D_1}{D_1 D_2}\right) \\
X_1^2 &= \frac{2t D_1 D_2 \ln\left(\frac{D_2}{D_1}\right)}{D_2 - D_1} \\
X_1 &= \pm \sqrt{\frac{2t D_1 D_2 \ln\left(\frac{D_2}{D_1}\right)}{D_2 - D_1}}
\end{aligned} \tag{5.7}$$

Since we have used asymmetric potential fields, only the positive root of this equation was of interest. The optimal barrier length for a pair of particles at a given off time can be determined from Eq. (5.7). If we first consider short off time case where the orientations of the contours do not change much with time, there is some flexibility in the value that can be chosen. The separation time in the first stage of sorting is much smaller than it is for the second stage, so it does not need to be considered. In the first stage of sorting, the limiting factor is the minimum feature size possible in the potential field (this is similar to the case of the spherical particles), inferring that the more frequently the process can be repeated in the given period of time, the better the sorting will be. It should be noted that only the barrier length needed to be considered as it determined the initial off time to be used.

Once the minimum feature size is available to determine the barrier length, and hence, the off time, the backflow distance can then be calculated. This depends on the proportion of particles that can be allowed to progress in the opposite direction of the desired motion. Ideally this should be zero, but that would necessitate an infinite backflow length. For the results presented here, a maximum allowable backflow of 0.01% was chosen. The actual length can be determined from the equation

$$\Pr(X > l_{\text{backflow}}) < 0.0001, \quad X \sim N(0, \sqrt{2D_{xx}t}), \tag{5.8}$$

where D_{xx} is the diffusion coefficients in the x direction for the given off time t and l_{backflow} is the backflow length. This equation determines the distance from the original position at which less than 0.01% of particles with diffusion coefficients D_{xx} at time t

will be found. This value was calculated for each particle size in the population and the largest value was chosen. As a rule of thumb, four to five times the barrier length should give a sufficiently large backflow length.

The on time was not considered, but was assumed to be long enough, so that all particles would have their long axis aligned along the y -axis and be located exactly at the bottom of their corresponding wells. The magnitude of the potential barrier was not considered and assumed to be sufficient to achieve the alignment and position conditions as outlined.

5.2.2 Stage two

Once the first stage of separation was complete, a given group of particles would be further separated by the use of a longer off time. With reference to Fig. (5.3) these are represented by blue circles. The use of a longer off time means that the rods are able to rotate by a significant amount, and hence, tend to lose their anisotropic behaviour.

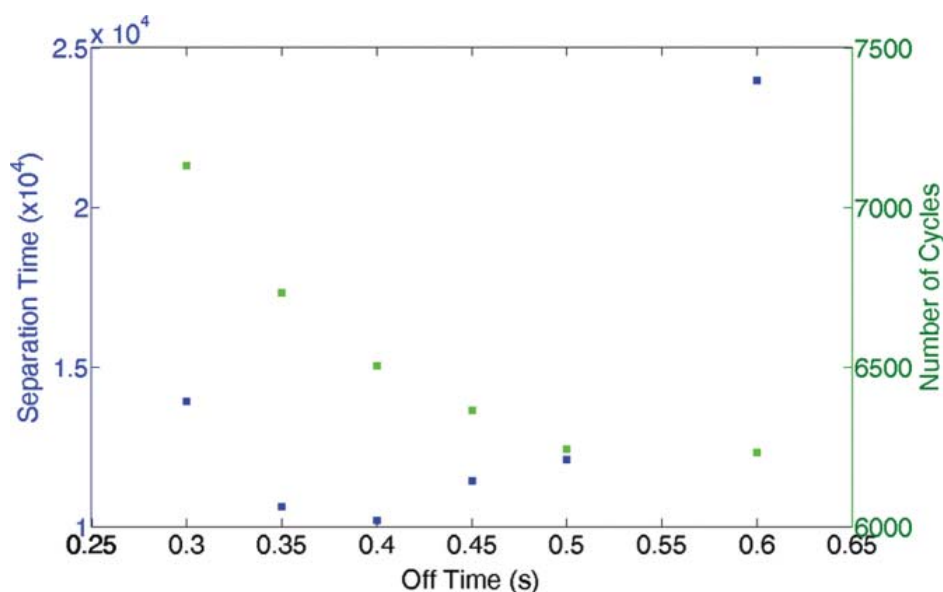


FIGURE 5.4: Separation time (blue squares) and number of cycles for separation (green squares) vs off time for three different rod sizes taken to stage 2 of sorting. Rod sizes used were $595.2 \times 168 \times 168$, $710.4 \times 120 \times 120$, and $864 \times 72 \times 72 \text{nm}^3$. Separation time has been defined as number of cycles for separation multiplied by the off time, and is shown as it is a more meaningful performance characteristic than number of cycles required to separate rod populations.

The process for optimization of the values will be similar, with the exception of the off time. The limitation for off time is not the barrier length that is required, but the total time it takes to sort the particles. In contrast to the first phase of sorting, here a longer off time gives a greater difference in the diffusion parameter, and hence, better sorting. However, this comes at a penalty of longer times needed. The optimum sorting

over a given period of time is, therefore, not necessarily associated with the case where the diffusion coefficients are most diverse but rather on other factors. A plot of the total separation time (number of cycles multiplied by off time) and of the number of cycles required for separation against a range of off times can be seen in Fig. (5.4). The minimum value of separation time obtained was at an off time of 0.4s and this appears to be close to the exact minimum. Varying the off time greatly from this value increases the separation time dramatically, and hence, it is desirable to have a good estimate for the off time that minimizes the separation time.

5.2.3 Results and Discussion

With a method for determining the key parameters defined, the sorting performance can be predicted. We consider an initial population of rods with a range of diameters from 72 to 168 nm and a range of lengths from 528 to 969.9 nm. These are shown in Table (5.1).

Since we use an approximate representation of the system in 2D, justified by a very small height component, the theoretical diffusion coefficients should be affected by hydrodynamic interactions. To account for this in our simulations, the theoretical values have been multiplied by a scale factor, taken as the ratio of the experimentally determined value from Han et al, to the theoretical value for a rod of the same dimensions. These scale factors are shown in Table (5.2). This approximation should provide sufficient accuracy in simulations as Han et al. found that particles did not deviate far from the central plane of confinement, i.e., only moved in approximately 2D.

The first phase of sorting uses an off time of $30\mu\text{s}$, an associated barrier length of 101.66 nm, and a backflow length of 500 nm. These parameters are sufficient to ascertain the probability distribution of each particle size, and hence, the probability of each rod geometry moving forward (or backward) along the asymmetric potential by one or multiple wells. This is used to calculate the probability distributions over multiple cycles using

$$\vec{a}_n = T\vec{a}_{n-1}, \quad (5.9)$$

where \vec{a}_n is the population vector for a particular rod size after n cycles and T is the population transition matrix. Each entry of \vec{a}_n corresponds to a single potential well and T_{ij} is the probability of a rod in well i moving to well j in a single cycle. The resulting distribution is shown in Fig. (5.5) as a plot of the 10th and 90th percentile boundaries of rod populations as the number of cycles increases [(a) and (c)] and the number of particles present in each well after 20 000 cycles [(b) and (d)]. Once completed, the band of rods shown as blue in Fig. (5.5a) and (5.5b), need to be passed through the second

TABLE 5.1: Actual rod dimensions used in simulations, along with percentage differences compared to a $960 \times 120 \times 120\text{nm}^3$ base rod and diffusion coefficients in the laboratory x direction at both early and late off times. Entries are arranged in the same way as Fig. (5.3), with the top set corresponding to the red circles, center set to blue circles and bottom set to black circles

Red circles			
	$[-45\%, +40\%]$	$= 528 \times 168\text{nm}$	
	$D_{xx}(0.03)$	$= 2.0670 \times 10^{-13}$	
	$[-33\%, +0\%]$	$= 643.2 \times 120\text{nm}$	
	$D_{xx}(0.03)$	$= 2.0776 \times 10^{-13}$	
	$[-18\%, +40\%]$	$= 787.2 \times 72\text{nm}$	
	$D_{xx}(0.03)$	$= 2.0599 \times 10^{-13}$	
Blue circles			
	$[-38\%, +40\%]$	$= 595.2 \times 168\text{nm}$	
	$D_{xx}(0.03)$	$= 1.8400 \times 10^{-13}$	
	$D_{xx}(0.4)$	$= 2.8483 \times 10^{-13}$	
	$[-26\%, +0\%]$	$= 710.4 \times 120\text{nm}$	
	$D_{xx}(0.03)$	$= 1.8485 \times 10^{-13}$	
	$D_{xx}(0.4)$	$= 3.0936 \times 10^{-13}$	
	$[-10\%, +40\%]$	$= 864 \times 72\text{nm}$	
	$D_{xx}(0.03)$	$= 1.8246 \times 10^{-13}$	
	$D_{xx}(0.4)$	$= 3.2959 \times 10^{-13}$	
Black circles			
	$[-30\%, +40\%]$	$= 672 \times 168\text{nm}$	
	$D_{xx}(0.03)$	$= 1.6276 \times 10^{-13}$	
	$[-17\%, +0\%]$	$= 796.8 \times 120\text{nm}$	
	$D_{xx}(0.03)$	$= 1.6174 \times 10^{-13}$	
	$[-1\%, -40\%]$	$= 969.6 \times 72\text{nm}$	
	$D_{xx}(0.03)$	$= 1.5792 \times 10^{-13}$	

TABLE 5.2: Scale factors used to adjust the theoretical diffusion coefficients in the three degrees of freedom considered.

Direction	X	Y	θ
Scale factor	0.2995	0.0984	0.2544

phase of sorting, in which the distributions achieved in two hours are shown Fig. (5.5c) and (5.5d).

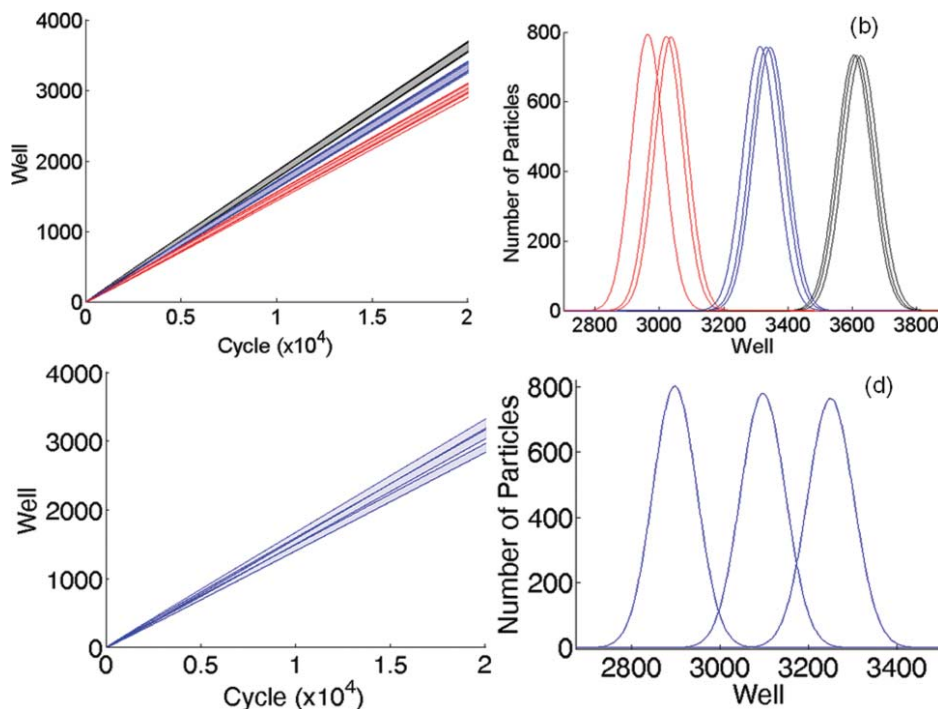


FIGURE 5.5: [(a) and (c)] Plots of 10th and 90th percentiles of expected rod populations vs cycles, and [(b) and (d)] expected number of particles in each potential well at 20,000 cycles using an initial population of 10,000 particles. These were determined for [(a) and (b)] first stage sorting using $30\mu\text{s}$ off time with nine different rod dimensions (as shown in Table 5.1) along three contours (overlaid dots in Fig. 5.3), and [(c) and (d)] second stage sorting using 400 ms off time with the blue population from the first stage (curve colours correspond to circles in Fig. 5.3).

There is a degree of control over the diffusion values to allow a greater range of rods to be sorted using this technique by altering the viscosity, temperature, or the degree of hydrodynamic interaction with the surrounding walls by controlling the height of the chamber. For example, for larger rods to be sorted, a shorter off time could be used in the second phase while keeping the same barrier length, and hence, reducing the total sorting time if the temperature was raised.

For small particles, the limiting factor is the barrier length required to accomplish sorting, whereas for larger particles, the sorting time is the prohibitive issue. Some of these limiting factors could be reduced if a greater difference in particle sizes is considered, as in many other particle sorting techniques previously studied [101, 220].

The ability to sort rodlike particles, particularly in the nanometer range, holds important implications for applications based on materials such as gold nanorods, wherein rod lengths have a role to play in their response toward plasmonic excitation using coherent light. This has been applied for enhanced large scale data recording [221], photothermal

surgery [222] and bioimaging [223]. It should also be noted that the color of Brownian noise, although not investigated here, may hold subtle effects on the ability to sort. Previous studies conducted on quasi-stationary stochastic systems have shown links between the colour of Brownian noise and the ratcheted transport [224, 225]. There may also be methods to accelerate diffusion as studied previously by Spagnolo et al [226, 227] to reduce the sorting time.

5.2.4 Conclusion

A new technique for sorting nanometer scale Brownian rods has been demonstrated. By exploiting the Brownian motion of these rods and using an asymmetric potential, a two stage sorting process can be used to isolate particles with specific dimensions. Simulation results have shown that rods with diameters ranging from 72 to 168 nm and a range of lengths from 528 to 969.6 nm can be sorted to achieve at least 80% separation within two hours. The size difference between the rods considered in this study is relatively small compared to previous studies examining the sorting of spherical nanoparticles. By increasing the size difference, the required barrier lengths could be increased and sorting times consequently reduced. It may also be possible to sort a greater range by altering the diffusion coefficients of the differently sized rods. Possibilities include changing either the temperature or the viscosity of the surrounding medium, or using the height of the chamber to govern the degree of hydrodynamic interaction. The analysis presented here provides a basis for the attributes needed for a physical rod sorting device.

5.3 Nano scale environment sensing scheme with Brownian nanorod and plasmon resonator

Consider the effect of an attractive force drawing the nanorod to contact the pillar, where it can be assumed that the force of attraction acts through the center of the two bodies (i.e. the stationary pillar and Brownian rod) is similar to that in [96] as depicted in Fig. (5.6a). The combination of the attractive force and Brownian perturbation gives rise to two distinct states, one in which the rod is moving freely (state I) and the other in which the rod contacts the pillar surface and consequently the diffusion coefficients are diminished (state II). It is important to note that the residence of the rod in either state is not exclusive. Even when there is no attractive force applied, the rod may sojourn by pure Brownian perturbation to contact the pillar thus switching states. Its departure from the pillar causes the opposite to occur. When an attractive force is applied, the proportion of time spent in each of the two states will be altered in accordance with

the magnitude of the force. In view that a surface plasmon leakage provides a distinct intensity based binary indication of residence in either state I or II, it should logically be possible then to deduce the conditions of the environment solely from this information. This will require a means to sensitively ascertain the state condition.

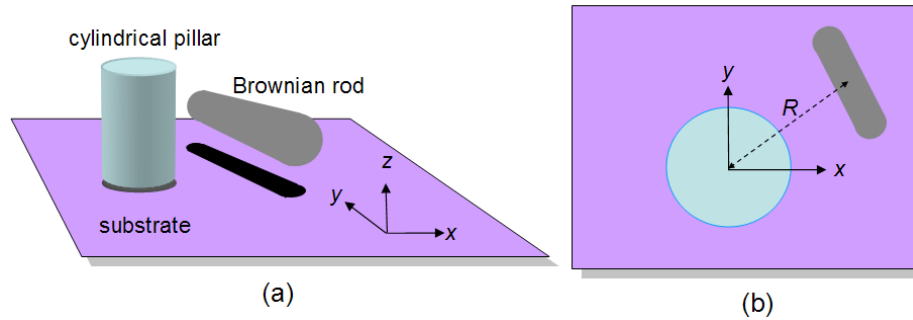


FIGURE 5.6: Schematic of a microenvironment sensing scheme in which a micron scale rod is drawn to a cylindrical pillar using an attractive force as viewed three dimensionally (a) and from the top (b). If motion is assumed to be exclusively in the x-y plane the Brownian rod motion can be monitored by a camera placed in the z-axis.

Fig. (5.7) provides a description of the nano environment sensing scheme. Apart from a nano scale rod being drawn to a cylindrical pillar using an attractive force, the cylindrical pillar serves as an optical plasmon resonator. Light is delivered through one distal end of the optical fiber and sensed at the other distal end. Despite having a small optical mode volume, optical resonators can possess ultra-high quality factors in water. The interaction between the resonator's evanescent field and its environment can shift the resonance frequency of the optical mode, such that when a nanoparticle attaches to the resonator surface it induces a wavelength shift, that is dependent on the polarizability and position of the nanoparticle, the electric field of the resonator, and the optical volume [228]. This shift is normally used as an indicator of nanoparticle attachment. If the nanoparticle is metallic, a localized surface plasmon resonance effect should result, potentially creating a larger effect on the resonator output. Metallic nanorods support both the longitudinal and transverse plasmon modes, with the plasmon resonances polarized along and orthogonal to the length axis of the nanorod. The proximity of the nanorod with the resonator can potentially create an even stronger effect on the resonator output.

In our scheme, these disruptions to the optical signals from the resonator, as a result of a Brownian rod contacting the cylinder, enables the states I and II to be determined temporally and more importantly sensitively. What is attractive is that no imaging is required. This circumvents the well known difficulty of resolving nano scale objects in real time. We also seek to harness the use of single wavelength tracking which circumvents to use of spectral signature.

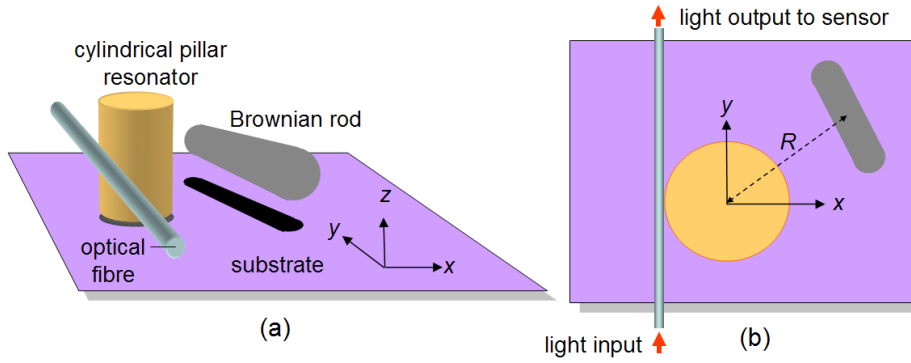


FIGURE 5.7: Schematic of the proposed nano environment sensing scheme in which a nano scale rod is drawn to a cylindrical pillar using an attractive force as viewed three dimensionally (a) and from the top (b). The cylindrical pillar serves as a plasmonic optical resonator sensor with light input and output through the optical fiber. The contact of the Brownian nano rod with the cylinder causes changes to the optical signal. Under this scheme, no imaging of the nano rod is required.

5.3.1 Modeling

There are two parts to the modeling; one to establish the ability of nanorods to extinct the plasmon resonator signals such that it is appropriate for sensing, and the other to investigate if the state change conditions as a result of Brownian perturbation and attractive force are able to reveal information about the environment. For the former, we model the system shown in Fig. (5.7) using the Finite Difference Time Domain (FDTD) method, whereby the input beam is guided along an optical fiber that couples into the optical resonator. The optical resonator comprises a 40nm inner dielectric core with a refractive index of $n_c = 3.4$ and a 10nm outer gold (Au) shell. We simulate using a Gaussian beam with a center wavelength of $\lambda_c = 550\text{nm}$ having full width half maximum (FWHM) of 200nm. Light inputs into the fiber at one distal end and we monitor the transmittance at the other distal end. The nanorod is oriented with a rotation of θ , such that $\theta = 0^\circ$ and $\theta = 90^\circ$ correspond to the vertical and horizontal alignments respectively as shown in Fig. (5.7). The gap d denotes the distance between the outer shell of the pillar and the nanorod so that $d = 0$ is the contact situation. The dispersive property of gold is represented with the Drude-Lorentz oscillator model with coefficients given in Table (3.1).

The width of the tapered fiber is taken to be 200nm. This is a typical subwavelength diameter optical fiber that can provide strong evanescent coupling [229, 230]. It should be noted that the drifting of single mode fibers in the range of micrometers can cause significant changes [231]. We assume that the means to limit these spurious movements are incorporated.

For any application of product of charges of magnitude q_p on the pillar and rod, this creates an attractive force

$$F = \frac{\varepsilon q_p}{R^2} \quad (5.10)$$

that draws the nanorod towards the cylindrical pillar, with ε being the permittivity of the medium in which the rod resides, and R the centroid distance between the rod and pillar. The Brownian diffusion perturbations provide the random counteracting forces that oppose this. Eq. (5.2) was used to calculate the diffusion coefficients of the rod when free and in order to obtain the values for the diffusion coefficients when the rod was tethered, the free diffusion coefficients were multiplied by scale factors of 0.0720, 0.6729 and 0.2838 for changes in the diffusion coefficients D_a , D_b and D_θ respectively, as previously observed. For the translational diffusion coefficients this is based on the rod having a length of $6.81\mu\text{m}$, 60nm and diameter of 25nm and moving in de-ionized water. A 100nm diameter cylindrical pillar was also applied. In the simulations, it was assumed that the attractive force did not affect the rotation of the rod. Collisions between the rod and the pillar were treated as inelastic, with the velocity of the rod becoming zero on contact with the pillar. A time step size of $\delta t = 1/300\text{s}$ was found to be sufficient for simulations at a test temperature of 293K . For consistency, the particle was always started from the same position with its centroid lying on the x -axis and its long axis parallel to the y -axis.

5.3.2 Results

We first simulate for the horizontal and vertical orientations of the nanorod for three gap values $d = 0, 2.5\text{nm}, 10\text{nm}$. The transmission distribution is shown in Fig. (5.8) for the two alignments $\theta = 0^\circ$ and $\theta = 90^\circ$. For all parameters, there is a noticeable resonance at $\lambda = 525\text{nm}$. This corresponds to the primary mode of the plasmonic resonator. At this resonance wavelength, there appears to be very little dependence on the gap value d , and some small dependence on the orientation. Hence, contrary to intuition, tracking for changes at the resonance wavelength will be less sensitive. There is a noticeable dip in the spectral signatures at the vicinity of 600nm . This is likely due to coupling effects of two difference shapes (i.e. a cylinder with nanorod) which essentially creates a hetero dimer. A recent study of the interaction of nanorods with nanospheres revealed strong Fano resonance effects that led to dramatic spectral changes [232].

We now investigate the transmission profiles for five difference values of $d = 0, 2.5\text{ nm}, 5.0\text{ nm}, 7.5\text{ nm}, 10\text{ nm}$ and for $0^\circ \leq \theta \leq 90^\circ$. For convenience, we symbolize the transmission data matrix $S_{\lambda_n, \theta_m}^{d_p}$ where λ_n , θ_m , d_p correspond to the n^{th} wavelength,

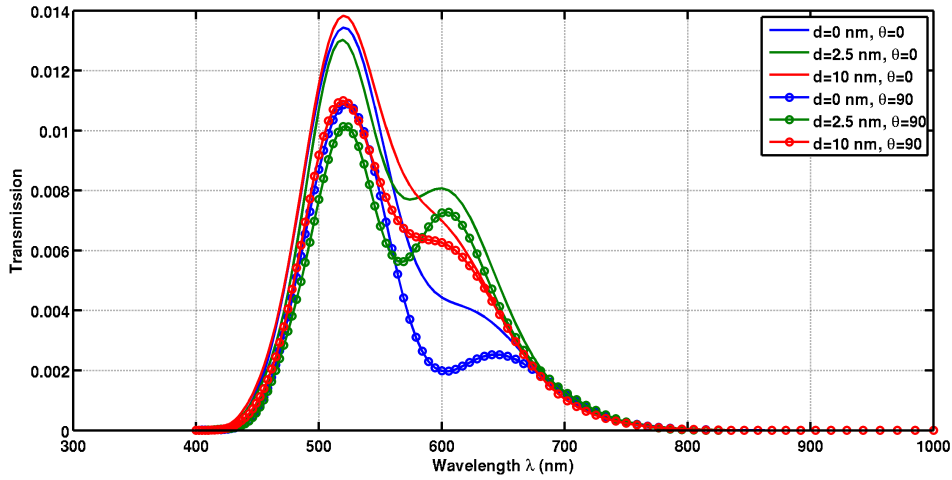


FIGURE 5.8: Transmission spectra of a nano-rod placed a distance, $d = 0$ (contact), $d = 2.5\text{nm}$ and $d = 10\text{nm}$, indicated by the blue, green and red lines respectively. The orientation of the particle is either vertical, $\theta = 0^\circ$, or horizontal $\theta = 90^\circ$ indicated by the non-marked and marked lines, respectively.

m^{th} angle and p^{th} gap value respectively. The surface plot of $S_{\lambda_n, \theta_m}^{d_p}$, for the set of d values sampled is shown in Fig. (5.9).

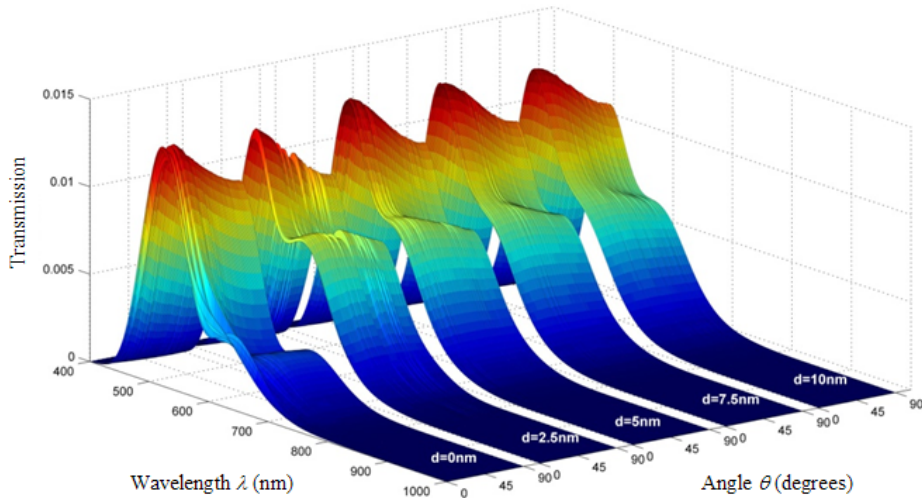


FIGURE 5.9: Transmission spectra for gap values $d = 0, 2.5\text{ nm}, 5\text{ nm}, 7.5\text{ nm}, 10\text{ nm}$ over a continuous range of angle from 0° to 90° . The absolute value of the transmission spectra is given here to better illustrate the surface curvature.

We now define the difference between the contact transmission data matrix (i.e. $S_{\lambda_n, \theta_m}^{d_p}$) and the q^{th} gap non-contact transmission data matrix $S_{\lambda_n, \theta_m}^{d_q}$ as

$$D_{\lambda_n, \theta_m}^{0, q} = \text{abs}(S_{\lambda_n, \theta_m}^{d_0} - S_{\lambda_n, \theta_m}^{d_q}) \quad (5.11)$$

for $q = 1, 2, 3, 4$. With this, it is possible to define the aggregated difference in transmission as

$$W_n^{(0,q)} = \sum_m D_{\lambda_n, \theta_m}^{(0,q)} \quad (5.12)$$

This essentially reduces a three dimensional data set to a one dimensional summed difference expression. The results for $W_n^{(0,q)}$ where $q = 1, 2, 3, 4$ are shown in Fig. (5.10). They conclusively show that there is distinct change in transmission at 600nm across all angles of orientation when the gap changes from contact to non-contact or vice-versa. This suggests that when operated at the wavelength of 600nm, a noticeable transmission change occurs when there is contact regardless of the nanorod's orientation. The use of a single wavelength tracking offers the advantage of obviating the use of spectrum readings, which are typically slower and impose greater demands on instrumentation. If we take any specific orientation angle, the transmission plots in Fig. (5.11) (also at 600nm) show distinct perceptibility with the gap value $d = 0$. In fact, it can be seen that this perceptibility is distinct notwithstanding the orientation angle. Hence by using a cut-off transmission, it should be possible to confirm that the nanorod contacts the pillar. This is an important feature as in practice the nanorod is able to, due to Brownian motion, contact the pillar at various orientation angles.

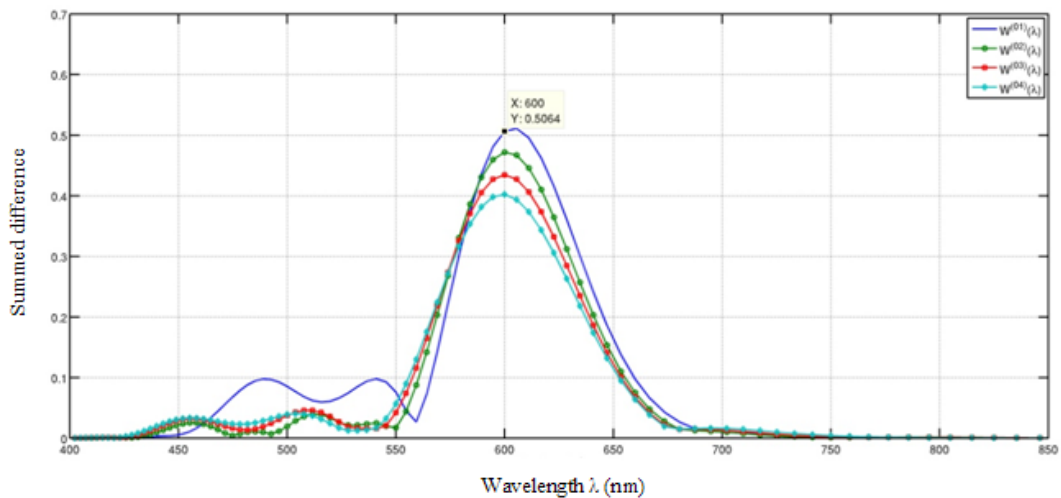


FIGURE 5.10: Aggregated differences of the transmission spectra over all angles between all contact and non-contact combinations, i.e. $W(0,q)(\lambda)$ were $q = 1, 2, 3, 4$. The plot shows that between contact and non-contact cases there is a distinguished difference of transmission at 600nm. This feature allows for unique detection of contact between nanorod and cylindrical pillar.

It is possible to define two distinct states pertaining to the position of the nanorod in relation to the cylindrical pillar. One is when the rod is moving freely (state I) and the other with the rod contacting the cylindrical surface (state II). In the erstwhile approach of interrogating the environment using translational and rotational trajectories

of a particle, both a rod and a sphere can yield the required information when residence is in state I. When the probe resides in state II, only the rotational information can be used due to rotational and translational coupling. Since a sphere cannot yield the rotational information readily, only the use of a rod is feasible to provide the information necessary to determine the environment. By interrogating the proportion of time of the residence in states I and II as we propose here instead, there is no impediment to using a sphere. Nanorods however, as shown, cause improved extinction of the plasmon resonance signal in the rod. This in turn offers improved accuracy in ascertaining whether the rod is under state I or II residence with the cylindrical pillar.

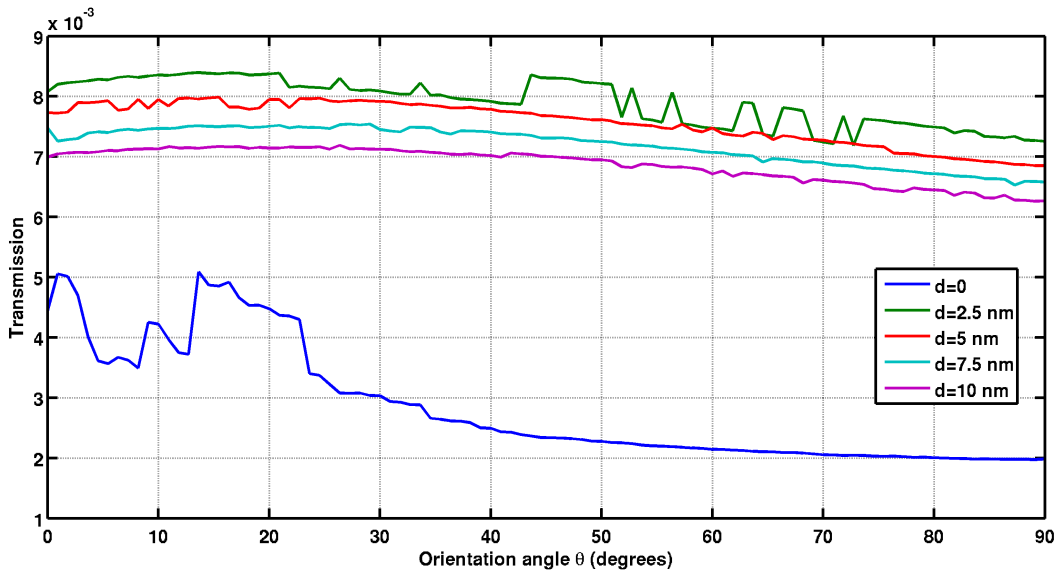


FIGURE 5.11: Transmission readings at 600nm showing distinct perceptibility when gap value $d = 0$. The orientation angle does affect the distinct perceptibility.

A convenient metric to use is f , the proportion of incidences when the rod is in state I, i.e. free. With the efficient optical sensing system described previously, this can be determined to a high degree of accuracy. Fig. (5.12) provides plots of f against the normalized charge product calculated from 18,000 samples at temperatures 272K, 323K and 373K. As expected, increasing the magnitude of the charges such that the force is attractive reduces the proportion of time spent in state I. That there was shifting of the plots indicated sensitivity to temperature. Nevertheless, distinctive S-shape trends are observed, indicating that there are ranges in the normalized charge products in which relatively good sensitivity responses are possible. Fig. (5.13) provides plots of f against temperature (in the range 273K to 373K) at the various normalized charge products. It can be seen that all the trends are highly linear in the cases, having Pearson product-moment correlation coefficients above 0.98. At different normalized charge products however the slope values (i.e. of df/dT) are different. The significantly higher values of df/dT infer heightened detection sensitivity. Fig. (5.14) furnishes a plot of the

approximated values of df/dT against the normalized charge product. It can be seen that the df/dT is maximal when the normalized charge product value is -200. This value is naturally only useable for the dimensions applied in the simulation.

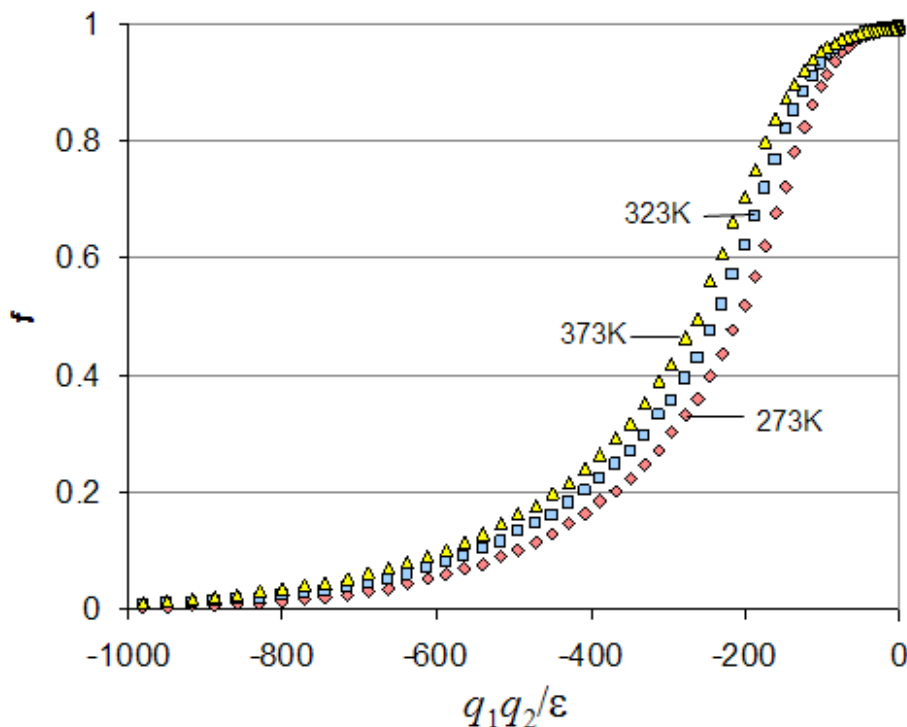


FIGURE 5.12: Plots of f (the fraction of time in state I) against the normalized charge product calculated from 18,000 samples at 0, 25, and 100°C. All simulations started with the rod touching the edge of the pillar. Increasing the magnitude of the charges such that the force is attractive reduces the proportion of time spent in state I

It is important to note that uncertainty in the environment estimation diminishes by increasing the number of sample points in state I and II. This uncertainty can be determined by calculating the sample standard deviation of 100 diffusion coefficients at each value of N , which represents the number of samples. If we consider the application of temperature sensing, a restriction of the uncertainty to one standard deviation (which corresponds to 0.5K) will require 744,344 and 657,492 sample points to be observed in states I and II respectively. Based on camera recordings made at 50 fps, this will require monitoring the rod over 14,887 and 13,150 seconds in states I and II respectively. However, considering that standard photo-detectors with 50MHz sampling rate are now readily available, the monitoring times with the current scheme should correspondingly be lowered to 0.015 and 0.013 seconds instead. This portends a significant advantage in the ability to sense environments that are temporally changing.

We have opted to depict the attractive force of the nanorod to the pillar using charges. Since optical plasmonic force schemes have been reported to be able to trap particles

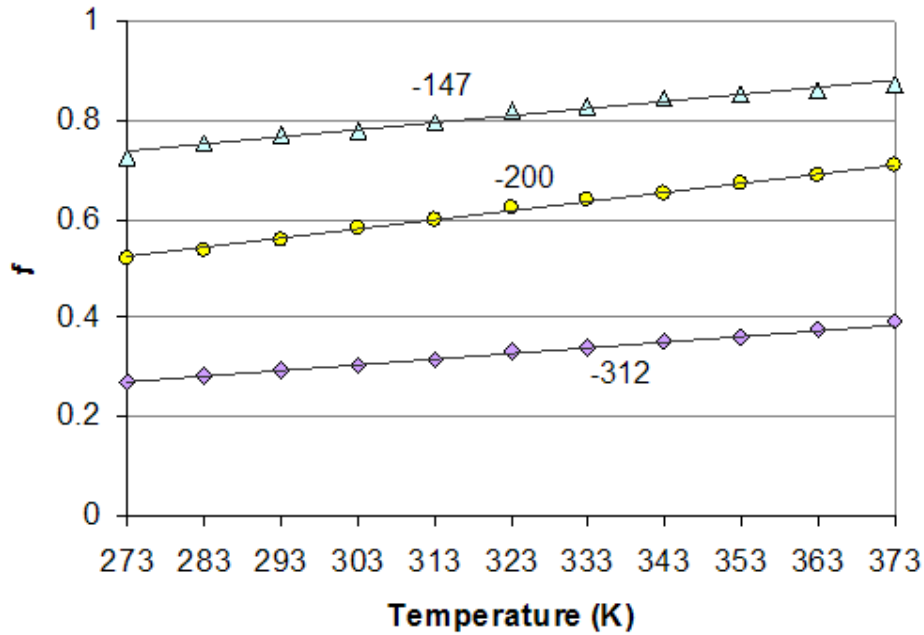


FIGURE 5.13: Plots of f (the fraction of time in state I) against temperature calculated from 18,000 samples at various normalized charge products. All simulations started with the rod touching the edge of the pillar. It can be seen that all the trends are approximately linear

[233], there is plausible scope to apply an all plasmon approach in the scheme. A challenge to do this, however, lies in the ability to introduce sufficient optical power for trapping (which is significantly higher than that needed for sensing). An added caution lies in the tendency of heat to be generated from strong plasmon fields [222, 234] which will affect the environment to be sensed. We also note that while optical fibers are widely reported to coupling light into and out of resonators, and depicted here, recent waveguide coupling designs [235] may offer the ability to improve the coupling efficiency and to aid in the creation of integrated devices.

5.3.3 Conclusion

This work investigated the use of a surface plasmon based optical resonator to sense the nano scale environment from the Brownian perturbations of nanorod drawn to a cylindrical pillar by attractive forces. Using simulations of an optical resonator that comprises a 40 nm inner dielectric refractive index of 3.4 core with a 10 nm outer gold shell, and driven by a Gaussian beam with center wavelength 550 nm, noticeable resonance was found at 525nm. At this resonance wavelength, however, there was very little dependence on the gap value. Hence, tracking for changes a the resonance wavelength would be rather insensitive. A one dimensional summed difference expression $W_n^{(0,q)}$

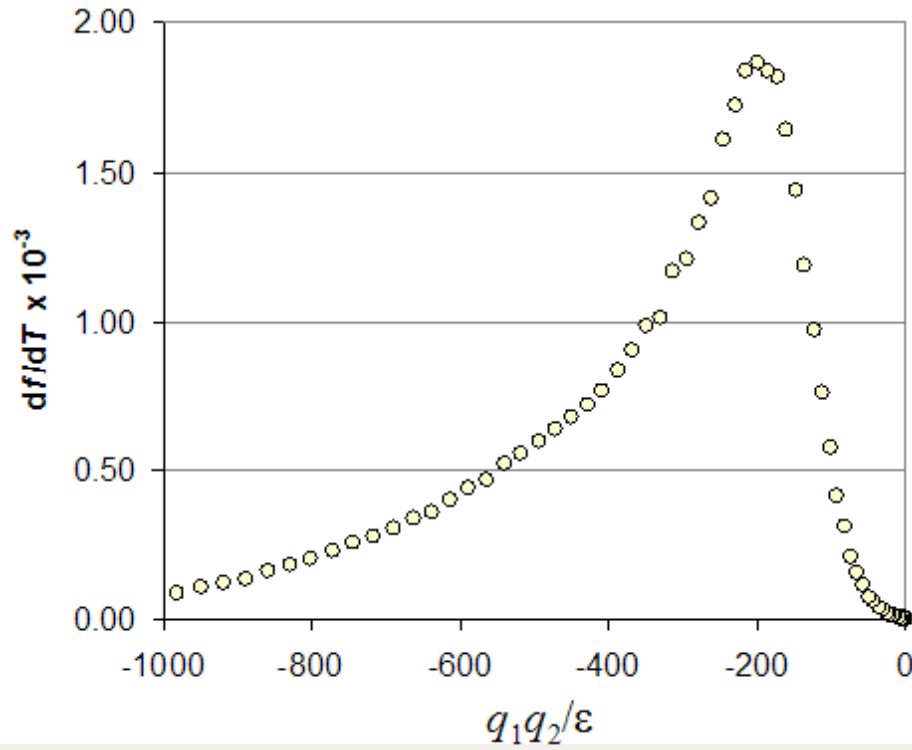


FIGURE 5.14: Plot of the approximated values of df/dT (taken between 273 K to 373 K) against the normalized charge product. Higher values of df/dT indicate higher sensitivity. A normalized charge of -200 gave a maximal value of df/dT .

was derived to reduce the difficulty of analyzing a three dimensional data set composed of λ_n , θ_m , d_p . Using this expression, it was shown that there was a distinct change in transmission at 600 nm across all angles of orientation when the gap changes from contact to non-contact or vice-versa. This meant that operation at this wavelength would produce a noticeable transmission change when there was contact regardless of nanorod orientation. The use of a single wavelength tracking offers the advantage of obviating the use of spectrum readings, which are typically slower and impose greater demands on instrumentation. With distinct perceptibility with zero gap value notwithstanding the orientation angle, it would be possible to apply a cut-off transmission threshold to confirm if the nanorod contacts the pillar. This feature is important as Brownian motion could cause the nanorod to contact the pillar at various orientation angles in practice. In analyzing the Brownian driven movement, two distinct states that define the position of the nanorod in relation to the cylindrical pillar are when the nanorod was moving freely (state I) and when the nanorod was contacting the cylindrical surface (state II). Using the metric f that defined the proportion of incidence when the nanorod was in state I, increases in the magnitude of the charges was found to reduce f . The distinct S-shape trends of plots f against normalized charge magnitude indicated that there were ranges in the normalized charge products in which relatively good linear sensitivity responses

were possible. At these regions, the Pearson product-moment correlation coefficients were found to be above 0.98. In correlating to the temperature T , df/dT was found to be maximal when the normalized charge product value was -200. From an uncertainty estimation conducted, a restriction of the uncertainty to one standard deviation (which corresponds to 0.5K) will require 744,344 and 657,492 sample points to be observed in states I and II respectively. Based on camera recordings made at 50 fps, this will require monitoring the rod 14,887 and 13,150 seconds in states I and II respectively but with standard photo-detectors with 50MHz sampling rate, the monitoring times are lowered 0.015 and 0.013 seconds instead. The approach here offers a significant advantage in the ability to sense environments that are temporally changing.

5.4 Chapter Summary

In this chapter, a new technique for sorting nanometer scale Brownian rods has been demonstrated. By exploiting the Brownian motion of these rods and using an asymmetric potential, a two stage sorting process can be used to isolate particles with specific dimensions. Simulation results have shown that rods with diameters ranging from 72 to 168 nm and a range of lengths from 528 to 969.6 nm can be sorted to achieve at least 80% separation with two hours.

Furthermore, we investigated and developed a novel means to sense a nanoscale environment. Capitalizing on the surface plasmonic interaction between a Gold nanorod and a plasmonic whispering gallery, a perceptible change in transmission was found at all distance and orientation values.

The findings described in this chapter have been reported in the following publications:

1. I. Gralinski, A. Neild, T.W. Ng, M. Muradoglu, Sorting of Brownian rods by use of an asymmetric potential *Journal of Chemical Physics*. 134 (2011) 064514., enclosed in Appendix (B.3).
2. M. Muradoglu, C.Y. Lau, I. Gralinski, T.W. Ng Nano scale environment sensing scheme with Brownian nanorod and plasmon resonator. *Plasmonics*. (2013), enclosed in Appendix (B.10).

Chapter 6

Discrete Liquid Mechanics

6.1 Introduction

The technology of handling small liquid volumes in biochemical analysis, commonly referred to as microfluidics, was initially based on continuous flow and closed architectures. Issues such as clogging (when particulates or cells are present), access impediments, and difficulties in integration and scaling due to the flow at any one location being dependent on the flow properties of the entire system, have resulted in increasing interest to apply discrete, open, and independently controllable sample volumes instead.

Discrete volumes of liquid allow the microfluidic function to assume a set of basic repeated operations, whereby one unit of fluid can be moved over one unit of distance. This facilitates the use of hierarchical and cell-based approaches for microfluidic biochip designs that offer flexible and scalable system architectures as well as high fault tolerance capabilities. Moreover, because the volumes can be controlled independently, such systems offer greater potential to be reconfigured whereby groups of unit cells in an array can be altered to change their functionality.

A critical component of droplet based microfluidic systems lies in the formation of uniform droplets and particles. Since biological and chemical properties of microparticles are strongly affected by both the size and morphology, it is essential to be able to generate these structures at well-defined volumes and composition. Obtaining fine control over size, shape, and monodispersity of droplets is of utmost importance in droplet microfluidics. Furthermore, the use of superhydrophobic surfaces to provide a means to transport discrete analytes or samples poses further difficulty in droplet dispensation. For example, a unit of fluid that is deposited by means of a flexible pipette tip- that permits volumes down to around $10\mu\text{L}$ - can potentially contact and damage the nano

and micro features of the surface that endow superhydrophobicity. To this end, we address the need to deliver drops of specific volumes on superhydrophobic surfaces from cost effective storage media such as paper in Section (6.2). In the process, we will show the nature of how small aerosols form on these surfaces before evolving into single drops.

The next issue we examine is the microplate (multiwell plate or microtiter plate), which has become a standard tool in analytical research and clinical diagnostics. Again, there is a trend towards testing smaller liquid volumes that allows for an increased number of assays that can be conducted per plate thereby increasing throughput, and importantly, reduces the sample quantity needed per assay. In dealing with miniaturized assays, alternative approaches have been developed to handle, prepare and test small liquid volumes without the need for complex or precise machinery or limitations from wetting. Yet, there is also impetus to create microplates that are cost effective enough to be available for use in resource-limited laboratories so that diagnostic outcomes can be achieved in a more timely fashion. One approach that has been advanced recently to address this without affecting the efficacy in optical diagnosis is through the use of samples in between rods. In Section (6.3), we investigate the feasibility of using the capillary bridges developed between solid bodies (rods) to interrogate the contact angle development under the effect of evaporation. In addition, we also seek to ascertain the progress of volume change. These findings will help to provide insights on the ability to relate wetting to analyte characteristics and mitigate evaporation in biochemical microplating schemes developed for use in resource-limited laboratories.

Finally, in order to fully utilize the benefits of cell assays, means of retaining cells at defined locations over time are required. This was first performed by localized surface modifications or chemical immobilization in microfluidic networks. More recently, hydrodynamic effects working in tandem with applied field gradients that induce forces on cells, such as electrical, optical, magnetic, or acoustic fields, have been attempted. These methods generally require investment of time, resource and expertise to develop. Most researchers conducting cell based assay investigations in the laboratory, however, frequently seek approaches that eschew these demands. An approach, based on biomimicry, to anchor and trap particles is put forward in Section (6.4).

6.2 Precise drop dispensation

We advance a novel approach here, in which the spray from an acoustic nebulizer is sent to a superhydrophobic receptacle and the volume ascertained precisely using a weighing scale. The approach is depicted in Fig. (6.1).

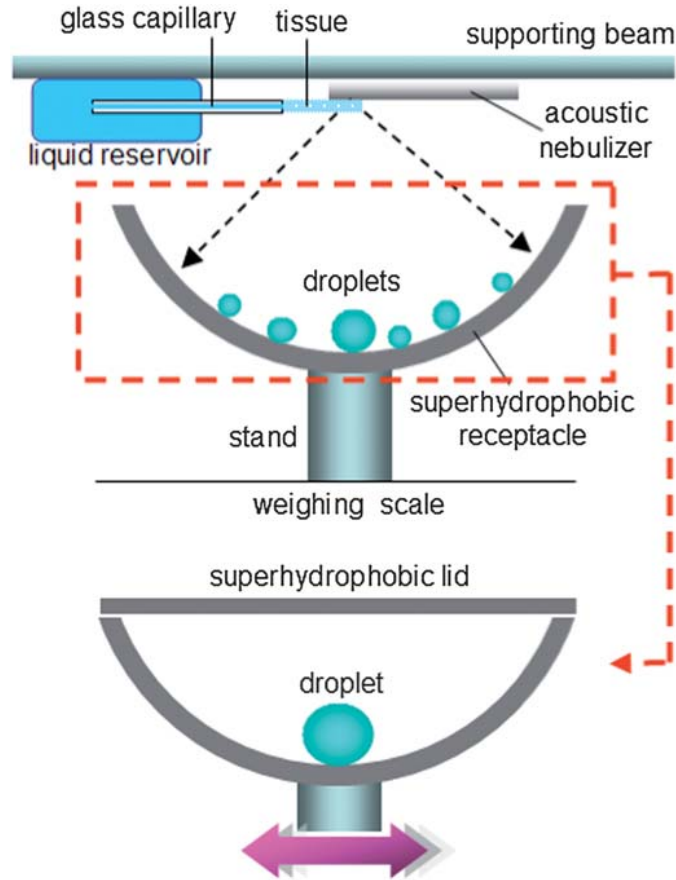


FIGURE 6.1: Schematic description of the scheme to obtain precise volumes of drops on superhydrophobic surfaces. A surface acoustic wave nebulizer delivers a spray of aerosol droplets onto the receptacle in which the exact volume is determined using an accurate weighing scale. By covering with a superhydrophobic lid and gentle shaking, a single drop is created.

A liquid supply chain was created out of a reservoir that delivers to a short capillary tube section, whose tip is placed in contact with a surface acoustic wave (SAW) nebulizer running at 30 MHz frequency using a small piece of tissue paper that constituted a capillary wick [236]. The SAW device was constructed out of a low-loss piezoelectric substrate, specifically, a 127.86° y-x rotated single-crystal lithium niobate (LiNbO_3) substrate, with pairs of chromium-aluminium interdigital transducers fabricated on one side via standard UV photolithography. When an AC signal is supplied to the transducer at its resonant frequency, the SAW in the form of a Rayleigh wave propagates along the LiNbO_3 surface from the transducer at about 3900ms^{-1} . Although the surface displacement amplitudes are only in the 1-10nm range, the accelerations are extremely high (about 10^7ms^{-2}) due to excitation at frequencies over 10 MHz. These huge surface accelerations are transmitted into the liquid placed on the substrate, inducing acoustic streaming [237]. When the energy is sufficient (i.e. electrical power supplied in the 1-3W range), destabilization of the liquid's free surface occurs. This leads to a breakup of

capillary waves, generating a spray of aerosol droplets through a process known as SAW atomization or nebulization [238, 239]. When this spray of aerosol is channeled onto a semi-spherical superhydrophobic receptacle, larger drops develop on the receptacle surface from multiple coalescence events that are influenced by gravity (which tend to draw them towards the receptacle trough).

6.2.1 Materials and Methods

The receptacle was fashioned out of a copper sheet (1mm thickness), polished earlier to remove all visible scratches using silicon carbide electro-coated waterproof abrasive paper (KMCA, WET/DRY S85 P600), by an 8.5 mm radius ball indenter. Prior to use, the receptacle surface was first cleaned using absolute ethanol, allowed to air dry, and then immersed in a 24.75mM aqueous solution AgNO_3 for 1 minute to form the micro and nano-structures. After this, the surface was rinsed with copious amounts of distilled water followed by absolute ethanol before being allowed to air dry. Once dried, it was immersed in a 1mM solution of the surface modifier $\text{CF}_3(\text{CF}_2)_7\text{CH}_2\text{CH}_2\text{SH}$ in absolute ethanol for 5 minutes. After removal, it was again rinsed with copious amounts of distilled water, followed by absolute ethanol, and then air dried.

The micro- and nano-structures developed by immersing the copper coupons into the aqueous solution of AgNO_3 were formed by an electroless deposition process. This process is similar to electrolytic plating except that no external electrodes are needed [240]. In electroless deposition, the metal ions are typically reduced into metals by the introduction of a reducing agent. A variety of procedures with different reagents have been demonstrated for electroless deposition of silver [241, 242]. In the process conducted here, however, the deposition was able to proceed without any external reducing agent. Rather, a galvanic displacement mechanism occurred in which the silver cations in solution were reduced just as copper from the surface was oxidized.

For a side experiment to study the nano- and micro-structures forming in relation to wetting, we created coupons 20 by 20 mm in size out of the same copper sheet (1mm thickness) and using the same polishing and cleaning process as previously described. The coupons were then immersed in the 24.75 mM aqueous solution of AgNO_3 for selected periods ranging from 2 seconds to 120 seconds before being removed to air dry. After drying, the morphology of the superhydrophobic surface was characterized with an FEI Quanta 3D FEG scanning electron microscope (SEM). The elemental composition was characterized by an X-ray energy dispersive spectrometer (EDS) associated with the SEM. The wetting characteristics were evaluated by placing $5\mu\text{L}$ of sessile drops of

water on each surface (after immersing into the surface modifying solution) and then determining the contact angle.

The weight of the liquid delivered to the receptacle, which could be correlated to volume, was determined using a weighing scale (A& D GR-200 with 0.0001 g precision) on which the receptacle is placed. Once the required volume was achieved, aerosol delivery from the nebulizer was terminated, a superhydrophobic lid placed over the receptacle, and the assembly shaken gently to merge the drops together into one. Apart from ensuring that no liquid spilled out of the receptacle, the lid also served to limit the effects of evaporation, which is significant for small drop volumes. Experiments were conducted to establish the liquid (Milli-Q water) delivery characteristics when the power to the nebulizer was kept constant at 2 W.

Lastly, the effect of nebulization on the structure functionality of enhanced green fluorescent protein (EGFP) was evaluated. This C-terminally His₆-tagged fluorescent protein was isolated from genetically modified *Escherichia coli* and purified to near homogeneity by automated affinity chromatography using 1mL bed volume Mini Profinity IMAC cartridges on the Profina Protein Purification System (Bio-Rad) under the default program settings of the Native IMAC method with integrated desalting into sodium phosphate buffer (pH 7.4). The His₆-tagged EGFP was checked for purity by SDS-PAGE and quantified using the BCA protein assay (Pierce, USA). Samples of the protein were nebulized at different powers, collected in capillary tubes, imaged together using a fluorescence microscope (Olympus BX61), and the intensities extracted using the ImageJ software.

6.2.2 Results and Discussion

The SEM micrographs of structures formed in association with various immersion times of the copper coupons into the silver nitrate solution are presented in Fig. (6.2). The background striated structures are seen at 2 seconds were formed due to the polishing process. On the substrate, very small granules started to be deposited at numerous nucleation sites. These granules grew in size with longer immersion times until about 10-20 seconds. At the 20 seconds mark, the granules appeared to shrink slightly in size while exhibiting greater dendritic growth from the surface of each granule. From then onwards, the dendritic structures began to proliferate on the existing granular structures, developing later into fern-like foliage. The distinct differences between these two types of structures (granular and dendritic) are shown more clearly in the higher magnification micrographs provided in Fig. (6.3).

The time dependent morphology changes appear to indicate that granular growth beyond a certain size was not feasible, although granular structures were more preferentially

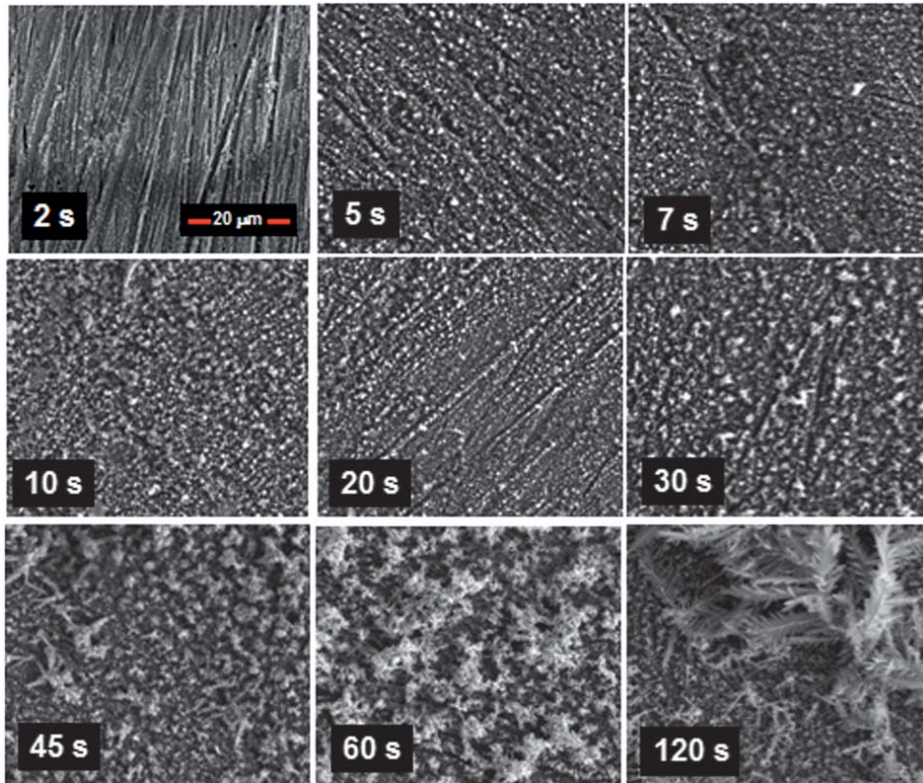


FIGURE 6.2: Scanning electron micrographs obtained from immersing the copper coupons into the silver nitrate solution for different lengths of time followed by air drying. It can be seen that granular structures developed with short period immersion, whilst dendritic structures formed with longer period immersion.

formed just after nucleation. This is likely due to the natural tendency of the process to maintain or increase the surface area to volume ratio in order not to limit the rate of deposition. Taking a sphere for example, the surface area to volume ratio scales according to $3/r$, where r is the radius, inferring that the surface area to volume ratio reduces as the sphere increases in size. Thus, the formation of dendritic structures offers an avenue by nature to circumvent this obstacle. This argument is supported somewhat by the XRD maps obtained that revealed no significant elemental changes in the structures.

After the surfaces were treated with the modifier, we found that immersion for at least 7 seconds into the silver nitrate solution was all that was needed to ensure superhydrophobicity of the surfaces. At this stage, the structures, as can be seen in Fig. (6.2), appeared to be predominantly granular. From previous studies, it is known that granular structures alone are a sufficient catalyst for superhydrophobicity [243]. Hence, the subsequent dendritic structures are not needed to maintain the non-wetting characteristic, although they seemed not to have a role in modifying it. The micrograph at 5

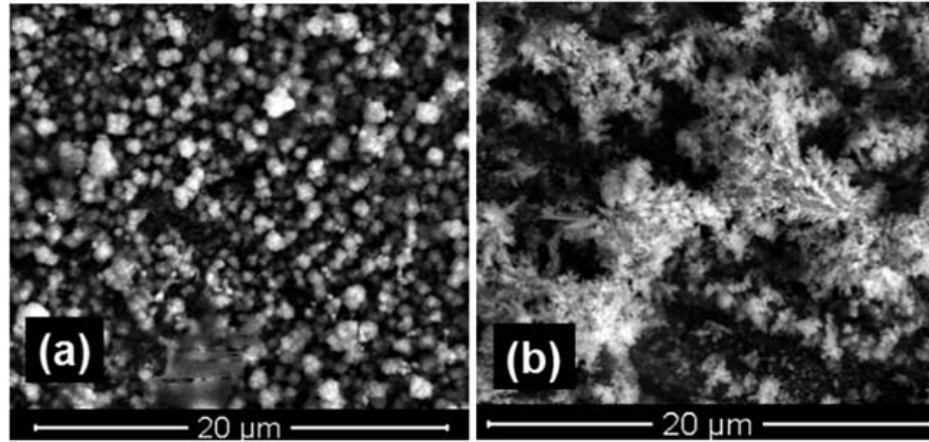


FIGURE 6.3: Scanning electron micrographs at higher magnifications that provide a clearer picture of the (a) granular and (b) dendritic structures developed.

seconds immersion also showed significant coverage of granular structures over the substrate. This presented an interesting conundrum as to why superhydrophobicity could not be sustained at this stage. On more careful examination, we found patches on the substrate surface where the granular structures were not yet fully developed. It appears then that the superhydrophobic state requires not just significant numbers of granular structures to be present on the surface but also uninterrupted coverage of the structure.

We move now to discuss the experimentation results in obtaining the drops. During each run on liquid deposition, the nebulizer was cyclically pulsed on for 5 seconds and off for 5 seconds. This was done to accommodate the response time of the weighing scale. Fig. (6.4) presents results of the mass recorded in relation to time in which the nebulizer was operated for three typical runs. Highly linear trends are observed, indicating that fixed quanta of liquid were dispensed with each pulsed operation of the nebulizer for a specific run. While the data for two of the runs were almost identical, the gradient for a third run was significantly altered. This was due to the process that happens in the tissue as it served to draw liquid out from the reservoir before perturbations from the SAW device are able to dislodge it for delivery. In the course of this process, factors that affect the transfer of liquid in and out of the tissue (such as temperature and airborne particles attaching to the fibers) likely caused the flow rate to vary with each run.

This result implied that an open-loop operation using a pre-calibration without a weighing scale was not feasible. Due to the ability of the SAW driver nebulizer to operate nearly instantly, from zero to full power and to zero power again in approximately 1 microsecond, there was no ‘lagging volume’ delivered when the nebulizer was turned off. Hence, the limiting factor for accurate volume dispensation was only that dictated by the mass resolution of the weighing scale. In the current case, the volume resolution

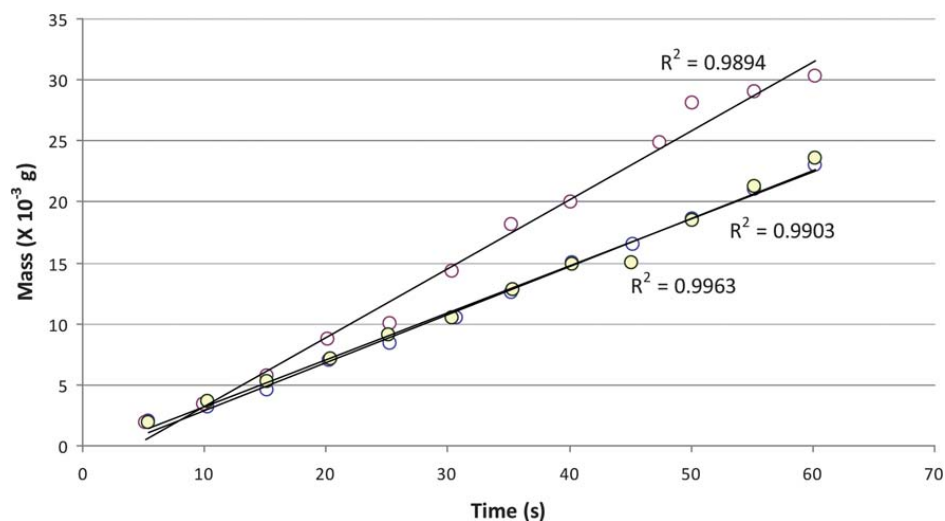


FIGURE 6.4: Plots of the readings from the weighing scale against the operation time of the nebulizer. The trends from each run are highly linear, albeit the slope variation indicates that pre-calibrated operation without the weighing scale was not feasible.

was $1\mu\text{L}$ based on the density of water being 1000kgm^{-3} and the weighing scale's mass resolution being 0.0001g . The response of the weighing scale also determined the time needed, since the off times could be shortened if it settled faster. We have also found that good isolation from draft and ambient vibrations was crucial to maintaining accuracy.

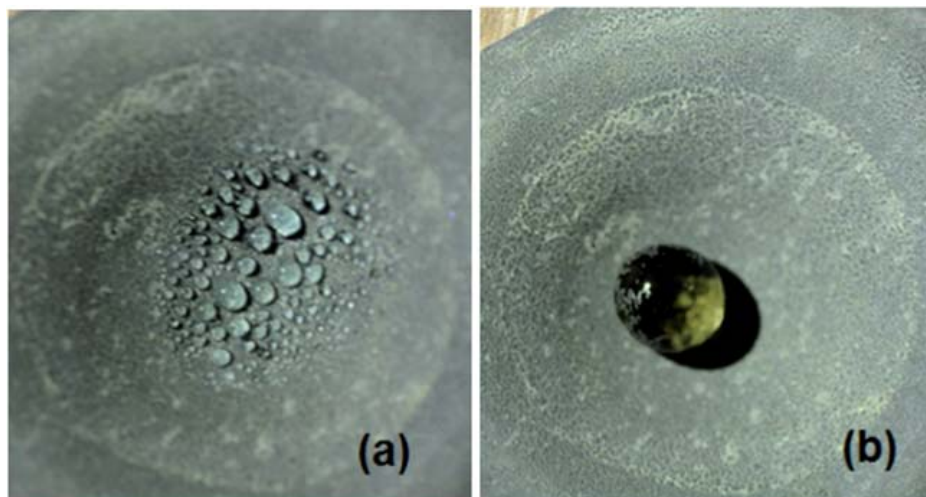


FIGURE 6.5: Images of (a) multiple nebulized droplets formed on the surface of the receptacle and (b) a single drop that results after shaking the receptacle.

The formation of multiple drops in the receptacle (Fig. 6.5a) of up to $3\mu\text{L}$ by volume (by estimation) before the gentle shaking operation was applied to dislodge them to form a final single drop (Fig. 6.5b) presents an interesting conundrum. Experiments with drops of this volume typically show that they move easily when dispensed on superhydrophobic surfaces. In fact, earlier dynamical studies conducted show that very small forces (in the

nano-Newton range) are needed to move water drops on this surface [152]. Coupled with the curvature of the receptacle, this should then result in a single drop forming all the time even when no shaking was introduced. This apparent anomalous behaviour can be explained by the Cassie and Wenzel wetting states of superhydrophobic surfaces [244]. When a drop impinges on a wetting surface, it is known that it will first expand rapidly [245]. With sufficient momentum of the drop, the surface microstructures are able to impale the liquid surface. As the liquid loses kinetic energy, the drop will eventually settle into a static state, leading to the observation of stickiness. On a non-wetting surface, alternatively, stronger capillary and hydrodynamic forces develop to impede this impalement process. Consequently, the drop is able to bounce off and lose energy through a succession of bounces.

When drops of larger sizes impinge on a superhydrophobic surface, there is very high likelihood that the impalement process will not occur. Upon settlement from bouncing, they are expected to develop a high proportion of Cassie states at the three-phase contact line, facilitating easy sliding and rolling of the liquid body along the surface Fig. (6.6a). We, of course, ignore for convenience the situation where the bouncing drops collide with each other in mid air. With individual aerosol drops (which are smaller in size) landing on the surface, however, the probability of impalement is increased since higher Laplace pressures develop on them [244, 245]. The impalement process essentially develops high degrees of the Wenzel wetting state on the surface as liquid fills into the crevices between the microstructures Fig. (6.6b). As more aerosols arrive, they either merge with those already on the surface or grow to the extent of coalescence with other surface-residing aerosols. In the absence of sufficiently large perturbations to convert the predominant Wenzel states into Cassie states [246], the drop coalesced from aerosols remains adherent on the inclined surface even at larger volumes for which an equivalent volume drop deposited upon the surface would be in the predominant Cassie state from the start Fig. (6.6c). The formation of multiple drops on the surface, (Fig 6.5a, appears to indicate some links with the process of condensation. However, previous studies conducted with condensation have shown a tendency for surfaces to lose their superhydrophobicity [247], likely arising from damages to the surface structures during the process. That a single drop could be attained here (after shaking) with no apparent loss in superhydrophobic behaviour (Fig 6.5b) shows differences in the underlying mechanisms.

While the drops are attached to the surface with a predominant Wenzel wetting state, the shaking of the receptacle imbues them with energy (see Fig. 6.7). With sufficient momentum, the drop will be able to dislodge from the surface to leave behind a thin film of liquid. Due to the direction of the shaking, this will occur more like a shearing operation, tearing the drop from the liquid embedded in the microstructures [152]. The very small volume of the thin liquid film left behind renders it easily evaporable while

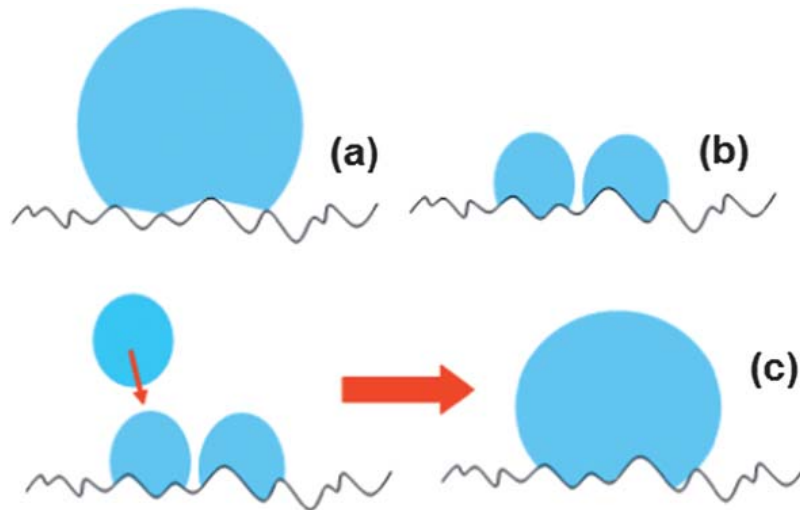


FIGURE 6.6: Illustrations depicting predominantly high (a) Cassie and (b) Wenzel wetting states of relatively larger drops and aerosols residing respectively on superhydrophobic surfaces. (c) When further aerosols arrive at the surface, they merge with existing aerosols on the surface to create larger volumes that coalesce with other surface bound aerosols. Due to the lack of a sufficiently large perturbation, the predominant Wenzel states cannot convert to Cassie states, allowing the liquid body to stay on the inclined surface with larger volumes.

the drop now functions in predominant Cassie state. We contend that the ability of the liquid film to evaporate quickly plays a role in the conversion process, since a previous study using lotus leaves has shown that extensive pre-wetting using condensation over the surface (which creates a thin film of liquid in the Wenzel state) will cause a loss in superhydrophobic behaviour of drops locating later over it [248]. Strictly speaking then, the description of the wetting state change here does not refute the notion that the Wenzel state is strongly irreversible. Wetting state changes are often thought of as pertaining to the entire body of liquid. The ability of the liquid body to separate hence imbues the “liberated” component with the capacity to seek another predominant wetting state. Evidence of the ability of drops to separate on superhydrophobic surfaces has been reported, albeit in a different context [249].

It is also apt at this point to mention that conception of a fully Cassie state is not viable due to the heterogeneity of the microstructures developed (see Fig. 6.2). It has been previously established that the spacing between protruding microstructures and the height of the protruding microstructures dictate whether a drop will assume Cassie or Wenzel states [250]. An interesting rumination relates to the interesting result of Jin et al. [251] that showed the possibility for superhydrophobic surfaces to possess strong adhesive forces by virtue of high van der Waals forces acting. Will it be possible to achieve the Wenzel to Cassie state changes with lowered movement of the drop during

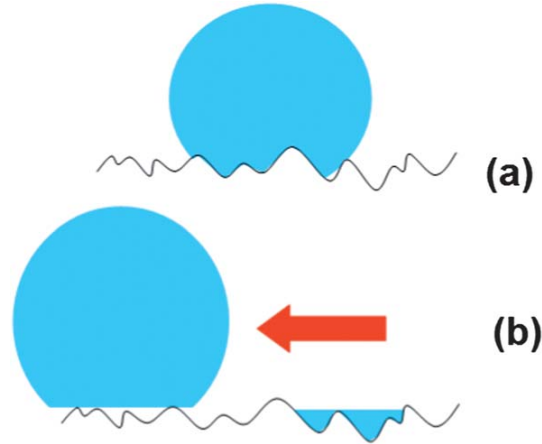


FIGURE 6.7: Illustrations depicting predominantly high (a) Wenzel wetting state of a drop on the surface in which with sufficient momentum developed (in the direction of the arrow) will (b) cause the drop to dislodge and leave behind a thin film of liquid. The very small volume of the latter renders it easily evaporable while the former now functions as a drop in the Cassie state.

the shaking process? That has advantageous implications in terms of practical device development.

An ability to mathematically model the formation of a single drop from the spray of aerosol droplets will be instructive, although likely an involved undertaking due to the stochastic and dynamical nature of the mechanisms involved in (i) aerosols arriving at the receptacle surface, (ii) aerosols growing into drops, (iii) drops detaching from the surface under gravity, and (iv) drops coalescing. In the context of (iv), the unexpected drop-drop bouncing behaviour recently uncovered on superhydrophobic surfaces [252] portends greater complexity in the modeling. We present here an elementary description of the extent of aerosol coverage on the surface that has implications for the mechanics of aerosols growing into drops.

6.2.3 Analysis of aerosol formation

A single aerosol that arrives as sphere with radius r' (which can be estimated to a high degree of accuracy using optical methods [253, 254]) on a semi-spherical surface of radius R will result in a liquid body that is governed by the equilibrium three-phase contact angle θ . The residence of a single aerosol on a semi-spherical surface can be depicted by the intersection of two spheres (smaller one of the drop, and larger one of the surface) as shown in Fig. (6.8). Since $\angle OAB = \angle O'AB = 90^\circ$, the contact angle θ is given by

$$\theta = 180^\circ - \phi \quad (6.1)$$

This is related to r (radius of the drop on the surface), R (radius of surface), and a

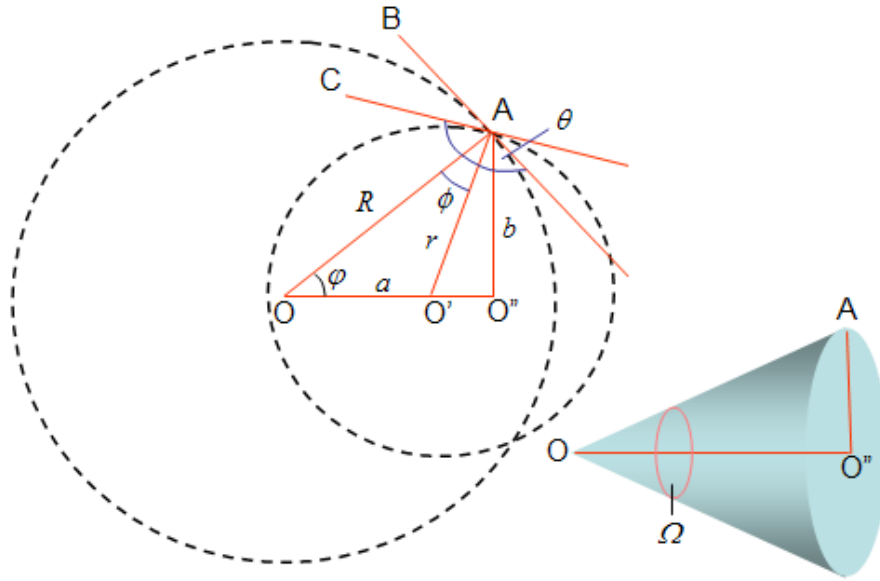


FIGURE 6.8: The residence of the aerosol droplet on the surface can be described using a model comprising two spheres that intersect with each other. The relevant parameters can be related, through the equations that can be solved, to the solid angle.

(distance between centers) via

$$a^2 = R^2 + r^2 - 2rR\cos\phi = R^2 + r^2 + 2rR\cos\theta \tag{6.2}$$

We next seek to establish the volume of liquid residing on the spherical surface. If the larger sphere is centered at $(0, 0, 0)$ and the smaller sphere at $(a, 0, 0)$ in Cartesian coordinates, we have

$$(x - a)^2 + (R^2 - x^2) = r^2 \tag{6.3}$$

Solving for x , we have

$$x = \frac{a^2 - r^2 + R^2}{2a} \tag{6.4}$$

If we apply this to the equation of the larger sphere, we have

$$y^2 + z^2 = R^2 - x^2 = \frac{4a^2R^2 - (a^2 - r^2 + R^2)^2}{4a^2} \tag{6.5}$$

Hence, at the point of intersection, we have a circle of radius b given by

$$b = \frac{1}{2a}\sqrt{4a^2R^2 - (a^2 - r^2 + R^2)^2} \tag{6.6}$$

This creates two caps of respective heights

$$h_R = R - x = \frac{(r - R + a)(r + R - a)}{2a} \quad (6.7a)$$

$$h_r = r - a + x = \frac{(R - r + a)(r + R - a)}{2a} \quad (6.7b)$$

Since the equation of volume of a spherical cap is known, we have

$$\begin{aligned} V &= V(R, h_R) + V(r, h_r) \\ &= \frac{\pi(R + r - a)^2(a^2 + 2ar - 3r^2 + 2aR + 6rR - 3R^2)}{12a} \end{aligned} \quad (6.8)$$

The extent of coverage of a single aerosol drop on the substrate surface can be conveniently depicted by the solid angle Ω in which

$$\Omega = 2\pi(1 - \cos\phi) = 2\pi \left(1 - \frac{\sqrt{R^2 - a^2}}{R} \right) \quad (6.9)$$

The maximum solid angle that can be subtended from a point source is 4π radians. If the radius r' of aerosol delivered is known, this parameter can be related to the volume V by assuming the aerosol to be a sphere using $V = 4\pi(r')^3/3$. In Eq. (6.8) then, r' with R will relate to a and r . Using Eqs. (6.2) and (6.9), we can then relate r' and R instead to θ and Ω .

The solid angle provides a convenient depiction of the extent of coverage taken from an assumed point source (the nebulizer). This is rather akin to the delivery of light from a point source in radiometry [255]. Fig. (6.9) presents plots of Ω against r'/R for various values of θ . As r' and R were $5\mu\text{m}$ and 8.5mm , respectively, the abscissa values were normalized to $\mathcal{O}(10^{-3})$. The definition of superhydrophobicity is loosely correlated to a value of θ ranging from 120° to 180° . In the figure, the variations in the solid angles calculated based on this are significant. If we consider the case of $\theta = 120^\circ$, changing r'/R from 2×10^{-3} to 4×10^{-3} increases the solid angle by 4.2 times. An increase in the solid angle is generally favourable as it implies a greater probability for the aerosols that arrive later to impinge on those already on the surface. This improves the chance of growth towards drops and thus also propensity for them to detach and roll towards the base of the receptacle. If the aerosol radius were to be kept constant, reducing R would achieve this. It should be noted, however, that too small a value of R will increase the chances of the spray envelope to fall outside the receptacle, thereby causing material loss. The solid angle values with $\theta = 170^\circ$ alternatively are small, which is seemingly negative in terms of increasing the probability of aerosol coalescence on the surface. Nevertheless, the adhesion forces of drops with higher θ values are also typically

smaller, enabling even a small aerosol drop to roll down to the base. In addition, the values of Ω remain relatively invariant with r'/R when θ is closer to 180° .

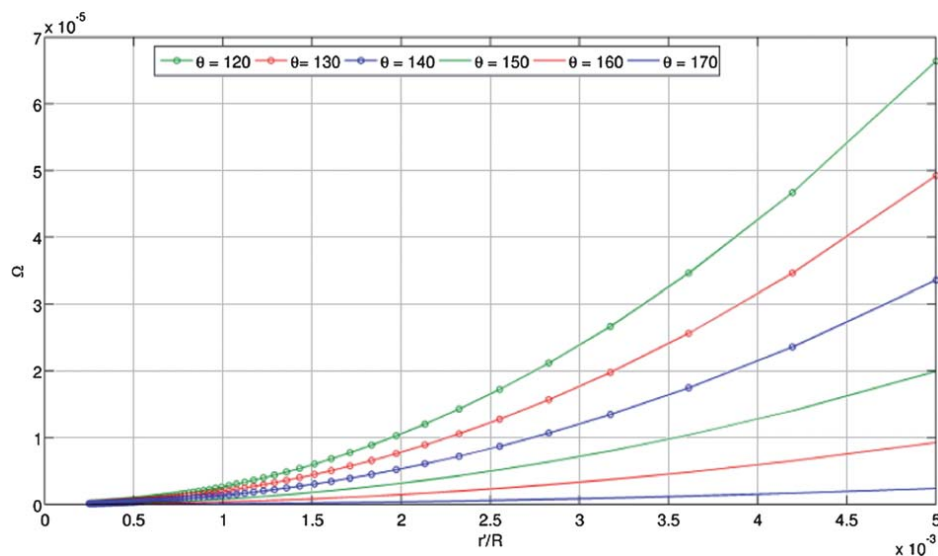


FIGURE 6.9: Plots of the solid angle Ω subtended by an aerosol droplet that arrives as a sphere with radius r' on a semi-spherical surface of radius R for various equilibrium three-phase contact angles θ . The residence of the aerosol droplet on the surface can be described using a model comprising two spheres that intersect with each other. The relevant parameters can be related, through the equations that can be solved, to the solid angle.

With nebulizer powers of 1.1W, 1.3W, 1.52W and 2.05W, the fluorescence intensity readings, normalized to the reading without nebulization, were 0.81, 0.77, 0.80, and 0.84 respectively. This indicated some expected loss in fluorescence, not inconsistent with previous results assessing post-nebulized protein viability, although different levels of power in the range used did not seem to have a varying effect. Samples that were nebulized also retained their fluorescence activity with no signs of any post deterioration in emission intensity after storage for a week at 4°C . GFP fluorescence is known to be affected by pH [256], dissolved oxygen [257], and high temperatures [258]. It is possible that a slight disruption of the structural integrity of EGFP, in particular its fluorophore, may have been caused by strong initial perturbations delivered to the sample. All samples in a fluorimetric assay, therefore, should comprise equal volumes of EGFP or fluorescent protein marker equivalently nebulized to ensure consistency in measurements made.

6.2.4 Conclusion

We have identified that a galvanic displacement mechanism in an electroless deposition process occurred in which the silver cations in solution were reduced just as copper from

the surface was oxidized and was responsible for creating the micro- and nano-scaled structures that endow superhydrophobicity on the copper substrate. A time dependent morphology change from granular to dendritic with longer immersion into the silver nitrate solution was found. This indicated that granular growth beyond a certain size was not feasible, although granular structures were more preferentially formed just after nucleation. The dendritic structure formation was likely due to the natural tendency of the process to maintain or increase the surface area to volume ratio not to limit the rate of deposition. An immersion for at least 7 seconds into the silver nitrate solution was all that was needed to ensure super-hydrophobicity of the surfaces. This allowed for the deduction that the dendritic structures were not needed to maintain the non-wetting characteristics, although they seemed not to have a role in modifying it. Also, the superhydrophobic state required not just significant numbers of the granular structures to be present, but also interrupted coverage on the surface. In using the proposed technique, having the nebulizer cyclically pulsed on for 5 seconds and off for 5 seconds was needed to accommodate the response time of the weighing scale. Highly linear trends were observed, indicating that fixed quanta of liquid were dispensed with each pulsed operation of the nebulizer for a specific run. However, the flow rate may be altered and this was due to factors that affected the transfer of liquid in and out of the tissue (such as temperature and airborne particles attaching to fibers). With individual aerosols landing on the receptacle surface, the probability of impalement was increase since higher Laplace pressures developed on them. The impalement process then developed high degrees of the Wenzel state on the surface. With sufficient momentum from shaking, the drop was able to dislodge from the surface leaving behind a thin film of liquid. The very small volume of the thin liquid film rendered it easily evaporable while the drop then functioned in a predominant Cassie state. In using EGFP samples for verification, fluorescence emission could be retained to about 80% of its original level and was not affected by different levels of power used on the SAW device. In summar, we have developed a practical approach to deposit micro-liter volume drops on superhydrophobic surfaces stably and precisely. This is expected to facilitate biochemical applications using these surfaces.

6.3 Contact angle and volume retention effects from capillary bridge evaporation in biochemical microplating

In this work, we investigate the feasibility of using the capillary bridges developed between solid bodies to interrogate the contact angle development under the effect of evaporation. In addition, we also seek to ascertain the progress of volume change. These

finding will help to provide insight on the ability to relate wetting to analyte characteristics and mitigate evaporation in biochemical microplating schemes developed for use in resource-limited laboratories.

6.3.1 Theoretical considerations

When surface tension dominates, the shape of a sessile drop on a surface can be assumed to be semi-spherical. From geometry (see Fig. 6.10), it is rather easy to establish that the volume is related to the radial distance of the drop on the surface a by

$$V = \frac{\pi a^3(1 - \cos\theta)^2(2 + \cos\theta)}{3\sin^3\theta} \quad (6.10)$$

where θ is the contact angle and R is the radius of curvature. The liquid bridge that

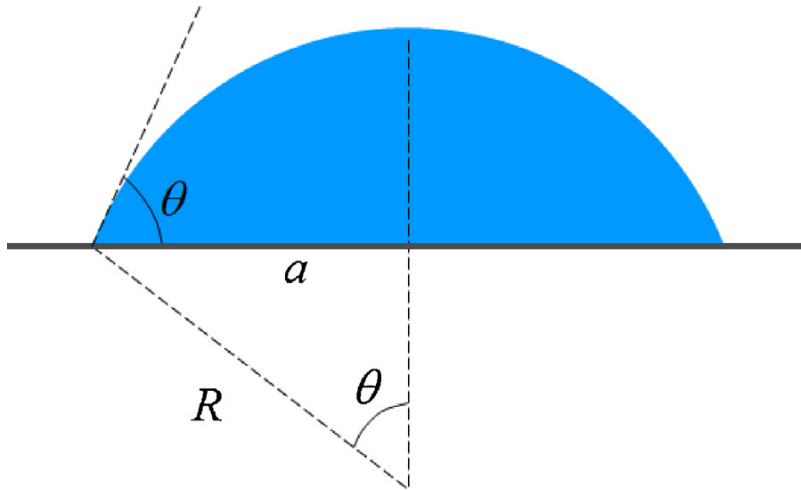


FIGURE 6.10: Schematic description of a sessile drop where its shape is semi-spherical. The volume can be determined using the measurable parameters of θ and a

forms between two flat surfaces under a strong surface tension effect assumes three different shapes, depending on the contact angle. In the case where $\theta < 90^\circ$, we have from Fig. (6.11a)

$$\frac{h}{R} = \cos\theta \quad (6.11)$$

where h is the half height of the liquid bridge. The length of AB is then given by

$$\|AB\| = \sqrt{R^2 - (h - y)^2} = \sqrt{\frac{h^2}{\cos^2\theta} - (h - y)^2}. \quad (6.12)$$

For a vertical distance of y from the solid surface, the horizontal distance can be determined using

$$x = a + h \tan \theta - \|AB\| = a + h \tan \theta - \sqrt{\frac{h^2}{\cos^2 \theta} - (h - y)^2}. \quad (6.13)$$

The volume of the liquid bridge can thus be computed using

$$V = 2 \int_{y=0}^{y=h} \pi x^2 dy \quad (6.14)$$

In the case where $\theta > 90^\circ$, we have from Fig. (6.11b)

$$\frac{h}{R} = \cos(180^\circ - \theta) \quad (6.15)$$

The length of AB in this case is then given by

$$\|AB\| = \sqrt{R^2 - (h - y)^2} = \sqrt{\frac{h^2}{\cos^2(180^\circ - \theta)} - (h - y)^2} \quad (6.16)$$

The horizontal distance based on a vertical distance of y from the solid surface can thus

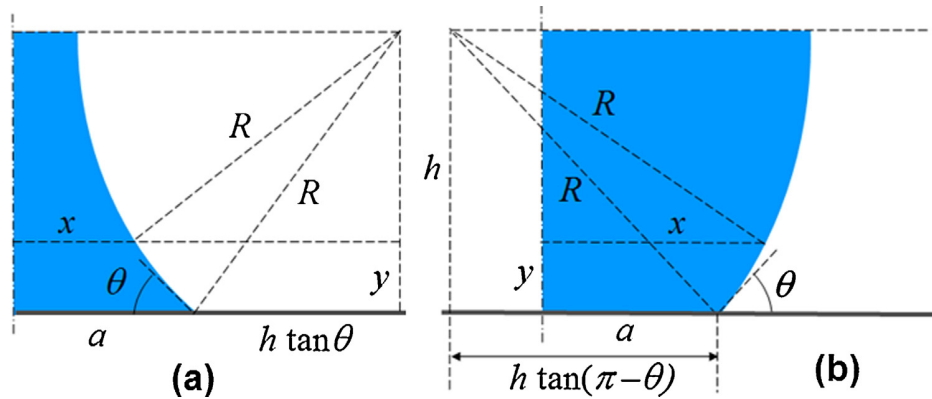


FIGURE 6.11: Schematic description of the half height and width of a symmetrical capillary bridge between two flat surfaces when (a) $\theta < \pi/2$, and (b) $\theta > \pi/2$. The volume can be calculated using the parameters θ , h and a

be determined by

$$x = a + h \tan(180^\circ - \theta) + \|AB\| = a + h \tan(180^\circ - \theta) + \sqrt{\frac{h^2}{\cos^2(180^\circ - \theta)} - (h - y)^2} \quad (6.17)$$

The volume can then be determined using Eq. (6.16). In the case where $\theta = 90^\circ$, the liquid bridge is essentially a cylinder. Hence the volume in this case is given by

$$V = \pi a^2(2h) = 2\pi a^2 h \quad (6.18)$$

When a small but sufficient amount of liquid is brought into the gap of three two narrowly spaced wettable rods, the liquid forms a short bridge the surface of which can be assumed to be constant mean curvature. As more and more liquid is added to the bridge, it lengthens in the direction of the axes until it forms a long cylindrical body to a good approximation, and has a constant cross section except in the region of the terminal menisci. The volume of liquid can then be taken as the product of this cross-section and the length. If we take the rods to be of equal distance z from each other (Fig. 6.12a), the distance between the centroid O' to the center of each rod is given by

$$d = \frac{\sin(\pi/6)}{\sin(2\pi/3)} z = \frac{z}{3} \quad (6.19)$$

Suppose that the contacts of capillary bridge with the uppermost rod are at A and C (Fig. 6.12b). If this subtends an angle of 2Φ on the rod, we can trace out the triangle $O'OA$ in Fig. (6.12c), such that

$$\frac{r}{\sin\Phi} = \frac{c}{\sin\phi} \quad (6.20a)$$

$$r\cos\Phi + r\cos\phi = d \quad (6.20b)$$

From Eqs. (6.20a) and (6.20b) we have

$$\phi = \tan^{-1} \left(\frac{r\sin\Phi}{d - r\cos\Phi} \right) \quad (6.21)$$

The area of the triangle $O'OA$ is thus

$$\text{Area}(O'OA) = \frac{1}{2} r d \sin\Phi \quad (6.22)$$

From the triangle $O'AB$ (Fig. 6.12d), we are able to determine that

$$\mu = \frac{\pi}{3} - \phi \quad (6.23)$$

In addition, the area of the triangle $O'AB$ is given by

$$\text{Area}(O'AB) = \frac{1}{2} c^2 \sin 2\phi \quad (6.24)$$

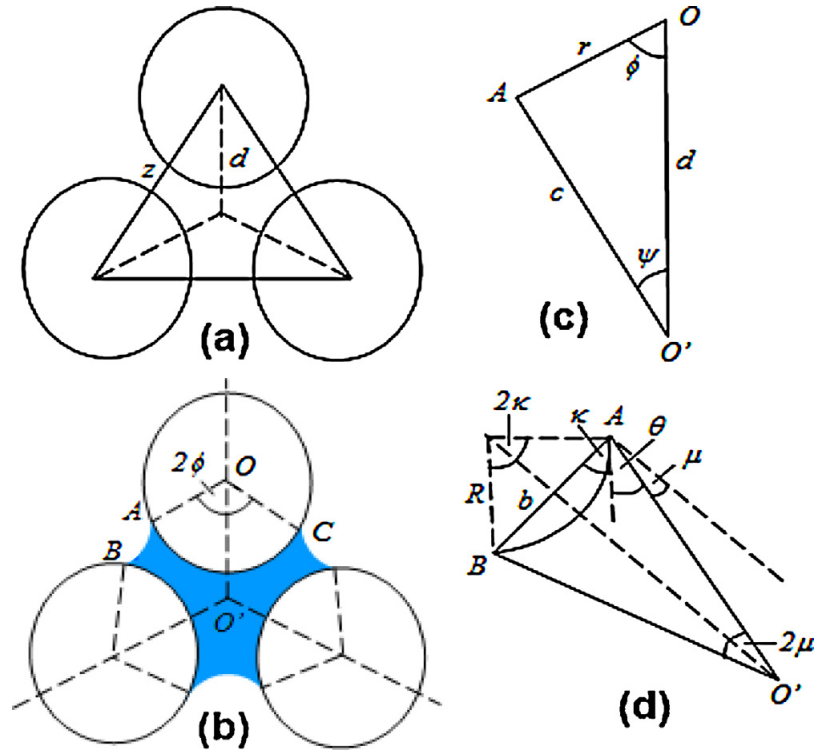


FIGURE 6.12: Schematic description of (a) the cross-section of three rods of equal diameter located with equal distance z to each other. The contacts of capillary bridge (at points A and C) with the rod, shown in (b) subtend an angle of 2ϕ on it. The areas computer of $OO'A$ in (c), $O'AB$ and the semicircle AB in (d), and OAC in (b) permit the volume of the capillary bridge to be determined

The length of the chord AB can be found using

$$b = 2c\sin\mu \tag{6.25}$$

In Fig. (6.12d), it can be seen that the arc AB is subtended through an angle of 2κ by the radius R . Since

$$\kappa = \frac{\pi}{2} - (\mu + \theta) \tag{6.26}$$

it is possible to find that

$$\begin{aligned} R &= \frac{b}{2\sin\kappa} = \frac{b}{2\sin(\pi/2 - (\mu + \theta))} \\ &= \frac{b}{2\cos(\mu + \theta)} \end{aligned} \tag{6.27}$$

This will allow the area of the semicircle cap AB to be approximated using

$$\begin{aligned} \text{Area}(\nabla AB) &\approx \frac{R^2}{2}(2\kappa - \sin 2\kappa) \approx \frac{b^2}{8\cos^2(\mu + \theta)} \\ &\times \left\{ 2 \left(\frac{\pi}{2} - (\mu + \theta) \right) - \sin 2 \left(\frac{\pi}{2} - (\mu + \theta) \right) \right\} \\ &\approx \frac{b^2}{8\cos^2(\mu + \theta)} \{ (\pi - (\mu + \theta)) - \sin 2(\mu + \theta) \} \end{aligned} \quad (6.28)$$

The area of the subtended arc OAC is simply

$$\text{Area}(OAC) = \left(\frac{2\Phi}{2\pi} \right) \pi r^2 = \phi r^2 \quad (6.29)$$

Summarily, the cross section comprising the liquid body is given by

$$\text{Area} = 6 \times \text{Area}(O'OA) + 3 \times \text{Area}(ABO) - 3 \times \text{Area}(\nabla AB) - 3 \times \text{Area}(OAC) \quad (6.30)$$

The input of parameters, z , r , Φ and θ into Eq. (6.19), (6.20a), (6.21), (6.23) and (6.25) permit d , c , ϕ , μ and b to be determined. From these parameters, Eqs. (6.22), (6.24), (6.26) and (6.29) can be solved to allowed the cross-sectional area of liquid to be determined via Eq. (6.30).

6.3.2 Materials and methods

The experimental sample used was enhanced green fluorescent protein (EGFP) carrying a C-terminal polyhistidine tag, isolated from genetically modified *Escherichia coli* and purified by immobilized metal affinity chromatography. After elution of the proteins from the chromatographic matrix, the sample was desalted into sodium phosphate buffer (pH 7.4), checked from purity by SDS-PAGE (sodium dodecyl sulfate-polyacrylamide gel electrophoresis), and quantified using the BCA (bisinchoninic acid) protein assay (Pierce). Sodium phosphate (NaPO_4) buffer was used to prepare a series of dilutions for the purified EGFP sample ranging from 65 to 1300ng/ μL . These solutions were delivered using a manual pipette (Biohit mLine Mechanical Pipette, 10-100 μL).

The experiments conducted on flat surfaces comprised glass slides, silanized glass slides, and silicone surface slides; which gave different levels of hydrophobicity. For experiments on rods, capillary tubes of outer diameter 1 mm were used. Images were recorded using microscope lenses (Infiniprobe) attached to CCD video camera (Hitachi, KP-D20AU). From the images recorded, the required dimensional information was extracted using the ETHSCSA Image Tool Version 3.0 software.

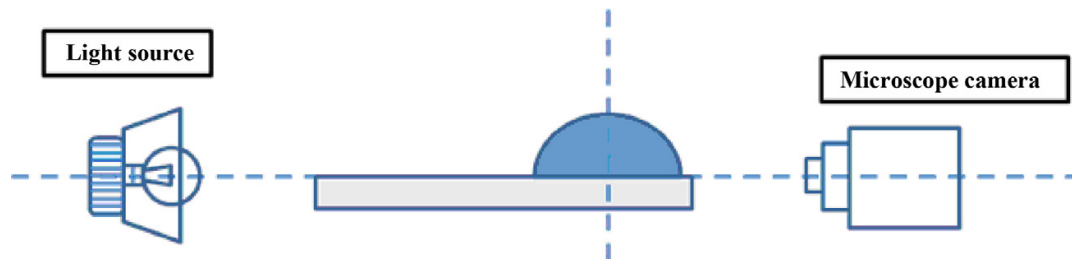


FIGURE 6.13: Schematic depiction of the experimental setup used for recording the liquid bridge between two flat surfaces, with (a) providing a front view of the setup where the dotted lines show the axes of symmetry and where the main imaging axis is through the center marked point. The side view (b) of the setup shows the imaging axis with the light source being opposite to the microscope camera and the illumination axis along the imaging axis.

Liquid drops of the same volume ($3\mu\text{L}$) were deposited onto each flat surface using a manual pipette. The imaging axis was kept parallel to the glass plate along its surface, and perpendicular to the droplet symmetry line when viewing the setup from the side (see Fig. 6.13). A bright LED light source was placed opposite to the microscope camera to illuminate the droplet for clearer imaging, along the imaging axis. The droplet was deposited close to the edge of the plate on the imaging side so that the droplet and the end of the plate were almost equally focused.

From the video recordings an image file was produced at each time interval until the evaporation of the drop was complete. Based on the images recorded, the contact angle θ and drop radii on the surface a information was determined (Fig. 6.10).

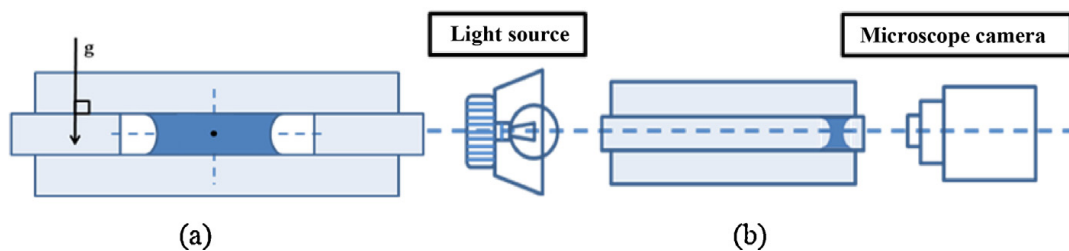


FIGURE 6.14: Schematic depiction of the experimental setup used for recording the liquid bridge between two flat surfaces, with (a) providing a front view of the setup where the dotted lines show the axes of symmetry and where the main imaging axis is through the center marked point. The side view (b) of the setup shows the imaging axis with the light source being opposite to the microscope camera and the illumination axis along the imaging axes.

Liquid drops of equal volume ($3\mu\text{L}$) were deposited between two rectangular flat surfaces placed in parallel to each other and perpendicular in relation to gravity. The distance between the surfaces was maintained at 0.475 mm using two spacers (Fig 6.14a). The imaging axis was kept parallel to the glass plate, so that it passes through the center point of the liquid bridge at the intersecting symmetry lines. The LED light source

was placed opposite to the microscope camera to illuminate the liquid bridge along the imaging axis. The droplet was deposited close to the edge of the plates on the imaging side so that the liquid bridge and the ends of the plates were equally focused for imaging (Fig. 6.14b).

Video recordings were made until the complete evaporation of the liquid bridge. From the images obtained prior to the liquid bridge breakdown, values of the parameters θ and a were determined (see Fig. 6.11).

To measure the capillary bridges between rods, the setup consisted of three glass rods placed parallel to each other with their axes perpendicular to gravity. The rods were positioned so that their respective axial centers formed the vertices of an equilateral triangle with 3.733 mm side length (see Fig. 6.15a). The rods were fixed in this configuration through fitted holes in two transparent, rectangular plastic plates kept in parallel and fixed with adhesive at the adjoining interfaces. Liquid was deposited close to one end of the rods so that the liquid and rods could be simultaneously focused. The transparent, plastic plates were used to enable light from the light source to pass through to illuminate the liquid bridge. This resulted in high contrast images amenable for dimensional measurements. With liquid dispensed between the rods, images were recorded with the main imaging axis parallel to the axes of the rods and passing through the center point of the visualized equilateral triangle (see Fig 6.15b). An additional camera view was used to capture the length of the liquid bridge such that the imaging axis was parallel to gravity and perpendicular to the main imaging axis (Fig. 6.15b). The illumination axis was kept along the main imaging axis, with the light source being opposite the microscope camera.

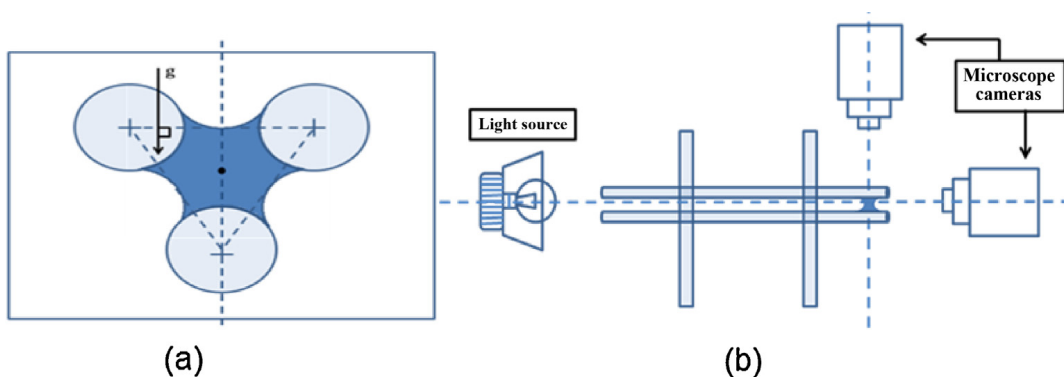


FIGURE 6.15: Schematic depiction (a) of the experimental setup for creating a liquid bridge (darkened areas) between glass rods in which the front view comprise dotted lines showing the position of the axial centers of the rods at the vertices of an equilateral triangle. In recording (b) the main imaging axis is through the center marked point is recorded using one camera, and another camera records perpendicular to this axis.

Liquid of constant volume ($3\mu\text{L}$) was deposited onto the rods and the changes in length and contact angles recorded simultaneously from the top and the front of the setup until complete evaporation of the liquid bridge. Video recordings were made until the complete evaporation of the liquid bridge. From the images obtained prior to the liquid bridge breakdown, values of the parameters θ and Φ could be determined (see. Fig. 6.12).

6.3.3 Results and discussion

The initial contact angle for sessile drop on glass was about 33° . This is higher than the typical equilibrium contact angle reported in literature, and is possibly caused by the deposition process which renders it closer to the advancing angle. From the time trace in Fig. (6.16), it is evident that this surface has a tendency to pin straight away, causing the contact angle to reduce continuously. There appears to be a two stage process for this wherein after 10 min the rate of contact angle decrease was more pronounced. With silanized glass, the initial contact angle was 42° . This is higher than the value on glass, which is expected. Compared with glass, the contact angle reduction on silanized glass was more gradual with evaporation. A second stage process occurred after about 28 min in which the contact angle reduced at a slightly faster rate. For silicone, the initial contact angle was about 113° indicating that the surface is hydrophobic. For the first 25 min, the contact angle reduced at a rate that is almost similar to that of glass. Beyond that, however, the contact angle starts to fall off at a rapid rate. On all surfaces, contact angles very close to zero at the end of evaporation were observed. In the evaporation process, it can be seen that contact line pinning is a dominant feature. The presence of hysteresis indicates that a four stage evaporation process may be in action [259].

The volume trace with time was estimated using Eq. (6.12) and presented in Fig. (6.17). It can be seen that rather linear rates were obtained with glass and silanized glass notwithstanding the two step contact angle reduction rates occurring on these surfaces. We surmise that since the rate changes were small, the effects on the linearity of volume change were minimal. In the case of silicone, the volume change distribution was far less linear due to the pronounced contact angle rate changes. It is also evident that the same drop volume was able to be retained 1.5 and 2 times longer on silanized glass and silicone surfaces respectively over glass surfaces. This result can be explained through the feature of evaporation rate occurring more rapidly at lower contact angles regions in the sessile drop. This same effect is also responsible for generating the capillary flow responsible for the coffee stain effect [260, 261].

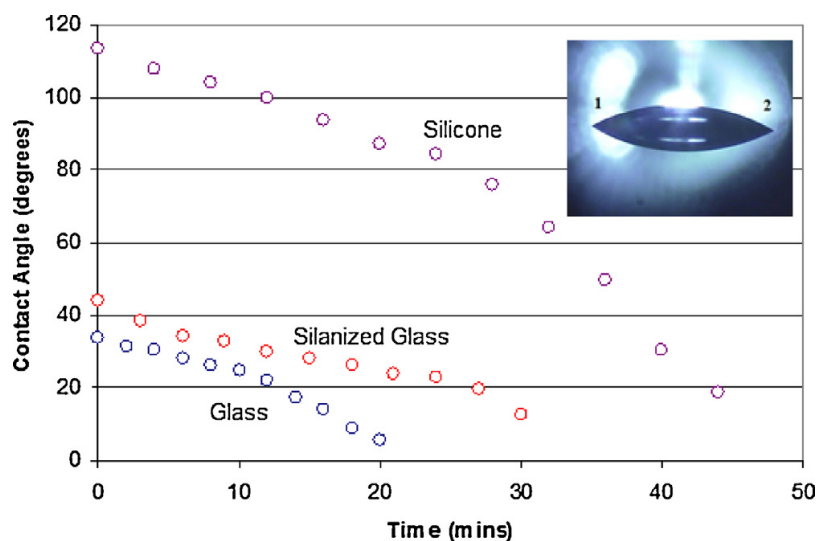


FIGURE 6.16: Trace of the contact angle progression with time as a $3\mu\text{L}$ sessile drop (see inset) is evaporated on the flat surfaces made of glass, silanized glass, and silicone. The contact angle is taken as the average of the angles marked 1 and 2 in the picture.

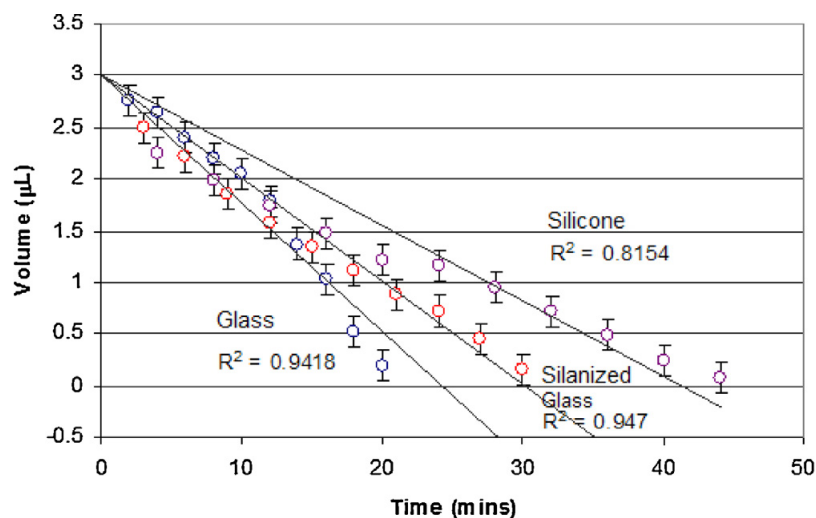


FIGURE 6.17: Trace of the remnant volume against time of a $3\mu\text{L}$ sessile drop as it is evaporated on the flat surfaces made of glass, silanized glass, and silicone.

In the case of the capillary bridge on glass, the starting contact angle was about the same as that of the sessile droplet. But instead of pinning, there was a high degree of stick-slipping of the contact line resulting in slow reduction of the contact angle. The effect of contact line sticking and slipping in liquid bridges has been actively studied [262]. The behaviour with silanized glass was almost similar with glass. An interesting behaviour, however, was observed with silicone. On this surface, the contact angle reduced drastically from 110° to 35° in the first 20 min. This sudden contact angle change appears strange but can be explained by the knowledge that the phase behaviour

of a fluid is strongly affected by confinement. The conditions for equilibrium of a liquid-vapor system confined in a solid geometry can be elucidated through entropy [263]. From thermodynamics, the change in entropy is known to be linked to temperature, pressure, and chemical potential. If this is extended to the interfaces of phases, it should then link to the tension and area of the interface as well. All the components acting at the interface can be taken to follow the Gibbs surface of tension approximation. With evaporation, the vapor phase has to form out of and coexist in an equilibrium state with a confined liquid phase. It has recently been shown that vapor formation with a convex meniscus is generally unfavourable from an inter-facial energy standpoint related to the action of entropy change [264]. This then helps to explain why the convex capillary bridge, in seeking to achieve improved stability, change over to a concave meniscus with the onset of evaporation. From 20 min onwards on the silicone surface, the contact line

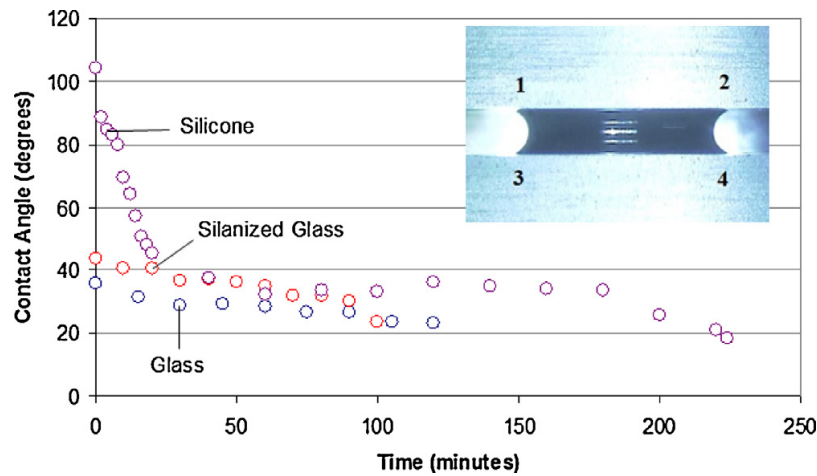


FIGURE 6.18: Trace of the contact angle progression with time as a $3\mu\text{L}$ capillary bridge (see inset) is evaporated between two flat surfaces made of glass, silanized glass, and silicone. The contact angle is taken as the average of the angles marked 1-4 in the picture.

was seen to undergo a strong sliding phase until the 180 min mark before late stage pinning caused the contact angle to reduce significantly. A point to note is that in all cases, the capillary bridge ruptured at around 20° . This is due to the influence of liquid capillary instability (due to curvature) that ensures that rupture occurred before the contact angle had chance to go to zero. In other words, it will not be possible to trace the contact angle developed on bridge all the way to total evaporation of the liquid body.

The volume of the capillary bridge was estimated using Eqs. (6.13) - (6.20a), from which the computed volume against time traces are shown in Fig. (6.19). Due to uncertainties involved in determining the parameters, the plots have larger error bars. The volume reduction trends in all cases appeared rather linear with R^2 values of 0.95 and above. It can be seen that the volume reduction rates of glass and silanized glass were about

the same which contrasts with the case of sessile drop evaporation. It appears then that the almost similar contact angle change trends here were responsible for this. Due to the rapid change of the contact angle over the first 20 min on silicone, the somewhat moderate departure from linearity of volume against time reduction in Fig. (6.19) was somewhat unexpected. However, the nature of the slope being steeper earlier in the process can be explained through the insights of Lord Kelvin [265] who formulated the relation

$$\frac{RT}{M} \log_e \left(\frac{p}{p_0} \right) = \frac{2\sigma}{\rho} \left(\frac{1}{R} - \frac{1}{R_0} \right) \quad (6.31)$$

with R being the gas constant, T the absolute temperature, M the molecular weight, σ the surface energy, ρ the density of the liquid, p the escaping tendency of the substance in a surface with radius of curvature R , and p_0 the escaping tendency in a surface with radius of curvature R_0 . If the value of R_0 is taken to be infinitely large indicating a flat surface), the equation provides a relation between the curvature of the liquid surface and the rate of evaporation. Where the surface is convex, the right-hand side of the equation is positive, while it is negative when the surface is concave. This is, of course, another way of saying that the escaping tendency of a convex surface is greater and a concave surface is less than that of a flat surface. On silicone flat surfaces, the capillary bridge that formed first starts off with a convex surface (which has higher liquid escaping tendency) and then converts into a concave surface during the first 20 min period. This then accounts for the initial stronger volume loss rate before reducing in time as shown in Fig. (6.19).

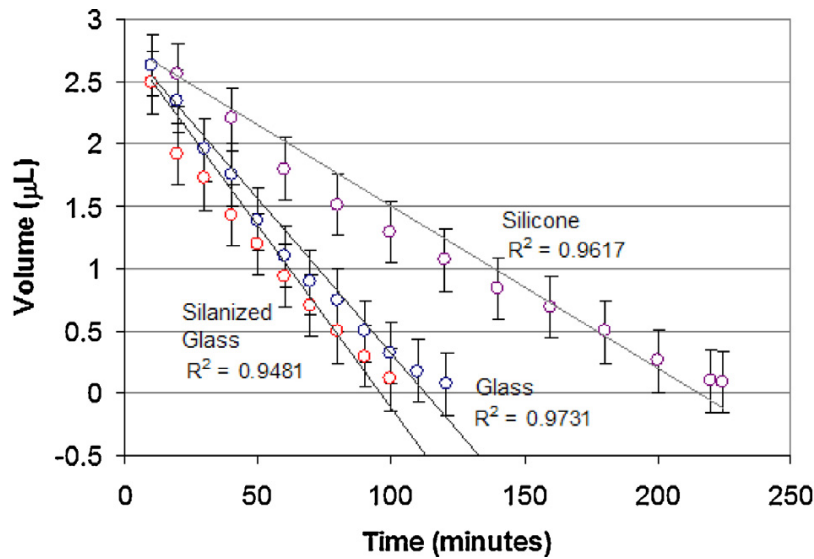


FIGURE 6.19: Trace of the remnant volume against time of a $3\mu\text{L}$ capillary bridge as it is evaporated between two flat surfaces made of glass, silanized glass, and silicone.

Due to the contact angles being almost the same after 20 min on all three surfaces (see Fig. 6.18), the ability of the silicone surface to retain liquid longer is somewhat curious.

However, it should be noted that in a highly constrained area, as is clearly the case with the capillary bridge formed between two flat surfaces, the vapor pressure distribution near the interface is markedly different from the case of a sessile drop. We believe that the initial convex to concave meniscus change with the capillary bridge formed between silicone surfaces to have resulted in a more saturated vapor pressure nearer to the interface. Consequently, this will have an effect of reducing the volumetric rate of liquid loss notwithstanding evaporation. In fact, keeping the same volume as a capillary bridge between two silicone surfaces extended the retention time by 5 times over the sessile drop on a silicone surface. This result has important implications when seeking to provide a cover for transparency microplates [154, 155] since it will create a capillary bridge. The use of hydrophobic transparencies should maintain analytes for longer from the effect of evaporation. The higher tendency to move on hydrophobic surfaces can be limited using scribed surfaces [155]. We also make mention here that the thickness of the substrates used is important to avoid the effect of surface tension induced deformation recently uncovered [266].

On inspecting the trace of contact angle against time for a capillary bridge between three rods (see Fig. 6.20), it can be seen that it is susceptible to rupture at a rather large angle (40°). In addition the time taken for the liquid to rupture was about 1.75 times longer than that of total evaporation of the sessile drop. This is attributed to the liquid-gas area being much larger than between two flat plates. The starting contact angle was much higher (70°) even though the surface was glass. In explaining this, it is important to contrast between the capillary bridge forming between the three cylinders with that inside a capillary tube. With the latter, the liquid-gas interface occurs only at the two distal ends of the tube. With the cylinders, the interface occurs all along the length. In such a case, it cannot be assumed that the extent of wetting to be constant throughout the length. This has similarities to the situation of a thread of liquid resting on a surface wherein the behaviour depends on the boundary condition at the contact line. In studies that investigated the equilibrium shape of a liquid confined to hydrophilic stripes, bulges have been shown to occur [267]. It is conceivable then that a similar effect had occurred, albeit this is difficult to observe and confirm along the liquid length. Such an effect (bulging) will then account for the increased contact angles observed at the distal ends where recording is made. It is also important to note that the contact angle at rupture occurred at values two times higher than that between flat surfaces. It will appear that the thread effect also has the effect of causing higher levels of instability that resulted in the capillary bridge rupturing earlier.

Fig. (6.21) and (6.22) present the breakdown traces of the contact angles developed on each of the three glass rods, as well as the top and bottom of the two glass flat surfaces in the evaporation experiments conducted. It can be seen that the fluctuations

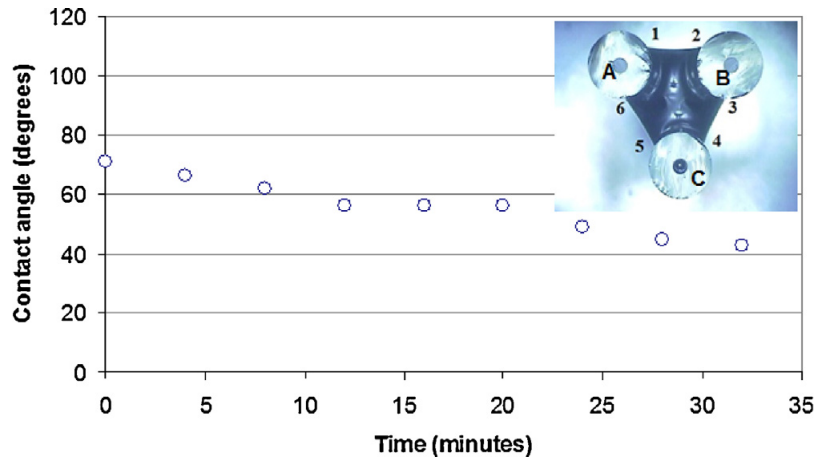


FIGURE 6.20: Trace of the contact angle progression with time as a $3\mu\text{L}$ capillary bridge (see inset) is evaporated between three rods (A-C) made of glass. The contact angle is taken as the average of the angles marked 1-6 in the picture.

in contact angle of the capillary bridge on glass cylinders are much higher than on flat glass surfaces. We attribute this also to the thread effect since this will have an effect of altering the symmetry of liquid in contact with each of the cylindrical surfaces. This result allowed us to infer that using the three rod approach to trace the contact angle development with time will not be practical.

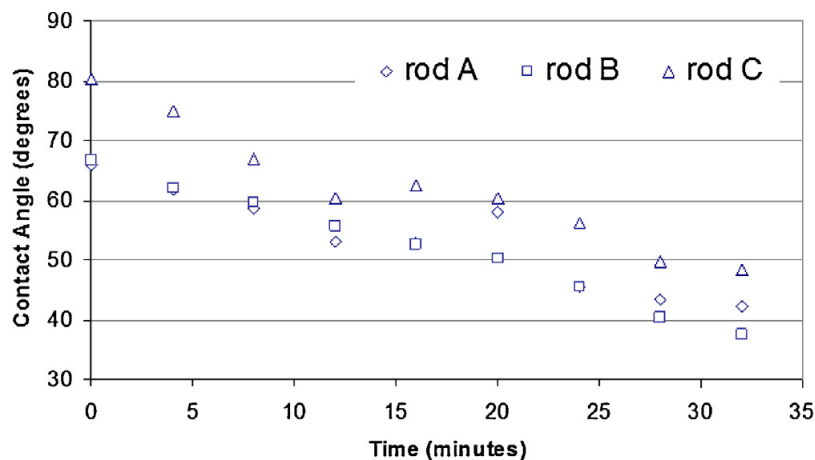


FIGURE 6.21: Breakdown trace of the contact angles developed on the three glass rods in Fig. (6.20) with time as a $3\mu\text{L}$ capillary bridge is evaporated between them. Significant fluctuations (in the order of 20°) can be observed.

The fact that the contact angles could vary significantly between the rods and the effect of liquid threads being significant, makes volume estimation through the equations developed earlier to be fraught with high levels of uncertainty. Nevertheless, the equations still provide some useful insights into the process. Based on the estimated average values of $\theta = 72^\circ$, $\Phi = 61^\circ$ initially and $\theta = 42^\circ$, $\Phi = 44^\circ$ after rupture, the area change is estimated to be -31.5% . The length of capillary bridge change (measure directly) was

found to be approximately -72%. It is clear then that the length change is above two times the cross sectional area change of the capillary during the evaporation. Fig. (6.23) provides a map of the liquid bridge cross sectional area against various values of θ and Φ . It is intuitive then that the amount of liquid that can be retained is lowered when θ and Φ are similarly lowered.

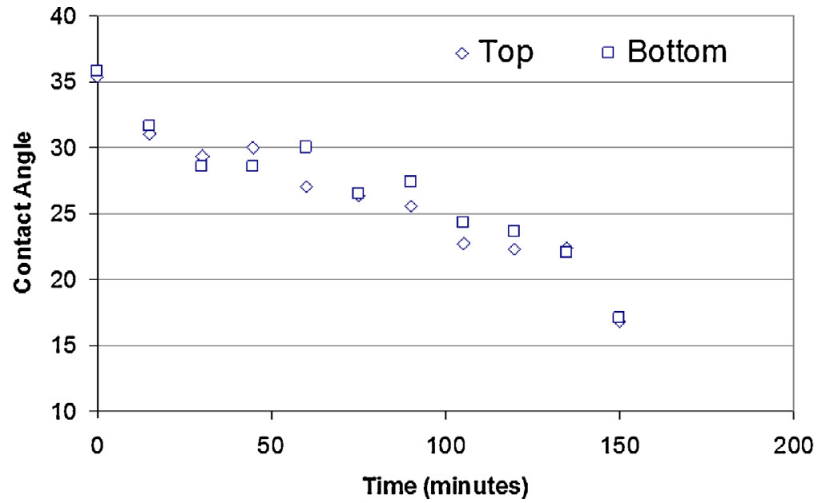


FIGURE 6.22: Breakdown trace of the contact angles developed on the top and bottom of the two glass flat surfaces in Fig. (6.18) with time as a $3\mu\text{L}$ capillary bridge is evaporated between them. The fluctuations are noticable much smaller ($< 5^\circ$).

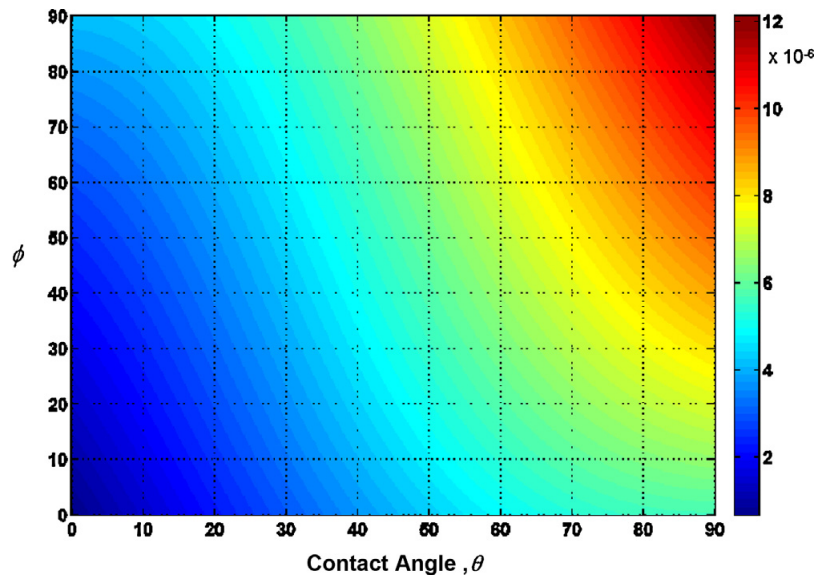


FIGURE 6.23: Map of the cross sectional area of the capillary bridge held between three liquid rods calculated for various values of θ and Φ . The units are in m^2 and area based on $z = 3.733\text{mm}$ and $r = 1\text{mm}$ in Fig. (6.12).

6.3.4 Conclusion

The experiments with sessile drop evaporation show the contact angle versus time trends to roughly comprise two linearly reducing rates; one slower followed by one that is faster. The difference is more pronounced with silicone as oppose to glass and silanized glass. This caused a strong departure from volume reduction linearity using silicone. The use of silicone improved the drop retention capability by 2 times over glass. The experiments with capillary bridge evaporation between two flat surfaces show similar strong linear contact angle reduction and thus volume reduction trends with time using glass and silanized glass. With silicone, there was a steep contact angle reducing rate in the early stage followed by a more gradual reducing rate later. The steep process was attributed to the liquid-vapor interface accommodating for thermodynamic entropy changes during evaporation, which favour forming a concave over a convex meniscus. The initial convex meniscus also resulted in faster volume reduction as stipulated by Kelvin's relation on escape tendency. The much slower volume reduction rate with silicone flat surfaces found presented a conundrum since the contact angle development with time during the later stages was similar to that between glass and silanized glass surfaces. This was attributed to the initial convex to concave meniscus change in a confined space that resulted in a more saturated vapour pressure nearer to the interface. With the same volume, the capillary bridge between two silicone surfaces extended the retention time of the sessile drop on a silicone surface by over 5 times. This makes it favourable for use as a means to limit the effects of evaporation in small volume biochemical microplating. The use of contact angle measurements using this approach however needs to take into account the different evaporation mechanics scheme existing between a sessile drop and a capillary bridge between two flat surfaces. Also the range of measurements is limited to the point where rupture occurred, which we found to be around 20° notwithstanding the different surface types. In the experiments with capillary bridge between three rods, rupture occurred at a rather large angle (40°). In addition, the time taken for the liquid to rupture was only about 1.75 times longer than that of total evaporation of the sessile drop. The starting contact angle was much higher (70°) and was attributed to wetting being not constant throughout the length. This has similarities to the situation of a thread of liquid resting on a surface wherein the behaviour depends on the boundary condition at the contact line. The same effect is also responsible for the higher fluctuations in contact angle trend over that on flat surfaces, making it impractical to be used for characterization measurements. Due to these fluctuations, attempts to estimate volume based on the liquid bridge geometry would be subject to large levels of uncertainty. By using the geometrical equations and approximate parameter changes, the length change was found to be above two times the cross sectional area change of the capillary during evaporation. The results here indicate

that when evaporation is significant, creating capillary bridges for the transparency microplates offer the best ability to retain volumes while allowing the contact angle to be interrogated.

6.4 Scale-like cantilever cell traps

Skins with scales (scuts) are a prominent feature in reptiles such as snakes. Various suggestions have been advanced to elucidate their function, including (i) a kind of zip-fastener supporting the molding process by holding old and new skin together until the old skin is entirely shed [268], (ii) surface strengthening [269], (iii) anti-contamination [270], and (iv) anti-fouling. Recently, in an attempt to better understand how snakes are able to travel through narrow openings, despite being restricted from using coiled motion propulsion, evidence of a concertina-type movement, aided by the directional frictional anchors provided by the ventral scales, had been confirmed by observing the locomotion of corn snakes (*Pantherophis guttatus*) [271].

The *Azolla*, alternatively, is a genus of small aquatic ferns widely distributed around the world. Its branches and stems are covered with small, alternate, overlapping leaves which resemble scales under a cursory observation. Affixed to these leaves are populations of the cyanobacterium *Anabaena azollae* which the *Azolla* shares a symbiotic relationship with. Underwater, the shape of these leaves has long been suspected of helping to trap minerals such as phosphorus, which can be abundant in waterways during chemical runoffs. This then allows the cyanobacterium, which fixes atmospheric nitrogen, to feed the *Azolla*, allowing it to grow at great speeds [272]. This efficient trapping capacity also renders it ideal for phytoremediation, where heavy metals from polluted aquatic ecosystems can be removed, disposed, or recovered. Such an approach, which is inspired by the workings of biological scale-like structures that assist in directional frictional anchoring and trapping, is described here [273].

6.4.1 Materials and Methods

The substrate used was a typical submicron film supported on a silicon frame (Ted Pella Inc, Redding, CA, USA). The area to be worked on was fabricated from chemically robust, low-stress, planar silicon nitride (Si_3N_4) film and the area is supported by a rigid 3 mm silicon frame. The area of the thin film portion was 1.5 mm and its thickness was 200 nm. Focused ion beam milling was conducted using a FIB-SEM dual system (Helios Nanolab 600, FEI company, Hillsboro, USA). The ion beam voltage and current were kept at 30kV and 0.28nA respectively. The diameter of the scale-shaped fabricated

was $10\mu\text{m} - 20\mu\text{m}$ in which the cutting angle was fixed at 315° . The dwell time for each ion beam burst was kept at 10^5ns in which 5 passes were made. The total time taken to create each scale-like cantilever was 2 minutes and 30 seconds. After shaping the cantilever, its center was bombarded with the ion beam of the same accelerating voltage and ion current causing the scale to tilt downwards. Naturally, the dual FIB-SEM system used provided the advantage that each step of the fabrication process could be closely monitored within the same equipment.

Due to the flexible nature of the structures generated, contact methods to determine its 3D profile were not suitable. For this, an optical profilometer (Bruker, GT-K1) was used. The profilometer was loaded on a pneumatic vibration-isolation table (Newport) fitted with active high attenuation isolation and calibrated using step height standards (Bruker, Veeco). The area surrounding the cantilever was taken as the zero height from which the depth was determined. Analysis was done on the Vision 64 (Ver. 5.10) software.

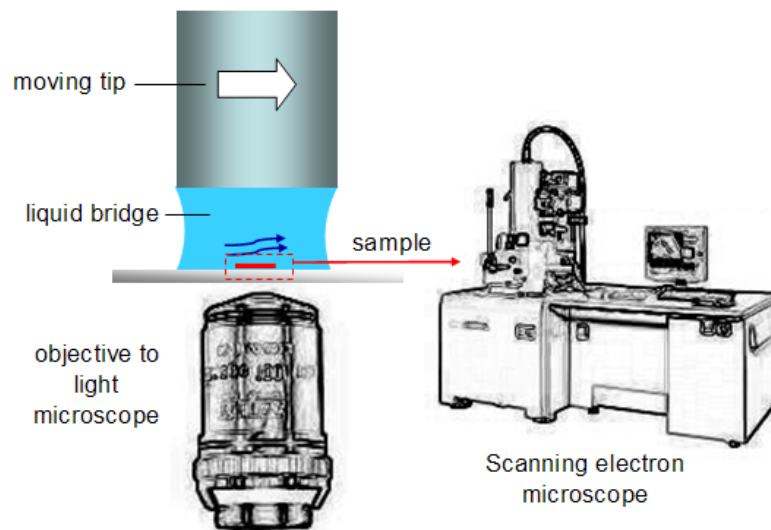


FIGURE 6.24: Schematic description of the ability to use a moving tip to trap particles in a liquid bridge on a structured substrate. A light microscope is useable to observe the trapping of the particles as they are still in the liquid medium. For higher resolution imaging, the sample is dried and placed in an SEM

For the FIB process leading to the creation of the cantilever structures, it is instructive to evaluate the interaction of ions with matter. To do this, we applied the computer programs associated with the Stopping and Range of Ions in Matter (SRIM). SRIM is based on a Monte Carlo simulation method, namely the binary collision approximation with a random selection of the impact parameter of the next colliding ion.

A natural question that comes to mind is whether there is any advantage in the structural creation of scale-like cantilevers. Using the mechanical design software Solidworks and

associated analysis packages, we modeled cantilevers that are rectangular and circular in shape with the finite element analysis (FEA) method. Four types of cantilever geometries were tested, including a rectangle of inverse aspect ratio (1.618:1) with the long edge fixed, a scale-like plate with 315° central angle fixed at the chord, a square cantilever, and a rectangle of aspect ratio (1:1.618) with the short edge fixed. Since the eventual goal was to accomplish cell trapping, the effective lengths were kept to the scale range matching that of cells. All the cantilevers were prepared on $25\mu\text{m} \times 25\mu\text{m}$, 200nm thick membrane models in Solidworks. The width of the kerf is related to the ion beam size and was speculated by observing the kerf width of fabrication product, which was approximately 200 nm.

The manner in which particles accumulate at the cantilever can be modeled as a delivery point in a spatially random manner in a plane. When the points make contact with the scale shape its ability to be retained or to move away can be related to the prescribed conditions imposed. This has some parallels with the way bulk granular materials, when poured onto a horizontal surface, form a conical pile [274]. The computer modeling should then essentially apply a cellular automata (CA) approach which is an alternative to continuum and discrete element models for predicting the flow of granular materials [275]. With this, the flow field can be divided into cells that each possesses a finite number of states. The current state of each cell is a function of its state and those of its neighbours at the previous time-step. This function is governed by update rules that define the interactions that can occur between particles moving around a lattice connecting adjacent cell centers. The rules themselves can incorporate mass and momentum conservation albeit in a simple, discrete manner.

The simulations are based on a robust block cellular automata algorithm. It assumes a basic neighbourhood interaction rule that is able to model basic piling and toppling of particles onto a surface. The particles are assumed to be uniform blocks of “mass ” that can conserve momentum and pile in a lattice structure. In this model we assumed that there are no inter-particle or surface forces. The lattice of cells (used in computation) is divided into non-overlapping blocks and the transition rule applied to a whole block at a time rather than a single cell. Block cellular automata are useful for simulations of physical quantities, because it is straightforward to choose transition rules that obey physical constraints such as reversibility and conservation laws. A 2×2 block rule set known as the Margolus neighbourhood [276], written in Matlab, was used to propagate particles that randomly appear above the obstacle surface. We consider each cell to be of a rectangular shape where the cell’s x and y dimensions dictate the repose angle. When run over a period of time, an equilibrium piling structure can be seen above the obstacle surface. This is then used as a basis to consider the piling behaviour.

The trapping experimentation on the substrate was conducted using $1\mu\text{m}$ polystyrene microbeads in suspension and gram-negative bacterial cells (*Klebsiella pneumoniae*) solution after glutaraldehyde fixation. Before the experiments were conducted, the membrane surface was washed by absolute ethanol and dried in air. The polystyrene beads, originally in solution at 10%v/v in deionized water, was diluted 50 times before being used. The isolated bacteria *Klebsiella pneumoniae* was cultured and incubated until it reached approximately 10^8CFU/mL (colony-forming units per milliliter). The samples were then fixed with 2.5% glutaraldehyde in phosphate-buffered saline (PBS) for 20 min and stored at 4°C based on safety protocols. Glutaraldehyde cross-links the proteins of cells and is standard chemical used in fixation. Fixation is a chemical process by which biological cells are preserved from decay, thereby preventing autolysis or putrefaction. Fixation terminates any ongoing biochemical reactions, and may also increase the mechanical strength or stability of treated cells. Prior to conducting the experiments on the fabricated scale structure, the cells were washed two times with Milli-Q water and re-suspended in Milli-Q water to remove only the supernatants. Hence, the bacteria concentration remained at 10^8CFU/mL during the tests. There are no salts existing in the solution that can be deposited. During the test a manual pipette was used to dispense $100\mu\text{L}$ of each solution onto the substrate as a drop. In the experiments, a tip was placed to contact the drop such that it created a liquid bridge (see. Fig. 6.24). As the tip was moved, it could create a flow within the liquid bridge [177, 178], from which the fabricated shape on the substrate could trap the contents. Two imaging modes are used. In one, the substrate was allowed to completely dry before it was placed into a scanning electron microscope for imaging. In another mode, the substrate, whilst still in liquid medium, is imaged directly using an inverted optical microscope (Nikon Eclipse E200) with a $40\times$ objective.

6.4.2 Results and Discussion

The SEM image of a typical cantilever that has been manufactured correctly using the FIB is shown in Fig. (6.25a). The small ion beam size and translational precision made it possible to shape the cantilever out with good definition. Using a higher ion beam current, to speed up processing, resulted in a warped shape of the cantilever (Fig. 6.25b) due to locked-in induced stresses. The measured profile of the cantilever and of its surroundings is given in Fig. (6.27a). It can be seen that the surrounding surface was maintained planar except for the machined-out shape. From a horizontal profile section measured (Fig. 6.27b), it can be seen that a regular tilting of the cantilever at 6 degrees could be achieved. We inspected the vertical profile sections and found almost

no warping of the cantilever. This demonstrates that locked-in induced stresses were limited, making it possible to create good working shaped cantilevers.

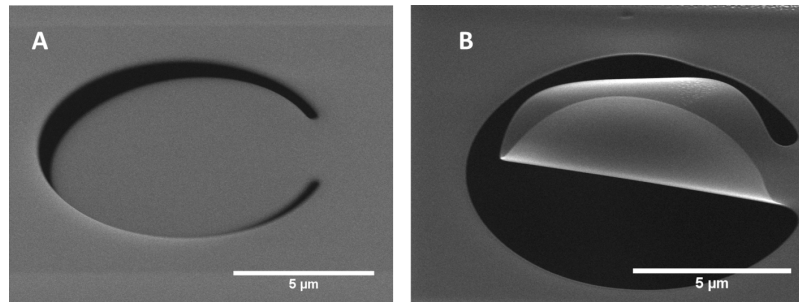


FIGURE 6.25: Precision ion beam machining with the right parameters which creates a well structured scale-like cantilever in (a). The use of a too large diameter ion beam can produce warping in the cantilever as shown in (b)

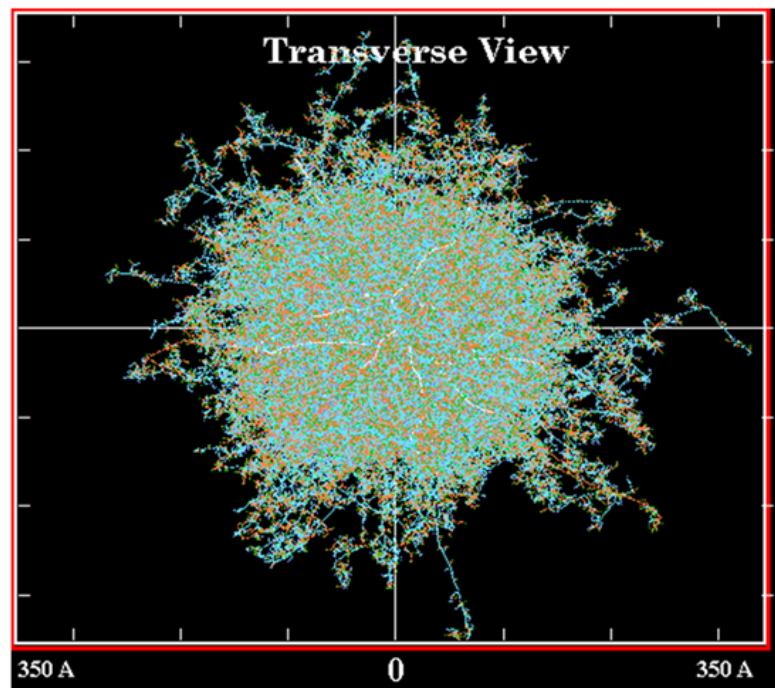


FIGURE 6.26: SRIM simulation of 1000 Ga ion against Si_3N_4 monolayer. The pattern of ion ablation is nearly circular. Due to this the ends of the cut were smooth despite the kerf size being 200nm.

The ion-structure interaction was simulated using SRIM by impinging 1000 Gallium (Ga) ions on a Si_3N_4 substrate. The results of this simulation is shown in Fig. (6.26), where it can be seen that the interaction volume of the ion implantation on the material surface was limited to 30 nm. This translates to the volume on the target surface that is affected by the energetic Ga ions, thus indicating that the ions bombarded only a small extent of the surface each time during the cut out process. The highly localized

ion processing area resulted in smooth edges where the milling terminated despite the kerf size being limited to 200 nm (see Fig. 6.25).

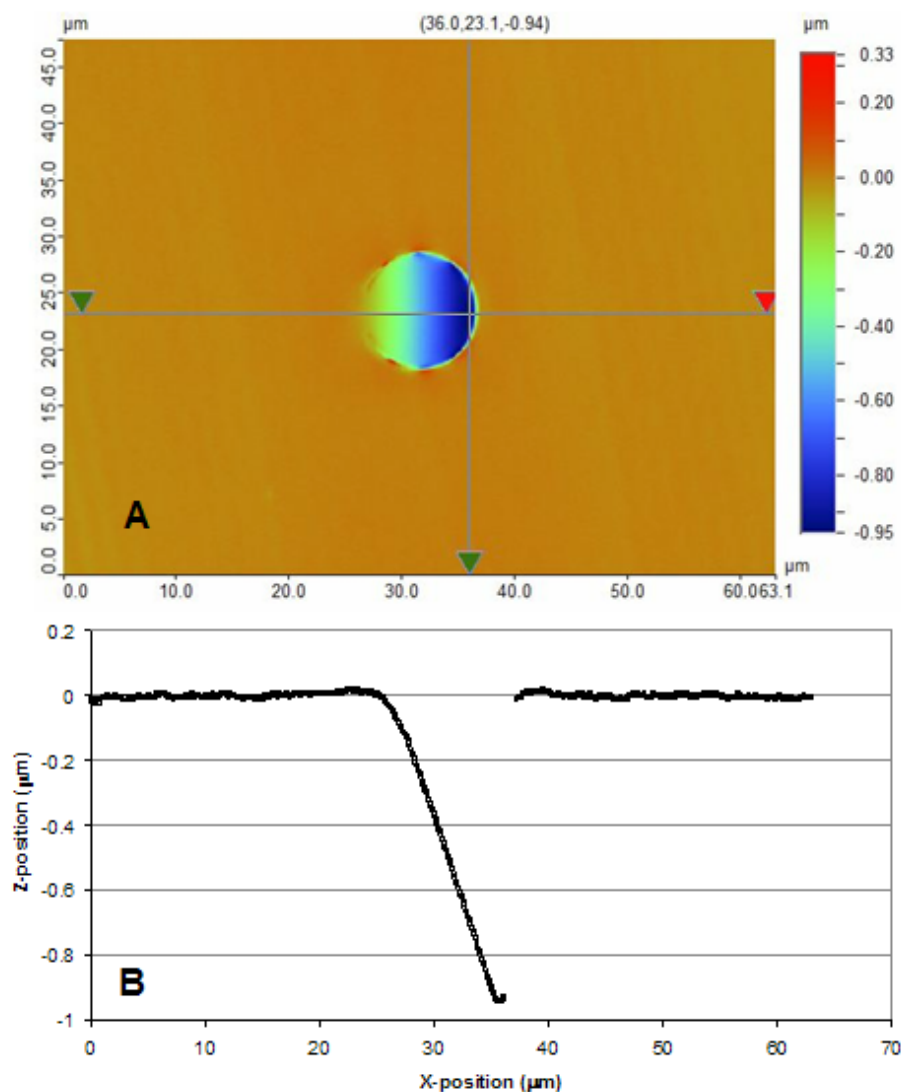


FIGURE 6.27: Optical profilometry (a) map of the fabricated cantilever which shows good topographic control in the manufacture. Taking a (b) central horizontal section of the created cantilever shows a tilt of angle 6° .

The mechanical properties of silicon nitride based cantilevers, produced by low pressure chemical vapour deposition (LPCVD) technique, were analyzed using FEA modeling. A 1kPa normal pressure was applied to all the membrane surfaces with the cantilevers resting at the equilibrium position. The stress distributions of the four types of cantilevers together with the resultant deformation is shown in Fig. (6.28). In all cases, it can be seen that the corners of the fixed end experienced the highest levels of stress concentrations and the mode of deflection was regular. From the probability density function of the stress values shown in Fig. (6.29), all the four data sets conform to the log-normal distribution with a goodness of fit value (also often referred to as the p-value)

of larger than 0.98. Furthermore, it can be seen that the majority of stress values range between 0 to 3MPa.

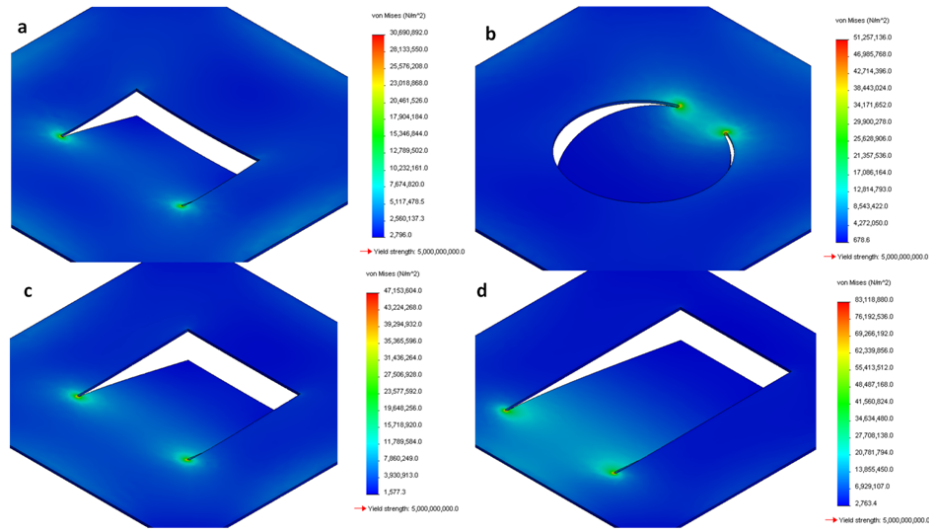


FIGURE 6.28: FEA stress analysis results of (a) rectangular cantilever with inverse aspect ratio 1.618:1; (b) scale-like cantilever with 315° central angle; (c) square cantilever; (d) rectangular cantilever with aspect ratio 1:1.618. The effective lengths are kept at $10\mu\text{m}$ in all cases. The corners of the fixed end are clearly areas of high stress concentration from a similar force imposed on all nodes.

Fig. (6.30a) depicts the stress distribution as a statistical box plot at the edges when a 1kPa normal pressure is applied. The box indicates data points that are between the first and third quartiles, while the asterisks denote values that are 1.5 times larger than the third quartile. Despite the first and third quartiles of stress for the rectangular cantilever (1.618:1) being in the same region, the asterisks indicate a large amount of stress values that are over 50MPa, which when correlated with Fig. (6.28) occur mostly near the region where the cantilever and membrane are connected. This eliminates the rectangular shaped cantilever with the short edge fixed from any trapping application. The thin and fragile membrane is thus prone to fracture under higher stresses and this has also been experimentally experienced from time to time during the handling of the membrane in solutions containing particles and bacteria.

Although the rectangular cantilever fixed at the long edge exhibited the lowest amount of stress, this geometry is difficult to fabricate if the process were to be scaled down, in particular when the effective length of trapping for the cantilever needs to be reduced to about $1\mu\text{m}$. This is because manufacturing of the shorter sides in the sub-micron range will be especially challenging. The stress values of the scale-like and square cantilevers were close to each other. Nevertheless, the square cantilever has two more weak points located at right angles to the cut (4MPa). Furthermore, the stresses along the edges of the scale-like cantilever were more evenly distributed. The box plots in Fig. (6.30b)

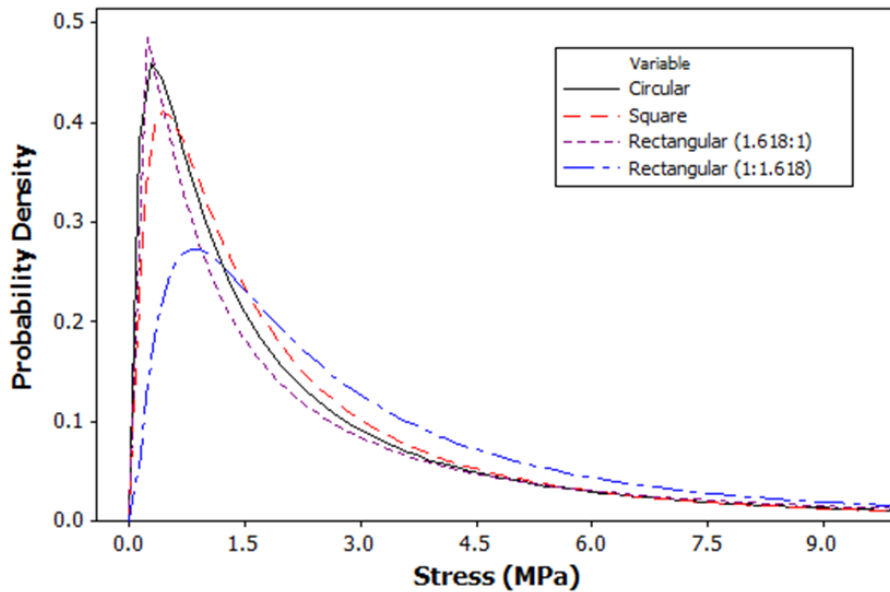


FIGURE 6.29: The probability density function of stress distributions for the four different types of cantilevers modeled. These curves indicate a goodness of fit value (also often referred to as the p-value) of larger than 0.98. They indicate that the majority data of circular and square cantilever stress values range between 0 and 3MPa.

alternatively depict the deflection of points at the edges when a 1kPa normal pressure was applied. Here, it can be seen that despite the extreme stress of the rectangular cantilever (1:1.618) appearing to be the smallest, it only undergoes a limited deflection under the same pressure as shown in Fig. (6.30b). Thus a higher pressure is required to produce the necessary deflection to trap cells.

Fig. (6.31) provides the maximum stress and tip deflection change with the central angle of circular cantilever under 1kPa normal pressure. It can be inferred that there was a direct correlation between the membrane response in terms of maximum stress and deflection. This is an important result as it is typically desirable for the cantilever to deflect but not by too much when the forces are applied. Increasing the deflection will generally enable larger particles to be trapped by essentially creating a taller obstacle. This will entail changing the central angle should the effective length be held constant. A major advantage of the scale-like cantilever is that the degree of deflection can be simply altered by changing the central angle. Hence the performance of the cantilever can be manipulated easily without changing the length-scale of the cantilever too much.

As a result, a scale-like cantilever is favoured not only in a biomimetic context, but also in terms of limiting stress, attaining the right amount of deflection, and the ease of structural strength manipulation. It should be noted, however, that the maximum stress developed during fabrication is also increased, which increases the likelihood of fracture failure. Consequently, there are limits to trying to keep the effective length

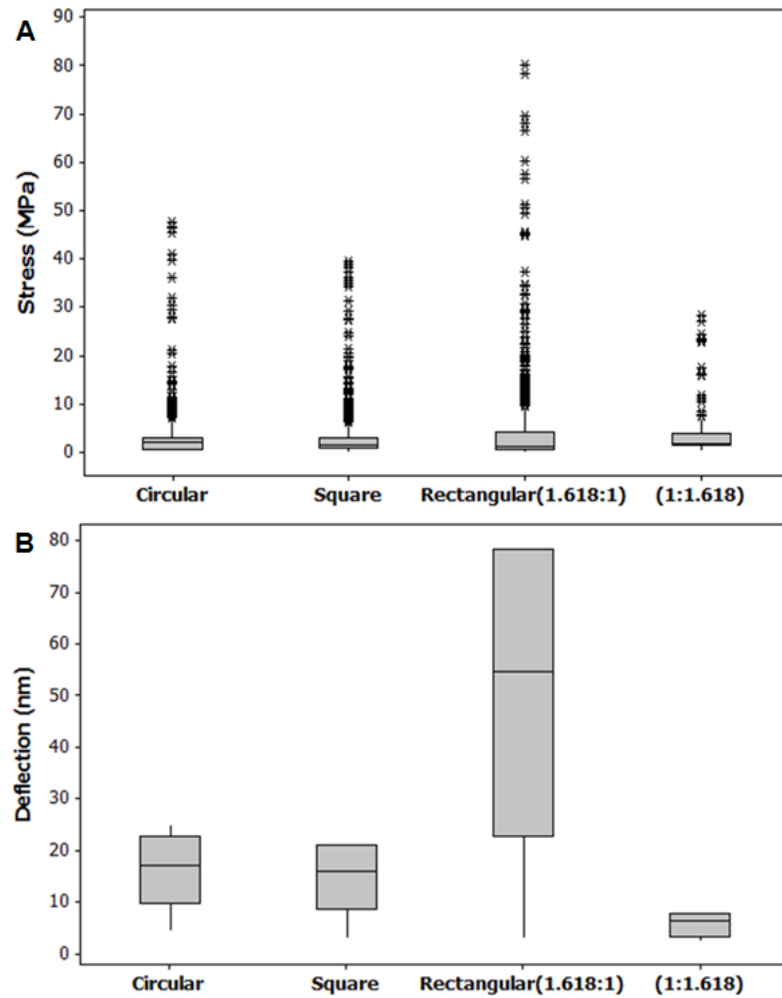


FIGURE 6.30: (a) Box plots of the stress distribution for the edge of cuts with 1kPa normal pressure for the four different types of cantilevers simulated. The box includes the data points between first quartile and third quartile of the data set, while the asterisks are values larger than 1.5 times of third quartile. With the (b) box plots of deflection of points around cantilever edges with 1kPa normal pressure the number of data points larger than 1.5 times of third quartile was substantially lower

constant to trap larger particles. Fig. (6.31) also shows the relation between the normal pressure and opening angle of a same size cantilever predicted by FEA simulation in Solidworks. The opening angle of the cantilever increases with increase in the normal pressure. A 6 degrees cantilever deflection, for instance, can be achieved by applying approximately 45kPa of normal pressure, which translate to the momentum of Ga ions accelerated by a voltage of 30kV and ion current of 0.28nA with $1\mu\text{s}$ exposure. It should be noted that this approximation is interpolated from the nominal mechanical properties of the membrane available in literature. In practice, a portion of ion momentum could be dispersed during sputtering, resulting in the lock-in stresses in the structure which could affect the measurement. It is plausible that the actual Young's modulus of the membrane could first be determined using AFM force spectroscopy. This may then provide a more

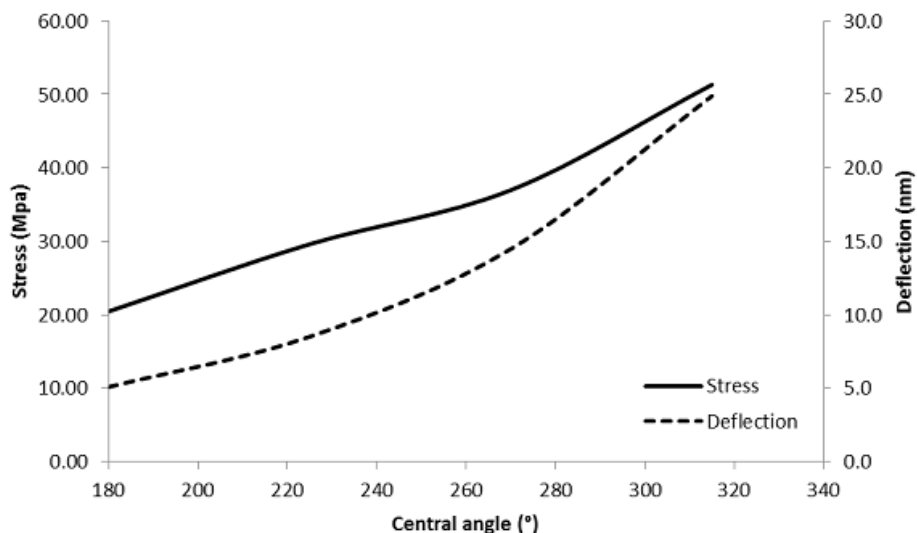


FIGURE 6.31: Distributions of the maximum stress and tip deflection change with the central angle of the circular cantilever under 1kPa normal pressure. The trends show that control of deflection through the right ion beam delivery should also be considered in relation to the maximum stress developed.

empirical depiction of the cantilever's deflection from the ion beam bombardment. From an application perspective, the size of particles to be trapped will be proportional to the deflection of the cantilever. For a given effective length, this will dictate the central angle and the maximum stress during fabrication. These factors guide the effective length and thus size of the cantilever to be used.

At this stage, it is pertinent to mention that we assume that the process of machining the cantilever shapes out will result in small residual stresses since the interaction volume is limited to 30nm. After the cantilever shape is cut out, a dose of Ga atoms bombards the cantilever to bend it. Hence, the momentum of the Ga atoms is taken to be responsible in generating the uniformly distributed normal pressure which causes the cantilever to deflect to the position that is useable for trapping. Admittedly, a certain degree of spring back will occur. We however assume that this is negligible. We note that since a dose of ion beam was used to cause the cantilever to bend, the amount of deflection could conceivably be adjusted by the beam strength. The level of control this way however will likely not be that good. We envisage that the additional positioning of a physical block behind the cantilever may be a better way to limit the deflection and thus fix the central angle.

With a random delivery of simulated particles on the scale-like obstacle, the piling was found to form a triangular collection (see Fig. 6.32 top). This was not surprising as this was essentially a conversion from a cone collection in the 3D case. The equilibrium triangular shape was dependent on the ability of each point to remain in relation to

the slope condition that it has been programmed to withstand. This condition, also called the angle of repose, is the steepest angle of descent of the slope relative to the horizontal plane when piled material on the slope face is on the verge sliding. This condition was imposed through the cellular automata algorithm to better represent the maximum piling height achieved on the circular surface for a given angle of repose. The plot given at the bottom of Fig. 8 shows the normalized parameter of height of the pile h against obstacle radius R , to observe an increasing trend with the repose angle θ .

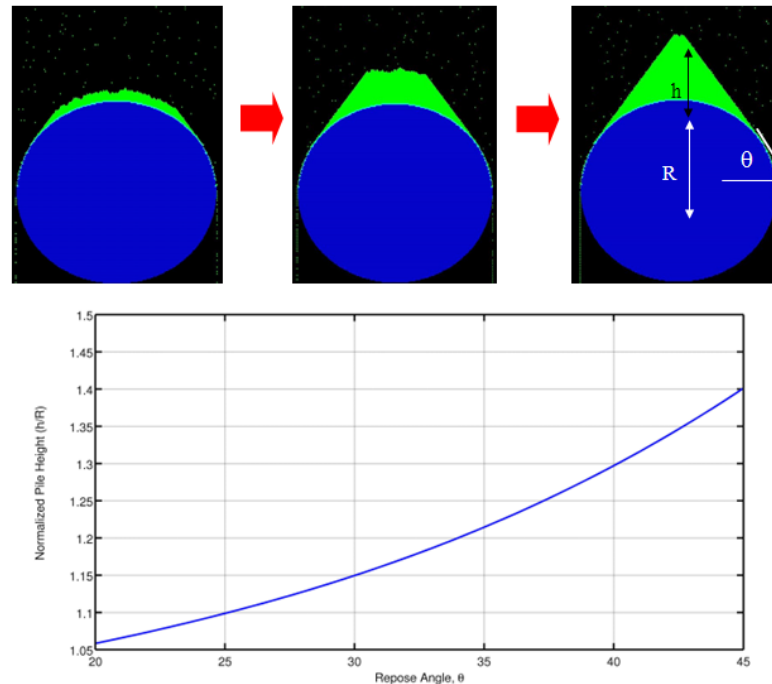


FIGURE 6.32: Snapshots (top) of the simulation of the piling process in progress which leads to a triangular collection. The piling characteristic is described by the height of the pile h , in relation to the radius of the obstacle R , and the repose angle θ . The results from simulated piling indicate that the equilibrium triangular shape was dependent on the ability of each point to remain in relation to the slope condition that can be withstood. The plot (below) shows a normalized parameter of height of the pile h against obstacle radius R , to follow an increasing trend with the repose angle θ .

Experimental verification of the trapping ability is shown in Fig. (6.33) for polystyrene beads and the fixed *Klebsiella pneumoniae*. In the case of polystyrene beads, the basic triangular piling structure was observed. However, an extended tail and a fanning out around the obstacle were also evident. This can be attributed to the aggregation tendency of polystyrene beads that acts on top of the piling behaviour. Some factors influencing aggregation are size and concentration, surface charge level, and the nature and concentration of ions in the suspending medium.

A different scenario is played out with the bacteria sample. Here, the triangular pile up before the cantilever is absent. It can be seen, however, that the bacteria cells were

able to slip inside the cantilever's opening despite the size of the bacteria being larger than the gap. This leaves us to conclude that the cells, unlike the beads, were more pliable and thus able to accomplish this. Recent investigations have found that, due to the structural and compositional heterogeneity of bacterial cell surfaces, the softer outer layer tended to deform in order to concentrate the stress toward the more rigid, hard core [277]. Furthermore, the ability of bacterial cells in general to flatten themselves out considerable while still avoiding structural damage lends itself to this observation.

The squeezing into the gap was also likely the contributing factor for the absence of the triangular pile up. Under reverse flow conditions, the ability to trap was decreased significantly for both beads and bacteria (see Fig. 6.33c,d). Hence, scale-like cantilevers offers a directional trapping feature in relation to the flow and orientation of the cantilever. It should be noted that the samples in Fig. (6.33) were recorded using an SEM. As such the substrate surface appears opaque. In reality, the substrate is thin and will permit viewing of its underside with an optical microscope. Hence, while the bacteria may be able to squeeze into the gap of the cantilever, they can still be imaged, thus allowing biochemical analysis modes to be implemented.

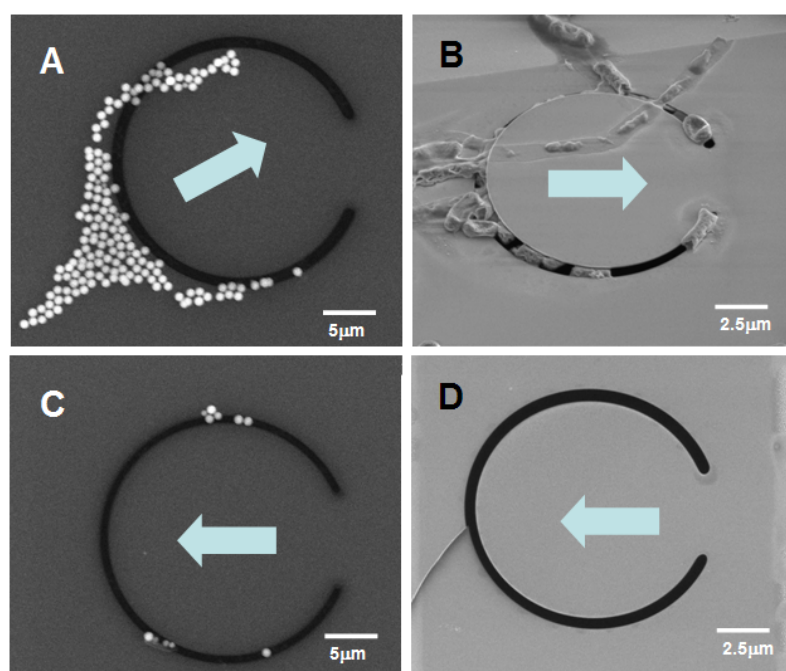


FIGURE 6.33: Experimental record of the trapping of $1\mu\text{m}$ polystyrene beads using the scale-like cantilever in (a) which shows piling with particle aggregation. The trapping of bacterial cells in (b) shows capacity to slip into the gap of the cantilever despite the size of the bacteria being larger. The directions of the flow in all cases are indicated by arrows. When the direction of flow was reversed with the $1\mu\text{m}$ polystyrene beads (c) and bacterial cells (d), there was diminished trapping ability. This demonstrates a directional trapping capacity.

To permit the substrate to remain in the liquid media we utilized the optical microscopy imaging to ascertain the consistency of trapping. Naturally, the image sharpness from optical microscopy is lower but nevertheless allows the measurement of trapping efficiency (Fig. 6.34). Fig. (6.34c) presents the number of particles trapped by the cantilever from a series of ten runs. In every run, the beads were reliably trapped, showing consistency and practicability of the approach. The average number of particles trapped was 67 beads with a standard deviation of 17. The significant number of beads trapped infers feasibility in using this approach as a platform for developing biochemical analysis applications.

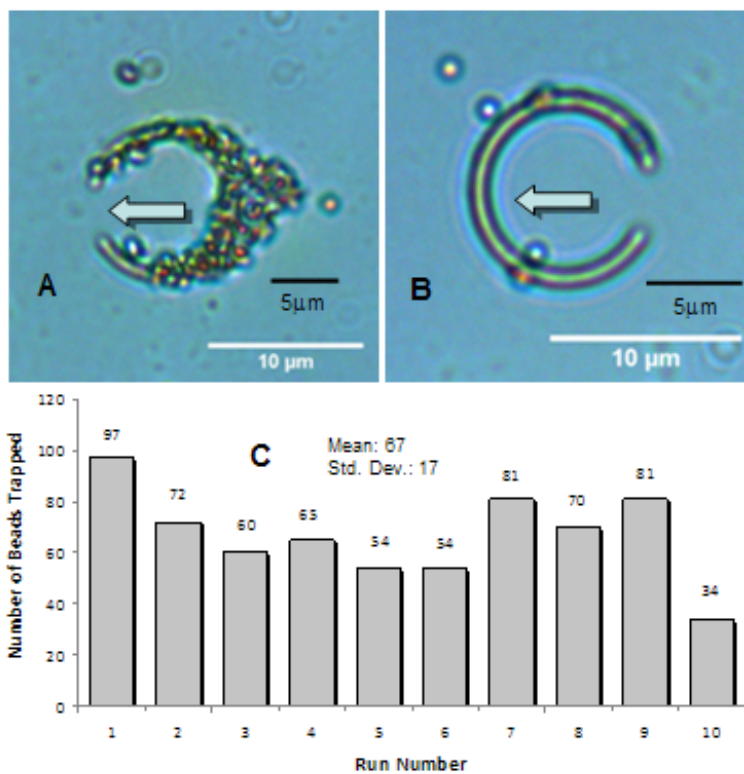


FIGURE 6.34: Typical optical microscopy images recorded of the $1\mu\text{m}$ polystyrene beads in liquid interacting with the scale-like cantilever where flow in one direction traps them (a) while flow in the opposite direction clears them off (b). For the flow causing the particles to be trapped, the distribution of the number of beads at each run, indicated in (c), has an average of 67 beads trapped with a standard deviation of 17.

The ease with which trapping could be done here using an open flow generation arguably offers an ability to create simpler cellular analysis devices. In doing so, it presents a different pathway to creating devices in applications such as the capture of circulating tumor cells, in which 3D-nanostructured substrate coated with cancer cell capture agents are effective but typically applied within closed channel fluidic networks [278]. The recent ability to concentrate particles at the moving contact line even as a drop undergoes a

squeeze flow from a sandwich [279, 280], coupled with nanostructures created at the scale-like interface are possible future developments for this trapping approach. This could also benefit from the feature of low sample loss when highly non-wetting elements are used to generate the squeeze flow [154]. Care, however, has to be exercised that when the three-phase contact line travels over the cantilever, so that surface tension does not cause the cantilevers to bend excessively and fracture. It is conceivable that any structures patterned on the surface that impede flow are also workable. However, the formation of these structures in the micron and nanometer scale will typically require a photolithographic process involving chemical etching. The approach here is simpler to execute and does not involve any wet processing steps which create effluents that harm the environment.

6.4.3 Conclusion

The construction of a scale-like cantilever on chemically robust, low-stress, planar silicon nitride film supported by a rigid silicon frame using focused ion beam machining is described. Through SEM and optical profilometry imaging, the approach was found to be able to create regular tilting of the cantilever with almost no warping of the cantilever. With Monte Carlo simulation based on SRIM, it was found that the interaction volume of the ions on the material surface was limited to tens of nanometers. This accounted for the ability for the edges of the ion beam milling termination to be smooth despite the kerf size limited to 200 nm. Finite element analysis showed stress concentrations to be located mostly near the regions where cantilever and membrane were connected. The scale-like cantilever was found to be the best architecture in terms of limiting stress concentration without difficulty in manufacture and having stresses more evenly distributed along the edge. It also had a major advantage in that the degree of deflection can be simply altered by changing the central angle. Hence the dynamic performance of the cantilever can be manipulated easily without varying the length-scale of the cantilever too much. From a piling simulation conducted, it was found that a random delivery of simulated particles on to the scale-like obstacle should create a triangular collection. In the experimental trapping of polystyrene beads in suspension, the basic triangular piling structure was observed, but with extended tail and a fanning out around the obstacle. This was attributed to the aggregation tendency of polystyrene beads that acts on top of the piling behavior. In the case with fixed bacterial cells, the triangular pile up behind the cantilever was absent and the bacteria cells were able to slip inside the cantilever's opening despite the size of the bacteria being larger than the gap. This meant that the cells, unlike the beads, were more pliable and thus able to accomplish this. In ascertaining the consistency of trapping over 10 runs, the average number of particles

trapped was 67 beads with a standard deviation of 17. The significant number of beads trapped infers feasibility in using this approach as a platform for developing biochemical analysis applications. Overall, the scale-like cantilever, which is inspired biologically, has been found to offer a viable way to trap small populations of material in suspension in an open access manner.

6.5 Chapter Summary

In this chapter, we investigated and established a novel approach to dispense droplets using the spray from an acoustic nebulizer to deposit onto a superhydrophobic receptacle. Using a precise weighing scale precise drops of volumes were achieved. The volume dispensed was found to vary linearly with the operation time of the nebulizer.

We also investigated the feasibility of using the capillary bridges developed between solid bodies to interrogate the contact angle development under the effect of evaporation. The experiments showed that the contact angle versus time trends roughly comprise two linearly reducing rates; one slower followed by one that is faster. The difference is more pronounced with silicone as oppose to glass and silanized glass. This caused a strong departure from volume reduction linearity using silicone. By using the geometrical equations and approximate parameter changes, the length change was found to be above two times the cross sectional area change of the capillary during evaporation. The results here indicate that when evaporation is significant, creating capillary bridges for the transparency microplates offer the best ability to retain volumes while allowing the contact angle to be interrogated.

Finally, a biologically inspired scale-like cantilever was developed to trap particles. The scale-like cantilever was found to be the best architecture in terms of limiting stress concentration without difficulty in manufacture and having stresses more evenly distributed along the edge. In the experimental trapping of polystyrene beads in suspension, a basic triangular piling structure was observed, but with extended tail and a fanning out around the obstacle. In the case with fixed bacterial cells, the triangular pile up behind the cantilever was absent and the bacteria cells were able to slip inside the cantilever's opening despite the size of the bacteria being larger than the gap. Overall, the scale-like cantilever, was found to be a viable way to trap small populations of material in suspension in an open access manner.

The findings described in this chapter have been reported in the following publications:

1. B. Liu, J. Fu, A. Somers, M. Muradoglu, T.W. Ng, Scale-like cantilever cell traps. RSC Advances. 4 (2014) 2652-2660, enclosed in Appendix (B.9).

2. T. Hunyh, M. Muradoglu, O.W. Liew, T.W. Ng, Contact angle and volume retention effects from capillary bridge evaporation in biochemical microplating. *Colloids and Surfaces A: Physicochemical and Engineering Aspects*. 436 (2013) 647655, enclosed in Appendix ([B.8](#)).
3. T. Vuong, A. Qi, M. Muradoglu, B.H.-P. Cheong, O.W. Liew, C.X. Ang, J. Fu, L. Yeo, J. Friend, T.W. Ng, Precise drop dispensation on superhydrophobic surfaces using acoustic nebulization. *Soft Matter*. 9 (2013) 3631-3639, enclosed in Appendix ([B.6](#)).

Chapter 7

Conclusions

The primary area of investigation in this thesis was the development of particle manipulation mechanisms using nano-optic technologies. Two technologies, specifically, the optical tweezer and plasmonics were extensively numerically modeled to further investigate and design nano-optic devices capable of particle manipulation. The numerical methods employed were the Generalized Lorenz-Mie Theory (GLMT) and Finite Difference Time Domain (FDTD) methods. This allowed for the precise simulation of Maxwell's equations in the micro-nano scale fully capable of all nano-optic phenomena that occurs at that scale (See Chapter 3). Having established these models, the force exerted by an optical tweezer at points much beyond and below the focal point were successfully calculated (Chapter 4.2). The results showed that by locating the focus of the beam either above or below the subject matter, a push or pull, relative to the beam axis, was observed. Further experimental results confirmed these findings. The ability to push particles in this rather simple way, provided an effective way to transport particles drastically reducing the chances of photodamage to living matter that can typically occur with conventional optical tweezers. Expanding on this idea, it was shown that these findings provided a means to develop a gentle and tunable stirring effect on particles. The simulations, which included the effects of liquid dynamics, showed that by moving a medium containing particles past a laser beam arranged in the manner discussed, the expected global and local deflection trajectories could be seen to stir particles. Experiments using polystyrene microbeads and red blood cells further confirmed the optical stirring effect. It is envisaged that this approach portends the capability to provide mechanical stimuli to cells in a small liquid volume bioreactor that is free of flow. Essentially, this provides a better realization of lab-on-a-chip systems.

Next, a comprehensive computation comprising approximately 1,960,000,000 scattering combinations of particle radius r , refractive index ratio and numerical aperture of the

beam was conducted. For each configuration, a further scan to determine the axial trapping efficiency revealed an interesting optical trapping landscape. The iso-surface of the landscape followed a clam-shell like contour with ridges that offered a way to engineer applications by controlling the parameters used. It was observed that there was a significant volume space based on specific parameter combinations that did not allow optical trapping. Typically, these regions were in agreement with conventional models. However, more interestingly, there were sharp ridge (finger-like) regions in the parameter space that permitted trapping unlike previous models. The investigation showed that in these ridge regions an interference condition was being excited that reduced the electromagnetic backscattering of the particles thus permitting trapping.

Furthermore, by examining specific points in the computed parameter volume space, we uncovered difficulties in using the trapping efficiency and stiffness metrics to define how well particles were drawn into and held in the trap. An alternative calculation based on the maximum forward and restoration values of the trapping efficiency in the axial sense, which we called the trapping quality, provided a more practical metric. Essentially, this was a measure of how symmetric the potential well was. Having observed these features a number of manipulation mechanism that exploited them were proposed. Firstly by exploiting the high specificity of the ridge regions, i.e. small parameter changes can mean particles are trapped or freed, a mechanism for effective particle sorting was shown. Secondly, the optical trapping blind spots were shown to be advantageous in applications that use optical forces for particle translation and not trapping. Finally, the optical trapping map generated was shown to be useful in multiparameter change dynamics, such as the trapping of a swelling particle that could be used for drug delivery.

To conclude the work done in optical particle manipulation, a corrugated structure was designed to sustain a surface mode excited by a subwavelength aperture as shown in Chapter (4.3). By carefully placing a secondary grated structure some distance from the original structure to facilitate phase matching, a strong reflection of the surface mode was produced, creating a strong optical standing wave field that could be harnessed for particle trapping. This concept was demonstrated in the form of linear field traps. With careful design, the ability to create optical traps of various geometries using the same principles is envisaged.

Moving onto the first support area in this thesis, that being Brownian dynamics, an investigation into a new technique to sort nanometer scale Brownian rods was demonstrated in Chapter (5). By exploiting the Brownian motion of these rods and using an asymmetric potential, a two stage sorting process could be used to isolate particles with specific dimensions. Simulation results showed that rods with diameters ranging from 72 to 168 nm and a range of lengths from 528 to 969.6 nm could be sorted to achieve at least

80% separation within two hours. Furthermore, a novel means to sense a nanoscale environment was developed by using a surface plasmon based optical resonator to sense the nanoscale environment from the Brownian perturbations of nanorod that was tunable drawn to a cylindrical pillar (resonator) by attractive forces. Using simulations of an optical resonator that comprises a 40 nm inner dielectric refractive index of 3.4 core with a 10 nm outer gold shell, and driven by a Gaussian beam with center wavelength 550 nm, noticeable resonance was found at 525nm. At this resonance wavelength, however, there was very little dependence on the gap value. A one dimensional summed difference expression $W_n^{(0,q)}$ was derived to show that there was a distinct change in transmission at 600 nm across all angles of orientation when the gap changes from contact to non-contact or vice-versa. This meant that operation at this wavelength would produce a noticeable transmission change when there was contact regardless of nanorod orientation. In analyzing the Brownian driven movement, two distinct states that define the position of the nanorod in relation to the cylindrical pillar are when the nanorod was moving freely (state I) and when the nanorod was contacting the cylindrical surface (state II). The metric f , which defines the proportion of incidence when the nanorod was in state I, was found to reduce when there was an increase in magnitude of forces. The distinct S-shape trends of plots f against normalized charge magnitude indicated that there were ranges in the normalized charge products in which relatively good linear sensitivity responses were possible. At these regions, the Pearson product-moment correlation coefficients were found to be above 0.98. In correlating to the temperature T , df/dT was found to be maximal when the normalized charge product value was -200. From an uncertainty estimation conducted, a restriction of the uncertainty to one standard deviation (which corresponds to 0.5K) will require 744,344 and 657,492 sample points to be observed in states I and II respectively. Based on camera recordings made at 50 fps, this will require monitoring the rod for 14,887 and 13,150 seconds in states I and II respectively but with standard photo-detectors with 50MHz sampling rate, the monitoring times are lowered 0.015 and 0.013 seconds instead. The approach that was developed offered significant advantage in the ability to sense temporally changing environments.

The final support area in this thesis was Discrete Liquid Mechanics. In Chapter (6), a novel approach to dispense droplets using the spray from an acoustic nebulizer to deposit onto a superhydrophobic receptacle was shown. Using a precise weighing scale precise drops of volumes were achieved. The volume dispensed was found to vary linearly with the operation time of the nebulizer. In developing the superhydrophobic surface, it was identified that a galvanic displacement mechanism in an electroless deposition process occurred in which the silver cations in solution were reduced just as copper from the surface was oxidized and was responsible for creating the micro- and nano-scaled structures that endow superhydrophobicity on the copper substrate. A time dependent

morphology change from granular to dendritic with longer immersion into the silver nitrate solution was found. This indicated that granular growth beyond a certain size was not feasible, although granular structures were more preferentially formed just after nucleation. The dendritic structure formation was likely due to the natural tendency of the process to maintain or increase the surface area to volume ratio not to limit the rate of deposition. An immersion for at least 7 seconds into the silver nitrate solution was all that was needed to ensure super-hydrophobicity of the surfaces. This allowed for the deduction that the dendritic structures were not needed to maintain the non-wetting characteristics, although they seemed not to have a role in modifying it.

Furthermore, the feasibility of capillary bridges developed between solid bodies to interrogate the contact angle development under the effect of evaporation was investigated. The experiments showed that the contact angle versus time trends roughly comprise two linearly reducing rates; one slower followed by one that is faster. The difference is more pronounced with silicone as oppose to glass and silanized glass. This caused a strong departure from volume reduction linearity using silicone. By using the geometrical equations and approximate parameter changes, the length change was found to be above two times the cross sectional area change of the capillary during evaporation. The results here indicate that when evaporation is significant, creating capillary bridges for the transparency microplates offer the best ability to retain volumes while allowing the contact angle to be interrogated.

Finally, a biologically inspired scale-like cantilever was developed to trap particles. The scale-like cantilever was found to be the best architecture in terms of limiting stress concentration without difficulty in manufacture and having stresses more evenly distributed along the edge. In the experimental trapping of polystyrene beads in suspension, a basic triangular piling structure was observed, but with extended tail and a fanning out around the obstacle. In the case with fixed bacterial cells, the triangular pile up behind the cantilever was absent and the bacteria cells were able to slip inside the cantilever's opening despite the size of the bacteria being larger than the gap. Overall, the scale-like cantilever, was found to be a viable way to trap small populations of material in suspension in an open access manner.

Appendix A

Formulas

A.1 Translation Addition Theorem

The translation addition theorem is used to translate a set of vector spherical harmonics from one coordinate system onto another coordinate system. The vector translation coefficients can be expressed in terms of the scalar translation coefficients $C_{n'}^{(m,n)}$ which can be found via various recursion relations. The starting point for calculating the scalar coefficients is

$$C_{n'}^{(0,0)} = \sqrt{2n'+1} h_{n'}^{(1)}(2k_1 d) \quad (\text{A.1})$$

From here, the relation

$$\begin{aligned} C_{n'}^{(0,n+1)} = & \frac{1}{(n+1)} \sqrt{\frac{2n+3}{2n'+1}} \left(n' \sqrt{\frac{2n+1}{2n'-1}} C_{n'-1}^{(0,n)} \right. \\ & \left. + n \sqrt{\frac{2n'+1}{2n-1}} C_{n'}^{(0,n-1)} - (n'+1) \sqrt{\frac{2n+1}{2n'+3}} C_{n'+1}^{(0,n)} \right) \end{aligned} \quad (\text{A.2})$$

can be used to calculate the elements $C_{n'}^{(0,n)}$. The remaining terms in the matrix can be calculated using the relation

$$\begin{aligned} C_{n'}^{(m,n)} = & \sqrt{\frac{(n'-m+1)(n'+m)(2n'+1)}{(n-m+1)(n+m)(2n'+1)}} C_{n'}^{(m-1,n)} \\ & - 2k_1 d \sqrt{\frac{(n'-m+2)(n'-m+1)}{(n-m+1)(n+m)(2n'+1)(2n'+3)}} C_{n'+1}^{(m-1,n)} \\ & - 2k_1 d \sqrt{\frac{(n'+m)(n'+m-1)}{(n-m+1)(n+m)(2n'+1)(2n'-1)}} C_{n'-1}^{(m-1,n)}. \end{aligned} \quad (\text{A.3})$$

It should be noted that

$$C_{n'}^{(m,n)} = C_{n'}^{(-m,n)} \quad (\text{A.4})$$

We can find the vector translation coefficients using

$$\begin{aligned}
A_{n'}^{(m,n)} &= C_{n'}^{(m,n)} - \frac{2k_1 d}{n'+1} \sqrt{\frac{(n'-m+1)(n'+m+1)}{(2n'+1)(2n'+3)}} C_{n'+1}^{(m,n)} \\
&\quad - \frac{2k_1 d}{n'} \sqrt{\frac{(n'-m)(n'+m)}{(2n'+1)(2n'-1)}} C_{n'-1}^{(m,n)}, \\
B_{n'}^{(m,n)} &= -\frac{2ik_1 m d}{n'(n'+1)} C_{n'}^{(m,n)}.
\end{aligned} \tag{A.5}$$

Finally the following relations are valid

$$\begin{aligned}
A_{n'}^{(-m,n)} &= A_{n'}^{(m,n)} \\
B_{n'}^{(-m,n)} &= B_{n'}^{(m,n)}
\end{aligned} \tag{A.6}$$

Appendix B

Peer reviewed Publications

B.1 Publication List

The following are the list of publications associated with this thesis.

1. M. Muradoglu, C.Y. Lau, I. Gralinski, T.W. Ng Nano scale environment sensing scheme with Brownian nanorod and plasmon resonator. *Plasmonics*. (2013)
2. M. Muradoglu, Constructing microstructures using the optical trapping map of dielectric spheres, *Proceedings of SPIE Micro+Nano Materials, Devices, and Systems-Melbourne* (2013)
3. B. Liu, J. Fu, A. Somers, M. Muradoglu, T.W. Ng, Scale-like cantilever cell traps. *RSC Advances*. 4 (2014) 2652-2660.
4. T. Hunyh, M. Muradoglu, O.W. Liew, T.W. Ng, Contact angle and volume retention effects from capillary bridge evaporation in biochemical microplating. *Colloids and Surfaces A: Physicochemical and Engineering Aspects*. 436 (2013) 647655.
5. M. Muradoglu, T.W. Ng, Optical trapping map of dielectric spheres. *Applied Optics*. 52 (2013) 3500-3509. Featured in June 2013 Issue of *Laser Focus World*.
6. T. Vuong, A. Qi, M. Muradoglu, B.H.-P. Cheong, O.W. Liew, C.X. Ang, J. Fu, L. Yeo, J. Friend, T.W. Ng, Precise drop dispensation on superhydrophobic surfaces using acoustic nebulization. *Soft Matter*. 9 (2013) 3631-3639.
7. M. Muradoglu, T. Le, C.Y. Lau, O.W. Liew, T.W. Ng. Optical stirring in a droplet cell bioreactor. *Biomedical Optics Express*. 3 (2012) 2465-2470.

8. M. Muradoglu, W.S.-Y. Chiu, T.W. Ng Optical force lateral push-pulling using focus positioning. *Journal of the Optical Society of America B.* 29 (2012) 874-880.
9. M. Muradoglu, T.W. Ng, A. Neild, I. Gralinski, Tailored leaky plasmon waves from a subwavelength aperture for optical particle trapping on a chip. *Journal of the Optical Society of America B.* 28 (2011)
10. I. Gralinski, A. Neild, T.W. Ng, M. Muradoglu, Sorting of Brownian rods by use of an asymmetric potential *Journal of Chemical Physics.* 134 (2011) 064514.
11. M.S. Muradoglu, A.R. Baghai-Wadji, T.W. Ng, Prospects of Wannier functions in investigating photonic crystal all-optical devices for signal processing. *Journal of the Optical Society of America A.* 27 (2010) 757-765.

B.2 Tailored leaky plasmon waves from a subwavelength aperture for optical particle trapping on a chip

602 J. Opt. Soc. Am. B / Vol. 28, No. 4 / April 2011

Muradoglu *et al.*

Tailored leaky plasmon waves from a subwavelength aperture for optical particle trapping on a chip

M. S. Muradoglu, Tuck Wah Ng,* Adrian Neild, and Ian Gralinski

Laboratory for Optics, Acoustics & Mechanics, Department of Mechanical & Aerospace Engineering, Monash University, Clayton, VIC 3800, Australia

Received September 21, 2010; revised January 4, 2011; accepted January 12, 2011; posted January 13, 2011 (Doc. ID 135322); published March 2, 2011

Optical forces available on a chip that possess features of strong trapping at the subwavelength scale, in a coplanar geometry, and at specific and selective locations portend many useful applications. We demonstrate here a two-pronged approach to accomplish this. First, the plasmon fields emanating from a subwavelength aperture are manipulated so that they leak maximally to the sides on a surface through the use of tailored corrugations. Second, the location of secondary corrugation at some distance permits reflection of these leaky waves, which, with the coherence property of light used, generate optical standing wave fields capable of strong optical trapping. The linear optical forces generated with this scheme are presented here. © 2011 Optical Society of America

OCIS codes: 020.7010, 240.6680, 240.3900.

1. INTRODUCTION

A long-standing goal in particular manipulation has been to have suitable optical forces available on a chip so that a variety of procedures can be accomplished [1,2]. While important inroads have been recently reported [3], major challenges remain in acquiring the ability to attain strong optical trapping (i) at the subwavelength scale, (ii) in a coplanar geometry, and (iii) at specific and selective locations over the entire chip. The use of evanescent fields, in particular plasmon fields emanating from a subwavelength aperture [4] or from a probe [5], have been shown to be effective for some time in addressing issues (i) and (ii). Recent advances reported have begun to tackle (iii) as well, which holds great promise for lab-on-a-chip purposes. A seminal scheme reported for this involved creating plasmonic standing waves from the interference of laser beams [6], which essentially translated the known ability of standing waves to trap effectively at multiple sites in the axial sense (to the light axis) [7,8] to a lateral geometry. Yet, the alternative approach of tailoring metallic surfaces to create multiple trapping sites from whole-field illumination [9–11] [Fig. 1(a)] has been shown to be more convenient and practical. To progress on to feasible lab-on-a-chip applications, nevertheless, it will be necessary to attain the ability to carry out trapping at selected spatial locations at prescribed time sequences. This will be conceivably difficult to accomplish using schemes that depend on the whole-field light stimulation of plasmons [9–11] unless the onerous challenge of creating fine and high-intensity probe beams is met. A more practicable solution, in our opinion, requires somewhat of a revisit of the evanescent trapping approach reported by Okamoto and Kawata over a decade ago [4].

The strong beaming of light from subwavelength apertures surrounded by surface corrugations on a thin metal film was first demonstrated by Lezec *et al.* [12]. Since then, there have been substantial efforts made to understand the underlying physics of the phenomenon [13–16] with the interest of facilitating directional light beaming at the chip level [17–19]. An

interesting discovery has been the contribution of leaky plasmon waves in affecting the characteristics of light beaming [16]. There has been no report of efforts, to the best of our knowledge, to harness these leaky waves to create tailored optical trapping sites on the metallic surface. The ability to do this opens up the avenue of having multiple apertures on the surface with light addressable waveguides within the chip in order to maintain close control of optical trapping at specific and selective locations over the entire chip [see Fig. 1(b)].

2. THEORY AND DESIGN

At an interface between a metal and a dielectric, as shown in Fig. 1, a strongly enhanced optical near field confined near the metal surface can be excited. The wave vector of the surface plasmon field k_{spp} is given as

$$k_{\text{spp}}^2 = \frac{\epsilon_1(\omega)\epsilon_2(\omega)}{\epsilon_1(\omega) + \epsilon_2(\omega)} \left(\frac{\omega}{c}\right)^2, \quad (1)$$

where ω is the angular frequency and c is the speed of light. The wavelength of the field can be approximated by

$$\lambda_{\text{spp}} \approx \sqrt{\frac{\text{Re}\{\epsilon_1(\omega)\} + \text{Re}\{\epsilon_2(\omega)\}}{\text{Re}\{\epsilon_1(\omega)\} \cdot \text{Re}\{\epsilon_2(\omega)\}}}. \quad (2)$$

The terms $\epsilon_1(\omega)$ and $\epsilon_2(\omega)$ represent the complex frequency-dependent dielectric function of the metal and dielectric, respectively. In the case of noble metals, such as silver (Ag), there are two types of contributions to the dielectric constant of the metal; one is from the inner d electrons, which describe interband transitions, and the other is from the free conduction electrons. The latter contribution can be modeled by applying the Drude–Sommerfeld theory for free-electron gas [20], which produces the Drude model solution of

0740-3224/11/040602-06\$15.00/0

© 2011 Optical Society of America

Muradoglu *et al.*

Vol. 28, No. 4 / April 2011 / J. Opt. Soc. Am. B 603

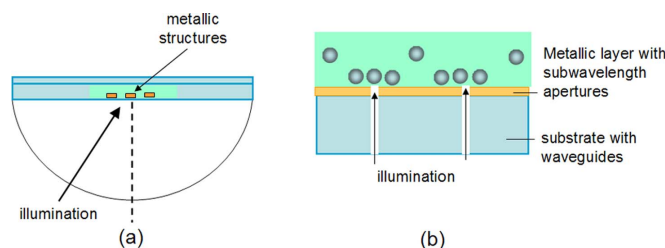


Fig. 1. (Color online) (a) Optical scheme of illuminating metallic structures in a whole-field manner to create localized plasmon field for trapping [9–11]. (b) Envisaged approach of having illumination delivered from individually addressable waveguides within a substrate to subwavelength apertures in the metallic layer to create switchable surface plasmon sites for trapping, which in the process will facilitate many lab-on-a-chip procedures.

$$\frac{d\mathbf{P}_{\text{mec}}}{dt} + \frac{d\mathbf{P}_{\text{field}}}{dt} = \int_s \vec{\mathbf{T}} \cdot \mathbf{n} ds. \quad (5)$$

In Eq. (5), \mathbf{P}_{mec} , $\mathbf{P}_{\text{field}}$, and $\vec{\mathbf{T}}$ refer to the mechanical momentum, the total electromagnetic momentum, and Maxwell's stress tensor, respectively. At optical frequencies, the time-averaged electromagnetic momentum is zero over one oscillation imparting the force as

$$\begin{aligned} \langle \mathbf{F} \rangle &= \left\langle \frac{d\mathbf{P}_{\text{mec}}}{dt} \right\rangle = \langle \vec{\mathbf{T}} \rangle \\ &= \left[\epsilon_0 \mathbf{E} \otimes \mathbf{E} - \mu_0 \mu \mathbf{H} \otimes \mathbf{H} - \frac{1}{2} (\epsilon_0 \mathbf{E}^2 + \mu_0 \mu \mathbf{H}^2) \mathbf{I} \right] \end{aligned} \quad (6)$$

where $\langle \vec{\mathbf{T}} \rangle$ represents the time-averaged Maxwell's stress tensor, \mathbf{I} the identity tensor, and \mathbf{E} and \mathbf{H} the electric field vector and magnitude respectively. To obtain the force field profile, the arbitrary particle is placed at all points of interest and all vector fields required to calculate $\langle \vec{\mathbf{T}} \rangle$ are obtained. The force that an arbitrary particle experiences in an electromagnetic field can be determined by suitably restricting and calculating the surface integral in Eq. (6) over the boundary of the particle.

3. SIMULATION

To design the height and width of the corrugations, we study the transmission spectra of a silver film by varying h and w corrugations on its surface at three lattice periodicities: $p = 400, 500, 600$ nm [Fig. 3(a)]. We do this by assuming the excitation source as a temporal Gaussian source located along the left boundary of the domain with a central wavelength of $\lambda = 1.5 \mu\text{m}$ and a pulse width of $\lambda = 1 \mu\text{m}$. We place a virtual line detector along the right boundary of the domain and

conduct a frequency response analysis. To perform all simulations, we used the fully vectorial finite-difference time-domain method [24].

Following this, we conducted a two-dimensional (2D) simulation along the surface of a silver film, surrounded by air, with a subwavelength slit through it and a set of tailored corrugations, with a height h and width w , of which the basic form is shown in Fig. 3(b). Throughout this study the subwavelength aperture width s and slab thickness t are fixed at 140 and 1000 nm, respectively. The simulation grid size was

a $20 \mu\text{m}$ by $8 \mu\text{m}$ rectangle with a pixel size of 20 nm, accounting for a total of 400,000 pixels per time step. We applied a perfectly matched layer with approximately 60 pixel thickness as the boundary condition to simulate an open boundary while truncating the computational domain. The input light source was assumed to be H_z polarized and continuous. The parameter q refers to the offset distance between the slit edge and the start of the periodic corrugations. This permits for small adjustments to the phase matching between the slit and the corrugations. We initially considered $q = w' = h' = p' = 0$. Running the simulation on an Intel I7-920 CPU, we attained an average 2D simulation time of 3 min (in single core operation).

From the simulated field vectors, we were able to obtain the optical trapping forces developed on a spherical polystyrene particle having radius of 80 nm and refractive index of 2.5. The media is assumed to be water having refractive index of 1. The particle is placed at each location of interest and the forces, using Eq. (6), are calculated.

4. RESULTS AND DISCUSSION

The resulting transmission spectra for different h and w combinations is shown in Fig. 4 for each value of p in Fig. 3(a). From all three transmission spectra plots we notice in general the occurrence of two sharp resonance peaks. This resonance behavior is most obvious for the system where $p = 500$ nm and $p = 600$ nm [Figs. 4(b) and 4(c)]. The two strongest resonant peaks seen in Fig. 4(b) occur for parameters $h = 150$ nm, $w = 250$ nm, and $p = 500$ nm at the two encircled locations A and B. The wavelength at A is approximately near the normalized center wavelength at $\lambda = 1.464a$ and at B it is approximately near $\lambda = 1.38a$. However, for a larger periodicity of $p = 600$ nm, the strongest resonant peaks occur for parameters $h = 150$ nm and $w = 200$ nm at the two encircled locations, A and B. The wavelength at A is near $\lambda = 1.715a$ and the second, B, is near $\lambda = 1.587a$.

The geometry shown in Fig. 3(a) requires excitation using light incident at an angle to provide the necessary excitation wave-vector components. To overcome this we utilize the angular wave-vector spectrum of a subwavelength aperture (slit) to provide the necessary parallel wave-vector components, as shown in Fig. 4. To determine the energy distribution of the resonance peaks shown in the transmission spectra (Fig. 4), we conducted a 2D fully vectorial simulation of Maxwell's equations along the surface of a silver film, surrounded by

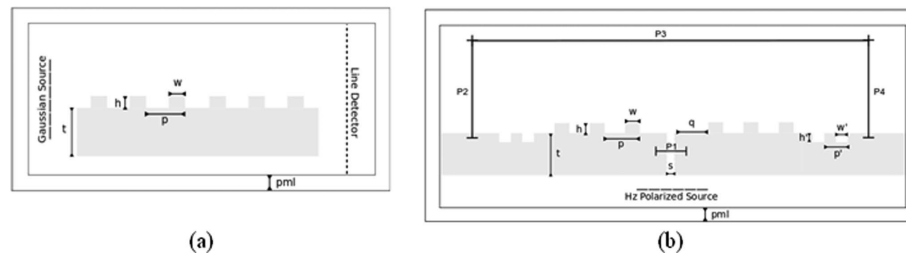


Fig. 3. (a) Simulation geometry with a lattice constant, groove height, and width of $p, h,$ and $w,$ respectively. The Gaussian source, located to the left, has a center wavelength of $\lambda = 1.5 \mu\text{m}$ and a pulse width of $\lambda = 1 \mu\text{m}$. (b) Simulation geometry with a subwavelength slit and tailored surface corrugations on a silver substrate. Throughout this study the subwavelength aperture width, $s,$ and slab thickness, $t,$ are fixed at 140 and 1000 nm, respectively.

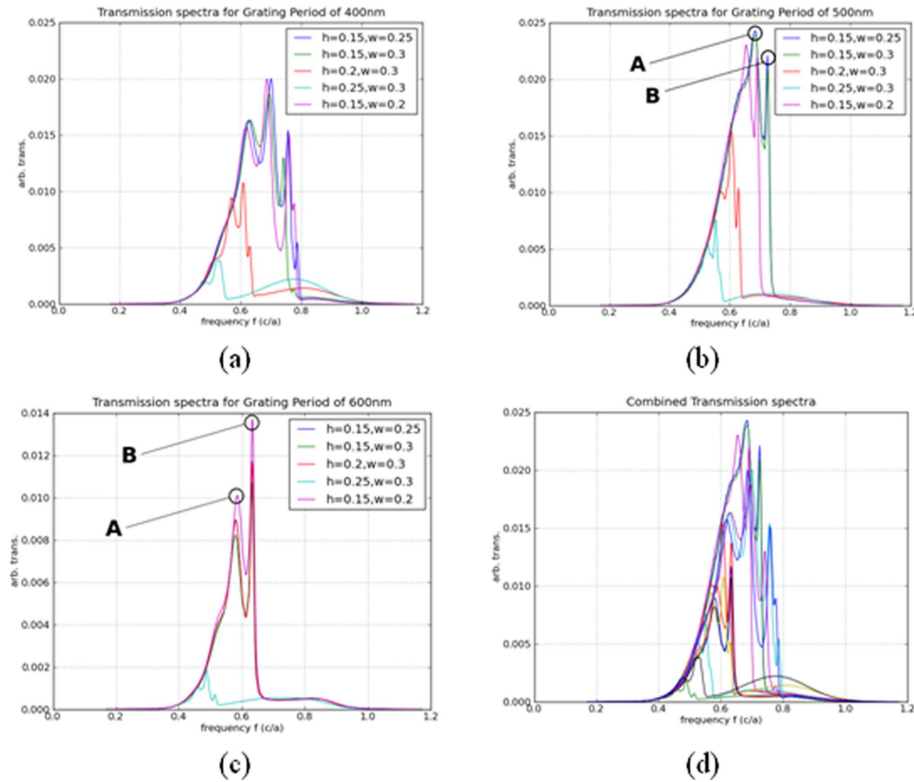


Fig. 4. (Color online) Transmission spectra for a grating period of (a) 400, (b) 500, and (c) 600 nm, respectively, at different h and w configurations. (d) Combined transmission spectra outlines the input Gaussian spectra. The highest resonance is observed when $h = 150$ nm, $w = 250$ nm, and $p = 500$ nm.

air, with a subwavelength slit through it and a set of tailored corrugations in Fig. 3(b).

We present in Fig. 5 a snapshot and animation as a contour plot of the electric field intensity ($\|E\|^2$) mode profiles of the two points A and B circled in Figs. 4(c) and 4(d). For a periodicity of $p = 500$ nm, we have used the configuration $h =$

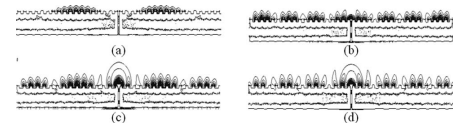


Fig. 5. Snapshots of the electric field intensity, $\|E\|^2$, shown as a contour plot along the metallic structure shown in Fig. 3(b) for (a) $p = 500$ nm, $\lambda = 1380$ nm, $h = 150$ nm, and $w = 250$ nm (Media 1); (b) $p = 500$ nm, $\lambda = 1464$ nm, $h = 150$ nm, and $w = 250$ nm (Media 2); (c) $p = 600$ nm, $\lambda = 1587$ nm, $h = 150$ nm, and $w = 200$ nm (Media 3); (d) $p = 600$ nm, $\lambda = 1715$ nm, $h = 150$ nm, and $w = 200$ nm (Media 4). Media 1 to Media 4 depict the corresponding animation sequences of (a) to (d).

150 nm and $w = 250$ nm [corresponds to the blue curve in Fig. 4(c)] and for a periodicity of $p = 600$ nm we have used the configuration $h = 150$ nm and $w = 200$ nm [corresponds to the pink curve in Fig. 4(d)].

The animations provided for each in the time domain clearly show the leaky surface plasmon propagation. Noticeable differences between the designs include the wavelength of the surface plasmon modes and the decay length into air.

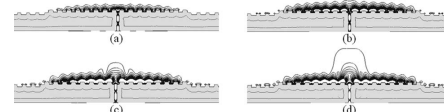


Fig. 6. Snapshots of the electric field intensity, $\|E\|^2$, shown as a contour plot along the metallic structure shown in Fig. 3(b) where $p = 500$ nm, $\lambda = 1380$ nm, $h = 150$ nm, $w = 250$ nm, $p' = 500$ nm, $h' = 125$ nm, $w' = 300$ nm, and (a) $q = 0$ (Media 5); (b) $q = 105$ nm (Media 6); (c) $q = 155$ nm (Media 7); (d) $q = 205$ nm (Media 8). Media 5 to Media 8 depict the corresponding animation sequences of (a) to (d).

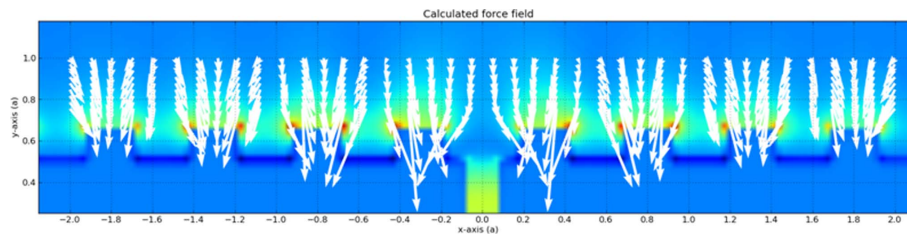


Fig. 7. (Color online) Optical trapping force developed on a spherical polystyrene particle with a radius of 80 nm and refractive index of 2.5 in water inserted into the design producing the electric intensity field of Fig. 6(b).

While the results indicate a possibility of channeling light power onto the surface, the manner of its propagation, in packets at the speed of light, *per se*, will not permit particle trapping. To facilitate this, the optical field has to be in the form of a standing wave. We achieved this by introducing structures at the distal ends away from the slit, shown in Fig. 4 with parameters w' , h' , and p' . The structures are designed using the transmission spectra obtained previously such that the transmission across its surface at the wavelength of interest is highly suppressed. This has the effect of causing the traveling packets of leaky waves to be reflected back. Since coherence is preserved, careful design will enable standing waves to develop.

Utilizing the design that produces the outcome of Fig. 5(a), we calculate the time-averaged electric field intensity, as shown in Figs. 6(a)–6(d) for different offset values of $q = 0, 105, 155,$ and 205 nm, respectively. The chosen parameters for the reflective corrugations at the ends are $p' = 500$ nm, $h' = 125$ nm, and $w' = 300$ nm. The manner with which the standing wave develops in time can be seen in the animation provided. Clearly for larger values of q , the structures begin to exhibit beaming behavior similar to those reported previously [12]. To compare the losses being beamed off the surface, we compare the time-averaged input power flux coming through the slit across line P1 with the power loss across P2, P3, and P4. We obtained efficiencies of 52.4%, 72.8%, 30.8%, and 15.4% for designs in Figs. 6(a)–6(d), respectively.

Using the design that produces the outcome in Fig. 6(b), we inserted into the simulation domain a spherical polystyrene particle with a radius of 80 nm and dielectric constant of 2.5. The particle is placed at each location of interest and the forces are calculated by using Eq. (6). The resulting force field is shown in Fig. 7. The ability to attain power efficiency of 72% offers effective optical trapping. It is noteworthy that, at this length scale, Brownian perturbations will serve to disperse the trapped nanoparticle from its intended trapped location [8,25,26]. The trapping potential extends to approximately 350 nm above the surface of the device, which again indicates that this scheme is feasible to trap nanoparticles. It should be noted that, by modifying the number of corrugations on either side of the slit, the width of the proposed trapping site can be modified. Furthermore, the decay into air can be somewhat increased by using a different mode profile. For example, it is obvious that the decay lengths of the modes in Fig. 5(c) are longer even though the mode profiles are more complex. This approach, however, would require the careful design of the reflective defects to preserve coherence.

While the method is demonstrated here with the situation of slit apertures on the surface, we envisage that the progression from 2D to an axis-symmetric three-dimensional optical trap should not be difficult. The optical trapping of particles into rings is typically achieved using an axicon [27]. As in the case of conventional traps, the resolution of the optical fields is limited by diffraction. Some efforts have been reported to utilize phase matching using photonic structures to permit subwavelength fields [28]. In our case, these rings will be inherently subwavelength with strong plasmon intensity fields. The availability of optical forces on a chip allows for the assembly of nanoparticles beyond the use of means such as evaporation, where a degree of randomness can be expected. Once held in place, tailored patches within the nanoparticle will be able to hold such assemblies in place when optical forces are switched off [29]. It is also conceivable that metallic nanoparticles instead of corrugations may be placed at the output of waveguides to create the optical trapping fields via a plasmon generating effect as well. Means to ensure that the nanoparticles stay at the site without the presence of light, where Brownian forces are significant, will, however, be needed for this.

5. CONCLUSIONS

The corrugated structure from a subwavelength aperture has been actively investigated to modify the directionality of beams. We demonstrate here the possibility of maximizing the leaking of light from the aperture along the surface via an appropriate corrugation geometry with silver. By carefully placing a secondary grated structure some distance from the original structure, we were able to produce strong reflection, which, with the coherent nature of light used, created strong optical standing wave fields that could be harnessed for particle trapping. We demonstrate this concept in the form of linear field traps. With careful design, we envisage the ability to create optical traps of various geometries without difficulty via the same principles as outlined.

ACKNOWLEDGMENTS

This work has been supported by the Australian Research Council Discovery Grant DP0878454.

REFERENCES

1. D. G. Grier, "A revolution in optical manipulation," *Nature* **424**, 810–816 (2003).
2. K. Dholakia and W. M. Lee, "Optical trapping takes shape: the use of structured light fields," *Adv. Atom. Mol. Opt. Phys.* **56**, 261–337 (2008).

Muradoglu *et al.*

Vol. 28, No. 4 / April 2011 / J. Opt. Soc. Am. B 607

3. M. Li, W. H. P. Pernice, C. Xiong, T. Baehr-Jones, M. Hochberg, and H. X. Tang, "Harnessing optical forces in integrated photonic circuits," *Nature* **456**, 480–484 (2008).
4. K. Okamoto and S. Kawata, "Radiation force exerted on sub-wavelength particles near a nanoaperture," *Phys. Rev. Lett.* **83**, 4534–4537 (1999).
5. P. C. Chaumet, A. Rahmani, and M. Nieto-Vesperinas, "Optical trapping and manipulation of nano-objects with an apertureless probe," *Phys. Rev. Lett.* **88**, 123601 (2002).
6. T. Cizmar, M. Siler, M. Sery, P. Zemanek, V. Garcés-Chavez, and K. Dholakia, "Optical sorting and detection of submicrometer objects in a motional standing wave," *Phys. Rev. B* **74**, 035105 (2006).
7. P. Zemánek, A. Jonáš, and M. Liška, "Simplified description of optical forces acting on a nanoparticle in the Gaussian standing wave," *J. Opt. Soc. Am. A* **19**, 1025–1034 (2002).
8. A. Neild, T. W. Ng, and W. M. S. Yiu, "Optical sorting of dielectric Rayleigh spherical particles with scattering and standing waves," *Opt. Express* **17**, 5321–5329 (2009).
9. A. N. Grigorenko, N. W. Roberts, M. R. Dickinson, and Y. Zhang, "Nanometric optical tweezers based on nanostructured substrates," *Nat. Photon.* **2**, 365–370 (2008).
10. M. Righini, G. Volpe, C. Girard, D. Petrov, and R. Quidant, "Surface plasmon optical tweezers: tunable optical manipulation in the femtonewton range," *Phys. Rev. Lett.* **100**, 186804 (2008).
11. Z. Fang, F. Lin, S. Huang, W. Song, and X. Zhu, "Focusing surface plasmon polariton trapping of colloidal particles," *Appl. Phys. Lett.* **94**, 063306 (2009).
12. H. J. Lezec, A. Degiron, E. Devaux, R. A. Linke, L. Martin-Moreno, F. J. Garcia-Vidal, and T. W. Ebbesen, "Beaming light from a subwavelength aperture," *Science* **297**, 820–822 (2002).
13. W. L. Barnes, W. A. Murray, J. Dintinger, E. Devaux, and T. W. Ebbesen, "Surface plasmon polaritons and their role in the enhanced transmission of light through periodic arrays of subwavelength holes in a metal film," *Phys. Rev. Lett.* **92**, 107401 (2004).
14. H. Gao, J. M. McMahon, M. H. Lee, J. Henzie, S. K. Gray, G. C. Schatz, T. W. Odom, "Rayleigh anomaly-surface plasmon polariton resonances in palladium and gold subwavelength hole arrays," *Opt. Express* **17**, 2334–2340 (2009).
15. Y. Gravel and Y. Sheng, "Rigorous solution for the transient surface plasmon polariton launched by subwavelength slit scattering," *Opt. Express* **16**, 21903–21913 (2008).
16. D. R. Jackson, J. Chen, R. Qiang, F. Capolino, and A. A. Oliner, "The role of leaky plasmon waves in the directive beaming of light through a subwavelength aperture," *Opt. Express* **16**, 21271–21281 (2008).
17. J. A. Dionne, L. A. Sweatlock, H. A. Atwater, and A. Polman, "Plasmon slot waveguides: towards chip-scale propagation with subwavelength-scale localization," *Phys. Rev. B* **73**, 035407 (2006).
18. Y. Liu, H. Shi, C. Wang, C. Du, and X. Luo, "Multiple directional beaming effect of metallic subwavelength slit surrounded by periodically corrugated grooves," *Opt. Express* **16**, 4487–4493 (2008).
19. F. Wang, M. Xiao, K. Sun, and Q.-H. Wei, "Generation of radially and azimuthally polarized light by optical transmission through concentric circular nanoslits in Ag films," *Opt. Express* **18**, 63–71 (2010).
20. P. Drude, "Zur elektronentheorie der metalle," *Ann. Phys.* **306**, 566–613 (1900).
21. P. B. Johnson and R. W. Christy, "Optical constants of the noble metals," *Phys. Rev. B* **6**, 4370–4379 (1972).
22. M. Nieto-Vesperinas, P. C. Chaumet, and A. Rahmani, "Near-field photonic forces," *Philos. Trans. R. Soc. A* **362**, 719–737 (2004).
23. S. A. Maier, *Plasmonics: Fundamentals and Applications* (Springer Science, 2007), pp. 42–52.
24. A. F. Oskooi, D. Roundy, M. Ibanescu, P. Bermel, J. D. Joannopoulos, and S. G. Johnson, "MEEP: a flexible free-software package for electromagnetic simulations by the FDTD method," *Comput. Phys. Commun.* **181**, 687–702 (2010).
25. T. W. Ng, A. Neild, and P. Heeraman, "Continuous and fast sorting of Brownian particles," *Opt. Lett.* **33**, 584–586 (2008).
26. A. Neild, T. W. Ng, and T. Woods, "Optimizing photophoresis and asymmetric force fields for grading of Brownian particles," *Appl. Opt.* **48**, 6820–6826 (2009).
27. J. Arlt and K. Dholakia, "Generation of high-order Bessel beams by use of an axicon," *Opt. Commun.* **177**, 297–301 (2000).
28. J. J. Miret and C. J. Zapata-Rodríguez, "Diffraction-free propagation of subwavelength light beams in layered media," *J. Opt. Soc. Am. B* **27**, 1435–1445 (2010).
29. Z. Zhang and S. C. Glotzer, "Self-assembly of patchy particles," *Nano Lett.* **4**, 1407–1413 (2004).

B.3 Sorting of Brownian rods by use of an asymmetric potential

THE JOURNAL OF CHEMICAL PHYSICS **134**, 064514 (2011)

Sorting of Brownian rods by the use of an asymmetric potential

Ian Gralinski, Adrian Neild,^{a)} Tuck Wah Ng, and Murat S. Muradoglu
Laboratory for Optics, Acoustics and Mechanics, Monash University, Clayton, VIC 3800, Australia

(Received 13 October 2010; accepted 21 December 2010; published online 14 February 2011)

We present here a method for sorting nanometer scale Brownian rods by using a switching asymmetric periodic potential. A two stage sorting process is used to isolate particles with specific dimensions, with acceptable sorting times as well as realizable potential barrier lengths. The method was tested using computer simulations. The ability to sort the nanometer scale anisotropic particles, such as gold nanorods, portends important applications in large scale data recording, photothermal surgery, and bioimaging. © 2011 American Institute of Physics. [doi:10.1063/1.3537738]

I. INTRODUCTION

The Brownian motion of spherical particles in an unbounded fluid volume was first established by Einstein^{1,2} and Smoluchowski.³ In confined spaces, there is an interaction between the particles and the surrounding walls, and considerable advances have been made into understanding the ensuing motion under such conditions.⁴⁻⁶ When considering Brownian rods, it is necessary to consider the various rotational and translational frictions.^{7,8} In 2D, this leads to differential diffusion equations based on a rotational constant and translational constants parallel and perpendicular to the particle's long axis. The result is that the anisotropic behavior ensues in the short term and crosses over to isotropic behavior in the longer term (when considered from a static axis system) as shown recently experimentally.⁹ As for spheres, when the proximity of a wall is considered, hydrodynamic interactions occur. In the case of a rod this has been shown to significantly reduce the diffusion constants, the effect being the strongest on the translational diffusion coefficient along the rod when compared with that perpendicular to the length of the rod.¹⁰ A description of the mechanics for this was furnished via experiments using different chamber thicknesses, and thus, degrees of constraining.¹¹ It was found that when an ellipsoidal Brownian particle is approximately neutrally buoyant, it is most likely to reside close to the central plane of a thin fluid chamber,⁹ this being an entropic effect: the number of possible orientations is reduced when the center-of-mass of an elongated particle is close to a wall.¹² Such hydrodynamic interactions affecting rods have also been modeled recently.¹³

While Brownian motion is often detrimental to sorting as a consequence of fluctuating forces that lead to

distributions spreading,¹⁴ considerable work has been conducted to exploit the size based variations in diffusion as a sorting metric in itself. Asymmetric periodic potentials have been actively investigated to rectify the symmetric fluctuations in Brownian particles.¹⁵⁻²¹ A convenient scheme to accomplish this is via the switching on and off (conveniently described to as cycling) of a periodic but spatially anisotropic potential.^{16,17} Such stochastic ratchets have been demonstrated as capable of sorting spherical Brownian particles.¹⁸

In this work we theoretically examine the possibility of using such stochastic ratchets to sort populations of Brownian rods, investigating, in particular, the role that the crossover time from anisotropic to isotropic motion⁹⁻¹¹ takes in this process.

II. SORTING PRINCIPLE

There are several important features for Brownian based sorting using a pulsed asymmetric potential. We consider the case where the motion is confined to a plane in a fluidic chamber wherein an asymmetric potential can be imposed. This potential, during its on cycle, is assumed to collect particles at the force potential minima. Typically, this would correspond to lines within the plane of interest. An additional and reasonable assumption to make is for the rods to align along these lines. Within the off phase the motion of the particles is due to free diffusion Brownian effects. The Brownian motion of a rod can be described by the Langevin equations

$$\begin{bmatrix} \dot{x} \\ \dot{y} \\ \dot{\theta} \end{bmatrix} = \begin{bmatrix} \sqrt{2D_a} \cos^2 \theta + \sqrt{2D_b} \sin^2 \theta & (\sqrt{2D_a} - \sqrt{2D_b}) \cos \theta \sin \theta & 0 \\ (\sqrt{2D_a} - \sqrt{2D_b}) \cos \theta \sin \theta & \sqrt{2D_a} \sin^2 \theta + \sqrt{2D_b} \cos^2 \theta & 0 \\ 0 & 0 & \sqrt{2D_\theta} \end{bmatrix} \begin{bmatrix} \xi_x \\ \xi_y \\ \xi_\theta \end{bmatrix}, \quad (1)$$

where a dot indicates a time derivative and $\xi_{x,y,\theta}$ are the time derivatives of a delta-correlated random Wiener process, such that $\langle \xi_i(t) \xi_j(t') \rangle = \delta(t-t') \delta_{ij}$ with $i, j = x, y, \theta$. In other words, ξ_x , ξ_y , and ξ_θ are statistically independent

^{a)} Author to whom correspondence should be addressed.

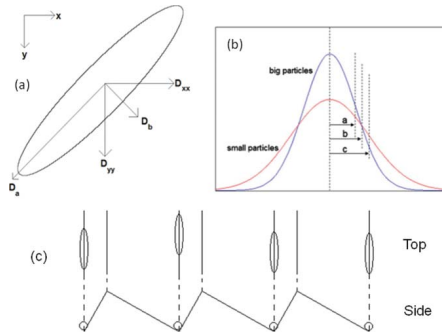
064514-2 Gralinski *et al.*J. Chem. Phys. **134**, 064514 (2011)

FIG. 1. (a) Directions of diffusion coefficients superimposed on a typical rod under consideration, with the static laboratory frame in the top left. (b) PDFs for small and large spheres at a given time t . The greatest difference in probability between the small and big spheres occurs at the intersection of the PDFs (marked as b). (c) Diagrammatic representation of the position and alignment of rods near the end of the on period from both top and side views.

noise sources. We note that the x and y axes are laboratory frames, and as such are static, as shown in Fig. 1(a). The translational and rotational motion is characterized by the diffusion coefficients, D_a , D_b , and D_θ , which describe the translation parallel to the length of the rod, the translation perpendicular to the length of the rod, and the rotation of the rod, respectively. The directions of D_a and D_b can be seen in Fig. 1(a). When considering motion in a bulk fluid volume, the values for these diffusion coefficients are given approximately by²²

$$\begin{aligned} D_a &= \frac{k_B T [\ln(2r) - 0.5]}{2\pi\eta_s L}, \\ D_b &= \frac{k_B T [\ln(2r) + 0.5]}{4\pi\eta_s L}, \\ D_\theta &= \frac{3k_B T [\ln(2r) - 0.5]}{\pi\eta_s L^3}, \end{aligned} \quad (2)$$

where k_B is the Boltzmann's constant, T is the temperature in Kelvin, $r = L/d$ is the aspect ratio (L and d are the length and the diameter of the fiber, respectively), and η_s is the viscosity of water at T . In a system that is highly confined in the third dimension (i.e., with a small height component), and hence, can be treated approximately as a 2D system, the actual values of the diffusion coefficients are considerably lower than these bulk values due to hydrodynamic interactions with the walls.¹⁰ As such, we scale the values in our simulations based on the experimental results obtained by Han *et al.*⁹

Clearly, it is the Brownian motion of a particle over the off cycle that dictates the potential minimum location that it will converge into once the asymmetric potential is turned on. For spherical particles, the probability density function (PDF) is based on a single diffusion constant D which depends on the radius of the particle. This PDF is normally distributed and is given by²³

$$\text{PDF}(x) = \frac{1}{\sqrt{4\pi Dt}} \exp\left(-\frac{x^2}{4Dt}\right), \quad (3)$$

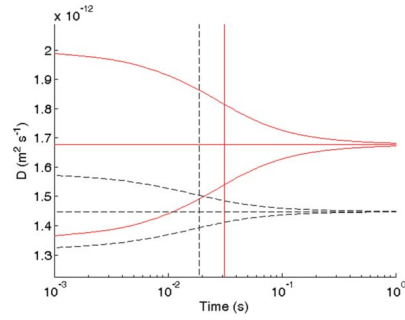


FIG. 2. Plot of D_{yy} (upper curves) and D_{xx} (lower curves) vs time for two different rods with dimensions $595.2 \times 168 \times 168 \text{ nm}^3$ (black, dashed) and $864 \times 72 \times 72 \text{ nm}^3$ (red, solid). Horizontal lines represent \bar{D} and vertical lines represent τ_θ .

where D is the diffusion coefficient at time t and x is the distance moved, such that for two particles of different sizes starting at the same minima at the start of the off cycle, one will see the smaller particle having a higher probability of moving further before the on cycle starts. The relative probabilities are shown with respect to the force potential in Fig. 1(b). Once the force field resumes, those particles which have passed the nearest maxima will move one step further along the chamber. The asymmetry of the potential will skew the probability of progression in one direction. With this in mind, the time over which the potential is off can be linked to the barrier length so that an optimized sorting scheme can be designed.²⁴

When examining the motion of Brownian rods, it is necessary to consider it in the fixed laboratory frame, x - y . At the end of an "on" cycle, the particles are aligned parallel to the y -axis and within wells spaced along the x direction as depicted in Fig. 1(c). Upon release from effects of the potential, the particles move according to Eq. (1) based on the three diffusion parameters linked to the rod geometry. However, when this motion is described by a diffusion coefficient in the laboratory frame, the value changes over time. Over short time periods, the particle aligned with its long axis, approximately along the y -axis, will diffuse preferentially along the y -axis. However, over longer periods of time, that initial rotational alignment with the y -axis is washed out by the ensuing random motion. The diffusion coefficients in the laboratory frame can be expressed as⁹

$$\begin{aligned} D_{xx}(t) &= \bar{D} - \frac{\Delta D \tau_\theta(t)}{2t}, \\ D_{yy}(t) &= \bar{D} + \frac{\Delta D \tau_\theta(t)}{2t}, \end{aligned} \quad (4)$$

where D_{xx} and D_{yy} are the diffusion coefficients in the x and y directions, respectively, and $\bar{D} = (D_a + D_b)/2$, $\Delta D = D_a - D_b$, and $\tau_\theta(t) = (1 - e^{-4D_\theta t})/4D_\theta$. These values are plotted in Fig. 2 for two rod sizes. It can be seen that there is an initial maximum difference in D_{xx} and D_{yy} . After a period of

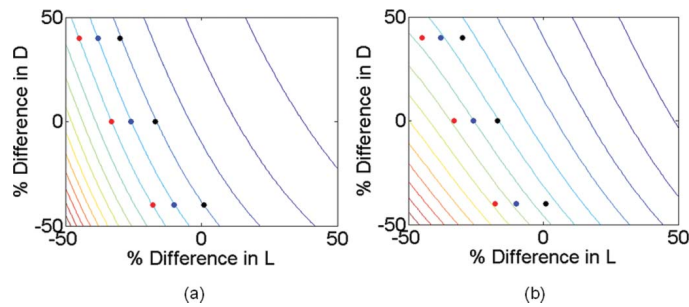


FIG. 3. Contour plots of diffusion coefficient in the laboratory x direction over a range of rod sizes taken at time (a) 30 and (b) 400 μs . The percentage difference in length (L) and diameter (D) are taken from a $960 \times 120 \times 120 \text{ nm}^3$ base rod. The circles on the plot indicate the rod sizes used in simulations, with the blue colored circles indicating the rods that were taken to the second stage of sorting. The red and black circles are rod sizes on adjacent contours at 30 μs , and are overlaid in (b) to emphasize the change in diffusion coefficient over time. The largest diffusion coefficients correspond to the smallest particle sizes in the lower left corner of the plot (red contours) and decrease toward the top right (blue contours). The colors of dots used correspond to the curves in Fig. 5.

time, this anisotropy is lost and the motion in both directions is equally likely. This period is characterized by the crossover time as expressed by

$$\tau_{\theta} = \frac{1}{2D_{\theta}}, \quad (5)$$

where τ_{θ} is the crossover time and D_{θ} is as defined earlier.

The dependence of a rod's diffusion coefficient (in a certain fixed direction) with time differs starkly with a sphere. In the case of the spheres the diffusion coefficient is independent of time; in addition [with reference to Fig. 1(b)] it is clear that the separation of particles is based on them having different diffusion values. Hence, a direct link is available²³ between the optimal barrier length and the off time, with the sorting capability limited only by the smallness of the minimal barrier length that can be created. However, for a rod with the diffusion coefficients in the x direction varying over time, the relationship becomes time dependent. The x direction is of importance as it dictates whether the rods will cross from one minimum to the next. Furthermore, different time periods can be used to separate different sets of rod sizes. The effect is depicted in Fig. 3, which shows a map of D_{xx} for a grid of particle sizes after two different periods of time have elapsed. Within these plots, rods on the same contour lines cannot be sorted at that off time as they have the same D_{xx} value. However, rods on different contour lines can be sorted. Thus, it can be seen that different clusters of rod sizes (diameter and length combinations) can form depending on the off time chosen. This is seen visually by the change of the angle of the contour lines, which occurs when comparing between the two plots. This means that a degree of sorting by length and diameter should be possible if a two stage process is used, one using an off time much lower than the crossover time, and the other using a value larger or close to the crossover time. We now examine the design of this two stage process in more detail.

A. Stage one

At very short and very long off times, the orientations of the equal diffusion contour lines in plots such as those shown in Fig. 3 do not change significantly. For a given off time, the choice of the barrier length has a direct impact on the amount of sorting that can be achieved per cycle.²³ With reference to Fig. 1(b), the barrier length determines where the PDFs are cut, i.e., what proportion of rods progress to the next potential well and the proportion that remains in the current well. This allows the optimal barrier lengths for sorting particles with similar diffusion coefficients to be calculated. The barrier length used is the optimal length for the pair of particles with the least amount of sorting achieved. This ensures that the particles that are hardest to separate have their optimal barrier lengths chosen. The optimal barrier length for a pair of particles at a given off time can be determined from the equation

$$l_{\text{barrier}} = \sqrt{\frac{2t D_1 D_2 \ln\left(\frac{D_2}{D_1}\right)}{D_2 - D_1}}, \quad (6)$$

where t is the off time and D_1, D_2 are the diffusion coefficients of each particle in the x direction corresponding to t . Equation (6) is derived in the Appendix. If we first consider the short off time case where the orientations of the contours do not change much with time, there is some flexibility in the value that can be chosen. The separation time in the first stage of sorting is much smaller than it is for the second stage, so it does not need to be considered. In the first stage of sorting, the limiting factor is the minimum feature size possible in the potential field (this is similar to case of the spherical particles²³), inferring that the more frequently the process can be repeated in the given period of time, the better the sorting will be. It should be noted that only the barrier length needed to be considered as it determined the initial off time to be used.

Once the minimum feature size is available to determine the barrier length, and hence, the off time, the backflow

distance can then be calculated. This depends on the proportion of particles that can be allowed to progress in the opposite direction of the desired motion. Ideally this should be zero, but that would necessitate an infinite backflow length. For the results presented in this paper, a maximum allowable backflow of 0.01% was chosen. The actual length can be determined from the equation

$$\Pr(X > l_{\text{backflow}}) < 0.0001, \quad X \sim N(0, \sqrt{2D_{xx}t}), \quad (7)$$

where D_{xx} is the diffusion coefficient in the x direction for the given off time t and l_{backflow} is the backflow length. This equation determines the distance from the original position at which less than 0.01% of particles with diffusion coefficient D_{xx} at time t will be found. This value was calculated for each particle size in the population and the largest value was chosen. As a rule of thumb, four to five times the barrier length should give a sufficiently large backflow length.

The on time was not considered, but was assumed to be long enough, so that all particles would have their long axis aligned along the y -axis and be located exactly at the bottom of their corresponding wells. The magnitude of the potential barrier was not considered and assumed to be sufficient to achieve the alignment and position conditions as outlined.

B. Stage two

Once the first stage of separation was complete, a given group of particles would be further separated by the use of a longer off time. With reference to Fig. 3 these are represented by blue circles. The use of a longer off time means that the rods are able to rotate by a significant amount, and hence, tend to lose their anisotropic behavior.

The process for optimization of the values will be similar, with the exception of the off time. The limitation for off time is not the barrier length that is required, but the total time it takes to sort the particles. In contrast to the first phase of sorting, here a longer off time gives a greater difference in the diffusion parameter, and hence, better sorting. However, this comes at a penalty of longer times needed. The optimum sorting over a given period of time is, therefore, not necessarily associated with the case where the diffusion coefficients are most diverse but rather on other factors. A plot of the total separation time (number of cycles multiplied by off time) and of the number of cycles required for separation against a

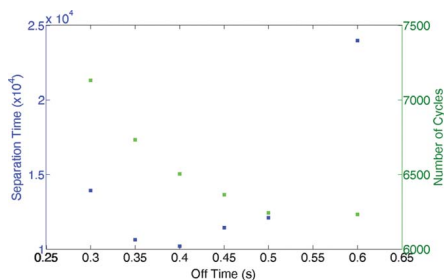


FIG. 4. Separation time (blue squares) and number of cycles for separation (green squares) vs off time for three different rod sizes taken to stage 2 of sorting. Rod sizes used were $595.2 \times 168 \times 168$, $710.4 \times 120 \times 120$, and $864 \times 72 \times 72$ nm³. Separation time has been defined as number of cycles for separation multiplied by the off time, and is shown as it is a more meaningful performance characteristic than number of cycles required to separate rod populations.

range of off times can be seen in Fig. 4. The minimum value of separation time obtained was at an off time of 0.4 s and this appears to be close to the exact minimum. Varying the off time greatly from this value increases the separation time dramatically, and hence, it is desirable to have a good estimate for the off time that minimizes the separation time.

III. RESULTS AND DISCUSSIONS

With a method for determining the key parameters defined, the sorting performance can be predicted. We consider an initial population of rods with a range of diameters from 72 to 168 nm and a range of lengths from 528 to 969.6 nm. These are shown in Table I.

Since we use an approximate representation of the system in 2D, justified by a very small height component, the theoretical diffusion coefficients should be affected by hydrodynamic interactions. To account for this in our simulations, the theoretical values have been multiplied by a scale factor, taken as the ratio of the experimentally determined value from Han *et al.*⁹ to the theoretical value for a rod of the same dimensions. These scale factors are shown in Table II. This approximation should provide sufficient accuracy in simulations

TABLE I. Actual rod dimensions used in simulations, along with percentage differences compared to a $960 \times 120 \times 120$ nm³ base rod and diffusion coefficients in the laboratory x direction at both early and late off times. Entries are arranged in the same way as in Fig. 3, with the left column corresponding to the red circles, center column to blue circles, and right column to black circles.

$[-45\%, +40\%] = 528 \times 168$ nm $D_{xx}(0.03) = 2.0670 \times 10^{-13}$	$[-38\%, +40\%] = 595.2 \times 168$ nm $D_{xx}(0.03) = 1.8400 \times 10^{-13}$ $D_{xx}(0.4) = 2.8483 \times 10^{-13}$	$[-30\%, +40\%] = 672 \times 168$ nm $D_{xx}(0.03) = 1.6276 \times 10^{-13}$
$[-33\%, +0\%] = 643.2 \times 120$ nm $D_{xx}(0.03) = 2.0776 \times 10^{-13}$	$[-26\%, +0\%] = 710.4 \times 120$ nm $D_{xx}(0.03) = 1.8485 \times 10^{-13}$ $D_{xx}(0.4) = 3.0936 \times 10^{-13}$	$[-17\%, +0\%] = 796.8 \times 120$ nm $D_{xx}(0.03) = 1.6174 \times 10^{-13}$
$[-18\%, -40\%] = 787.2 \times 72$ nm $D_{xx}(0.03) = 2.0599 \times 10^{-13}$	$[-10\%, -40\%] = 864 \times 72$ nm $D_{xx}(0.03) = 1.8246 \times 10^{-13}$ $D_{xx}(0.4) = 3.2959 \times 10^{-13}$	$[+1\%, -40\%] = 969.6 \times 72$ nm $D_{xx}(0.03) = 1.5792 \times 10^{-13}$

TABLE II. Scale factors used to adjust the theoretical diffusion coefficients in the three degrees of freedom considered.

Direction	X	Y	θ
Scale factor	0.2995	0.0984	0.2544

as Han *et al.*⁹ found that particles did not deviate far from the central plane of confinement, i.e., only moved in approximately 2D.

The first phase of sorting uses an off time of 30 μ s, an associated barrier length of 101.66 nm, and a backflow length of 500 nm. These parameters are sufficient to ascertain the probability distribution of each particle size, and hence, the probability of each rod geometry moving forward (or backward) along the asymmetric potential by one or multiple wells. This is used to calculate the probability distributions over multiple cycles using

$$\vec{a}_n = T \vec{a}_{n-1}, \quad (8)$$

where \vec{a}_n is the population vector for a particular rod size after n cycles and T is the population transition matrix. Each entry of \vec{a}_n corresponds to a single potential well and T_{ij} is the probability of a rod in well i moving to well j in a single cycle. The resulting distribution is shown in Fig. 5 as a plot of the 10th and 90th percentile boundaries of rod populations as the number of cycles increases [(a) and (c)] and the number of particles present in each well after 20 000 cycles [(b) and (d)]. Once completed, the band of rods shown as blue in Figs. 5(a) and 5(b), need to be passed through the second phase of sort-

ing, in which the distributions achieved in 2 h are shown in Figs. 5(c) and 5(d).

There is a degree of control over the diffusion values to allow a greater range of rods to be sorted using this technique by altering the viscosity, temperature, or the degree of hydrodynamic interaction with the surrounding walls by controlling the height of the chamber. For example, for larger rods to be sorted, a shorter off time could be used in the second phase while keeping the same barrier length, and hence, reducing the total sorting time if the temperature was raised.

For small particles, the limiting factor is the barrier length required to accomplish sorting, whereas for large particles, the sorting time is the prohibitive issue. Some of these limiting factors could be reduced if a greater difference in particle sizes is considered, as in many other particle sorting techniques previously studied.^{18,23}

The ability to sort rodlike particles, particularly in the nanometer range, holds important implications for applications based on materials such as gold nanorods, wherein rod lengths have a role to play in their response toward plasmonic excitation using coherent light. This has been applied for enhanced large scale data recording,²⁵ photothermal surgery,²⁶ and bioimaging.²⁷ It should also be noted that the color of the Brownian noise, although not investigated here, may hold subtle effects on the ability to sort. Previous studies conducted on quasistationary stochastic systems have shown links between the color of the Brownian noise and the ratcheted transport.^{28,29} There may also be methods to accelerate diffusion as studied previously by Spagnolo *et al.*^{30,31} to reduce the sorting time.

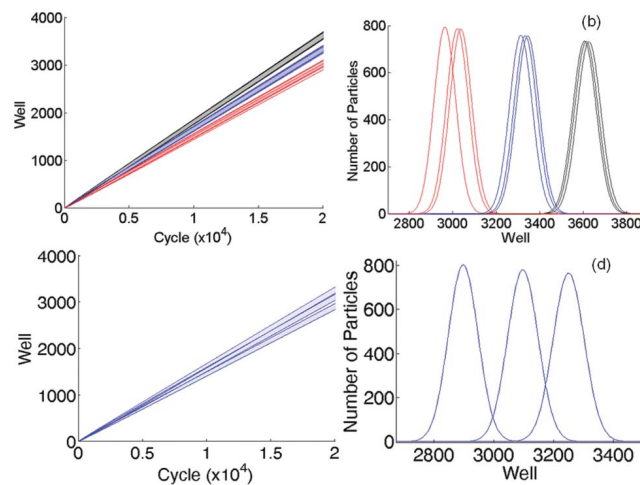


FIG. 5. [(a) and (c)] Plots of 10th and 90th percentiles of expected rod populations vs cycles, and [(b) and (d)] expected number of particles in each potential well at 20 000 cycles using an initial population of 10 000 particles. These were determined for [(a) and (b)] first stage sorting using 30 μ s off time with nine different rod dimensions (as shown in Table I) along three contours (overlaid dots in Fig. 3), and [(c) and (d)] second stage sorting using 400 ms off time with the blue population from the first stage (curve colors correspond to circles in Fig. 3).

IV. CONCLUSIONS

A new technique for sorting nanometer scale Brownian rods has been demonstrated. By exploiting the Brownian motion of these rods and using an asymmetric potential, a two stage sorting process can be used to isolate particles with specific dimensions. Simulation results have shown that rods with diameters ranging from 72 to 168 nm and a range of lengths from 528 to 969.6 nm can be sorted to achieve at least 80% separation within 2 h. The size difference between the rods considered in this study is relatively small compared to previous studies examining the sorting of spherical nanoparticles. By increasing this size difference, the required barrier lengths could be increased and sorting times consequently reduced. It may also be possible to sort a greater range by altering the diffusion coefficients of the differently sized rods. Possibilities include changing either the temperature or the viscosity of the surrounding medium, or using the height of the chamber to govern the degree of hydrodynamic interaction. The analysis presented here provides a basis for the attributes needed for a physical rod sorting device.

APPENDIX: BARRIER LENGTH DERIVATION

Here we provide a derivation of Eq. (6).

Take two particles with diffusion coefficients D_1 and D_2 at an off time t . These are normally distributed as described by the following PDFs:

$$X_1 \sim N(0, \sqrt{2D_1t}) \quad \text{and} \quad X_2 \sim N(0, \sqrt{2D_2t}).$$

The greatest difference between two normally distributed cumulative density functions occurs when their PDFs intersect, so we are interested in the points where $X_1 = X_2$. This is also the point at which we wish to put our barrier.

Equating PDFs leads to

$$\frac{1}{\sqrt{4\pi D_1t}} \exp\left(\frac{-X_1^2}{4D_1t}\right) = \frac{1}{\sqrt{4\pi D_2t}} \exp\left(\frac{-X_2^2}{4D_2t}\right),$$

$$\sqrt{\frac{D_2}{D_1}} = \exp\left(\frac{X_1^2}{4D_1t} - \frac{X_1^2}{4D_2t}\right) \quad (\text{since } X_1 = X_2),$$

$$\frac{1}{2} \ln\left(\frac{D_2}{D_1}\right) = \frac{X_1^2}{4t} \left(\frac{1}{D_1} - \frac{1}{D_2}\right),$$

$$2t \ln\left(\frac{D_2}{D_1}\right) = X_1^2 \left(\frac{D_2 - D_1}{D_1 D_2}\right),$$

$$X_1^2 = \frac{2t D_1 D_2 \ln\left(\frac{D_2}{D_1}\right)}{D_2 - D_1},$$

$$X_1 = \pm \sqrt{\frac{2t D_1 D_2 \ln\left(\frac{D_2}{D_1}\right)}{D_2 - D_1}}.$$

Since we have used asymmetric potential fields, only the positive root of this equation was of interest.

- ¹A. Einstein, *Ann. Phys.* **17**, 549 (1905).
- ²A. Einstein, *Ann. Phys.* **19**, 371 (1906).
- ³M. Smoluchowski, *Ann. Phys.* **21**, 756 (1906).
- ⁴P. S. Burada, P. Hänggi, F. Marchesoni, G. Schmid, and P. Talkner, *Chem. Phys. Chem.* **10**, 45 (2009).
- ⁵J. W. Swan and J. F. Brady, *Phys. Fluids*, **19**, 113306 (2007).
- ⁶J. W. Swan and J. F. Brady, *Phys. Fluids*, **22**, 103301 (2010).
- ⁷F. Perrin, *J. Phys. Radium*, **5**, 497 (1934).
- ⁸F. Perrin, *J. Phys. Radium*, **7**, 1 (1936).
- ⁹Y. Han, A. M. Alsayed, M. Nobili, J. Zhang, T. C. Lubensky, and A. G. Yodh, *Science* **314**, 626 (2006).
- ¹⁰B. Bhaduri, A. Neild, and T. W. Ng, *Appl. Phys. Lett.* **92**, 084105 (2008).
- ¹¹Y. Han, A. M. Alsayed, M. Nobili, and A. G. Yodh, *Phys. Rev. E* **80**, 011403 (2009).
- ¹²J. Elgeti and G. Gompper, *Europhys. Lett.* **85**, 38002 (2009).
- ¹³J. T. Padding and W. J. Briels, *J. Chem. Phys.* **132**, 054511 (2010).
- ¹⁴A. Neild, T. W. Ng, and W. M. S. Yui, *Opt. Express*, **17**, 5321, (2009).
- ¹⁵M. O. Magnasco, *Phys. Rev. Lett.* **71**, 1477 (1993).
- ¹⁶C. R. Doering, W. Horsthemke, and J. Riordan, *Phys. Rev. Lett.* **72**, 2984 (1994).
- ¹⁷C. R. Doering, *Physica A* **254**, 1 (1998).
- ¹⁸L. Gorre-Talini, S. Jeanjean, and P. Silberzan, *Phys. Rev. E* **56**, 2025 (1997).
- ¹⁹A. A. Dubkov and B. Spagnolo, *Phys. Rev. E* **72**, 041104 (2005).
- ²⁰A. Haljas, R. Mankin, A. Sauga, and E. Reiter, *Phys. Rev. E* **70**, 041107 (2004).
- ²¹J. Rousselet, L. Salome, A. Ajdari, and J. Prost, *Nature* **370**, 446 (1994).
- ²²H. Brenner, *Int. J. Multiphase Flow* **1**, 195 (1974).
- ²³A. Neild, T. W. Ng, and T. Woods, *Appl. Opt.* **48**, 6820–6826 (2009).
- ²⁴T. W. Ng, A. Neild, and P. Heeraman, *Opt. Lett.* **33**(6), 584 (2008).
- ²⁵P. Zijlstra, J. W. M. Chon, and M. Gu, *Nature* **459**, 410 (2009).
- ²⁶H. Kang, B. Jia, J. Li, D. Morrish, and M. Gu, *Appl. Phys. Lett.* **96**, 063702 (2010).
- ²⁷Y. Zhang, J. Yu, D. J. Birch, and Y. Chen, *J. Biomed. Opt.* **15**, 020504 (2010).
- ²⁸S. A. Guz and M. V. Sviridov, *Chaos* **11**, 605 (2001).
- ²⁹B. C. Bag and C.-K. Hu, *J. Stat. Mech.* **2**, P02003 (2009).
- ³⁰B. Spagnolo, A. A. Dubkov, and N. V. Agudov, *Physica A* **340**, 265 (2004).
- ³¹B. Spagnolo and A. A. Dubkov, *Eur. Phys. J. B* **50**, 299–303 (2006).

B.4 Optical force lateral push-pulling using focus positioning

874 J. Opt. Soc. Am. B / Vol. 29, No. 4 / April 2012

Muradoglu *et al.*

Optical force lateral push–pulling using focus positioning

Murat Muradoglu, Wesley Sung-Yee Chiu, and Tuck Wah Ng*

Laboratory for Optics, Acoustics, and Mechanics, Department of Mechanical and Aerospace Engineering, Monash University, Clayton, Victoria 3800, Australia

Received October 13, 2011; revised December 23, 2011; accepted December 23, 2011; posted December 23, 2011 (Doc. ID 156336); published March 30, 2012

The placement of the beam focus corresponding with the center of living matter (such as cells) in an optical tweezer can result in photodamage. We advance a scheme here that locates the focus of the beam either above or below the matter to pull and push relative to the beam axis in a predominant lateral sense based on the resultant action of scattering and gradient forces. Switching to a laser that acts oppositely serves to restore the axial position of the matter. Although an exact value could not be derived due to the statistical nature of Brownian perturbations and time frame considerations, we simulated the optical force fields to visualize the effective force envelope. The lateral optical push–pull operation was conducted experimentally on polystyrene beads in which the motion manipulation efficacy was characterized. © 2012 Optical Society of America

OCIS codes: 140.7010, 350.4855.

1. INTRODUCTION

The ability to move small-scale matter in a prescribed fashion optically is attractive in many areas of inquiry. The phenomenon known as photophoresis has been known for a long time in which the studies of Hettner [1] have shed much understanding. Direct photophoresis is caused by the transfer of photon momentum to a particle by refraction and reflection [2], and particle movement occurs when the particle is transparent and has an index of refraction larger compared to its surrounding medium. Indirect photophoresis occurs as a result of an increase in the kinetic energy of molecules when particles absorb incident light only on the irradiated side, thus creating a temperature gradient within the particle [3,4]. Direct photophoresis has been used in accomplishing operations [5,6]. When the light beam is sufficiently focused, the forces developed are strong enough to detach cells from adherent surfaces in a technique known as laser catapulting [7,8].

Light manipulation of matter advanced significantly with the work of Ashkin *et al.* [9] in which a single small piece of matter could be held in place using a method commonly known as laser tweezing. The ensuing efforts to harness this capability have been wide [10,11]. The ability to hold single matter in place is essentially gained through the gradient force component of the beam, which is strongest at the waist. That this is also the location of highest intensity of the beam presents a problem in manipulating cells, where there have been reports of photodamage [12–14]. The small and localized nature of light in surface plasmon trapping presents a possible solution [15] in which tailored leaky waves using surface corrugations from a subwavelength aperture offer the opportunity for flexible design [16]. Nevertheless, this is currently limited to matter manipulation at the surface and not in the medium.

Experiments to manipulate matter are often done in a fluid chamber that is limited in the axial dimension and as such involves matter moving more significantly in the lateral sense. It

is essentially not necessary to use tweezing to do this, although it is difficult to introduce a photophoretic force due to the constraints of applying illumination in the lateral sense. Airy beams offer a means of applying a light beam axially while obtaining accentuated matter motion in the lateral sense, albeit more in a ballistic manner [17]. We show, through numerical modeling and experimentation, that the axial and lateral positions of the matter relative to the beam focus position can be harnessed for this.

2. APPROACH

Consider the model of a dielectric sphere located at (x_p, z_p) along with a ray of light propagating in the positive z direction that is refracted from a lens with its focal point located at (x_f, z_f) . The force distribution associated with the sphere located at varying distances along the x axis, while restrained to $z_p = z_f$, shows some capability of particle movement, albeit only to a small extent [18]. The situation differs when the particle center is located within the regions indicated by I and II within the ray envelope depicted in Fig. 1(b). In the region denoted by I, where $z_p < z_f$, the asymmetry of forces will result in the combined scattering and gradient forces pulling the particle laterally toward the beam axis and also upward in the z direction. In the region denoted by II, where $z_p > z_f$, the scattering and gradient forces work against each other. At some distance z_e above the focal point, these two forces come into equilibrium and trap the particle. At points beyond the equilibrium, i.e., $z > z_e$, the gradient force dominates by pulling particles downward to z_e and laterally toward the beam axis, creating an effective potential well. While this is well known, we are interested in points well beyond z_e . We expect another equilibrium point, z_T , where the scattering force regains dominance and pushes particles upward and away from the beam axis.

We thus propose a switching system between two light sources to accomplish lateral positioning with light irradiation on a spherical particle, depicted in Fig. 2. We propose to

Muradoglu *et al.*

Vol. 29, No. 4 / April 2012 / J. Opt. Soc. Am. B 875

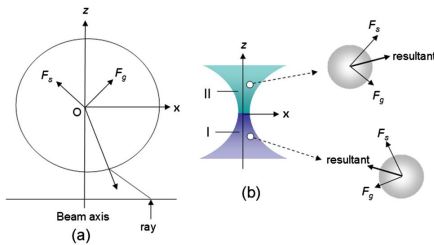


Fig. 1. (Color online) (a) Geometry of an incident ray giving rise to scattering F_s and gradient F_g forces and (b) the forces when sphere is located at regions below and above the focus.

achieve this by controlling (x_f, z_f) , i.e., the location of the beam focal point. With the laser arriving from the objective lens (state A), locating the focal point above the sphere so that $z_f > z_p$, the particle can be moved toward the beam axis and upward. Alternatively, locating the focal point below the sphere so that $z_f < z_p$, the particle can be moved away from the beam axis and upward. At this point, it is important to point out the possible action of buoyancy and sedimentation. If the particle is denser than the medium, sedimentation will limit movement of the particle upward, and one then will have motion almost exclusively in the lateral sense. However, if the particle is of equal or lower density than the medium, there will be a movement of particle axially upward as well as laterally. In this case, switching the laser to one that arrives from the opposite direction applies the basic photophoretic force to restore the sphere's axial position. As particle positioning is accomplished without it entering the beam focus, the propensity for photodamage is reduced.

In order to verify this scheme, it is vital to be able to obtain the optical force characteristics on the particle. On the surface, an approach that appears to work is to derive the optical force that is just enough to overcome the particle's static frictional force, as one should experience in the case of a solid resting on a solid. The situation with a particle located in liquid medium is however more complex due to the presence of Brownian forces that sets a particle in constant random motion and the friction force [19,20]. These movements are significant even at a micrometer scale. The ability of the particle to overcome inertia is limited by the intrinsic Brownian behavior that is statistical and also determined by the time frame in

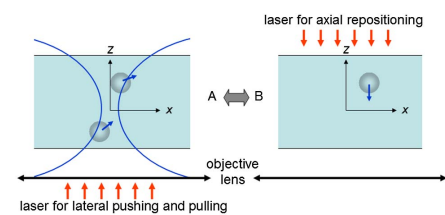


Fig. 2. (Color online) Proposed scheme where locating the beam focus below or above the sphere (state A) moves it laterally predominantly while a beam in the opposite direction (state B) restores the sphere axially.

question. Nevertheless, one should be able to derive an order of magnitude of the force needed from simulations of the optical force and then correlate it with the experimental findings.

3. NUMERICAL MODELING

We are interested in spherical particles of sizes that are known to violate ray optics, i.e., $a \approx \lambda$. For this reason we use the generalized Mie-Lorentz theory to calculate the optical forces. We have utilized a number of modified functions available in the Optical Tweezer toolbox [21]. The technique utilized in [21] relies on an over determined point-matched multipole expansion of the Gaussian beam. We use the vector spherical wave function addition theorem to obtain off-axis sphere positions. Because of the natural asymmetry of such a shift, the number of expansion terms required becomes significant and grows rapidly for large translations.

We simulate with an incident x -polarized TEM_{00} Gaussian beam with a numerical aperture (NA) of 0.98 and wavelength of $1.06 \mu\text{m}$. The surrounding medium is assumed to be water with a refractive index of $n = 1.33$ resulting in a beam angle of approximately 47° . Placing polystyrene particles with a refractive index of 1.59 and $3 \mu\text{m}$ radius at a grid of points, we produced a map of the optical force field. The results are expressed in units of force efficiency Q , where the optical force is given by $F = nPQ/c$, in which P is the beam power at the focus and c is the speed of light in free space. In carrying out the simulation, we found that we had to significantly limit the grid size due to the rapidly growing number of expansion terms required at points far from the focal point. Such an approach will suffice in the context of our analysis. Execution times and memory requirements depended significantly on the translation distance from the focal point.

4. EXPERIMENTATION

Experimentation was done on a conventional laser single beam trapping system (Cell Robotics, Inc.) operating at a wavelength of 1064 nm and having full power of 5 W . Video sequences were captured using a video camera (Moticam 2000) and digitized for image analysis. The setup of the system that was applied on an inverted microscope configuration is given in Fig. 3. Polystyrene beads of $6 \mu\text{m}$ diameter (Bangs Laboratories) were used. In order to reduce sticking to surfaces, Triton-X100 reagent (Sigma Aldrich) was added to the bead suspension [22]. The bead solution was then placed in a chamber created by sealing two coverslips. The laser trap was operated using a $60\times$ objective having an NA of 0.98. The positioning of the bead relative to the beam center was done by visual estimation and tracking the movement of the stage in the x , y , and z direction (available from the driver software).

5. RESULTS AND DISCUSSION

We first consider the optical force simulations. In order to approach this more systematically, we demarcate three beam axis distance regions relative to the beam center: (i) the focal point region (from -4 to $4 \mu\text{m}$), (ii) the post-focal-point region (4 to $16 \mu\text{m}$) and (iii) the pre-focal-point region (-13 to $-4 \mu\text{m}$). For the focal-point region, we have the optical force profiles for the x - [Fig. 4(a)] and z - [Fig. 4(b)] axes components calculated for a particle of radius $3.0 \mu\text{m}$. This is the region that is most reported. In relation to the x -axis component, one finds

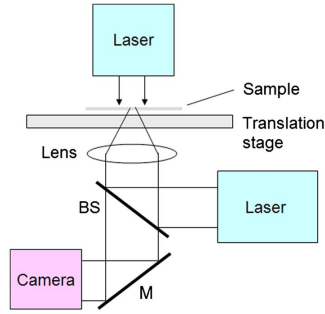


Fig. 3. (Color online) Schematic description of the optical push-pull setup used. BS, beam splitter; M mirror.

an island of maximal efficiency of approximately 0.5 located away from the z axis a distance of $3 \mu\text{m}$. The nature of this force distribution indicates that pulling in particles from radial distances further away is rather improbable. With the z -axis component, one finds a region of zero force (located about $3 \mu\text{m}$ from the focal point) that corresponds to z_{es} , the “sweet spot” of conventional single beam trapping wherein the gradient force and scattering force are in equilibrium.

If we shift our attention to the post-focal-point region, we find the x -axis force component undergoing a crossover [indicated by the green line marked with a zero in Fig. 5(a)] between the pulling and pushing forces. From a zoomed-in plot of the pushing region [Fig. 5(c)], one finds the interesting transition line, z_T , in which particles should be pushed away from the beam axis (in the x direction). Such a situation confirms that, as long as the z -axis position is above the crossover, the particle should never be able to enter the beam axis as long as

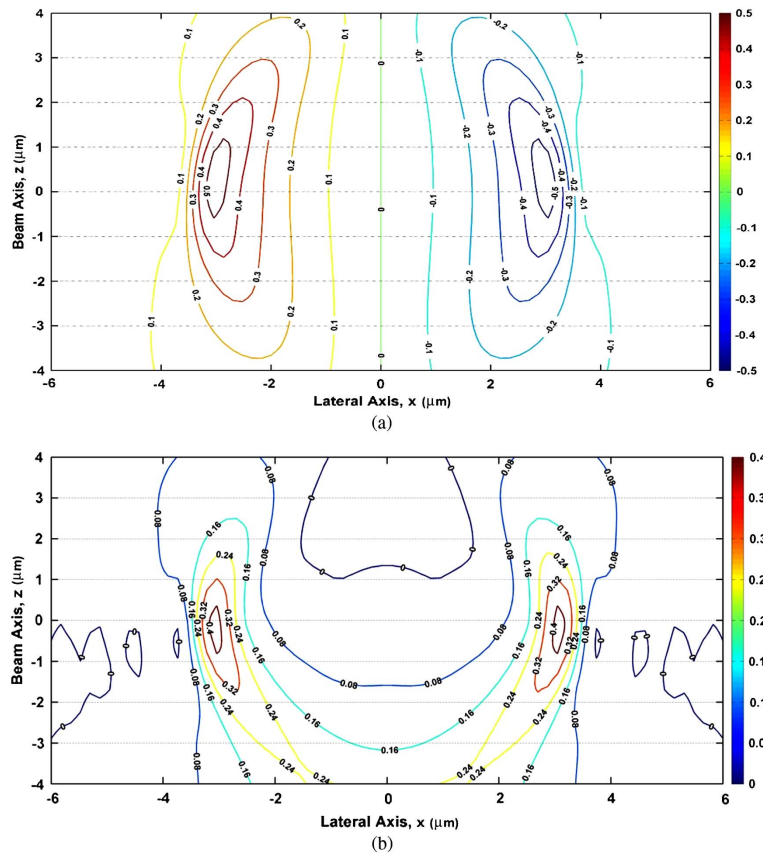


Fig. 4. (Color online) Contour plots of the optical force efficiency on a $3 \mu\text{m}$ polystyrene particle shown separated into its (a) y component Q_y and (b) z component Q_z , within the central trapping region. The results indicate the well-known equilibrium point located slightly above the focal point.

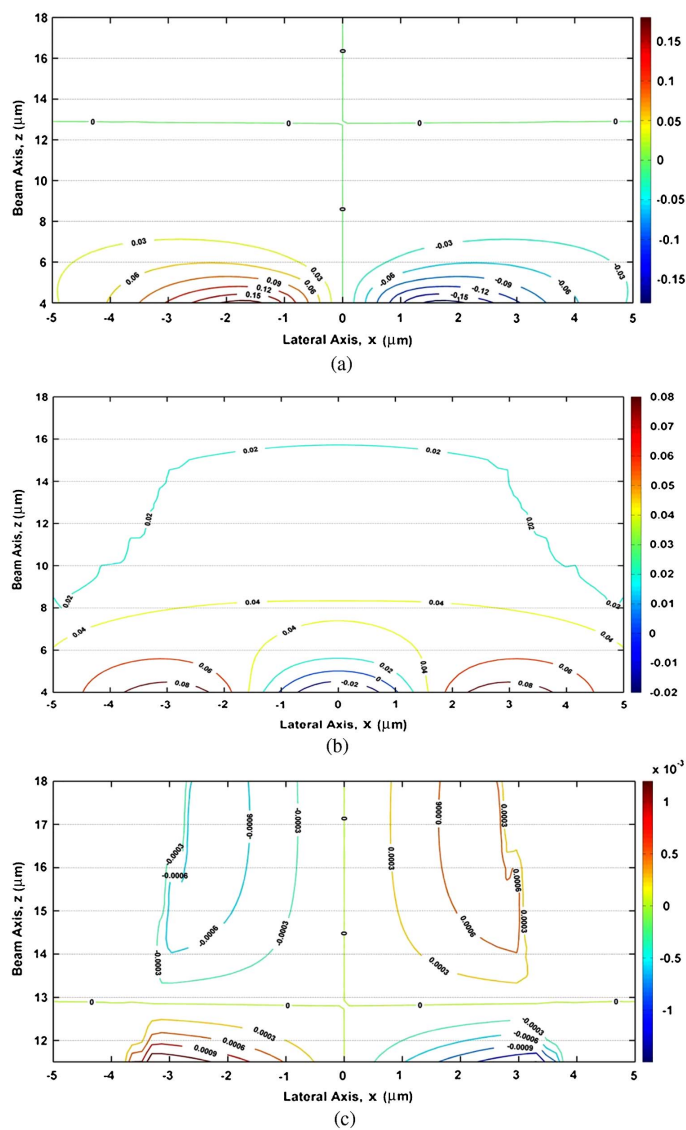


Fig. 5. (Color online) Contour plots of the optical force efficiency on a $3\ \mu\text{m}$ polystyrene particle shown separated into its (a) y component Q_y and (b) z component Q_z , at points 4 to 16 μm above the focal point. The transition line (green line) in (a) indicates the boundary where the optical forces switch polarity, i.e., from pulling to pushing. (c) y component Q_y for the region near the transition line.

the laser is on. This seems to be counterintuitive for a focused laser beam. No force changeover, however, exists for the z component of the force, which remains positive throughout

[Fig. 5(b)]. It is noteworthy that the magnitude of force efficiency in the x direction is 6×10^{-4} , which is almost 3 orders lower than in the central region. To better understand the

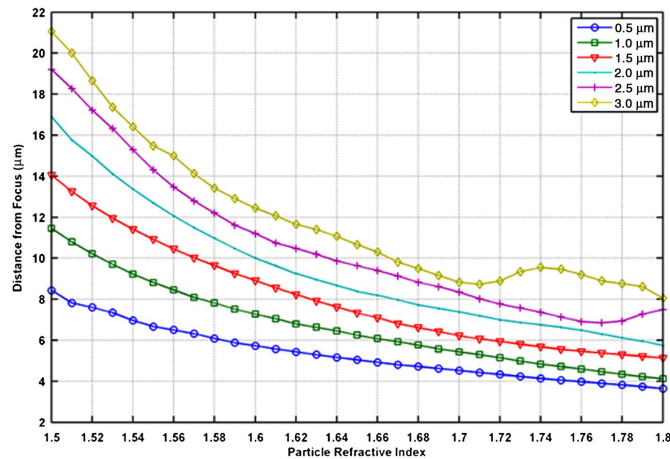


Fig. 6. (Color online) Plots of distance to transition line, z_T , versus particle refractive index. Each line corresponds to a different particle size.

transition line, we simulated for varying particle size and refractive index combinations. The results are presented in Fig. 6, where the x axis and y axis indicate the refractive index and the distance from the focal point to the transition line, respectively. We find that the use of a lower refractive index pushes the transition line higher and a smaller particle size pushes the transition line lower. The relationship between these parameters is not linear, and we also observe that the transition line does not always appear as a straight line but rather a curved line for a large refractive index and particle size. As the particle refractive index approaches that of water ($n = 1.33$), the results show that an asymptote will appear, i.e., there cannot be any transition line. In the case of red blood cells, which we model as having a refractive index of 1.4 [23] and radius $3 \mu\text{m}$, the transition line occurs much further upward at $z_T \approx 34 \mu\text{m}$. This imputes that as long as one operates in the post focal region, living material such as cells cannot be drawn into the laser beam where laser damage can occur.

In the case of the pre-focal-point region, one finds the x -component force [Fig. 7(a)] and z -component force [Fig. 7(b)] maps that draw particles toward the beam axis and upward. As it is computationally onerous to extend this to a larger coverage, we consider the case of the x - and z -components force plots for various x -axis distances at a fixed z -axis distance of -13 to $-4 \mu\text{m}$. Here we find a more significant drop off in the z -component force when further away from the beam axis. This translates to particles being drawn in toward the beam axis. Such a trend conforms toward the envelope of the light beam. It will appear then that the use of a larger NA lens should increase the propensity of movement toward the beam axis. Overall, the simulation results show that it is possible to support the particle manipulation scheme described earlier.

The experimental results shown in Fig. 8(a) gives an example image recorded with the beam focus located axially above some surrounding particles. The particles were found to be

drawn toward the beam axis (denoted by cursor). Figure 8(b) alternatively is an example image in which the beam focus is axially placed below a surrounding particle. In this case, the particle was seen to be nudged away from the beam axis. Both cases are illustrated more readily from the video footage provided. The particles are observed to be slightly blurry as the laser beam focus corresponds with the imaging focus.

To experimentally characterize the pull and push effect of the method, a single particle was selected in which its center was located by image focusing. The laser focus was then set at a z -axis setting and some x -axis distance from the particle center. With the laser switched on, the x -axis distance of the beam focus was slowly brought in until particle experiences movement. This process was repeated for various z -axis distance settings for one data set. These data sets were collected at 20%, 40%, and 50% of full power of the system.

The results are depicted in Fig. 9. The most apparent feature is the asymmetry of each distribution about the axial beam focus position. It is clear that the ability of the particle to be pulled toward the beam axis is significantly greater than for it to be pushed away. This follows the trends found in the numerical simulations. One also finds a greater capability for pushing and pulling to be accomplished when the axial distance between the sphere center and beam focus is increased, which on the surface appears rather counterintuitive. This behavior is attributed to the light ray envelope as it refracts from the lens. Nevertheless, there are upper limits with which this can occur. With 50% full power for instance, the ability to pull and push particles from the surrounding is limited to about 65 and $30 \mu\text{m}$, respectively. It should be noted that, when operating at high powers, the particle will experience greater intensity as it gets closer toward the beam focus. With cells, this will translate to greater propensity for photodamage. Strategies that can be adopted to ameliorate this include tuning the laser power according to the particle to beam axis distance or

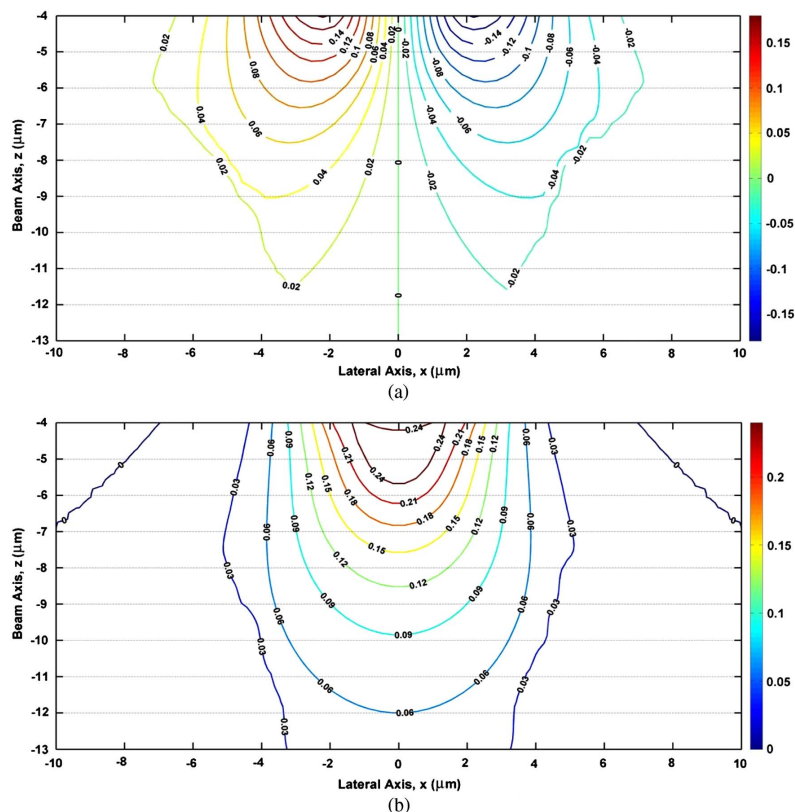


Fig. 7. (Color online) Contour plots of the optical force efficiency on a $3\ \mu\text{m}$ polystyrene particle shown separated into its (a) y component Q_y , and (b) z component Q_z , at points 4 to $13\ \mu\text{m}$ below the focal point.

shifting the beam axis. The latter remedy runs the risk of drawing in or pushing away unintended particles in the vicinity. Overall, one finds this scheme most suited for short-range lateral particle actuation.

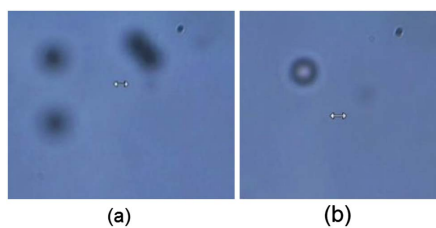


Fig. 8. (Color online) Images of laser beam focus located axially (a) above and (b) below particles. The former pulls and the latter pushes particles laterally with respect to the beam axis (cursor). (Media 1)

The results also indicate that the lower limit of lateral influence (near the beam focus) is reserved for pulling the bead to the beam axis rather than pushing away from it. With 50% full power, the bead experienced a pull when it came within $10\ \mu\text{m}$ of the beam axis. With 40% full power, it needed to come to within $6\ \mu\text{m}$. Both are for the beam focus located at an axial distance of $5\ \mu\text{m}$ above the bead center. In order to experience a push, the bead must not be further than $18\ \mu\text{m}$ from the beam axis at 50% full power at zero axial distance between bead center and beam focus. With 40% full power, the bead will experience pushing only if it were within about $12\ \mu\text{m}$ from the beam axis.

The higher propensity of pulling rather than pushing relative to the beam axis presents a real possibility of the bead being drawn quickly into the focus. Once trapped within, maximal photodamage can readily occur. In light of this, it might be prudent to use the pull operation to draw a particle from further away toward the beam axis but when it is sufficiently near to switch over to a pushing mode. This then allows the

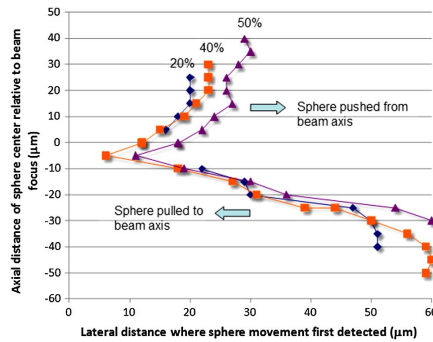


Fig. 9. (Color online) Plots of lateral distances where sphere movement were first detected against axial distances of beam focus relative to sphere center at different optical powers (percent of maximum). The axes units are in micrometers.

particle to be nudged to its intended lateral position. Our simulations have indicated that refractive index and size changes will not draw particles into the beam. In our experiments we found that the axial positions did not alter significantly. This was likely due to the polystyrene beads having density (1.05 g/cm^3) greater than water as mentioned earlier. Hence, using just the laser trap alone may suffice, although there is the option to restore the axial position otherwise.

It should be noted that the manipulation of submicrometer particles will need to take into account the significant Brownian motion influence at this length scale [6,24]. The strategy described here will not quench this motion as well as placing the particle inside the trap. Nevertheless, it should still offer the ability to locate such sized matter within a reasonable region of constraint. It should be noted that the measurements have a high degree of uncertainty as it is essentially difficult to establish the exact moment a particle starts to move.

6. CONCLUSIONS

In summary, we have proposed a scheme that locates the focus of the beam either above or below the matter to pull and push it relative to the beam axis in a predominant lateral sense using the resultant action of scattering and gradient forces. Numerical simulation and experimental results confirm this approach. This simple approach offers remedy to photodamage of living matter held using conventional optical tweezers.

ACKNOWLEDGMENTS

Parts of this work were made possible by support from Australian Research Council Discovery project grants DP0878454 and DP120100583. T. W. N. acknowledges funding support from the Monash NSMRF and ESG schemes. Technical support by I. Hatzinisiriou is appreciated.

REFERENCES

- G. Hettner, "Zur Theorie der Photophorese," *Z. Phys.* **37**, 179–192 (1926).

- A. Ashkin, "History of optical trapping and manipulation of small-neutral particle, atoms, and molecules," *IEEE J. Sel. Top. Quantum Electron.* **6**, 841–856 (2000).
- T. Iwaki, "Effect of internal flow on the photophoresis of a micron-sized liquid droplet," *Phys. Rev. E* **81**, 066315 (2010).
- C. Y. Soong, W. K. Li, C. H. Liu, and P. Y. Tzeng, "Theoretical analysis for photophoresis of a microscale hydrophobic particle in liquids," *Opt. Express* **18**, 2168–2182 (2010).
- M. Tamagawa, H. Morishiro, and H. Watarai, "Microgravity laser-photophoresis of high density microparticles in water," *Colloids Surf. A* **220**, 279–284 (2003).
- T. W. Ng, A. Neild, and P. Heeraman, "Continuous sorting of Brownian particles using coupled photophoresis and asymmetric potential cycling," *Opt. Lett.* **33**, 584–586 (2008).
- A. Vogel, V. Homeffer, K. Lorenz, N. Linz, G. Hüttmann, and A. Gebert, "Principles of laser microdissection and catapulting of histologic specimens and live cells," *Methods Cell Biol.* **82**, 153–205 (2007).
- A. Siddiqi, T. W. Ng, and A. Neild, "Specific collection of adherent cells using laser release in a droplet-driven capillary cell," *J. Biomed Opt.* **15**, 065003 (2010).
- A. Ashkin, J. M. Dziedzic, J. E. Bjorkholm, and S. Chu, "Observation of a single-beam gradient force optical trap for dielectric particles," *Opt. Lett.* **11**, 288–290 (1986).
- D. G. Grier, "A revolution in optical manipulation," *Nature* **424**, 810–816 (2003).
- K. Dholakia, "An optical physicist sees the light," *Nature* **457**, 1061 (2009).
- K. König, H. Liang, M. W. Berns, and B. J. Tromberg, "Cell damage in near-infrared multimode optical traps as a result of multiphoton absorption," *Opt. Lett.* **21**, 1090–1092 (1996).
- H. Schneckenburger, A. Hendinger, R. Sailer, M. H. Gschwend, W. S. Strauss, M. Bauer, and K. Schütze, "Cell viability in optical tweezers: high power red laser diode versus Nd:YAG laser," *J. Biomed Opt.* **5**, 40–44 (2000).
- U. Mirsaidov, W. Timp, K. Timp, M. Mir, P. Matsudaira, and G. Timp, "Optimal optical trap for bacterial viability," *Phys. Rev. E* **78**, 021910 (2008).
- X. Miao and L. Y. Lin, "Trapping and manipulation of biological particles through a plasmonic platform," *IEEE J. Sel. Top. Quantum Electron.* **13**, 1655–1662 (2007).
- M. Muradoglu, T. W. Ng, A. Neild, and I. Gralinski, "Tailored leaky plasmon waves from a subwavelength aperture for optical particle trapping on a chip," *J. Opt. Soc. Am. B* **28**, 602–607 (2011).
- J. Baumgartl, M. Mazilu, and K. Dholakia, "Optically mediated particle clearing using Airy wavepackets," *Nat. Photon.* **2**, 675–678 (2008).
- A. Ashkin, "Forces of a single-beam gradient laser trap on a dielectric sphere in the ray optics regime," *Biophys. J.* **61**, 569–582 (1992).
- H. J. H. Clercx and P. P. J. M. Schram, "Brownian particles in shear flow and harmonic potentials: a study of long-time tails," *Phys. Rev. A* **46**, 1942–1950 (1992).
- B. Lukic, S. Jeney, Z. Sviben, A. J. Kulik, E.-L. Florin, and L. Forró, "Motion of a colloidal particle in an optical trap," *Phys. Rev. E* **76**, 011112 (2007).
- T. A. Nieminen, V. L. Y. Loke, A. B. Stilgoe, G. Knoner, A. M. Branczyk, N. R. Heckenberg, and H. Rubinsztein-Dunlop, "Optical tweezers computational toolbox," *J. Opt. A* **9**, S196–S203 (2007).
- M. Nayeria, R. Karlsson, and J. Bergenholtz, "Surfactant effects on colloidal interactions: Concentrated micellar solutions of nonionic surfactant," *Colloids Surf. A* **368**, 84–90 (2010).
- Y. K. Park, M. Diez-Silva, G. Popescu, G. Lykotrafitis, W. Choi, M. S. Feld, and S. Suresh, "Refractive index maps and membrane dynamics of human red blood cells parasitized by *Plasmodium falciparum*," *Proc. Natl. Acad. Sci. USA* **105**, 13730–13735 (2008).
- A. Neild, J. T. Padding, Y. Lu, B. Bhaduri, W. J. Briels, and T. W. Ng, "Brownian diffusion transitions of carbon nanofibers under wall interaction," *Phys. Rev. E* **82**, 041126 (2010).

B.5 Optical stirring in a droplet cell bioreactor

Optical stirring in a droplet cell bioreactor

Murat Muradoglu,¹ Thuong Le,¹ Chun Yat Lau,¹ Oi Wah Liew,² and Tuck Wah Ng^{1,*}

¹Laboratory for Optics, Acoustics, and Mechanics, Monash University, Clayton, VIC3800, Australia

²Cardiovascular Research Institute, Centre for Translational Medicine, 14, Medical Drive, 117599 Singapore

Abstract: In the context of a bioreactor, cells are sensitive to cues from other cells and mechanical stimuli from movement. The ability to provide the latter in a discrete fluidic system presents a significant challenge. From a prior finding that the location of the focus of a laser below particles relative to the beam axis producing a pushing effect in a predominant lateral sense, we advance an approach here that generates a gentle and tunable stirring effect. Computer simulation studies show that we are able to characterize this effect from the parameters that govern the optical forces and the movement of the particles. Experimental results with polystyrene microbeads and red blood cells confirm the notions from the simulations.

© 2012 Optical Society of America

OCIS codes: (170.4520) Optical confinement and manipulation; (170.3890) Medical optics instrumentation; (140.7010) Laser trapping.

References and links

1. J. Chen, Z. Yu, L. Zhang, and G. Chen, "Microfluidic bioreactors for highly efficient proteolysis," *Curr. Chem. Biol.* **3**(3), 291–301 (2009).
2. H. N. Vu, Y. Li, M. Casali, D. Irimia, Z. Megeed, and M. L. Yarmush, "A microfluidic bioreactor for increased active retrovirus output," *Lab Chip* **8**(1), 75–80 (2008).
3. E. Figallo, C. Cannizzaro, S. Gerecht, J. A. Burdick, R. Langer, N. Elvassore, and G. Vunjak-Novakovic, "Micro-bioreactor array for controlling cellular microenvironments," *Lab Chip* **7**(6), 710–719 (2007).
4. M. He, J. S. Edgar, G. D. M. Jeffries, R. M. Lorenz, J. P. Shelby, and D. T. Chiu, "Selective encapsulation of single cells and subcellular organelles into picoliter- and femtoliter-volume droplets," *Anal. Chem.* **77**(6), 1539–1544 (2005).
5. S. Daniel, M. K. Chaudhury, and P. G. de Gennes, "Vibration-actuated drop motion on surfaces for batch microfluidic processes," *Langmuir* **21**(9), 4240–4248 (2005).
6. H. Y. Tan, T. W. Ng, A. Neild, and O. W. Liew, "Point spread function effect in image-based fluorescent microplate detection," *Anal. Biochem.* **397**(2), 256–258 (2010).
7. J. K. K. Lye, T. W. Ng, and W. Y. L. Ling, "Discrete microfluidics transfer across capillaries using liquid bridge stability," *J. Appl. Phys.* **110**(10), 104509 (2011).
8. J. J. Zhong, K. Fujiyama, T. Seki, and T. Yoshida, "A quantitative analysis of shear effects on cell suspension and cell culture of *perilla frutescens* in bioreactors," *Biotechnol. Bioeng.* **44**(5), 649–654 (1994).
9. W. Y. Sim, S. W. Park, S. H. Park, B. H. Min, S. R. Park, and S. S. Yang, "A pneumatic micro cell chip for the differentiation of human mesenchymal stem cells under mechanical stimulation," *Lab Chip* **7**(12), 1775–1782 (2007).
10. A. Ashkin, "History of optical trapping and manipulation of small-neutral particle, atoms, and molecules," *IEEE J. Sel. Top. Quantum Electron.* **6**(6), 841–856 (2000).
11. T. Iwaki, "Effect of internal flow on the photophoresis of a micron-sized liquid droplet," *Phys. Rev. E Stat. Nonlin. Soft Matter Phys.* **81**(6), 066315 (2010).
12. A. Vogel, V. Horneffer, K. Lorenz, N. Linz, G. Hüttmann, and A. Gebert, "Principles of laser microdissection and catapulting of histologic specimens and live cells," *Methods Cell Biol.* **82**, 153–205 (2007).
13. A. Siddiqi, T. W. Ng, and A. Neild, "Specific collection of adherent cells using laser release in a droplet-driven capillary cell," *J. Biomed. Opt.* **15**(6), 065003 (2010).
14. A. Ashkin, J. M. Dziedzic, J. E. Bjorkholm, and S. Chu, "Observation of a single-beam gradient force optical trap for dielectric particles," *Opt. Lett.* **11**(5), 288–290 (1986).
15. K. König, H. Liang, M. W. Berns, and B. J. Tromberg, "Cell damage in near-infrared multimode optical traps as a result of multiphoton absorption," *Opt. Lett.* **21**(14), 1090–1092 (1996).
16. U. Mirsaidov, W. Timp, K. Timp, M. Mir, P. Matsudaira, and G. Timp, "Optimal optical trap for bacterial viability," *Phys. Rev. E Stat. Nonlin. Soft Matter Phys.* **78**(2), 021910 (2008).
17. M. Muradoglu, W. S. Y. Chiu, and T. W. Ng, "Optical force lateral push-pulling using focus positioning," *J. Opt. Soc. Am. B* **29**(4), 874–880 (2012).

18. T. A. Nieminen, V. L. Y. Loke, A. B. Stilgoe, G. Knoner, A. M. Branczyk, N. R. Heckenberg, and H. Rubinsztein-Dunlop, "Optical tweezers computational toolbox," *J. Opt. A, Pure Appl. Opt.* **9**(8), S196–S203 (2007).
19. B. H. P. Cheong, V. Diep, T. W. Ng, and O. W. Liew, "Transparency-based microplates for fluorescence quantification," *Anal. Biochem.* **422**(1), 39–45 (2012).
20. H. Li, J. R. Friend, and L. Y. Yeo, "Microfluidic colloidal island formation and erasure induced by surface acoustic wave radiation," *Phys. Rev. Lett.* **101**(8), 084502 (2008).
21. J. Whitehill, A. Neild, T. W. Ng, and M. Stokes, "Collection of suspended particles in a drop using low frequency vibration," *Appl. Phys. Lett.* **96**(5), 053501 (2010).
22. H. Xia, J. Wang, Y. Tian, Q. D. Chen, X. B. Du, Y. L. Zhang, Y. He, and H. B. Sun, "Ferrofluids for fabrication of remotely controllable micro-nanomachines by two-photon polymerization," *Adv. Mater. (Deerfield Beach Fla.)* **22**(29), 3204–3207 (2010).
23. B. Weiss, W. Hilber, R. Holly, P. Gittler, B. Jakoby, and K. Hingerl, "Dielectrophoretic particle dynamics in alternative-current electro-osmotic micropumps," *Appl. Phys. Lett.* **92**(18), 184101 (2008).
24. J. A. King and W. M. Miller, "Bioreactor development for stem cell expansion and controlled differentiation," *Curr. Opin. Chem. Biol.* **11**(4), 394–398 (2007).
25. N. K. Inamdar, L. G. Griffith, and J. T. Borenstein, "Transport and shear in a microfluidic membrane bilayer device for cell culture," *Biomicrofluidics* **5**(2), 022213 (2011).
26. C. M. Potter, M. H. Lundberg, L. S. Harrington, C. M. Warboys, T. D. Warner, R. E. Berson, A. V. Moshkov, J. Gorelik, P. D. Weinberg, and J. A. Mitchell, "Role of shear stress in endothelial cell morphology and expression of cyclooxygenase isoforms," *Arterioscler. Thromb. Vasc. Biol.* **31**(2), 384–391 (2011).
27. K. Yamamoto, T. Sokabe, T. Watabe, K. Miyazono, J. K. Yamashita, S. Obi, N. Ohura, A. Matsushita, A. Kamiya, and J. Ando, "Fluid shear stress induces differentiation of Flk-1-positive embryonic stem cells into vascular endothelial cells in vitro," *Am. J. Physiol. Heart Circ. Physiol.* **288**(4), H1915–H1924 (2005).
28. J. R. Glossop and S. H. Cartmell, "Effect of fluid flow-induced shear stress on human mesenchymal stem cells: differential gene expression of IL1B and MAP3K8 in MAPK signaling," *Gene Expr. Patterns* **9**(5), 381–388 (2009).
29. Z. Yang, W. H. Xia, Y. Y. Zhang, S. Y. Xu, X. Liu, X. Y. Zhang, B. B. Yu, Y. X. Qiu, and J. Tao, "Shear stress-induced activation of Tie2-dependent signaling pathway enhances reendothelialization capacity of early endothelial progenitor cells," *J. Mol. Cell. Cardiol.* **52**(5), 1155–1163 (2012).
30. M. Murga-Ramirez, M. T. Collados-Larumbe, K. E. Johnson, M. J. Rivas-Arreola, L. M. Carrillo-Cocom, and M. M. Álvarez, "Hydrodynamic conditions induce changes in secretion level and glycosylation patterns of Von Willebrand factor (vWF) in endothelial cells," *J. Biosci. Bioeng.* **109**(4), 400–406 (2010).
31. Y. Ban, Y. Y. Wu, T. Yu, N. Geng, Y. Y. Wang, X. G. Liu, and P. Gong, "Response of osteoblasts to low fluid shear stress is time dependent," *Tissue Cell* **43**(5), 311–317 (2011).

1. Introduction

A bioreactor, in the context of cell culture, refers to a device or system meant to grow cells or tissues. Traditionally, cell cultivation processes required the screening of large numbers of cell lines in shake flask cultures. The need to carry out a vast number of development cultivations has led to the increasing widespread deployment of small-scale bioreactor systems that offer miniaturized and high throughput solutions. This has led to efforts in incorporating microfluidics [1–3] which has resulted in arguably the smallest bioreactor possible using optical tweezers [4]. In the realm of microfluidics, there is a trend towards the use of discrete volume systems that offer flexible and scalable system architectures as well as high fault tolerance capabilities [5–7]. Moreover, because sample volumes can be controlled independently, such systems have greater ability for reconfiguration whereby groups of unit parts in an array can be altered to change their functionality.

Cells are often sensitive to their microenvironment in which cues from other cells, and mechanical stimuli from movement are crucial [8,9]. The ability to provide the latter in a discrete fluidic system presents a significant challenge. The ability to use light to move matter is linked to the photophoresis effect. Direct photophoresis is caused by the transfer of photon momentum to a particle by refraction and reflection [10], when the particle is transparent and has an index of refraction larger compared to its surrounding medium. Indirect photophoresis occurs as a result of an increase in the kinetic energy of molecules when particles absorb incident light only on the irradiated side, thus creating a temperature gradient within the particle [11]. When the light beam is sufficiently focused, the forces developed are strong enough to detach cells from adherent surfaces in a technique known as laser catapulting [12,13]. Laser tweezing, alternatively, is accomplished through the gradient force component of a focused laser beam, which is strongest at the waist [14]. That this is also the location of highest intensity of the beam presents a problem in manipulating cells, where there have been

reports of photodamage [15,16]. Intuitively, the capacity to provide mechanical stimuli will benefit from a gentle ‘stirring’ of the contents within with as little photodamage as possible. Whilst it is conceivable that direct photophoresis may provide the means of doing this, such a system will generally be difficult to fabricate. An approach that locates the focus of the beam either above or below in order to pull and push particles relative to the beam axis in a predominant lateral sense was recently reported [17]. We show here that this approach offers the ability for generating a gentle and tunable stirring effect.

2. Approach

In region I in Fig. 1(a), the asymmetry of forces will result in the combined scattering and gradient forces pulling the particle laterally towards the beam axis and also upwards in the z -direction. In region II, the scattering and gradient forces work against each other resulting in a lateral force that pushes particles away from the beam axis. At some distance above the focal point these two forces come into equilibrium and trap the particle. At points beyond the equilibrium, the gradient force dominates by pulling particles downwards and laterally towards the beam axis creating an effective potential well.

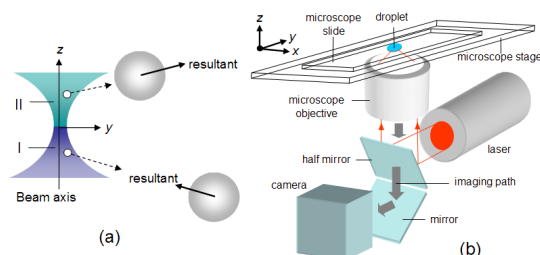


Fig. 1. (a) The geometry of an incident focused laser beam that gives rise to scattering and gradient forces such that the resultant forces when sphere located at regions below (I) and above (II) the focus moves the sphere towards and away from the beam axis respectively. The setup to accomplish optical stirring (b) involves focusing the laser beam close to the bottom surface of the droplet and using the microscope stage to move the slide and droplet in the x - y plane.

In being able to stir effectively without the particle ever falling into the beam focus (where photodamage may occur) it would be necessary for the particle to only reside in the region denoted by II. We thus propose a system described in Fig. 1(b) whereby the laser beam is focused within the liquid medium but close to the bottom surface of the droplet. Coincidentally, this is also the region where the particles (if they are large enough) will settle by gravitational sedimentation. For sedimentation to be facilitated or hastened, an auxiliary light source from above can be used to create a photophoretic force downwards. Stirring is accomplished simply by moving the slide and droplet around in the x - y plane using the microscope stage. One strategy will be to perform a line scan along the x direction followed by step movements in the y direction or vice-versa. The degree with which a particle ‘bounces off’ the laser beam center will depend on the relative position between the particle and beam center, the translator’s speed, the laser beam power for a specific particle’s refractive index and size, and hydrodynamic effects.

3. Numerical modeling

Spherical particles of sizes $a \approx \lambda$, where λ is the light wavelength, and a is the particle radius are known to violate the ray optics condition. In this regime we calculate the optical forces using the Generalized Mie-Lorentz Theory (GMLT) [18]. We simulate with an incident x -

polarized TEM₀₀ Gaussian beam under a numerical aperture (NA) of 0.98 and wavelength of 1.06 μm . The surrounding medium is assumed to be water with a refractive index of $n = 1.33$. Placing polystyrene particles with a refractive index of 1.59 and 3 μm radius at a grid of points we produced and stored a map of the optical force efficiency. The units of optical force efficiency Q , can be related to the optical force, F , by $F = nPQ/c$ in which P is the beam power at the focus, and c is the speed of light in free space. In carrying out the optical force simulation, we found that we had to significantly limit the grid size due to the rapidly growing number of expansion terms required at points far from the focal point. Due to the inherent rotational symmetry about the z -axis, we limit our calculations to only the x - z plane. Once a map of Q over the x - z plane in region II was obtained, the dynamic equations of motion were applied to an inertial frame, i.e. the microscope stage moving at a constant speed, v_p , over the fixed laser beam. In this model, the very low Reynolds number (much less than 1), dictates that the Stokes drag term is linearly dependent on velocity. Hydrodynamic effects associated with the relative position of the particle to the coverslip walls were neglected.

4. Experimental

Experimentation was done on a conventional laser single beam trapping system (Cell Robotics Inc.) operating at a wavelength of 1064nm and having a rated full power of 5W. Video sequences were captured using a video camera (Moticam 2000) and digitized for image analysis. Polystyrene beads of 6 μm diameter (Bangs Laboratories) were used. In order to reduce sticking to surfaces, Triton-X100 reagent (Sigma Aldrich) was added to the bead suspension. The bead solution was then placed as droplet in a circular shallow chamber created by varnish or silicone tape [19]. The laser trap was operated using a 60X objective having a numerical aperture (NA) of 0.98. Similar experiments were also conducted with red blood cells from sheep (R3378 Sigma Aldrich). These samples, originally in dry powder form and glutaraldehyde treated, were rehydrated using 0.9% sodium chloride solution.

5. Results and discussion

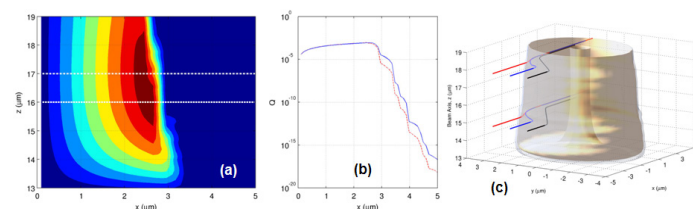


Fig. 2. (a) Contour plot of the optical force efficiency, Q , in the x - z plane beyond the transition line. (b) Plot of optical force efficiency, Q , along $z = 16\mu\text{m}$ and $z = 17\mu\text{m}$ as indicated by the solid and dashed lines, respectively. The optical force efficiency drops off rapidly after 3.5 μm . Based on this observation we safely neglect optical force calculations beyond 8 μm to lessen computational demands. The trajectories of particles at different starting locations with $z = 15\mu\text{m}$ and $z = 18\mu\text{m}$ is shown in (c). The magnitude of the sum of x and y force components is rendered in as an iso-surface. The line colors indicate the entry point of particles in the x - y plane, with black being at $x = 4\mu\text{m}$, $y = 0.5\mu\text{m}$, blue at $x = 4\mu\text{m}$, $y = 1.5\mu\text{m}$, and red at $x = 4\mu\text{m}$, $y = 2.5\mu\text{m}$.

We begin with the beam modeling results. The calculated optical force efficiency, Q , in the x - z plane is shown in Fig. 2. As previously reported, the transition from pulling to pushing occurs at some distance above the focal point of the laser beam [17], which in this case is at 13 μm . As can be seen in Fig. 2(a), the optical force efficiency is highest at around $z = 16.5\mu\text{m}$ at a lateral distance of about 2.5 μm away. Beyond a lateral distance of 3 μm , the order of Q drops rapidly as is shown in Fig. 2(b). This limits the region of influence of the laser. Based on this observation, we safely approximate the optical force at points beyond 8 μm as zero.

The trajectory of a particle at various starting positions with respect to the laser beam is shown in Fig. 2(c), where the shaded iso-surface represents the magnitude of the summed optical force. One finds the deflection effect less pronounced when the particle is further away from the path passing through the beam center. Also the deflection is not strictly planar, although it will appear to be when viewed through the microscope. Nevertheless, the significant lateral deflection should give rise to a stirring effect.

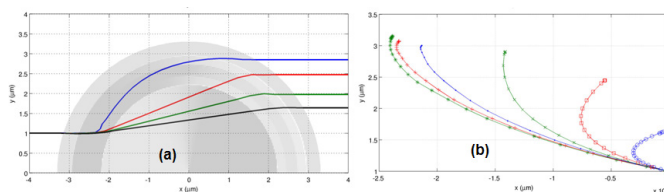


Fig. 3. (a) Plot of particle trajectories at optical powers 10mW (black), 15mW (green), 20mW (red), 35mW (blue) at $z = 19\mu\text{m}$. (b) Plot of local displacements of particles on microscope stage for $z = 16\mu\text{m}$ at various power levels starting from the right to left, 10mW (blue-circle), 20mW (red-box), 25mW (green-cross), 40mW (blue-dotted), 100mW (red-star) and 200mW (green-star). The optical stirring effect can be controlled by changing laser power.

The displacement of the particle at various laser powers with respect to the stationary laser and moving stage are shown in Figs. 3(a) and 3(b), respectively. The results show that the extent of stirring of the particles can be controlled by varying the applied power. The stirring effect saturates at higher laser powers since the order of the optical force efficiency drops rapidly after $3\mu\text{m}$, as was shown in Fig. 2(b).

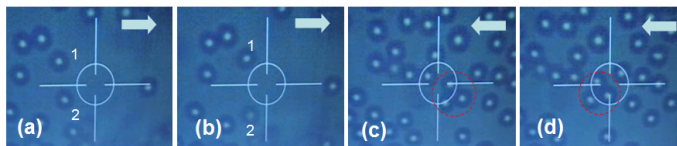


Fig. 4. With the laser beam located axially below the polystyrene beads and having sufficient power, the image sequence (a) before and (b) after shows the particles numbered 1 and 2 laterally pushed away from the beam center. With the laser beam located axially below the polystyrene beads but having insufficient power, the image sequence (c) before and (d) after shows the cluster of particles circled in red unaffected by the beam. The arrow shows the general direction of travel of the particles (see Media 1).

The experimental results shown in Figs. 4-5 comply with the modeling results. With 40% power, the polystyrene particles identified as 1 and 2 in Figs. 4(a)–4(b) can be seen to depart from their general motion paths such that they are pushed away from the laser beam center. The manner of the pushing is more strongly lateral rather than axial, which confirms a gentle stirring effect. That the particles never meet the beam center also meant that the propensity for photothermal or phototoxicity damage is diminished. When the laser beam power was reduced to 10%, one finds the cluster of particles identified in Figs. 4(c)–4(d) being able to move past the laser beam center almost without being affected. Hence, the optical stirring effect requires a certain threshold for operation. This is consistent with the modeling results.

The optical stirring effect was found to be operational with red blood cells as well, as indicated in Fig. 5 This illustrates the viability of the method applied to living organisms. A modeling of the forces will be more involved due to the shape complexity of these cells over simple shapes such as spheres and rods. The experimental results, however, indicate that a simple scaling effect, as far as the optical stirring effect is concerned, may be in operation.

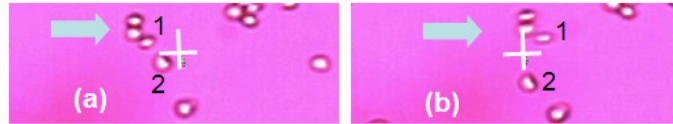


Fig. 5. With the laser beam located axially below the particles and having sufficient power, the image sequence (a) before and (b) after shows the red blood cells numbered 1 and 2 laterally pushed away by the beam. The arrow shows the general direction of travel of the cells (see Media 1).

At this juncture, we should mention that acoustic [20,21], magnetic [22], and dielectrophoretic [23] devices are also able to create a swirling motion that is able to move particles and cells around. The strong motion of material within the liquid medium associated with the effect will generally not be amenable for cells or to guide cells towards desired differentiation or biological response pathways. In both bioreactor and micro-bioreactor scale culture, a delicate balance or trade-off has to be reached in terms of the need to provide a perfusion or mixing function and controlling hydrodynamic shear stress. While perfusion and mixing provides a more homogenous environment by maintaining dissolved oxygen and nutrient concentrations and serves to reduce media cytotoxicity via recirculation effects, the consequent hydrodynamic shear forces, if on a high magnitude, are generally considered to have an adverse impact on cell survival and proliferation [24]. This is especially the case for shear sensitive cell types [25]. Evidences from studies also show that shear stress can have a significant influence on cellular morphology, growth patterns, and biological responses [26,27]. Different magnitudes of hydrodynamic shear stress evoke differential gene expression in signaling pathways in human bone marrow derived mesenchymal stem cells [28] and human endothelial progenitor cells [29], induce important changes in secretion and assembly of glycoproteins in mammalian cell cultures [30] as well as influence proliferation and osteoblastic differentiation [31]. Hence, in the setting of a static discrete droplet format, the gentle stirring afforded by our optical approach provides advantages of preserving cellular integrity and viability apart from promoting fidelity of biochemical and differentiation responses during cell culture and/or when performing cell-based assays.

6. Conclusions

The location of the focus of a laser below particles relative to the beam axis is known to produce a predominant pushing effect in the lateral sense. By moving the medium containing particles past a laser beam arranged in this manner, we have been able to develop an approach that creates a gentle and tunable stirring effect of particles. The computer simulations performed, enabled us to trace the expected deflection trajectories of the particles. Since the deflection effect is not enhanced beyond a certain laser power, this can be used as basis to find optimal powers for stirring. Experiments using polystyrene micro-beads and red blood cells confirm the optical stirring effect. This approach portends the capability to execute mechanical stimuli of cells in a small liquid volume bioreactor that is free of flow, leading to better realization of photonic lab-on-a-chip systems.

Acknowledgments

This work is made possible by funding from the Australian Research Council DP120100583. TW is thankful for the insight and inputs provided by Michael Berns at the Beckman Institute, UCI.

B.6 Precise drop dispensation on superhydrophobic surfaces using acoustic nebulization

Soft Matter

RSC Publishing

PAPER

[View Article Online](#)
[View Journal](#) | [View Issue](#)

Precise drop dispensation on superhydrophobic surfaces using acoustic nebulization†

Cite this: *Soft Matter*, 2013, **9**, 3631Thach Vuong,^a Aisha Qi,^{bc} Murat Muradoglu,^a Brandon Huey-Ping Cheong,^a Oi Wah Liew,^d Cui Xia Ang,^d Jing Fu,^e Leslie Yeo,^b James Friend^{bc} and Tuck Wah Ng^{*a}

The adhesion forces of liquid drops on superhydrophobic surfaces are typically in the nano-Newton range which presents problems in their dispensation from pipettes. Furthermore, since the liquid adheres more strongly to the pipette tip, some portion of the liquid will tend to remain on the tip, causing inaccuracy in the volume dispensed. We advance a novel approach here, in which the spray from an acoustic nebulizer is sent to a superhydrophobic receptacle and the volume ascertained precisely using a weighing scale. The superhydrophobic surface was identified to develop via a galvanic displacement mechanism in an electroless deposition process. A time dependent morphology change from granular to dendritic with longer immersion into the silver nitrate solution was found which indicated that granular growth beyond a certain size was not feasible, although granular structures were more preferentially formed just after nucleation. The dendritic structure formation was likely due to the natural tendency of the process to maintain or increase the surface area to volume ratio in order not to limit the rate of deposition. An immersion for at least 7 seconds into the silver nitrate solution, when the granular structures were predominant, was all that was needed to ensure superhydrophobicity of the surfaces. Also, the superhydrophobic state required not just significant numbers of the granular structures to be present but also interrupted coverage on the surface. On using the technique, a single drop was created by subsequently covering the receptacle with a lid and shaking it gently. The volume dispensed was found to vary linearly with the operation time of the nebulizer. We elucidated the observed increased ability of drops to reside on inclines using wetting mechanics and presented an elementary mathematical description of the extent of aerosol coverage on the surface, which has implications for the mechanics of aerosol growth into drops. The structural changes in enhanced green fluorescent protein (EGFP) observed after acoustic dispensation necessitated all samples in a fluorimetric assay to involve equal nebulized volumes of the fluorescent protein marker for measurement consistency.

Received 2nd January 2013
Accepted 30th January 2013

DOI: 10.1039/c3sm00016h

www.rsc.org/softmatter

1 Introduction

Superhydrophobic surfaces are illustrated in nature through the well-known examples of lotus leaves and the legs of water striders.^{1,2} There has been a recent proliferation in methods reported to artificially mimic these surfaces.^{3–7} While the original opportunity of superhydrophobicity was in self-cleaning,⁸ there is now substantial effort aimed at harnessing it for

biochemical applications^{9–14} since the ability to transport analytes or samples is a crucial component. This is aided by the increasing awareness that continuous and closed microfluidic flow devices are inherently difficult to integrate and scale due to the flow at any one location being dependent on the flow properties of the entire system. Discrete, independently controllable sample volumes, alternatively, permit the microfluidic function to assume a set of basic repeated operations, whereby one unit of fluid can be moved over one unit of distance, thus facilitating the use of hierarchical and cell-based approaches for microfluidic biochip designs that offer flexible and scalable system architectures as well as high fault tolerance capabilities. Moreover, because sample volumes can be controlled independently, such systems offer greater potential to be reconfigured whereby groups of unit cells in an array can be altered to change their functionality.

The adhesion forces of liquid drops on superhydrophobic surfaces are typically in the nano-Newton range.¹⁵ Hence, this presents a real problem in their dispensation from pipettes. The

^aLaboratory for Optics, Acoustics and Mechanics, Monash University, Clayton, VIC 3800, Australia.

^bMicro/Nanophysics Research Laboratory, RMIT University, Melbourne, VIC 3000, Australia

^cMelbourne Centre for Nanofabrication, Clayton, VIC 3800, Australia

^dCardiovascular Research Institute, Yong Loo Lin School of Medicine, National University of Singapore, National University Health System, Centre for Translational Medicine, 14 Medical Drive, Singapore 117599

^eDepartment of Mechanical & Aerospace Engineering, Monash University, Clayton, VIC 3800, Australia

† Electronic supplementary information (ESI) available. See DOI: 10.1039/c3sm00016h



use of flexible pipette tips¹¹ permits drop volumes down to around 10 μL to be deposited, albeit this requires careful execution in order for them not to contact (from the tip springing back after dispensation) the surface and thus damage the nano and micro features that endow superhydrophobicity. It should also be noted that since the liquid adheres more strongly to the pipette tip, an unknown portion of the liquid will remain within the tip, causing substantial inaccuracy in the dispensed volume.

The quest to develop bioanalysis tools based on superhydrophobicity is also founded on the issues of availability and cost. Bioanalytical chemists in well endowed laboratories are often accustomed to having a plethora of convenient consumables and sophisticated instrumentation at their disposal. Many researchers in resource-limited developing countries, or field workers in remote locations far from modern conveniences, have been unable to take advantage of modern bioanalytical techniques due to a lack of infrastructure. This is unfortunate as it is these same researchers that usually have the greatest need for bioanalytical tools that will help diagnose diseases such as tuberculosis or malaria. Not surprisingly, there have been recent efforts expended to use alternative materials such as paper to serve as the analyte handling media.¹⁶ This approach, while useful for methods based on electrochemical detection, is not as effective for methods that are based on optical detection, that arguably offer the highest versatility and sensitivity. Alternative cost effective approaches have since been reported.^{17,18} Despite this, paper remains indispensable as a relatively cheap, compact and robust reservoir for test samples and biochemical analytes.

In this work, we seek to develop a technique that will allow us to deliver drops of specific volumes on superhydrophobic surfaces from cost effective storage media such as paper so that they can in turn be harnessed to be developed into cost effective devices that permit transport. In the process, we will study the nature of how small aerosols form on these surfaces before evolving into single drops.

2 Materials and methods

We advance the approach depicted in Fig. 1 to circumvent this problem. A liquid supply chain was created out of a reservoir that delivers to a short capillary tube section, whose tip is placed in contact with a surface acoustic wave (SAW) nebulizer running at 30 MHz frequency using a small piece of tissue paper that constituted a capillary wick.¹⁹ The SAW device was constructed out of a low-loss piezoelectric substrate, specifically, a 127.86° Y-X-rotated single-crystal lithium niobate (LiNbO_3) substrate, with pairs of chromium–aluminum interdigital transducers fabricated on one side *via* standard UV photolithography. When an AC signal is supplied to the transducer at its resonant frequency, the SAW in the form of a Rayleigh wave propagates along the LiNbO_3 surface from the transducer at about 3900 m s^{-1} . Although the surface displacement amplitudes are only in the 1–10 nm range, the accelerations are extremely high (about 10^7 m s^{-2}) due to excitation at frequencies over 10 MHz. These huge surface accelerations are transmitted into the liquid placed on the substrate, inducing acoustic streaming.²⁰ When

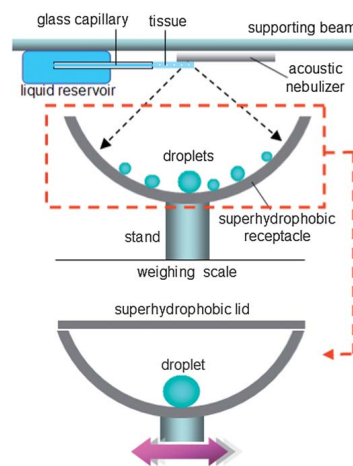


Fig. 1 Schematic description of the scheme to obtain precise volumes of drops on superhydrophobic surfaces. A surface acoustic wave nebulizer delivers a spray of aerosol droplets onto the receptacle in which the exact volume is determined using an accurate weighing scale. By covering with a superhydrophobic lid and gentle shaking, a single drop is created.

the energy is sufficient (*i.e.*, electrical power supplied in the 1–3 W range), destabilization of the liquid's free surface occurs. This leads to a breakup of capillary waves, generating a spray of aerosol droplets through a process known as SAW atomization or nebulization.^{21,22} When this spray of aerosol is channeled onto a semi-spherical superhydrophobic receptacle, larger drops develop on the receptacle surface from multiple coalescence events that are influenced by gravity (which tend to draw them towards the receptacle trough).

The receptacle was fashioned out of a copper sheet (1 mm thickness), polished earlier to remove all visible scratches using silicon carbide electro-coated waterproof abrasive paper (KMCA, WET/DRY S85 P600), by an 8.5 mm radius ball indenter. Prior to use, the receptacle surface was first cleaned using absolute ethanol, allowed to air dry, and then immersed in a 24.75 mM aqueous solution of AgNO_3 for 1 minute to form the micro and nano structures. After this, the surface was rinsed with copious amounts of distilled water followed by absolute ethanol before being allowed to air dry. Once dried, it was immersed in a 1 mM solution of the surface modifier $\text{CF}_3(\text{CF}_2)_7\text{CH}_2\text{CH}_2\text{SH}$ in absolute ethanol for 5 minutes. After removal, it was again rinsed with copious amounts of distilled water, followed by absolute ethanol, and then air dried.

For a side experiment to study the nano and microstructures forming in relation to wetting, we created coupons $20 \times 20 \text{ mm}$ in size out of the same copper sheet (1 mm thickness) and using the same polishing and cleaning process as previously used. The coupons were then immersed in the 24.75 mM aqueous solution of AgNO_3 for selected periods ranging from 2 seconds to 120 seconds before being removed to air dry. After drying, the



morphology of the superhydrophobic surface was characterized with an FEI Quanta 3D FEG scanning electron microscope (SEM). The elemental composition was characterized by an X-ray energy dispersive spectrometer (EDS) associated with the SEM. The wetting characteristics were evaluated by placing 5 μL of sessile drops of water on each surface (after immersing into the surface modifying solution) and then determining the contact angle.

In the technique, the weight of the liquid delivered to the receptacle, which could be correlated to volume, was determined using a weighing scale (A&D GR-200 with 0.0001 g precision) on which the receptacle is placed on. Once the required volume was achieved, aerosol delivery from the nebulizer was terminated, a superhydrophobic lid placed over the receptacle, and the assembly shaken gently to merge the drops together into one. Apart from ensuring that no liquid spilled out of the receptacle, the lid also served to limit the effects of evaporation, which is significant for small drop volumes. Experiments were conducted to establish the liquid (Milli-Q water) delivery characteristics when the power to the nebulizer was kept constant at 2 W.

Lastly, the effect of nebulization on the structural functionality of enhanced green fluorescent protein (EGFP) was evaluated. This C-terminally His₆-tagged fluorescent protein was isolated from genetically modified *Escherichia coli* and purified to near homogeneity by automated affinity chromatography using 1 mL bed volume Mini Profinity IMAC cartridges on the Profinity Protein Purification System (Bio-Rad) under the default program

settings of the Native IMAC method with integrated desalting into sodium phosphate buffer (pH 7.4). The His₆-tagged EGFP was checked for purity by SDS-PAGE (see ESI[†]) and quantified using the BCA protein assay (Pierce, USA). Samples of the protein were nebulized at different powers, collected in capillary tubes, imaged together using a fluorescence microscope (Olympus BX61), and the intensities extracted using the ImageJ software.

3 Results and discussion

The micro- and nano-structures developed by immersing the copper coupons into the aqueous solution of AgNO₃ were formed by an electroless deposition process. This process is similar to electrolytic plating except that no external electrodes are needed.²³ In electroless deposition, the metal ions are typically reduced into metals by the introduction of a reducing agent. A variety of procedures with different reagents have been demonstrated for electroless deposition of silver.^{24,25} In the process conducted here, however, the deposition was able to proceed without any external reducing agent. Rather, a galvanic displacement mechanism occurred in which the silver cations in solution were reduced just as copper from the surface was oxidized.

The SEM micrographs of structures formed in association with various immersion times of the copper coupons into the silver nitrate solution are presented in Fig. 2. The background striated structures seen at 2 seconds were formed due to the polishing process. On the substrate, very small granules started to be deposited at numerous nucleation sites. These granules

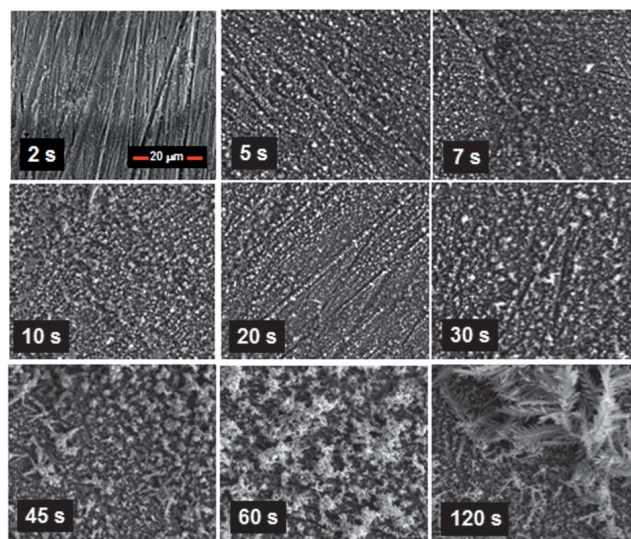


Fig. 2 Scanning electron micrographs obtained from immersing the copper coupons into the silver nitrate solution for different lengths of time followed by air drying. It can be seen that granular structures developed with short period immersion, whilst dendritic structures formed with longer period immersion.



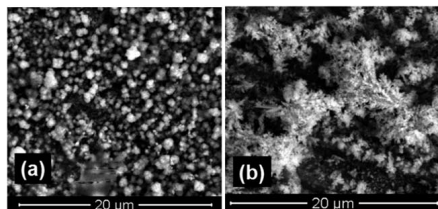


Fig. 3 Scanning electron micrographs at higher magnifications that provide a clearer picture of the (a) granular and (b) dendritic structures developed.

grew in size with longer immersion times until about 10–20 seconds. At the 20 seconds mark, the granules appeared to shrink slightly in size whilst exhibiting greater dendritic growth from the surface of each granule. From then onwards, the dendritic structures began to proliferate on the existing granular structures, developing later into fern-like foliage. The distinct differences between these two types of structures (granular and dendritic) are shown more clearly in the higher magnification micrographs provided in Fig. 3.

The time dependent morphology changes appear to indicate that granular growth beyond a certain size was not feasible, although granular structures were more preferentially formed just after nucleation. This is likely due to the natural tendency of the process to maintain or increase the surface area to volume ratio in order not to limit the rate of deposition. Taking a sphere for example, the surface area to volume ratio scales according to $3/r$, where r is the radius, inferring that the surface area to volume ratio reduces as the sphere increases in size. Thus, the formation of dendritic structures offers an avenue by nature to circumvent this obstacle. This argument is supported somewhat by the XRD maps obtained that revealed no significant elemental changes in the structures.

After the surfaces were treated with the modifier, we found that immersion for at least 7 seconds into the silver nitrate

solution was all that was needed to ensure superhydrophobicity of the surfaces. At this stage, the structures appeared to be predominantly granular. Previous studies have shown that granular structures alone were sufficient to cause superhydrophobicity.²⁶ Hence, we were able to conclude that the subsequent dendritic structures were not needed to maintain the non-wetting characteristic, although they seemed not to have a role in modifying it. The micrograph at 5 seconds immersion also showed significant coverage of granular structures over the substrate. This presented an interesting conundrum as to why superhydrophobicity could not be sustained at this stage. On more careful examination, we found that there were regions on the substrate surface where the granular structures were not fully developed. It appears then that the superhydrophobic state requires not just significant numbers of the granular structures to be present on the surface but also uninterrupted structure coverage.

We move now to discuss the experimentation results in obtaining the drops. During each run on liquid deposition, the nebulizer was cyclically pulsed on for 5 seconds and off for 5 seconds. This was done to accommodate the response time of the weighing scale. Fig. 4 presents results of the mass recorded in relation to time in which the nebulizer was operated for three typical runs. Highly linear trends are observed, indicating that fixed quanta of liquid were dispensed with each pulsed operation of the nebulizer for a specific run. While the data for two of the runs were almost identical, the gradient for a third run was significantly altered. This was due to the process that happens in the tissue as it served to draw liquid out from the reservoir before perturbations from the SAW device are able to dislodge it for delivery. In the course of this process, factors that affect the transfer of liquid in and out of the tissue (such as temperature and airborne particles attaching to the fibers) likely caused the flow rate to vary with each run.

This result implied that an open-loop operation using pre-calibration without using the weighing scale was not feasible. Due to the ability of the SAW driven nebulizer to operate nearly instantly, from zero to full power and to zero power again in

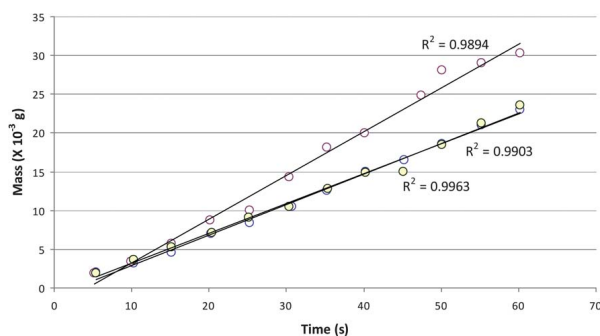


Fig. 4 Plots of the readings from the weighing scale against the operation time of the nebulizer. The trends from each run are highly linear, albeit the slope variation indicates that pre-calibrated operation without the weighing scale was not feasible.



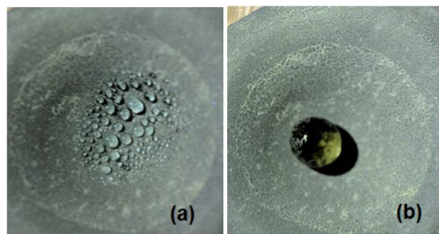


Fig. 5 Images of (a) multiple nebulized droplets formed on the surface of the receptacle and (b) a single drop that results after shaking the receptacle.

approximately 1 microsecond, there was no 'lagging volume' delivered when the nebulizer was turned off. Hence, the limiting factor for accurate volume dispensation was only that dictated by the mass resolution of the weighing scale. In the current case, the volume resolution was 1 μL based on the density of water being 1000 kg m^{-3} and the weighing scale's mass resolution being 0.0001 g. The response of the weighing scale also determined the time needed, since the off times could be shortened if it settled faster. We have also found that good isolation from draft and ambient vibrations was crucial to maintaining accuracy.

The formation of multiple drops in the receptacle (Fig. 5(a)) of up to 3 μL by volume (by estimation) before the gentle shaking operation was applied to dislodge them to form a final single drop (Fig. 5(b)) presents an interesting conundrum. Experiments with drops of this volume typically show that they move easily when dispensed on superhydrophobic surfaces. In fact, earlier dynamical studies conducted show that very small forces (in the nano-Newton range) are needed to move water drops on this surface.¹⁵ Coupled with the curvature of the receptacle, this should then result in a single drop forming all the time even when no shaking was introduced. This apparent anomalous behavior can be explained by the Cassie and Wenzel wetting states of superhydrophobic surfaces.²⁷ When a drop impinges on a wetting surface, it is known that it will first expand rapidly.²⁸ With sufficient momentum of the drop, the surface microstructures are able to impale the liquid surface. As the liquid loses kinetic energy, the drop will eventually settle into a static state, leading to the observation of stickiness. On a non-wetting surface, alternatively, stronger capillary and hydrodynamic forces develop to impede this impalement process. Consequently, the drop is able to bounce off and lose energy through a succession of bounces.

When drops of larger sizes impinge on a superhydrophobic surface, there is very high likelihood that the impalement process will not occur. Upon settlement from bouncing, they are expected to develop a high proportion of Cassie states at the three-phase contact line, facilitating easy sliding and rolling of the liquid body along the surface (Fig. 6(a)). We, of course, ignore for convenience the situation where the bouncing drops collide with each other in mid air. With individual aerosol drops (which are smaller in size) landing on the surface, however, the

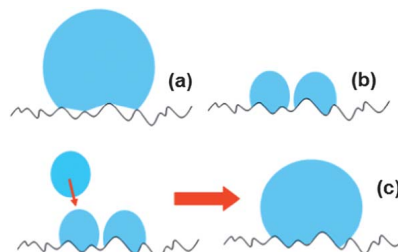


Fig. 6 Illustrations depicting predominantly high (a) Cassie and (b) Wenzel wetting states of relatively larger drops and aerosols residing respectively on superhydrophobic surfaces. (c) When further aerosols arrive at the surface, they merge with existing aerosols on the surface to create larger volumes that coalesce with other surface bound aerosols. Due to the lack of a sufficiently large perturbation, the predominant Wenzel states cannot convert to Cassie states, allowing the liquid body to stay on the inclined surface with larger volumes.

probability of impalement is increased since higher Laplace pressures develop on them.^{27,28} The impalement process essentially develops high degrees of the Wenzel wetting state on the surface as liquid fills into the crevices between the microstructures (Fig. 6(b)). As more aerosols arrive, they either merge with those already on the surface or grow to the extent of coalescence with other surface-residing aerosols. In the absence of sufficiently large perturbations to convert the predominant Wenzel states into Cassie states,²⁹ the drop coalesced from aerosols remains adherent on the inclined surface even at larger volumes for which an equivalent volume drop deposited upon the surface would be in the predominant Cassie state from the start (Fig. 6(c)). The formation of multiple drops on the surface (Fig. 5(a)) appears to indicate some links with the process of condensation. However, previous studies conducted with condensation have shown a tendency for surfaces to lose their superhydrophobicity,³⁰ likely arising from damages to the surface structures during the process. That a single drop could be attained here (after shaking) with no apparent loss in superhydrophobic behavior (Fig. 5(b)) shows differences in the underlying mechanisms.

While the drops are attached to the surface with a predominant Wenzel wetting state, the shaking of the receptacle imbues them with energy (see Fig. 7). With sufficient momentum, the drop will be able to dislodge from the surface to leave behind a thin film of liquid. Due to the direction of the shaking, this will occur more like a shearing operation, tearing the drop from the liquid embedded in the microstructures.¹⁵ The very small volume of the thin liquid film left behind renders it easily evaporable while the drop now functions in a predominant Cassie state. We contend that the ability of the liquid film to evaporate quickly plays a role in the conversion process, since a previous study using lotus leaves has shown that extensive pre-wetting using condensation over the surface (which creates a thin film of liquid in the Wenzel state) will cause a loss in superhydrophobic behavior of drops locating later over it.³¹ Strictly speaking then, the description of the



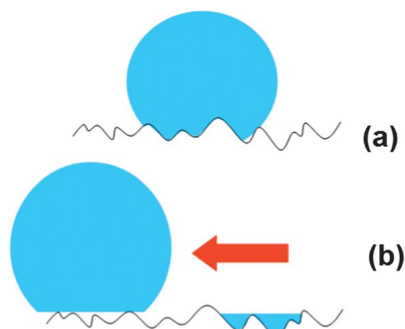


Fig. 7 Illustrations depicting the initial predominantly high (a) Wenzel wetting state of a drop on the surface in which with sufficient momentum developed (in the direction of the arrow) will (b) cause the drop to dislodge and leave behind a thin film of liquid. The very small volume of the latter renders it easily evaporable while the former now functions as a drop in the Cassie state.

wetting state change here does not refute the notion that the Wenzel state is strongly irreversible. Wetting state changes are often thought of as pertaining to the entire body of liquid. The ability of the liquid body to separate hence imbues the “liberated” component with the capacity to seek another predominant wetting state. Evidence of the ability of drops to separate on superhydrophobic surfaces has been reported, albeit in a different context.³²

It is also apt at this point to mention that the conception of a fully Cassie state is not viable due to the heterogeneity of the microstructures developed (see Fig. 2). It has been previously established that the spacing between protruding microstructures and the height of the protruding microstructures dictate

whether a droplet will assume Cassie or Wenzel states.³³ An interesting rumination relates to the interesting result of Jin *et al.*³⁴ that showed the possibility for superhydrophobic surfaces to possess strong adhesive forces by virtue of high van der Waals forces acting. Will it be possible to achieve the Wenzel to Cassie state changes with lowered movement of the drop during the shaking process? This has advantageous implications in terms of practical device development.

An ability to mathematically model the formation of a single drop from the spray of aerosol droplets will be instructive, although likely an involved undertaking due to the stochastic and dynamical nature of the mechanisms involved in (i) aerosols arriving at the receptacle surface, (ii) aerosols growing into drops, (iii) drops detaching from the surface under gravity, and (iv) drops coalescing. In the context of (iv), the unexpected drop-drop bouncing behavior recently uncovered on superhydrophobic surfaces³⁵ portends greater complexity in the modeling. We present here an elementary description of the extent of aerosol coverage on the surface that has implications for the mechanics of aerosols growing into drops.

A single aerosol that arrives as a sphere with radius r' (which can be estimated to a high degree of accuracy using optical methods^{36,37}) on a semi-spherical surface of radius R will result in a liquid body that is governed by the equilibrium three-phase contact angle θ . This can be described using a model comprising two spheres that intersect with each other. The parameters r' , R , and θ can be related to the solid angle Ω via equations (outlined in the Appendix) that can be solved. The solid angle provides a convenient depiction of the extent of coverage taken from an assumed point source (the nebulizer). This is rather akin to the delivery of light from a point source in radiometry.³⁸

Fig. 8 presents plots of Ω against r'/R for various values of θ . As r' and R were $5 \mu\text{m}$ and 8.5 mm , respectively, the abscissa values were normalized to $O(10^{-3})$. The values were found using

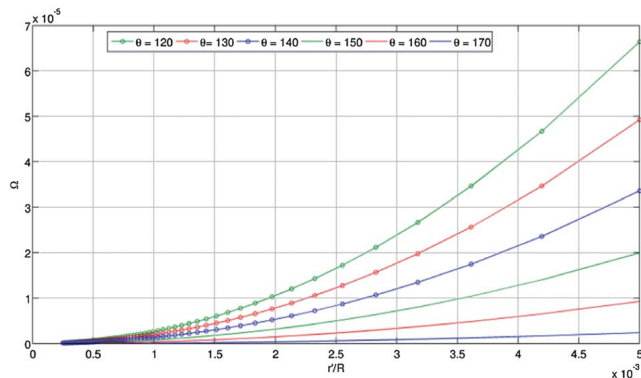


Fig. 8 Plots of the solid angle Ω subtended by an aerosol droplet that arrives as a sphere with radius r' on a semi-spherical surface of radius R for various equilibrium three-phase contact angles θ . The residence of the aerosol droplet on the surface can be described using a model comprising two spheres that intersect with each other. The relevant parameters can be related, via equations that can be solved, to the solid angle.



derivations given in the ESL.† The definition of superhydrophobicity is loosely correlated to a value of θ ranging from 120° to 180° . In the figure, the variations in the solid angles calculated based on this are significant. If we consider the case of $\theta = 120^\circ$, changing r/R from 2×10^{-3} to 4×10^{-3} increases the solid angle by 4.2 times. An increase in the solid angle is generally favorable as it implies a greater probability for the aerosols that arrive later to impinge on those already on the surface. This improves the chance of growth towards drops and thus also the propensity for them to detach and roll towards the base of the receptacle. If the aerosol radius were to be kept constant, reducing R would achieve this. It should be noted, however, that too small a value of R will increase the chances of the spray envelope to fall outside the receptacle, thereby causing material loss. The solid angle values with $\theta = 170^\circ$ alternatively are small, which is seemingly negative in terms of increasing the probability of aerosol coalescence on the surface. Nevertheless, the adhesion forces of drops with higher θ values are also typically smaller, enabling even a small aerosol drop to roll down to the base. In addition, the values of Ω remain relatively invariant with r/R when θ is closer to 180° .

With nebulizer powers of 1.1 W, 1.3 W, 1.52 W, and 2.05 W, the fluorescence intensity readings, normalized to the reading without nebulization, were 0.81, 0.77, 0.80, and 0.84 respectively. This indicated some expected loss in fluorescence, not inconsistent with previous results assessing post-nebulized protein viability,¹⁹ although different levels of power in the range used did not seem to have a varying effect. Samples that were nebulized also retained their fluorescence activity with no signs of any post deterioration in emission intensity after storage for a week at 4°C . GFP fluorescence is known to be affected by pH,³⁹ dissolved oxygen,⁴⁰ and high temperatures.⁴¹ It is possible that a slight disruption of the structural integrity of EGFP, in particular its fluorophore, may have been caused by strong initial perturbations delivered to the sample. All samples in a fluorimetric assay, therefore, should comprise equal volumes of EGFP or fluorescent protein marker equivalently nebulized to ensure consistency in measurements made.

4 Conclusions

We have identified that a galvanic displacement mechanism in an electroless deposition process occurred in which the silver cations in solution were reduced just as copper from the surface was oxidized and was responsible for creating the micro- and nano-scaled structures that endow superhydrophobicity on the copper substrate. A time dependent morphology change from granular to dendritic with longer immersion into the silver nitrate solution was found. This indicated that granular growth beyond a certain size was not feasible, although granular structures were more preferentially formed just after nucleation. The dendritic structure formation was likely due to the natural tendency of the process to maintain or increase the surface area to volume ratio in order not to limit the rate of deposition. An immersion for at least 7 seconds into the silver nitrate solution was all that was needed to ensure superhydrophobicity of the surfaces. This allowed for the deduction

that the dendritic structures were not needed to maintain the non-wetting characteristic, although they seemed not to have a role in modifying it. Also, the superhydrophobic state required not just significant numbers of the granular structures to be present, but also interrupted coverage on the surface. In using the proposed technique, having the nebulizer cyclically pulsed on for 5 seconds and off for 5 seconds was needed to accommodate the response time of the weighing scale. Highly linear trends were observed, indicating that fixed quanta of liquid were dispensed with each pulsed operation of the nebulizer for a specific run. However, the flow rate may be altered and this was due to factors that affected the transfer of liquid in and out of the tissue (such as temperature and airborne particles attaching to the fibers). With individual aerosols landing on the receptacle surface, the probability of impalement was increased since higher Laplace pressures developed on them. The impalement process then developed high degrees of the Wenzel state on the surface. With sufficient momentum from shaking, the drop was able to dislodge from the surface leaving behind a thin film of liquid. The very small volume of the thin liquid film rendered it easily evaporable while the drop then functioned in a predominant Cassie state. In using EGFP samples for verification, fluorescence emission could be retained to about 80% of its original level and was not affected by different levels of power used on the SAW device. In summary, we have developed a practical approach to deposit micro-liter volume drops on superhydrophobic surfaces stably and precisely. This is expected to facilitate biochemical applications using these surfaces.

Appendix

Analysis of aerosol formation on a semi-spherical surface

The residence of a single aerosol on a semi-spherical surface can be depicted by the intersection of two spheres (smaller one of the drop, and larger one of the surface) as shown in Fig. S1.† Since $\angle OAB = \angle O'AB = 90^\circ$, the contact angle θ is given by

$$\theta = 180^\circ - \phi. \quad (\text{A1})$$

This is related to r (radius of the drop on the surface), R (radius of the surface), and a (distance between centers) via

$$a^2 = R^2 + r^2 - 2rR\cos\phi = R^2 + r^2 + 2rR\cos\theta. \quad (\text{A2})$$

We next seek to establish the volume of liquid residing on the spherical surface. If the larger sphere is centered at $(0,0,0)$ and the smaller sphere at $(a,0,0)$ in Cartesian coordinates, we have

$$(x - a)^2 + (R^2 - x^2) = r^2. \quad (\text{A3})$$

Solving for x , we have

$$x = \frac{a^2 - r^2 + R^2}{2a}. \quad (\text{A4})$$

If we apply this to the equation of the larger sphere, we have



$$y^2 + z^2 = R^2 - x^2 = \frac{4a^2R^2 - (a^2 - r^2 + R^2)^2}{4a^2}. \quad (\text{A5})$$

Hence, at the point of intersection, we have a circle of radius b given by

$$b = \frac{1}{2a} \sqrt{4a^2R^2 - (a^2 - r^2 + R^2)^2}. \quad (\text{A6})$$

This creates two caps of respective heights

$$h_R = R - x = \frac{(r - R + a)(r + R - a)}{2a}, \quad (\text{A7})$$

$$h_r = r - a + x = \frac{(R - r + a)(r + R - a)}{2a}. \quad (\text{A8})$$

Since the equation of volume of a spherical cap is known, we have

$$V = V(R, h_R) + V(r, h_r) \\ = \frac{\pi(R + r - a)^2(a^2 + 2ar - 3r^2 + 2aR + 6rR - 3R^2)}{12a}. \quad (\text{A9})$$

The extent of coverage of a single aerosol drop on the substrate surface can be conveniently depicted by the solid angle Ω in which

$$\Omega = 2\pi(1 - \cos \phi) = 2\pi \left(1 - \frac{\sqrt{R^2 - a^2}}{R}\right). \quad (\text{A10})$$

The maximum solid angle that can be subtended from a point source is 4π radians. If the radius r of aerosol delivered is known, this parameter can be related to the volume V by assuming the aerosol to be a sphere using $V = 4\pi(r^3)/3$. In (A9) then, r with R will relate to a and r . Using (A2) and (A10), we can then relate r and R instead to θ and Ω .

Verification of protein purity

The quality of C-terminal His₆-tagged EGFP purification was determined using SDS-PAGE analysis by immobilized metal affinity chromatography (IMAC). The crude bacterial lysate (CL) containing His₆-tagged EGFP (indicated by the red arrow) was loaded onto an IMAC column prepacked with UNOsphere™ beads containing the chelating ligand iminodiacetic acid charged with nickel. The strong affinity of the His₆-tag for the transition metal results in efficient binding of the recombinant EGFP onto the column resin as indicated by the loss of the EGFP band in the flow through fraction (FT). Two wash buffer cycles (W1 and W2) effectively removed most of the contaminating proteins bound on the column. Finally, purified His₆-tagged EGFP (E + D) was eluted from the IMAC column by displacement with 250 mM imidazole and desalted into sodium phosphate buffer as a near homogeneous product (indicated by the red arrow in Fig. S2†).

Acknowledgements

TW, OW and Jing F. appreciate funding support from the Australian Research Council Grant DP120100583. James F.

wishes to acknowledge financial support from the Australian Research Council via grants DP120100013 and DP120100835, and the provision of facilities and equipment from the Melbourne Centre for Nanofabrication.

References

- 1 W. Barthlott and C. Neinhuis, *Planta*, 2001, **202**, 1.
- 2 X. Gao and L. Jiang, *Nature*, 2004, **432**, 36.
- 3 L. Y. L. Wu, Q. Shao, X. C. Wang, H. Y. Zheng and C. C. Wong, *Soft Matter*, 2012, **8**, 6232.
- 4 Y. Lai, X. Gao, H. Zhuang, J. Huang, C. Lin and L. Jiang, *Adv. Mater.*, 2009, **21**, 3799.
- 5 H. Zhou, H. Wang, H. Niu, A. Gestos, X. Wang and T. Lin, *Adv. Mater.*, 2012, **24**, 2409.
- 6 S. M. Kang, I. You, W. K. Cho, H. K. Shon, T. G. Lee, I. S. Choi, J. M. Karp and H. Lee, *Angew. Chem., Int. Ed.*, 2012, **49**, 9401.
- 7 Y. Li, L. Li and J. Sun, *Angew. Chem., Int. Ed.*, 2010, **49**, 6129.
- 8 R. Blossey, *Nat. Mater.*, 2003, **2**, 301.
- 9 A. I. Neto, C. A. Custódio, W. Song and J. F. Mano, *Soft Matter*, 2011, **7**, 4147.
- 10 X. Li, Y. Liu, A. Zhu, Y. Luo, Z. Deng and Y. Tian, *Anal. Chem.*, 2010, **82**, 6512.
- 11 F. Shao, T. W. Ng, O. W. Liew, J. Fu and T. Sridhar, *Soft Matter*, 2012, **8**, 3563.
- 12 J. Ballester-Beltrán, P. Rico, D. Moratal, W. Song, J. F. Mano and M. Salmerón-Sánchez, *Soft Matter*, 2011, **7**, 10803.
- 13 T. Vuong, B. H. P. Cheong, J. K. K. Lye, O. W. Liew and T. W. Ng, *Anal. Biochem.*, 2012, **430**, 53.
- 14 F. Gentile, G. Das, M. L. Coluccio, F. Mecarini, A. Accardo, L. Tirinato, R. Talerico, G. Cojoc, C. Liberale, P. Candeloro, P. Decuzzi, F. De Angelis and E. Di Fabrizio, *Microelectron. Eng.*, 2010, **87**, 798.
- 15 T. W. Ng and Y. Panduputra, *Langmuir*, 2012, **28**, 453.
- 16 E. Carrilho, S. T. Phillips, S. J. Vella, A. W. Martinez and G. M. Whitesides, *Anal. Chem.*, 2009, **81**, 5990.
- 17 B. H.-P. Cheong, V. Diep, T. W. Ng and O. W. Liew, *Anal. Biochem.*, 2012, **422**, 39.
- 18 X. Y. Li, B. H.-P. Cheong, A. Somers, O. W. Liew and T. W. Ng, *Langmuir*, 2013, **29**, 849.
- 19 A. Qi, L. Yeo, J. Friend and J. Ho, *Lab Chip*, 2010, **10**, 470.
- 20 J. Friend and L. Yeo, *Rev. Mod. Phys.*, 2011, **83**, 647.
- 21 A. Qi, L. Yeo and J. Friend, *Phys. Fluids*, 2008, **20**, 074103.
- 22 L. Yeo and J. Friend, *Biomicrofluidics*, 2009, **3**, 012002.
- 23 G. O. Mallory, J. B. Hajdu, *Electroless Plating: Fundamentals and Applications*, AESF, Orlando, FL, 1990.
- 24 S. G. Warrier and R. Y. Lin, *J. Mater. Sci.*, 1993, **28**, 4868.
- 25 H. Chang, C. H. Pitt and G. B. Alexander, *J. Mater. Sci.*, 1993, **28**, 5207.
- 26 J. T. Han, D. H. Lee, C. Y. Ryu and K. Cho, *J. Am. Chem. Soc.*, 2004, **126**, 4796.
- 27 A. Lafuma and D. Quéré, *Nat. Mater.*, 2003, **2**, 457.
- 28 D. Bartolo, F. Bouamrine, E. Verneuil, A. Buguin, P. Silberzan and S. Moulinet, *Europhys. Lett.*, 2006, **74**, 299.
- 29 J. B. Boreyko and C.-H. Chen, *Phys. Rev. Lett.*, 2009, **103**, 174502.



[View Article Online](#)

Paper

Soft Matter

- 30 B. Mockenhaupt, H.-J. Ensikat, M. Spaeth and W. Barthlott, *Langmuir*, 2008, **24**, 13591.
- 31 Y.-T. Cheng and D. E. Rodak, *Appl. Phys. Lett.*, 2005, **86**, 144101.
- 32 J. W. Krumpfer, P. Bian, P. Zheng, L. Gao and T. J. McCarthy, *Langmuir*, 2011, **27**, 2166.
- 33 J. B. Lee, H. R. Gwon, S. H. Lee and M. Cho, *Mater. Trans.*, 2010, **51**, 1709.
- 34 M. Jin, X. Feng, L. Feng, T. Sun, J. Zhai, T. Li and L. Jiang, *Adv. Mater.*, 2005, **17**, 1977.
- 35 H. Mertaniemi, R. Forchheimer, O. Ikkala and R. H. A. Ras, *Adv. Mater.*, 2012, **24**, 5738.
- 36 H. Zuo, Q. Liu, J. Wang, L. Yang and S. Luo, *Opt. Lett.*, 2010, **35**, 1380.
- 37 Y. Wang, S. Fan, X. Feng, G. Yan and Y. Guan, *Appl. Opt.*, 2006, **45**, 7456.
- 38 R. W. Boyd, *Radiometry and the Detection of Optical Radiation*, John Wiley & Sons, 1983.
- 39 S. Enoki, K. Saeki, K. Maki and K. Kuwajima, *Biochemistry*, 2004, **43**, 14238.
- 40 C. Zhang, X. H. Xing and K. Lou, *FEMS Microbiol. Lett.*, 2005, **249**, 211.
- 41 C. Zhang, M.-S. Liu and X.-H. Xing, *Appl. Microbiol. Biotechnol.*, 2009, **84**, 511.

Open Access Article. Published on 22 February 2013. Downloaded on 09/01/2014 01:35:40.
This article is licensed under a Creative Commons Attribution 3.0 Unported Licence.



B.7 Optical trapping map of dielectric spheres

Optical trapping map of dielectric spheres

Murat Muradoglu and Tuck Wah Ng*

Laboratory for Optics, Acoustics & Mechanics, Department of Mechanical & Aerospace Engineering,
Monash University, Clayton VIC3800, Australia

Received 10 January 2013; revised 11 March 2013; accepted 8 April 2013;
posted 17 April 2013 (Doc. ID 183153); published 15 May 2013

Many applications use a focused Gaussian laser beam to manipulate spherical dielectric particles. The axial trapping efficiency of this process is a function of (i) the particle radius r , (ii) the ratio of the refractive index of particle over the medium, and (iii) the numerical aperture of the delivered light beam. During what we believe is the first comprehensive simulation of its kind, we uncovered optical trapping regions in the three-dimensional (3D) parameter space forming an iso-surface landscape with ridge-like contours. Using specific points in the parameter space, we drew attention to difficulties in using the trapping efficiency and stiffness metrics in defining how well particles are drawn into and held in the trap. We have proposed an alternative calculation based on the maximum forward and restoration values of the trapping efficiency in the axial sense, called the trapping quality. We also discuss the manner in which the ridge regions may be harnessed for effective particle sorting, how the optical trapping blind spots can be used in applications that seek to eschew photothermal damage, and how trapping can proceed when many parameters change, such as when swelling occurs. © 2013 Optical Society of America

OCIS codes: (140.7010) Laser trapping; (350.4855) Optical tweezers or optical manipulation.
<http://dx.doi.org/10.1364/AO.52.003500>

1. Introduction

It is well known that light carries both linear and angular momentum that can exert observable force and torque on small matter. An optical trap or tweezer exploits this fundamental property to constrain objects in a potential well formed by laser light. Since its discovery [1,2], numerous applications have emerged to harness it [3–7]. Due to its high symmetry, numerical description of the optical trapping of spheres has been widely investigated [8–11].

When trapping a spherical particle using a focused Gaussian laser beam of wavelength λ , the efficiency Q [11] can be physically controlled by varying (i) the particle radius r , (ii) the ratio of the refractive index of particle over the medium $n = n_1/n_2$, and (iii) the numerical aperture (NA) of the delivered light beam, which is given by $NA = n_2 \sin \theta$, where n_2 is the refractive index of the medium after the lens and θ is

the half angle (see Fig. 1). With (iii), adjusting the size of an aperture placed before the lens offers a ready means of variation.

To the best of our knowledge, no map has been created to date that fully depicts the trapping efficiency with respect to the three parameters mentioned, presumably due to the intensive computational demands of such an endeavor. The existence of such a map will be invaluable not only to establish the operational ranges but also to exploit novel applications. In some erstwhile studies conducted, fingering landscapes have been revealed for relatively high refractive index materials with some explanations given for the cause of their existence [12,13]. High refractive index microspheres (made from materials such as silicon, which have $n = 3.5$) have good optical confinement properties, which makes them ideal for use in creating microcavities with very high Q -factor resonances [14,15].

In this work, we present what we believe is the first complete optical trapping map of dielectric spheres. From this map, we seek to elucidate the

1559-128X/13/153500-10\$15.00/0
© 2013 Optical Society of America

basis of the ridge region trapping characteristics with high refractive index material more clearly and outline a feasible way to harness it for applications.

2. Optical Forces on a Sphere by a Focused Beam

Consider an electromagnetic wave impinging upon a spherical particle of radius r with a refractive index of n_1 that is suspended in a liquid with refractive index of n_2 , (Fig. 1). In general, the particle scatters a quantity of the incident wave in all directions. If the beam is mostly deflected away from the original beam axis, a transverse force results; this force allows trapping in the radial direction. Scattering in the axial direction (i.e., forward or backward scattering) would result in forces that push or pull particles along the beam axis and is the bane of trapping.

While this analogy gives some physical insight, it cannot be used to predict trapping. A more apt condition to implement is to interrogate the force profile in the vicinity of the focal point to determine if a turning point in the potential energy exists. This is a reasonable condition since Gaussian beams have a symmetric scattering profile for radial displacement away from the beam axis for spherical particles. Hence, we only need to calculate the axial force on a particle.

Typically, the restoring force distribution is linear in relation to distance at the vicinity of the held particle. Using the simple analogy of a spring, where the restoring force is proportional to the displacement from equilibrium, the slope of this distribution depicts the stiffness of the trap. It also is important to consider the maximum restoring force since it depicts the magnitude needed to displace the particle.

3. Numerical Modeling

In the traditional modeling of optical tweezers, the particle size is assumed to be typically a few micrometers. Together with the more convenient paraxial

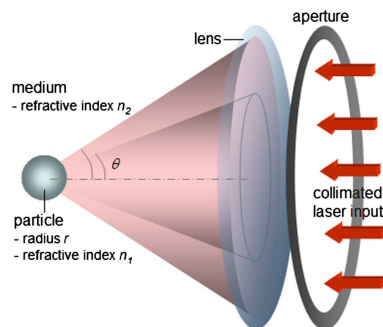


Fig. 1. Efficiency in trapping a spherical particle using a focusing laser beam is dependent on its radius r and refractive index n_1 , the refractive index of the medium n_2 , and the NA of the light beam, which is a function of the half-angle.

representation of a Gaussian beam (i.e., where the beam angle θ is relatively small and can be approximated by plane waves at different angles), this means that the ray optics regime should be relatively successful at predicting a close representation of the scattered field and resultant optical force. While this approach is sufficient, it lacks any real ability to represent the near-field diffraction effects that may occur as the wavelength approaches the radius of the particle. From models and experiments done in the past, interesting diffraction and interference effects are known to occur in this domain [16]. It has been previously reported [12] that the effects of these extremely narrow band forward scattering modes cause the formation of optical trapping “fingers.” The rationalization of these structures was based on the correlation of peaks in the extinction coefficients with the trapping. This basis is applicable only to lower NA Gaussian beams where the plane wave representation is closer.

In addressing the simulation findings found in [12], a later work has pointed out that force predictions made with particle radii much smaller than wavelength of light can be erroneous [17]. This is due to errors (by up to a factor of 10) generated with Bessel function routines with small input arguments when the recursive algorithm in MATLAB is used. For this reason, we have limited our domain of interest to within the Mie regime, wherein the lower particle radius limit is half the wavelength of light.

We simulated the case with a circularly polarized Gaussian beam focused at the origin $(0, 0, 0)$ and propagating along the z axis such that it impinges on a spherical particle with radius r , and refractive index n_1 that is placed in water ($n_2 = 1.33$). The three field components— $|E_x|$, $|E_y|$, and $|E_z|$ —of an x -polarized Gaussian beam were recovered by expanding with vector spherical wave functions (VSWF) in the focal plane x - y (Fig. 2). The fields are normalized to the maximum of $|E_x|$ and lengths are scaled to the wavelength λ .

We swept a three-dimensional (3D) parameter set, comprising (i) $1.3 \leq n_1 \leq 4.0$, (ii) $0.3 \leq \text{NA} \leq 1.2$, and (iii) $0.5\lambda \leq r \leq 4.0\lambda$. For each set of parameters, we conducted two trap searches. The first was a search in the axial sense; i.e., trapping along the beam axis, z (i.e., $-5 \mu\text{m} \leq z \leq 5 \mu\text{m}$) and $x = 0$. The second was a search for trapping in the radial sense; i.e., trapping in the x - y plane, where $-5 \mu\text{m} \leq x \leq 5 \mu\text{m}$ and $z = 0$. In both cases, when a zero crossing was found, we recorded the peak restoration force, $Q_{i,\text{RFmin}}$; if not found, we assumed that it was a nontrapping condition that set $Q_{i,\text{RFmin}} = 0$, where i was either x or y for radial trapping and z for axial trapping.

Since the computations were highly serial, we have reduced the order of some calculations from $O(n^3)$ to $O(n^2)$ and greatly increased performance through the use of batch parallelization. The code was compiled to run on a high-performance computing facility ideally suited to data-intensive tasks, comprised of up to 201 nodes, 1408 CPU cores,

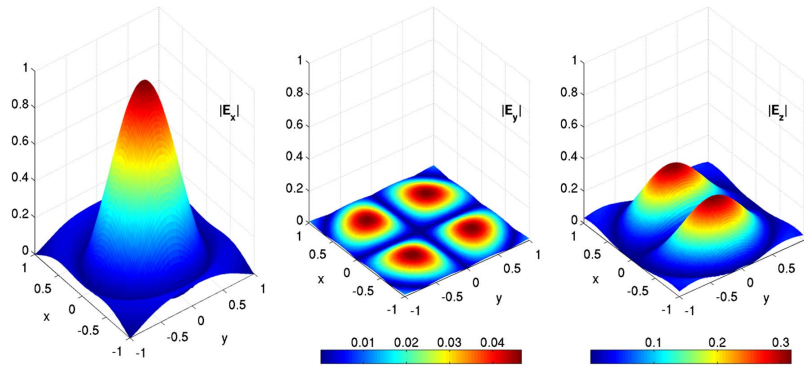


Fig. 2. Three field components $|E_x|$, $|E_y|$ and $|E_z|$ of an x-polarized Gaussian beam with a NA = 1.0 when recovered by expanding its beam coefficients with VSWF in the focal plane x - y . The fields are normalized to the maximum of $|E_x|$ and lengths are in units of wavelength, λ .

4376 GB RAM space, and operating at up to 12410 gigaflops per second. The total parameter grid consisted of 9,800,000 points. We obtained a computation speed of approximately 12 s per parameter per thread. The entire dataset as well as an interactive MATLAB user interface that calculates the optical forces and displays the trapping maps are available for download [18].

The computation results are expressed in units of force efficiency Q [19] where the optical force is given by $F = nPQ/c$, in which P is the beam power at the focus, and c is the speed of light in free space.

4. Results and Discussions

Figure 3 shows a 3D iso-surface of $Q_{z,RF\min} = -1 \times 10^{-10}$ (i.e., the axial optical trapping landscape), where the x , y , and z axis represent the particle radius ratio (r/λ), refractive index ratio (n_1/n_2), and NA, respectively. Interestingly, the iso-surface follows a clam-shell-like contour with ridges, providing a means to engineer applications by controlling the parameters, as will be discussed later. The volume space above the distribution represents the parameter combinations that do not lead to optical trapping. We refer to these combinations as optical

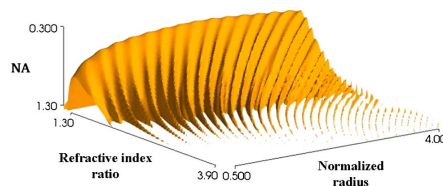


Fig. 3. Iso-surface of $Q_{z,RF\min} = -1 \times 10^{-10}$ representing the ability to conduct optical trapping calculated in relation to NA, particle refractive index ratio (n_1), and radius (r) values. The volume space above the distribution represents those parameters that do not lead to optical trapping.

trapping “blind spots.” Technically, however, the input laser is not blind to the particle and is still able to move the particle through scattering forces.

Figure 3 provides a more comprehensive overview of the optical trapping process, albeit more information can be gleaned by appropriate dissections. For instance, it appears that increases in the NA, as opposed to the refractive index or the radius, are solely responsible for creating the ridge structures that extend into the optical trapping space. When slice plots are made by keeping either the refractive index or radius constant, they manifest as finger landscapes [12], examples of which are depicted in Figs. 4(a) and 4(b). However, in the example slice plot in Fig. 4(c), obtained by keeping the NA fixed, the finger landscapes also are present.

Suppose that we select two parameter points from Fig. 4(c), $A = (2.1927, 1.2632)$ and $B = (2.1927, 1.4123)$, which lie on the finger region and another two, $C = (2.1927, 1.2105)$ and $D = (2.1927, 1.3509)$, which lie just outside the finger region. To simplify the discussion, we reference the parameter points as p_N where $N = A, B, C$ or D . At these points, we then calculate the force efficiency along the beam axis z , and provide the radiation patterns of the particles at different beam axis locations as shown in Figs. 5 and 6.

When comparing the radiation patterns of p_A and p_B against p_C and p_D at the positive peak before the equilibrium point (referred to as maximum forward restoration, $Q_{z,RF\max}$), we observe strong backscattering mode effects in all cases. As the particle approaches the focal point, the trapped particles at p_A and p_B should experience a faster change from strong backscattering to forward scattering. However, at the point of peak restoration force ($Q_{z,RF\min}$), the radiation patterns reveal that there is a smaller backscattering component for p_A and p_B as opposed to for p_C and p_D . These findings indicate the role played by scattering. Clearly, particles that

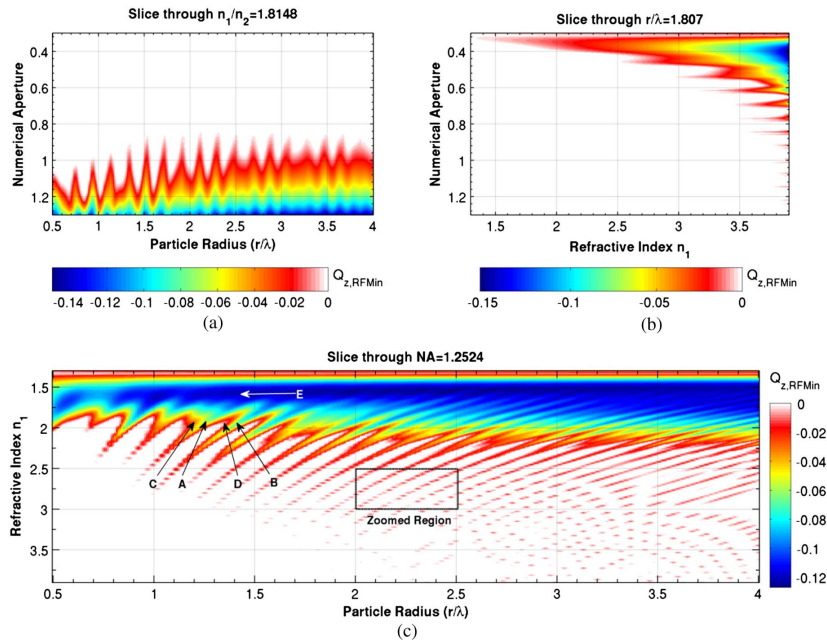


Fig. 4. Example slice plots from Fig. 3 obtained by keeping the (a) refractive index ratio, (b) normalized radius, and (c) NA fixed. Finger landscapes are observed in all three cases. The white areas correspond to $Q_{z,RFmin} = 0$, which indicates a nontrap condition.

backscatter too much cannot be trapped. However, this is a necessary condition. The sufficient condition for trapping also requires a forward-scattering component.

At first glance, Fig. 3 appears to have small islands where optical trapping occurs at locations just off the ridges. We zoomed into an example region ($2.0 \mu\text{m} \leq r \leq 2.5 \mu\text{m}$ and $2.5 \leq n_1 \leq 3.0$) by computing with smaller parameter value intervals for closer examination. We found the plots to form the fingers smoothly before they thinned out and vanished eventually (Fig. 7). Hence, the trapping islands observed in Fig. 3 were merely artifacts of using too low a sampling to resolve the trapping capabilities near the ridge regions.

The next issue is defining how well particles are drawn into and held in the trap. The former is often deduced from the magnitude of the trapping efficiency $Q_{z,RFmin}$ whilst the latter is determined from the stiffness. Both of these metrics are taken to be corresponding (i.e., high Q automatically should mean high stiffness). Such an assumption can be especially problematic at the ridge regions associated with trapping. The stiffness metric also assumes a linear relationship between force and displacement. Larger beads can show considerable deviation from

linearity, rendering problems in using stiffness as a descriptor.

In Fig. 4(c), the parameter points p_B and p_E , where $E = (1.5, 1.4123)$, both permit trapping. Nevertheless, their respective stiffness values of $0.198 \text{ Q}/\mu\text{m}$ and $0.0636 \text{ Q}/\mu\text{m}$ are significantly different, indicating that once trapped it should be harder to displace a particle from the condition of B . However, is this really the case? Is it also reasonable to assume that a particle will be drawn in with equal likelihood at conditions B and E ?

The potential energy distributions in relation to axial position for both parameter conditions are depicted in Fig. 8. Both particle parameters result in a zero-crossing and a restoration force. Nevertheless, it is intuitive that a particle should be more easily trapped in E than in B due to the creation of a deeper well-like potential.

This argument is also reasonable because particles are always brought in from a free position to a trapped position, rather than appearing at the trap position instantaneously. In other words, the momentum carried by a particle when it descends into the trap location, provided that it is not overdamped, will cause it to be more readily sustained in the case of p_E . Based on this information, it also is pertinent to note

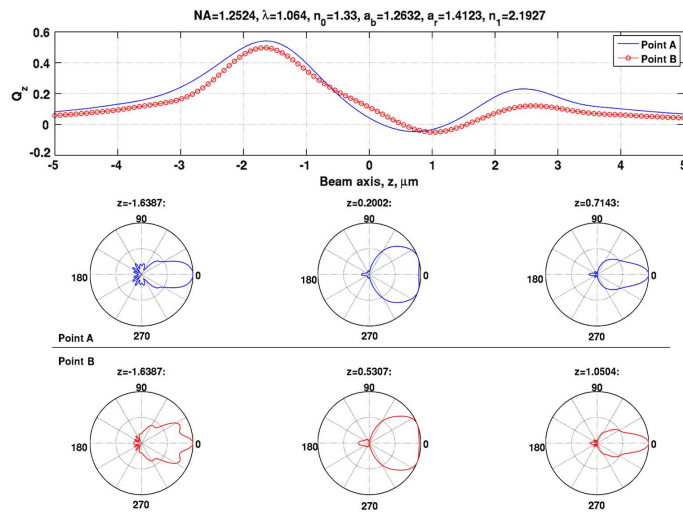


Fig. 5. Optical force efficiency, Q_z calculated on particles trapped under parameter conditions p_A and p_B placed at positions along the beam axis z . For both particles, the radiation pattern at different locations corresponding to the maximum forward restoration force, equilibrium point and maximum reverse restoration force also are shown.

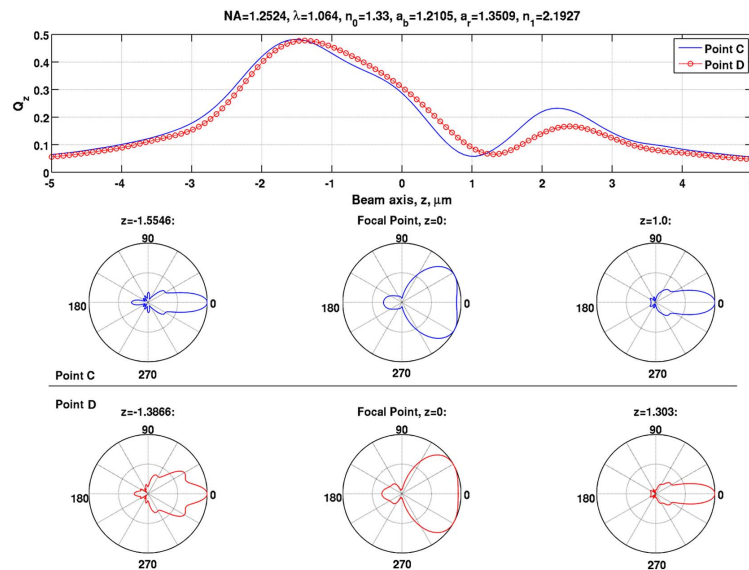


Fig. 6. Optical force efficiency, Q_z , calculated on particles trapped under parameter conditions p_C and p_D placed at positions along the beam axis z . For both particles, the radiation pattern at different locations corresponding to the maximum forward restoration force, focal point, and $z = 1.0 \mu\text{m}$ also are shown.

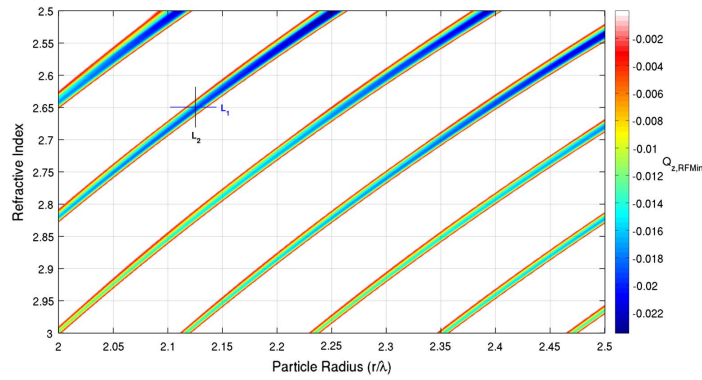


Fig. 7. Zoomed-in region for Fig. 3, ($2.0 \mu\text{m} \leq r \leq 2.5 \mu\text{m}$ and $2.5 \leq n_1 \leq 3.0$) with smaller parameter value intervals, which show that the fingers form smoothly before they are thinned out and eventually vanish. Two lines, L1 and L2, indicate that particles with a radius ratio between 2.115 and 2.135 would be selectively trapped, which illustrates the ability for sorting.

that the premise of a stiffer trap is only reasonable when comparing distributions that are strongly symmetrical (e.g., p_B) and not when they are highly asymmetrical (e.g., p_B). This is because the latter provides a lower energy obstacle path for the particle to depart from the trap.

It is not uncommon in particle motion simulations for the condition of overdamping to be applied, which, in turn, implies an inability of the particle to possess any inertia force. It is important to note, however, that the overdamped assumption is valid only for sufficiently large evolution time intervals. Furthermore, a particle that has descended into a potential well will not remain stationary there, since Brownian perturbations continue to exist.

Even under the assumption of overdamping, it has been shown that Brownian perturbations can cause particles to exit potential wells [20]. Clearly, any description that does not take into consideration the asymmetry of the well is problematic.

Despite these definition difficulties, it will be desirable to have at least some indication of the relative asymmetry of the trap. We contend that a more apt representation to use should be what we call the trapping quality, which is described by:

$$TQ = \begin{cases} 0 & Q_{z,RF \min} \geq 0 \\ \text{abs}\left(\frac{Q_{z,RF \min}}{Q_{z,RF \max}}\right) & Q_{z,RF \min} < 0 \end{cases} \quad (1)$$

where $\text{abs}()$ is the absolute function. This metric is reasonable because the forward restoration will always be higher due to the scattering and gradient components complementing each other in the forward direction. In contrast, they oppose each other during the reverse restoration process. In other words, we will always have $TQ < 1$, in which a value closer to 1 indicates a higher symmetry in the trap. Based on this metric, we computed that $TQ_B = 0.1$

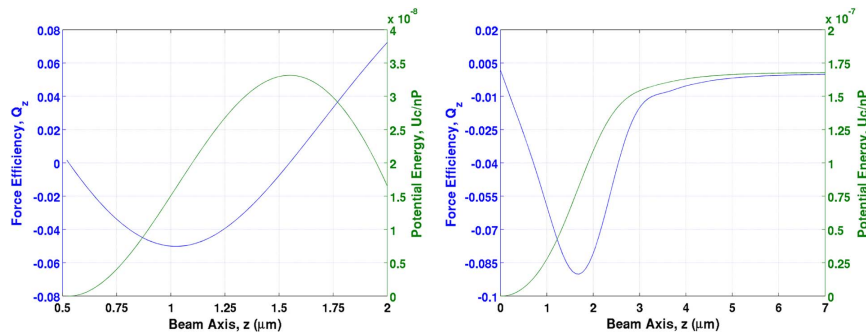


Fig. 8. Potential energy wells corresponding to a particle located in the safe region and on a trapping finger, depicted under conditions p_E and p_B , respectively.

and $TQ_E = 0.69$, which logically depicts the situation in which trapping should be more likely at p_E than in p_B (based on their potential distributions).

Note here that radial trapping behaves considerably differently than axial trapping. Trapping is often taken to mean that the axial and radial trapping events are mutually inclusive (i.e., radial trapping cannot occur unless there is axial trapping and vice versa). However, calculations with radial trapping will not reveal the landscapes in Fig. 3, meaning that there are no radial optical trapping blind spot structures in the parameter space. Determining whether particles are trapped or not, consequently, should not be based on the axial condition alone. This argument is supported by the experimental findings from previous works [21,22], where a transition from radial pulling to trapping or release was uncovered. More specifically, a particle that is sucked up from the bottom of the beam focus will head upward along the beam axis until it reaches the focus point wherein it will be either trapped or released upward and outward in a trajectory not unlike a water fountain spray.

The narrowing fingertips provide a highly selective and precise set of trapping parameters. Any small variation of the radius or refractive index would cause the particle to be set free. The trapping strength distribution along the two lines L_1 and L_2 in Fig. 7, and its derivative, are shown in Fig. 9. Figure 9(a) indicates that particles with radius ratio between 2.115 and 2.135 would be selectively trapped. In Fig. 9(b), alternatively, we find that particles with refractive index ratio between 2.615 and

2.642 would be trapped. Clearly, the selection of any line across the finger landscape permits the process to operate somewhat like a tunable bandpass filter; i.e., the ranges can be controlled by choosing a narrower or wider section of the finger. The narrower the finger is, the smaller the bandwidth will be and vice versa. That the gradient is steepest at the edges of the finger helps to enhance it selectively. However, it is the width of the finger that determines the range of tolerances of particle radius or refractive index that can be trapped. Because these factors can be independent of each other, as seen in Fig. 9, this imbues the capacity for effective sorting.

At this juncture, it is apt to mention the current status in particle sorting. While sorting approaches with fluid flow offer apparent higher throughputs, they are prone to channel effects [23,24]. The situation becomes more complicated when non Newtonian fluids are involved [25].

Let's consider an alternative approach based on our findings. Suppose we have an optical trap that scans a population of different sized particles of two distinct refractive indices in a plane. Through the right wavelength selection, it will be possible to trap particles of one refractive index while allowing those of another refractive index to be scattered (note that while the gradient force is not strong enough to hold the particle, it does not mean that the scattering force is absent). At the end of the scan, only particles of one refractive index will remain in the plane. With recent developments using tailored optics, it should be possible to develop multiple trapping (and removal) sites to increase the throughput

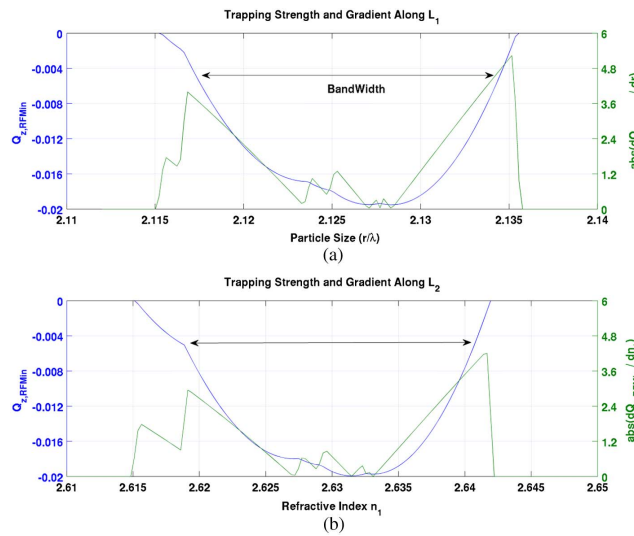


Fig. 9. Trapping strength and its gradient along the lines (a) L_1 and (b) L_2 as depicted in Fig. 7.

of such a process [26], albeit this may reduce the optical power at each trapping site. That the perturbation to remove selected particles is based on the optical scattering force makes this an all-optical sorting approach. This has potentially strong advantages over approaches that rely on coupled optical and Brownian forces [27], since the latter is a strongly stochastic process. At this point, we highlight interesting parallels between the effect of interference leading to parameter spaces that permit trapping-based sorting here and the use spatial interference fields itself to accomplish sorting [28,29].

The identification of blind spot optical trapping conditions in the map does not necessarily translate to seeking a design toward its total avoidance in actual applications. Such conditions are in fact useful when particle trapping is to be avoided altogether. While the positional manipulation of cells using optical traps is convenient, it is also fraught with the possibility of photodamage [30]. One obvious strategy is to use wavelengths that limit this effect. However, this has to take into account that the trapping strength also may be compromised, wherein compensating by using a higher optical power becomes self-defeating. It has recently been shown that placing

the laser trap position off-focus axially can create a strong lateral movement effect that can be harnessed for the manipulation of position [21,22]. To reduce the possibility of cells reaching the trap position (where laser intensity is also highest), operation under blind-spot conditions will be ideal. This is naturally achieved when the cells have refractive index close to that of the medium. While the direct trapping of cells does not occur at the fingering regions, this does not preclude using the trap to place microbeads that are laced with drugs at the location of cells, in a strategy that is often called targeted drug delivery. These beads may be made out of materials that fall in the fingering regions.

Arguably, the most potent use of the trapping map lies in situations where multiparameter variations are involved. Returning to the topic of targeted drug delivery, a popular mode of release involves swelling of the micro beads [31]. Suppose that we adopt a simple model in which a dielectric sphere of original radius $r_o = 2.095 \mu\text{m}$ and refractive index $n_1 = 2.506$ is placed in a medium with refractive index $n_2 = 1.33$. Under the assumption that the medium material fills into the bead uniformly and the bead maintains a spherical shape throughout swelling, the original volume V_o can be taken to undergo a volume increase ΔV under the relationship of $\Delta V = \alpha V_o$, where α depicts the progress of the swelling (i.e. $\alpha = 0$ when no swelling occurs) (Fig. 10). The refractive index of the bead can now be indicated by:

$$n'_1 = \frac{V_o n_1 + \Delta V n_2}{V_o + \Delta V} = \frac{V_o n_1 + \alpha V_o n_2}{V_o + \alpha V_o} = \frac{n_1 + \alpha n_2}{1 + \alpha} \tag{2}$$

The radius can also be described using α as

$$r = r_o (\sqrt[3]{1 + \alpha}) \tag{3}$$

On the parameter map using $\text{NA} = 1.2248$ [Fig. 11(a)], this will result in a trajectory where

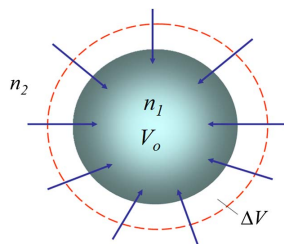


Fig. 10. Schematic description of situation where a spherical of volume V_o of refractive index n_1 undergoes swelling by absorbing material from the surrounding media of refractive index n_2 such that its volume increases by ΔV .

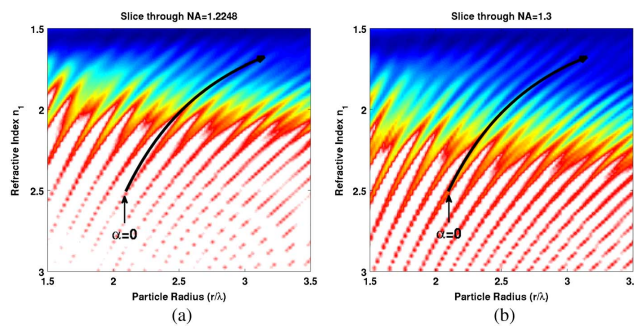


Fig. 11. Trajectory of a swelling dielectric sphere with an original radius $r_o = 2.095 \mu\text{m}$ and refractive index $n_1 = 2.506$, placed in a medium with refractive index $n_2 = 1.33$ for: (a) $\text{NA} = 1.2248$ and (b) $\text{NA} = 1.33$. The growth rate, α , was linearly increased from 0 to 2.0.

the particle is first trapped but strays into the condition of nontrapping with swelling increase of the sphere. That the trapping state is encountered again later is irrelevant since the particle would have been released from the hold of the potential well. If the NA is increased to $NA = 1.3$, particle trapping will be maintained throughout [Fig. 11(b)].

Finally, let's discuss study extensions. Interesting findings have been made regarding the momentum effects (and thus trapping effects) associated with polarization [32,33]. It is conceivable that polarization may offer an additional degree of parameter freedom when designing improved tools for all-optical sorting. In the same vein, oscillatory optical trapping with Monte Carlo inputs that create spatially and temporally modulated optical traps have been useful in microrheology and biophysics [34,35]. The interest in the latter is arguably from lowered photothermal damage due to the non continuous nature of the supplied laser beam. It also promises to be pertinent in the all-optical sorting approach proposed. Nevertheless, the effects of Brownian diffusion also must be considered [15].

5. Conclusions

A comprehensive computation was successfully conducted to ascertain the axial trapping efficiency, which is limiting, of spherical dielectric particles using a focused Gaussian laser beam based on (i) the particle radius r , (ii) the ratio of the refractive index of particle over the medium, and (iii) the NA of the delivered light beam. It yielded an iso-surface that follows a clam-shell-like contour with ridges that offer a way to engineer applications by controlling the parameters used.

It also was found that a volume space exists that based on specific parameter combinations that do not lead to optical trapping. The appearance of small islands of optical trapping at the locations just off the ridges were found to be artifacts of using too low a sampling to resolve the trapping capabilities near the ridge regions. By examining specific points in the computed parameter volume space, we uncovered difficulties using the trapping efficiency and stiffness metrics in defining how well particles are drawn into and held in the trap.

An alternative calculation based on the maximum forward and restoration values of the trapping efficiency in the axial sense, which is called the trapping quality, provided a more practical metric. The ridge regions of trapping offer high specificity on whether trapping can occur or not based on small parameter changes. Consequently, this may be harnessed for effective particle sorting. Finally we discussed how the optical trapping blind spots can be advantageous in applications that use optical forces for particle translation in which photothermal damage is eschewed. We also highlighted the use of the map to guide multiparameter changes during trapping.

Parts of this work were made possible by support from Australian Research Council Discovery Project

Grants DP0878454 and DP120100583. We appreciate the insights provided by M. W. Berns at the Beckman Laser Institute on cell and neuron interactions with lasers, and discussions with O. W. Liew at Cardiovascular Research Institute, Singapore.

References

1. A. Ashkin, "Acceleration and trapping of particles by radiation pressure," *Phys. Rev. Lett.* **24**, 156–159 (1970).
2. A. Ashkin, J. M. Dziedzic, J. E. Bjorkholm, and S. Chu, "Observation of a single-beam gradient force optical trap for dielectric particles," *Opt. Lett.* **11**, 288–290 (1986).
3. I. Perch-Nielsen, D. Palima, J. S. Dam, and J. Gluckstad, "Parallel particle identification and separation for active optical sorting," *J. Opt. A* **11**, 034013 (2009).
4. M. P. MacDonald, G. C. Spalding, and K. Dholakia, "Microfluidic sorting in an optical lattice," *Nature* **426**, 421–424 (2003).
5. M. Polin, Y. Roichman, and D. G. Grier, "Autocalibrated colloidal interaction measurements with extended optical traps," *Phys. Rev. E* **77**, 051401 (2008).
6. A. Neild, T. W. Ng, and W. M. Yui, "Optical sorting of dielectric Rayleigh spherical particles with scattering and standing waves," *Opt. Express* **17**, 5321–5329 (2009).
7. N. Hyun, C. Chandsawangbhuwana, Q. Zhu, L. Z. Shi, C. Yang-Wong, and M. W. Berns, "Effects of viscosity on sperm motility studied with optical tweezers," *J. Biomed. Opt.* **17**, 025005 (2012).
8. P. A. M. Neto and H. M. Nussenzveig, "Theory of optical tweezers," *Europhys. Lett.* **50**, 702–708 (2000).
9. T. A. Nieminen, V. L. Y. Loke, A. B. Stilgoe, G. Knoner, A. M. Branczyk, N. R. Heckenberg, and H. Rubinsztein-Dunlop, "Optical tweezers computational toolbox," *J. Opt. A* **9**, S196–S203 (2007).
10. M. J. Kendrick, D. H. McIntyre, and O. Ostroverkhova, "Wavelength dependence of optical tweezer trapping forces on dye-doped polystyrene microspheres," *J. Opt. Soc. Am. B* **26**, 2189–2198 (2009).
11. A. Ashkin, "Forces of a single-beam gradient laser trap on a dielectric sphere in the ray optics regime," *Biophys. J.* **61**, 569–582 (1992).
12. A. B. Stilgoe, T. A. Nieminen, G. Knoner, N. R. Heckenberg, and H. Rubinsztein-Dunlop, "The effect of Mie resonances on trapping in optical tweezers," *Opt. Express* **16**, 15039–15051 (2008).
13. K. J. Knox, D. R. Burnham, L. I. McCann, S. L. Murphy, D. McGloin, and J. P. Reid, "Observation of bistability of trapping position in aerosol optical tweezers," *J. Opt. Soc. Am. B* **27**, 582–591 (2010).
14. M. L. Gorodetsky, A. A. Savchenkov, and V. S. Ilchenko, "Ultimate Q of optical microsphere resonators," *Opt. Lett.* **21**, 453–455 (1996).
15. E. Xifré-Pérez, F. J. García de Abajo, R. Fenollosa, and F. Meseguer, "Photonic binding in silicon-colloid microcavities," *Phys. Rev. Lett.* **103**, 103902 (2009).
16. P. Chýlek and J. Zhan, "Interference structure of the Mie extinction cross section," *J. Opt. Soc. Am. A* **6**, 1846–1851 (1989).
17. B. Sun and D. G. Grier, "The effect of Mie resonances on trapping in optical tweezers: comment," *Opt. Express* **17**, 2658–2660 (2009).
18. Simulator for the optical trapping of spherical dielectric particles. www.biofuturex.com/LOAM/index-resource.html.
19. A. Ashkin, "Forces of a single-beam gradient laser trap on a dielectric sphere in the ray optics regime," *Biophys. J.* **61**, 569–582 (1992).
20. M. Bier, I. Derenyi, M. Kostur, and R. D. Astumian, "Intrawell relaxation of overdamped Brownian particles," *Phys. Rev. E* **59**, 6422–6432 (1999).
21. M. Muradoglu, W. S.-Y. Chiu, and T. W. Ng, "Optical force lateral push–pulling using focus positioning," *J. Opt. Soc. Am. B* **29**, 874–880 (2012).
22. M. Muradoglu, T. Le, C. Y. Lau, O. W. Liew, and T. W. Ng, "Optical stirring in a droplet cell bioreactor," *Biomed. Opt. Express* **3**, 2465–2470 (2012).

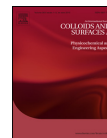
23. J.-P. Matas, J. F. Morris, and E. Guazzelli, "Inertial migration of rigid spherical particles in Poiseuille flow," *J. Fluid Mech.* **515**, 171–195 (2004).
24. D. DiCarlo, D. Irimia, R. G. Tompkins, and M. Toner, "Continuous inertial focusing, ordering, and separation of particles in microchannels," *Proc. Natl. Acad. Sci. USA*. **104**, 18892–18897 (2007).
25. J. Koo and C. Kleinstreuer, "Liquid flow in microchannels: experimental observations and computational analyses of microfluidics effects," *J. Micromech. Microeng.* **13**, 568–579 (2003).
26. Y. Zhang, Z. Liu, J. Yang, and L. Yuan, "A non-contact single optical fiber multi-optical tweezers probe: design and fabrication," *Opt. Commun.* **285**, 4068–4071 (2012).
27. T. W. Ng, A. Neild, and P. Heeraman, "Continuous and fast sorting of Brownian particles," *Opt. Lett.* **33**, 584–586 (2008).
28. P. Ják, T. Cizmár, M. Šerý, and P. Zemánek, "Static optical sorting in a laser interference field," *Appl. Phys. Lett.* **92**, 161110 (2008).
29. K. Dholakia, M. P. MacDonald, P. Zemánek, and T. Cizmár, "Cellular and colloidal separation using optical forces," *Methods Cell Biol.* **82**, 467–495 (2007).
30. K. König, H. Liang, M. W. Berns, and B. J. Tromberg, "Cell damage in near-infrared multimode optical traps as a result of multiphoton absorption," *Opt. Lett.* **21**, 1090–1092 (1996).
31. Y. N. Dai, P. Li, J. P. Zhang, A. Q. Wang, and Q. Wei, "Swelling characteristics and drug delivery properties of nifedipine-loaded pH sensitive alginate-chitosan hydrogel beads," *J. Biomed. Mater. Res. B Appl. Biomater.* **86**, 493–500 (2008).
32. A. M. Beckley, T. G. Brown, and M. A. Alonso, "Full Poincaré beams II: partial polarization," *Opt. Express* **20**, 9357–9362 (2012).
33. E. Madadi, A. Samadi, M. Cheraghian, and S. N. S. Reihani, "Polarization-induced stiffness asymmetry of optical tweezers," *Opt. Lett.* **37**, 3519–3521 (2012).
34. G.-B. Liao, P. B. Bareil, Y. Sheng, and A. Chiou, "One-dimensional jumping optical tweezers for optical stretching of bi-concave human red blood cells," *Opt. Express* **16**, 1996–2004 (2008).
35. Y.-X. Ren, J.-G. Wu, M.-C. Zhong, and Y.-M. Li, "Monte Carlo simulation of effective stiffness of time-sharing optical tweezers," *Chin. Opt. Lett.* **8**, 170–172 (2010).

B.8 Contact angle and volume retention effects from capillary bridge evaporation in biochemical microplating

Colloids and Surfaces A: Physicochem. Eng. Aspects 436 (2013) 647–655



Contents lists available at ScienceDirect
Colloids and Surfaces A: Physicochemical and Engineering Aspects

journal homepage: www.elsevier.com/locate/colsurfa

Contact angle and volume retention effects from capillary bridge evaporation in biochemical microplating

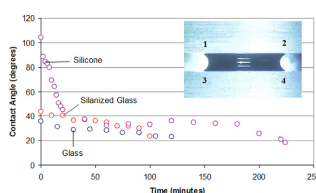
Trang Hunyh^a, Murat Muradoglu^a, Oi Wah Liew^b, Tuck Wah Ng^{a,*}

^a Laboratory for Optics & Applied Mechanics, Department of Mechanical & Aerospace Engineering, Monash University, Clayton, Victoria 3800 Australia
^b Cardiovascular Research Institute, Yong Loo Lin School of Medicine, National University of Singapore, National University Health System, Centre for Translational Medicine, 14 Medical Drive, Singapore 117599, Singapore

HIGHLIGHTS

- Capillary bridges to find contact angle and retain volumes for microplating under evaporation is studied.
- Capillary bridges between silicone flat surfaces had initial steep contact angle reduction.
- Capillary bridges between silicone flat surfaces extended the volume held by 5 times over sessile drops.
- Capillary bridges between hydrophobic flat surfaces offer best means to study wetting and restrict volume loss.
- Capillary bridges between 3 glass rods are unsuited for contact angle tracing and volume retention.

GRAPHICAL ABSTRACT



ARTICLE INFO

Article history:
 Received 26 February 2013
 Received in revised form 16 July 2013
 Accepted 30 July 2013
 Available online 7 August 2013

Keywords:
 Microplating
 Evaporation
 Contact angle
 Volume
 Liquid bridge
 Sessile drop

ABSTRACT

Biochemical microplating in resource-limited venues presents a challenge with important outcomes. The feasibility of using capillary bridges developed in schemes that apply transparencies and samples between rods with EGFP samples to interrogate wetting via the contact angle and to retain volumes for longer under evaporation was investigated here. The experiments with capillary bridge evaporation between two flat silicone surfaces found a steep contact angle reducing rate in the early stage followed by a more gradual reducing rate later. The steep process was attributed to the liquid–vapor interface accommodating for thermodynamic entropy changes during evaporation. The initial convex meniscus also resulted in faster volume reduction from Kelvin's relation on escape tendency. With the same volume, the two silicone surfaces extended the retention time of the sessile drop by over 5 times. This unexpected effect was attributed to the initial convex to concave meniscus change in a confined space that resulted in a more saturated vapor pressure nearer to the interface. This finding portends the favorable use of hydrophobic surfaces in transparency microplating. Its use in contact angle measurements however will be subject to the evaporation mechanics at confined areas. It is also limited by rupture. With capillary bridge between three rods, this occurred at higher angles. This approach did not improve volume retention from evaporation much and was prone to wetting not being constant along the bridge length. Higher fluctuations in the contact angle trend were found which made attempts to estimate volume based on geometry subject to large levels of uncertainty. Nevertheless, the geometrical equations and approximated parameter changes showed the length change to be above two times the cross sectional area change during evaporation. The results indicate that creating capillary bridges for the transparency microplates offer the best ability to retain volumes while allowing the contact angle to be interrogated.

© 2013 Elsevier B.V. All rights reserved.

* Corresponding author. Tel.: +61 3 99054647; fax: +61 3 99051825.

1. Introduction

The microplate (multiwell plate or microtiter plate) has become a standard tool in analytical research and clinical diagnostic testing laboratories. In microplate instrumentation, the trend is moving toward testing increasingly smaller liquid volumes [1–4]. Smaller test volumes (i) increase the number of assays that can be conducted per plate thereby increasing throughput, and (ii) reduce sample quantity needed per assay which is crucial when the test samples/reagents are scarce or expensive. In dealing with miniaturized assays, alternative approaches have been developed to handle small liquid volumes, their preparation and testing without the need for complex or precise machinery [1,4] or limitations from wetting [5]. Yet, there is also impetus to create microplates that are cost effective enough to be available for use in resource-limited laboratories so that diagnostic outcomes can be achieved in a more timely fashion. Two approaches that have been advanced recently to address this without affecting the efficacy in optical diagnosis are through the use of samples on transparencies [6,7] and between rods [8].

It is sometimes necessary to incubate samples for prolonged periods in microplates. In such situations, the influence of evaporation cannot be overlooked. One aspect that needs to be considered is the effect on wetting. The contact angle (CA) of a liquid on a solid surface is widely considered to be a key parameter that characterizes wetting behavior. The CA is most universally defined as the angle between the liquid–vapor and the solid–liquid interfaces, at the point where the three phases (solid, liquid, and gas) meet. Some treated surfaces are high-energy and permit liquids to spread spontaneously on them [9,10]. Most surfaces, however, do not exhibit this property, resulting in the formation of a drop. Surfaces that cause the CA to be smaller than 90° are defined as hydrophilic while those that engender a CA larger than 90° are classified as hydrophobic. By using chemical treatments to develop nano-scale structures on surfaces, it is possible to achieve contact angles that are close to 180° , which are increasingly harnessed for use in applications that require high degrees of non-wetting [11–13]. Arguably, the most widely used method to determine the CA of a sessile drop is by direct imaging of its side-profile [14–16]. In another method called the Wilhelmy balance, the contact angle is deduced from the force exerted by the liquid on a small plate or ring, which is advanced to and/or receded from the liquid [17]. The use of contact between a spherical lens and liquid bath has been advanced as yet another means of determining the contact angle [18], which apparently is suited for characterizing surfaces with very low contact angle hysteresis.

The sessile drop method is prone to the problem of evaporation due to the large proportion of liquid surface area exposed to air. From the outset, it has been established that the process involves stages where the drop is either pinned at the contact line, or that the contact line undergoes slipping. Efforts to characterize the evaporation of drops can arguably be traced to the analysis of Picknett and Bexon [19]. Since then, other models have appeared in an attempt to better account for evaporation flux distribution [20]. In all these models, the underlying basis of a sessile drop situated on a solid surface is that the adjacent air becomes saturated with vapor due to the rapid interchange of the molecules between the liquid and its vapor. The vapor is essentially then a thin saturated region that diffuses outward into the surrounding unsaturated air. Assuming a quasi-equilibrium process for slow evaporation in still air, the evaporation rate of the vapor Q can be taken to be represented by Fick's law such that

$$Q = \rho \frac{dV}{dt} = 4\pi DR(C_s - C_\infty) f(\theta) \quad (1)$$

where D is the vapor diffusivity in still air, R radius of drop surface curvature, C_s the saturated vapor concentration at drop surface, C_∞ the ambient vapor concentration determined by the relative humidity, and $f(\theta)$ = the dependence of evaporation rate on the contact angle. The models to describe the temporal evolution of a drop volume require the functional form of $f(\theta)$ and the temporal variations of R and θ to be known a priori. Recent studies have shown that $f(\theta)$ to be dependent on the nature of the surface since porous types can cause the liquid to imbibe in them such that it enters into a strongly Wenzel wetting state [21]. However, the determination of $f(\theta)$ may be side stepped if the objective is to trace the progression of the contact angle due to pinning and slipping. In addition, the volume trace may also be determined via computations based on the geometrical shape of the liquid body to sufficiently depict the mechanics.

In contrast to the sessile drop, an approach based on determining the height of a laser lighted meniscus in capillaries offers an alternative means to trace the contact angle progression with time [22]. The heightened level of liquid confinement offered there is helpful in reducing the extent of evaporation. Nevertheless, this approach is suited more to interrogating the wetting behavior of different liquids than variations in the surface itself as (i) modifying treatments and (ii) microscopic examination, will generally be difficult to carry out on the inner surfaces of the capillary. Clearly, surfaces that offer improved resistance to evaporation and are yet easily accessible will be beneficial.

Liquid bodies that are placed between surfaces will develop capillary bridges. The compression of this body between two flat parallel plates creates the condition for growth of the menisci in which its stability can be established [23]. This has also been studied in the case of tension, leading to important application implications in colloidal microstructure formation [24], biological system attachment [25] and flow generation and transfer [26]. Capillary bridges too form when the liquid body is placed between circular rods [27] and this has been recently applied to serve as a biochemical microplating device with the ability for mixing [8].

In this work, we investigate the feasibility of using the capillary bridges developed between solid bodies to interrogate the contact angle development under the effect of evaporation. In addition, we also seek to ascertain the progress of volume change. These findings will help to provide insights on the ability to relate wetting to analyte characteristics and mitigate evaporation in biochemical microplating schemes developed for use in resource-limited laboratories.

2. Theoretical considerations

2.1. Volumetric determination of a sessile drop

When surface tension dominates, the shape of a sessile drop on a surface can be assumed to be semi-spherical. From geometry (see Fig. 1), it is rather easy to establish that the volume is related to the radial distance of the drop on the surface a by

$$V = \frac{\pi a^3 (1 - \cos \theta)^2 (2 + \cos \theta)}{3 \sin^3 \theta} \quad (2)$$

where θ is the contact angle and R is the radius of curvature.

2.2. Volumetric determination of a capillary bridge between two flat plates

The liquid bridge that forms between two flat surfaces under a strong surface tension effect assumes three different shapes,

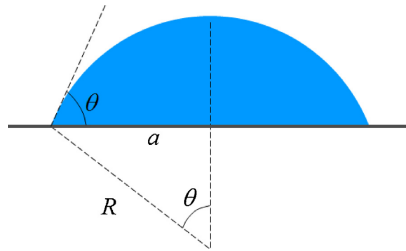


Fig. 1. Schematic description of a sessile drop where its shape is semi-spherical. The volume can be determined using the measurable parameters of θ and a .

depending on the contact angle. In the case where $\theta < 90^\circ$, we have from Fig. 2(a)

$$\frac{h}{R} = \cos \theta \tag{3}$$

where h is the half height of the liquid bridge. The length of AB is then given by

$$|AB| = \sqrt{R^2 - (h - y)^2} = \sqrt{\frac{h^2}{\cos^2 \theta} - (h - y)^2} \tag{4}$$

For a vertical distance of y from the solid surface, the horizontal distance can be determined using

$$x = a + h \tan \theta - |AB| = a + h \tan \theta - \sqrt{\frac{h^2}{\cos^2 \theta} - (h - y)^2} \tag{5}$$

The volume of the liquid bridge can thus be computed using

$$V = 2 \int_{y=0}^{y=h} \pi x^2 dy \tag{6}$$

In the case where $\theta > 90^\circ$, we have from Fig. 2(b)

$$\frac{h}{R} = \cos(180^\circ - \theta) \tag{7}$$

The length of AB in this case is then given by

$$|AB| = \sqrt{R^2 - (h - y)^2} = \sqrt{\frac{h^2}{\cos^2(180^\circ - \theta)} - (h - y)^2} \tag{8}$$

The horizontal distance based on a vertical distance of y from the solid surface can thus be determined by

$$x = a + h \tan(180^\circ - \theta) + |AB| = a + h \tan(180^\circ - \theta) + \sqrt{\frac{h^2}{\cos^2(180^\circ - \theta)} - (h - y)^2} \tag{9}$$

The volume can then be determined using Eq. (8). In the case where $\theta = 90^\circ$, the liquid bridge is essentially a cylinder. Hence the volume in this case is given by

$$V = \pi a^2(2h) = 2\pi a^2 h \tag{10}$$

2.3. Volumetric determination of a capillary bridge between three rods

When a small but sufficient amount of liquid is brought into the gap of three two narrowly spaced wettable rods, the liquid forms a short bridge the surface of which can be assumed to be constant mean curvature. As more and more liquid is added to the bridge, it lengthens in the direction of the axes until it forms a long cylindrical body to a good approximation, and has a constant cross section except in the region of the terminal menisci. The volume of liquid can then be taken as the product of this cross-section and the length. If we take the rods to be of equal distance z from each other (Fig. 3(a)), the distance between the centroid O' to the center of each rod is given by

$$d = \frac{\sin(\pi/6)}{\sin(2\pi/3)} z = \frac{z}{3} \tag{11}$$

Suppose that the contacts of capillary bridge with the uppermost rod are at A and C (Fig. 3(b)). If this subtends an angle of 2ϕ on the rod, we can trace out the triangle $O'OA$ in Fig. 3(c) such that

$$\frac{r}{\sin \phi} = \frac{c}{\sin \phi} \tag{12}$$

$$r \cos \phi + r \cos \phi = d \tag{13}$$

From (14) and (15) we have

$$\phi = \tan^{-1} \left(\frac{r \sin \phi}{d - r \cos \phi} \right) \tag{14}$$

The area of the triangle $O'OA$ is thus

$$\text{Area}(O'OA) = \frac{1}{2} r d \sin \phi \tag{15}$$

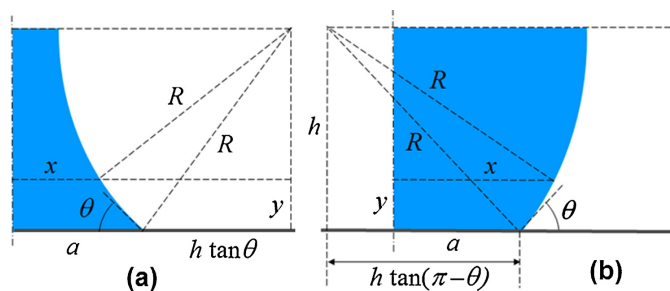


Fig. 2. Schematic description of the half height and width of a symmetrical capillary bridge between two flat surfaces when (a) $\theta < \pi/2$, and (b) $\theta > \pi/2$. The volume can be calculated using the parameters of θ , h , and a .

650

T. Hunyh et al. / Colloids and Surfaces A: Physicochem. Eng. Aspects 436 (2013) 647–655

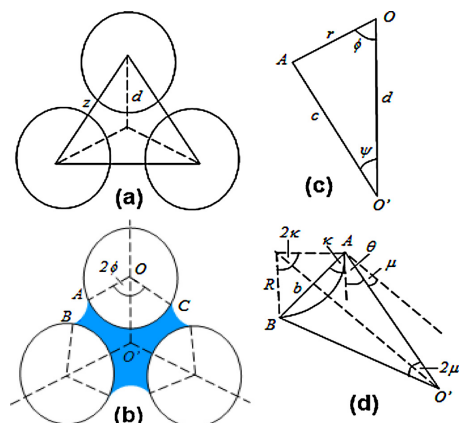


Fig. 3. Schematic description of (a) the cross-section of three rods of equal diameter located with equal distance z to each other. The contacts of capillary bridge (at points A and C) with the rod, shown in (b), subtend an angle of 2ϕ on it. The areas computed of OOA in (c), OAB and the semicircle AB in (d), and OAC in (b) permit the volume of the capillary bridge to be determined.

From the triangle $O'AB$ (Fig. 3(d)), we are able to determine that

$$\mu = \frac{\pi}{3} - \varphi \quad (16)$$

In addition, the area of the triangle $O'AB$ is given by

$$\text{Area}(O'AB) = \frac{1}{2}c^2 \sin 2\varphi \quad (17)$$

The length of the chord AB can be found using

$$b = 2c \sin \mu \quad (18)$$

In Fig. 3(d), it can be seen that the arc AB is subtended through an angle of 2κ by the radius R . Since

$$\kappa = \frac{\pi}{2} - (\mu + \theta) \quad (19)$$

it is possible to find that

$$R = \frac{b}{2 \sin \kappa} = \frac{b}{2 \sin (\pi/2 - (\mu + \theta))} = \frac{b}{2 \cos (\mu + \theta)} \quad (20)$$

This will allow the area of the semicircle cap AB to be approximated using

$$\begin{aligned} \text{Area}(\nabla AB) &\approx \frac{R^2}{2}(2\kappa - \sin 2\kappa) \approx \frac{b^2}{8 \cos^2(\mu + \theta)} \\ &\left\{ 2 \left(\frac{\pi}{2} - (\mu + \theta) \right) - \sin 2 \left(\frac{\pi}{2} - (\mu + \theta) \right) \right\} \\ &\approx \frac{b^2}{8 \cos^2(\mu + \theta)} (\pi - (\mu + \theta) - \sin 2(\mu + \theta)) \end{aligned} \quad (21)$$

The area of the subtended arc OAC is simply

$$\text{Area}(OAC) = \left(\frac{2\phi}{2\pi} \right) \pi r^2 = \phi r^2 \quad (22)$$

Summarily, the cross section comprising the liquid body is given by

$$\text{Area} = 6 \text{Area}(O'OA) + 3 \text{Area}(ABO) - 3 \text{Area}(\nabla AB) - 3 \text{Area}(OAC) \quad (23)$$

The input of parameters z , r , ϕ , and θ into Eqs. (11), (12), (14), (16), and (18) permit d , c , φ , μ , and b to be determined. From these parameters, Eqs. (15), (17), (19), and (22) can be solved to allow the cross-sectional area of liquid to be determined via Eq. (23).

3. Materials and methods

3.1. Materials

The experimental sample used was enhanced green fluorescent protein (EGFP) carrying a C-terminal polyhistidine tag, isolated from genetically modified *Escherichia coli* and purified by immobilized metal affinity chromatography. After elution of the proteins from the chromatographic matrix, the sample was desalted into sodium phosphate buffer (pH 7.4), checked for purity by SDS-PAGE (sodium dodecyl sulfate-polyacrylamide gel electrophoresis), and quantified using the BCA (bisinchoninic acid) protein assay (Pierce). Sodium phosphate (NaPO_4) buffer was used to prepare a series of dilutions for the purified EGFP sample ranging from 65 to 1300 ng/ μL . These solutions were delivered using a manual pipette (Biohit mLine Mechanical Pipette, 10–100 μL).

The experiments conducted on flat surfaces comprised glass slides, silanized glass slides, and silicone surface slides; which gave different levels of hydrophobicity. For experiments on rods, capillary tubes of outer diameter 1 mm were used. Images were recorded using microscope lenses (Infiniprobe) attached to CCD video camera (Hitachi, KP-D20AU). From the images recorded, the required dimensional information was extracted using the UTHSCSA Image-Tool Version 3.0 software.

3.2. Measurements of sessile drops on a flat surface

Liquid drops of the same volume (3 μL) were deposited onto each flat surface using a manual pipette. The imaging axis was kept parallel to the glass plate along its surface, and perpendicular to the droplet symmetry line when viewing the setup from the side (see Fig. 4). A bright LED light source was placed opposite to the microscope camera to illuminate the droplet for clearer imaging, along the imaging axis. The droplet was deposited close to the edge of the plate on the imaging side so that the droplet and the end of the plate were almost equally focused.

From the video recordings an image file was produced at each time interval until the evaporation of the drop was complete. Based on the images recorded, the contact angle θ and drop radii on the surface a information was determined (see Fig. 1).

3.3. Measurements of capillary bridges between two flat surfaces

Liquid drops of equal volume (3 μL) were deposited between two rectangular flat surfaces placed in parallel to each other and perpendicular in relation to gravity. The distance between the surfaces was maintained at 0.475 mm using two spacers (Fig. 5(a)). The imaging axis was kept parallel to the glass plates, so that it passes through the center point of the liquid bridge at the intersecting symmetry lines. The LED light source was placed opposite to the microscope camera to illuminate the liquid bridge along the imaging axis. The droplet was deposited close to the edge of the plates on the imaging side so that the liquid bridge and the ends of the plates were equally focused for imaging (Fig. 5(b)).

Video recordings were made until the complete evaporation of the liquid bridge. From the images obtained prior to the liquid bridge breakdown, values of the parameters θ and a were determined (see Fig. 2).

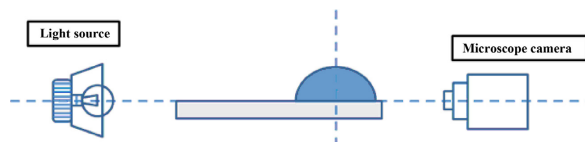


Fig. 4. Schematic description of the experimental setup for sessile drop recording. The side view of the setup shows the imaging axis with the light source placed opposite to the microscope camera and the illumination and imaging axes coinciding.

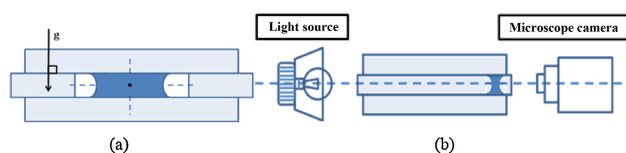


Fig. 5. Schematic depiction of the experimental setup used for recording the liquid bridge between two flat surfaces, with (a) providing a front view of the setup where the dotted lines show the axes of symmetry and where the main imaging axis is through the center marked point. The side view (b) of the setup shows the imaging axis with the light source being opposite to the microscope camera and the illumination axis along the imaging axis.

3.4. Measurements of capillary bridges between rods

In this case, the setup consisted of three glass rods placed parallel to each other with their axes perpendicular to gravity. The rods were positioned so that their respective axial centers formed the vertices of an equilateral triangle with 3.733 mm side length (see Fig. 6(a)). The rods were fixed in this configuration through fitted holes in two transparent, rectangular plastic plates kept in parallel and fixed with adhesive at the adjoining interfaces. Liquid was deposited close to one end of the rods so that the liquid and rods could be simultaneously focused. The transparent, plastic plates were used to enable light from the light source to pass through to illuminate the liquid bridge. This resulted in high contrast images amenable for dimensional measurements. With liquid dispensed between the rods, images were recorded with the main imaging axis parallel to the axes of the rods and passing through the center point of the visualized equilateral triangle (Fig. 6(b)). An additional camera view was used to capture the length of the liquid bridge such that the imaging axis was parallel to gravity and perpendicular to the main imaging axis (Fig. 6(b)). The illumination axis was kept along the main imaging axis, with the light source being opposite the microscope camera.

Liquid of constant volume ($3 \mu\text{L}$) was deposited onto the rods and the changes in length and contact angles recorded simultaneously from the top and front of the setup until complete evaporation of the liquid bridge. Video recordings were made until

the complete evaporation of the liquid bridge. From the images obtained prior to the liquid bridge breakdown, values of the parameters θ and ϕ could be determined (see Fig. 3).

4. Results and discussion

4.1. Sessile drops on flat surface

The initial contact angle for sessile drop on glass was about 33° . This is higher than the typical equilibrium contact angle reported in literature, and is possibly caused by the deposition process which renders it closer to the advancing angle. From the time trace in Fig. 7, it is evident that this surface has a tendency to pin straight away, causing the contact angle to reduce continuously. There appears to be a two stage process for this wherein after 10 min the rate of contact angle decrease was more pronounced. With silanized glass, the initial contact angle was 42° . This is higher than the value on glass, which is expected. Compared with glass, the contact angle reduction on silanized glass was more gradual with evaporation. A second stage process occurred after about 28 min in which the contact angle reduced at a slightly faster rate. For silicone, the initial contact angle was about 113° indicating that the surface is hydrophobic. For the first 25 min, the contact angle reduced at a rate that is almost similar to that of glass. Beyond that however the contact angle starts to fall off at a rapid rate. On all surfaces, contact angles very close to zero at the end of evaporation were observed.

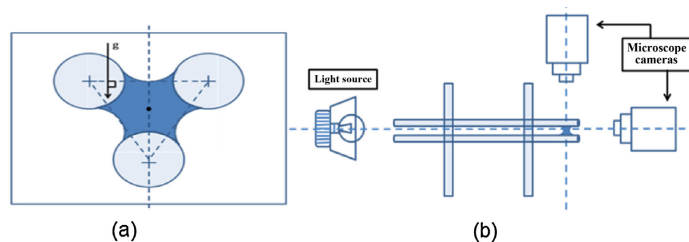


Fig. 6. Schematic depiction (a) of the experimental setup for creating a liquid bridge (darkened areas) between glass rods in which the front view comprise dotted lines showing the position of the axial centers of the rods at the vertices of an equilateral triangle. In recording (b) the main imaging axis is through the center marked point is recorded using one camera, and another camera records perpendicular to this axis.

652

T. Hunyh et al. / Colloids and Surfaces A: Physicochem. Eng. Aspects 436 (2013) 647–655

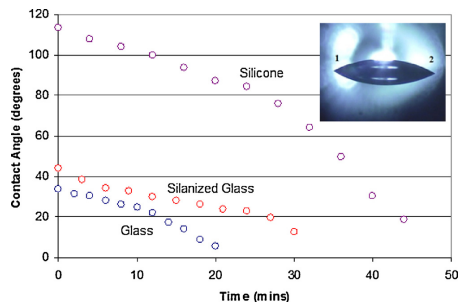


Fig. 7. Trace of the contact angle progression with time as a 3 μL sessile drop (see inset) is evaporated on the flat surfaces made of glass, silanized glass, and silicone. The contact angle is taken as the average of the angles marked 1 and 2 in the picture.

In the evaporation process, it can be seen that contact line pinning is a dominant feature. The presence of hysteresis indicates that a four stage evaporation process may be in action [28].

The volume trace with time was estimated using Eq. (4) and presented in Fig. 8. It can be seen that rather linear rates were obtained with glass and silanized glass notwithstanding the two step contact angle reduction rates occurring on these surfaces. We surmise that since the rate changes were small, the effects on the linearity of volume change were minimal. In the case of silicone, the volume change distribution was far less linear due to the pronounced contact angle rate changes. It is also evident that the same drop volume was able to be retained 1.5 and 2 times longer on silanized glass and silicone surfaces respectively over glass surfaces. This result can be explained through the feature of evaporation rate occurring more rapidly at lower contact angles regions in the sessile drop. This same effect is also responsible for generating the capillary flow responsible for the coffee stain effect [29,30].

4.2. Capillary bridges between two flat surfaces

In the case of the capillary bridge on glass, the starting contact angle was about the same as that of the sessile droplet. But instead of pinning, there was a high degree of stick-slipping of the contact line resulting in slow reduction of the contact angle. The effect of contact line sticking and slipping in liquid bridges has been actively studied [31]. The behavior with silanized glass was almost similar with glass. An interesting behavior, however, was observed with

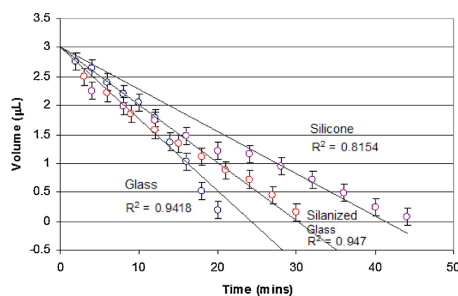


Fig. 8. Trace of the remnant volume against time of a 3 μL sessile drop as it is evaporated on the flat surfaces made of glass, silanized glass, and silicone.

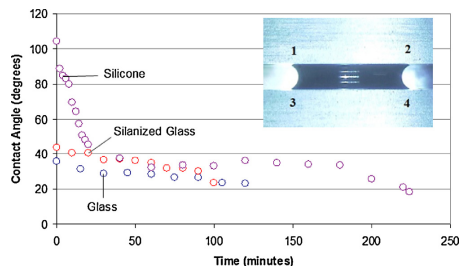


Fig. 9. Trace of the contact angle progression with time as a 3 μL capillary bridge (see inset) is evaporated between two flat surfaces made of glass, silanized glass, and silicone. The contact angle is taken as the average of the angles marked 1–4 in the picture.

silicone. On this surface, the contact angle reduced drastically from 110° to 35° in the first 20 min. This sudden contact angle change appears strange but can be explained by the knowledge that the phase behavior of a fluid is strongly affected by confinement. The conditions for equilibrium of a liquid–vapor system confined in a solid geometry can be elucidated through entropy [32]. From thermodynamics, the change in entropy is known to be linked to temperature, pressure, and chemical potential. If this is extended to the interfaces of phases, it should then link to the tension and area of the interface as well. All the components acting at the interface can be taken to follow the Gibbs surface of tension approximation. With evaporation, the vapor phase has to form out of and coexist in an equilibrium state with a confined liquid phase. It has recently been shown that vapor formation with a convex meniscus is generally unfavorable from an interfacial energy standpoint related to the action of entropy change [33]. This then helps to explain why the convex capillary bridge, in seeking to achieve improved stability, changed over to a concave meniscus with the onset of evaporation.

From 20 min onwards on the silicone surface, the contact line was seen to undergo a strong sliding phase until the 180 min mark before late stage pinning caused the contact angle to reduce significantly. A point to note is that in all cases, the capillary bridge ruptured at around 20° . This is due to the influence of liquid capillary instability (due to curvature) that ensures that rupture occurred before the contact angle had chance to go to zero. In other words, it will not be possible to trace the contact angle developed on bridge all the way to total evaporation of the liquid body.

The volume of the capillary bridge was estimated using Eqs. (5)–(12), from which the computed volume against time traces are shown in Fig. 10. Due to uncertainties involved in determining the parameters, the plots have larger error bars. The volume reduction trends in all cases appeared rather linear with R^2 values of 0.95 and above. It can be seen that the volume reduction rates of glass and silanized glass were about the same which contrasts with the case of sessile drop evaporation. It appears then that the almost similar contact angle change trends here were responsible for this. Due to the rapid change of the contact angle over the first 20 min on silicone, the somewhat moderate departure from linearity of volume against time reduction trend in Fig. 10 was somewhat unexpected. However, the nature of the slope being steeper earlier in the process can be explained through the insights of Lord Kelvin [34] who formulated the relation

$$\frac{RT}{M} \log_e \left(\frac{p}{p_0} \right) = \frac{2\sigma}{\rho} \left(\frac{1}{R} - \frac{1}{R_0} \right) \quad (26)$$

with R being the gas constant, T the absolute temperature, M the molecular weight, σ the surface energy, ρ the density of the liquid,

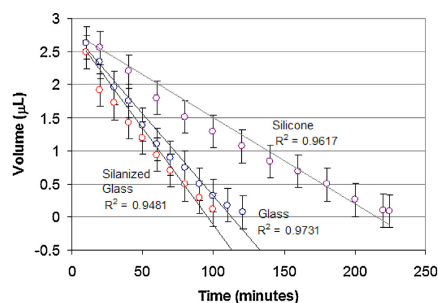


Fig. 10. Trace of the remnant volume against time of a 3 μL capillary bridge as it is evaporated between two flat surfaces made of glass, silanized glass, and silicone.

p the escaping tendency of the substance in a surface with radius of curvature R , and p_0 the escaping tendency in a surface with radius of curvature R_0 . If the value of R_0 is taken to be infinitely large (indicating a flat surface), the equation provides a relation between the curvature of the liquid surface and the rate of evaporation. Where the surface is convex, the right-hand side of the equation is positive, while it is negative when the surface is concave. This is, of course, another way of saying that the escaping tendency of a convex surface is greater and a concave surface is less than that of a flat surface. On silicone flat surfaces, the capillary bridge that formed first starts off with a convex surface (which has higher liquid escaping tendency) and then converts into a concave surface during the first 20 min period. This then accounts for the initial stronger volume loss rate before reducing in time as shown in Fig. 10.

Due to the contact angles being almost the same after 20 min on all three surfaces (see Fig. 9), the ability of the silicone surface to retain liquid longer is somewhat curious. However, it should be noted that in a highly constrained area, as is clearly the case with the capillary bridge formed between two flat surfaces, the vapor pressure distribution near the interface is markedly different from the case of a sessile drop. We believe that the initial convex to concave meniscus change with the capillary bridge formed between silicone surfaces to have resulted in a more saturated vapor pressure nearer to the interface. Consequently, this will have an effect of reducing the volumetric rate of liquid loss notwithstanding evaporation. In fact, keeping the same volume as a capillary bridge between two silicone surfaces extended the retention time by 5 times over the sessile drop on a silicone surface. This result has important implications when seeking to provide a cover for transparency microplates [6,7] since it will create a capillary bridge. The use of hydrophobic transparencies should maintain analytes for longer from the effect of evaporation. The higher tendency to move on hydrophobic surfaces can be limited using scribed surfaces [7]. We also make mention here that the thickness of the substrates used is important to avoid the effect of surface tension induced deformation recently uncovered [35].

4.3. Capillary bridges between three rods

On inspecting the trace of contact angle against time for a capillary bridge between three rods (see Fig. 11), it can be seen that it is susceptible to rupture at a rather large angle (40°). In addition the time taken for the liquid to rupture was about 1.75 times longer than that of total evaporation of the sessile drop. This is attributed to the liquid–gas area being much larger than between two flat plates. The starting contact angle was much higher (70°) even though the surface was glass. In explaining this, it is important

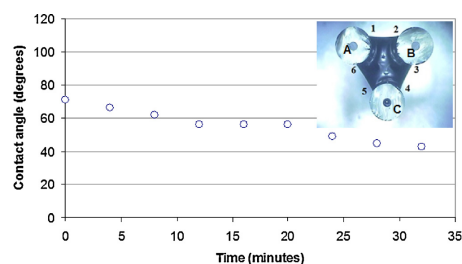


Fig. 11. Trace of the contact angle progression with time as a 3 μL capillary bridge (see inset) is evaporated between three rods (A–C) made of glass. The contact angle is taken as the average of the angles marked 1–6 in the picture.

to contrast between the capillary bridge forming between the three cylinders with that inside a capillary tube. With the latter, the liquid–gas interface occurs only at the two distal ends of the tube. With the cylinders, the interface occurs all along the length. In such a case, it cannot be assumed that the extent of wetting to be constant throughout the length. This has similarities to the situation of a thread of liquid resting on a surface wherein the behavior depends on the boundary condition at the contact line. In studies that investigated the equilibrium shape of a liquid confined to hydrophilic stripes, bulges have been shown to occur [36]. It is conceivable then that a similar effect had occurred, albeit this is difficult to observe and confirm along the liquid length. Such an effect (bulging) will then account for the increased contact angles observed at the distal ends where recording is made. It is also important to note that the contact angle at rupture occurred at values two times higher than that between flat surfaces. It will appear that the thread effect also has the effect of causing higher levels of instability that resulted in the capillary bridge rupturing earlier.

Figs. 12 and 13 present the breakdown traces of the contact angles developed on each of the three glass rods, as well as the top and bottom of the two glass flat surfaces in the evaporation experiments conducted. It can be seen that the fluctuations in contact angle of the capillary bridge on glass cylinders are much higher than on flat glass surfaces. We attribute this also to the thread effect since this will have an effect of altering the symmetry of liquid in contact with each of the three cylindrical surfaces. This result allowed us to infer that using the three rod approach to trace the contact angle development with time will not be practical.

The fact that the contact angles could vary significantly between the rods and the effect of liquid threads being significant, makes

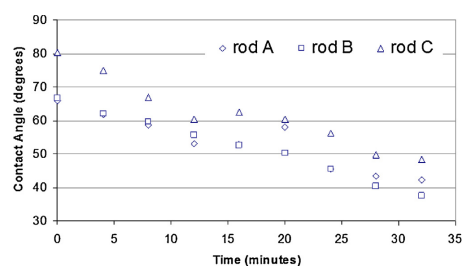


Fig. 12. Breakdown trace of the contact angles developed on the three glass rods in Fig. 11 with time as a 3 μL capillary bridge is evaporated between them. Significant fluctuations (in the order of 20°) can be observed.

654

T. Hunyh et al. / Colloids and Surfaces A: Physicochem. Eng. Aspects 436 (2013) 647–655

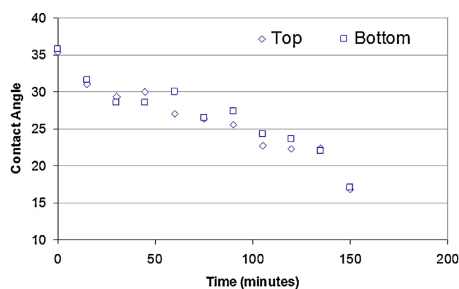


Fig. 13. Breakdown trace of the contact angles developed on the top and bottom of the two glass flat surfaces in Fig. 9 with time as a 3 μ L capillary bridge is evaporated between them. The fluctuations are noticeably much smaller ($<5^\circ$).

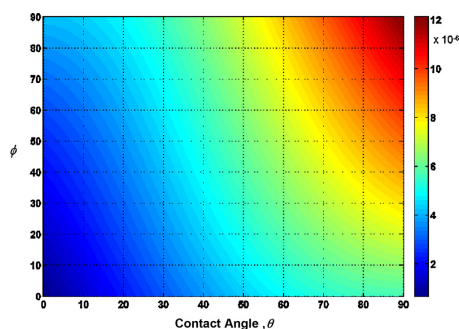


Fig. 14. Map of the cross sectional area of the capillary bridge held between three liquid rods calculated for various values of θ and ϕ . The units are in m^2 and are based on $z = 3.733$ mm and $r = 1$ mm in Fig. 3.

volume estimation through the equations developed earlier to be fraught with high levels of uncertainty. Nevertheless, the equations still provide some useful insights into the process. Based on the estimated average values of $\theta = 72^\circ$, $\phi = 61^\circ$ initially and $\theta = 42^\circ$, $\phi = 44^\circ$ after rupture, the area change is estimated to be -31.5% . The length of capillary bridge change (measured directly) was found to be approximately -72% . It is clear then that the length change is above two times the cross sectional area change of the capillary during the evaporation. Fig. 14 provides a map of the liquid bridge cross sectional area against various values of θ and ϕ . It is intuitive then that the amount of liquid that can be retained is lowered when θ and ϕ are similarly lowered.

5. Conclusions

The experiments with sessile drop evaporation show the contact angle versus time trends to roughly comprise two linearly reducing rates; one slower followed by one that is faster. The difference is more pronounced with silicone as opposed to glass and silanized glass. This caused a strong departure from volume reduction linearity using silicone. The use of silicone improved the drop retention capability by 2 times over glass.

The experiments with capillary bridge evaporation between two flat surfaces show similar strong linear contact angle reduction and thus volume reduction trends with time using glass and silanized glass. With silicone, there was a steep contact angle reducing rate in

the early stage followed by a more gradual reducing rate later. The steep process was attributed to the liquid–vapor interface accommodating for thermodynamic entropy changes during evaporation, which favor forming a concave over a convex meniscus. The initial convex meniscus also resulted in faster volume reduction as stipulated by Kelvin's relation on escape tendency. The much slower volume reduction rate with silicone flat surfaces found presented a conundrum since the contact angle development with time during the later stages was similar to that between glass and silanized glass surfaces. This was attributed to the initial convex to concave meniscus change in a confined space that resulted in a more saturated vapor pressure nearer to the interface. With the same volume, the capillary bridge between two silicone surfaces extended the retention time of the sessile drop on a silicone surface by over 5 times. This makes it favorable for use as a means to limit the effects of evaporation in small volume biochemical microplating. The use of contact angle measurements using this approach however needs to take into account the different evaporation mechanics scheme existing between a sessile drop and a capillary bridge between two flat surfaces. Also the range of measurement is limited to the point where rupture occurred, which we found to be around 20° notwithstanding the different surface types.

In the experiments with capillary bridge between three rods, rupture occurred at a rather large angle (40°). In addition, the time taken for the liquid to rupture was only about 1.75 times longer than that of total evaporation of the sessile drop. The starting contact angle was much higher (70°) and was attributed to wetting being not constant throughout the length. This has similarities to the situation of a thread of liquid resting on a surface wherein the behavior depends on the boundary condition at the contact line. The same effect is also responsible for the higher fluctuations in contact angle trend over that on flat surfaces, making it impractical to be used for characterization measurements. Due these fluctuations, attempts to estimate volume based on the liquid bridge geometry would be subject to large levels of uncertainty. By using the geometrical equations and approximate parameter changes, the length change was found to be above two times the cross sectional area change of the capillary during evaporation.

The results here indicate that when evaporation is significant creating capillary bridges for the transparency microplates offer the best ability to retain volumes while allowing the contact angle to be interrogated.

Acknowledgements

T.W. and O.W. acknowledge funding from the Australian Research Council Discovery Project DP120100583. T.W. appreciates discussions with Yang Yu at BIT, China on liquid body simulations.

References

- [1] L.J. Kricka, K. Imai, P. Fortina, Analytical ancestry: evolution of the array in analysis, *Clinical Chemistry* 56 (2010) 1797.
- [2] A. Zarowna-Dabrowska, E.O. McKenna, M.E. Schutte, A. Glidle, L. Chen, C. Cuestas-Ayllon, D. Marshall, A. Pitt, M.D. Dawson, E. Gu, J.M. Cooper, H. Yin, Generation of primary hepatocyte microarrays by piezoelectric printing, *Colloids and Surfaces B* 89 (2012) 126.
- [3] H. Rhode, M. Schulze, S. Renard, P. Zimmermann, T. Moore, G. Cumme, A. Horn, An improved method for checking HTS/uHTS liquid-handling systems, *Journal of Biomolecular Screening* 9 (2004) 726.
- [4] H.Y. Tan, T.W. Ng, A. Neild, O.W. Liew, Capillary wells microplate with side optical access, *Journal of Biomolecular Screening* 15 (2010) 1160.
- [5] G. Lu, H.Y. Tan, A. Neild, O.W. Liew, Y. Yu, T.W. Ng, Liquid filling in standard circular well microplates, *Journal of Applied Physics* 108 (2010) 124701.
- [6] B.H.-P. Cheong, V. Diep, T.W. Ng, O.W. Liew, Transparency based microplates for fluorescence quantification, *Analytical Biochemistry* 422 (2012) 39.
- [7] X.Y. Li, B.H.-P. Cheong, A. Somers, O.W. Liew, T.W. Ng, Surface-scribed transparency based microplates, *Langmuir* 29 (2013) 849.

- [8] B.H.-P. Cheong, J.K.K. Lye, S. Backhaus, O.W. Liew, T.W. Ng, Microplates based on liquid bridges between glass rods, *Journal of Colloid and Interface Science* 397 (2013) 177.
- [9] P.G. de Gennes, Wetting: statics and dynamics, *Reviews of Modern Physics* 57 (1985) 827.
- [10] A. Marmur, Equilibrium and spreading of liquids on solid surfaces, *Advances in Colloid and Interface Science* 19 (1983) 75.
- [11] C. Li, Y. Gao, S. Wang, Air-grid surface patterning provided by superhydrophobic surfaces, *Small* 8 (2012) 962.
- [12] C. Ye, M. Li, J. Hu, Q. Cheng, L. Jiang, Y. Song, Highly reflective superhydrophobic white coating inspired by poplar leaf hairs toward an effective "cool roof", *Energy & Environmental Science* 4 (2011) 3364.
- [13] F. Shao, T.W. Ng, O.W. Liew, J. Fu, T. Sridhar, Evaporative preconcentration and cryopreservation of fluorescent analytes using superhydrophobic surfaces, *Soft Matter* 8 (2012) 3563.
- [14] J.S. Allen, An analytical solution for determination of small contact angles from sessile drops of arbitrary size, *Journal of Colloid and Interface Science* 261 (2003) 481.
- [15] N.M. Dingle, M.T. Harris, A finite element based algorithm for determining interfacial tension (γ) from pendant drop profiles, *Journal of Colloid and Interface Science* 286 (2005) 670.
- [16] Y.-L. Hung, Y.-Y. Chang, M.-J. Wang, S.-Y. Lin, A simple method for measuring the superhydrophobic contact angle with high accuracy, *Review of Scientific Instruments* 81 (2010) 065105.
- [17] E. Ramé, The interpretation of dynamic contact angles measured by the Wilhelmy plate method, *Journal of Colloid and Interface Science* 185 (1997) 245.
- [18] F. Restagno, C. Poulard, C. Cohen, L. Vagharchakian, L. Leger, Contact angle and contact angle hysteresis measurements using the capillary bridge technique, *Langmuir* 25 (2009) 11188.
- [19] R.G. Picknett, R. Bexon, The evaporation of sessile or pendant drops in still air, *Journal of Colloid and Interface Science* 61 (1977) 336–350.
- [20] C. Bourges-Monnier, M.E.R. Shanahan, Influence of evaporation on contact angle, *Langmuir* 11 (1995) 2820–2829.
- [21] H. Song, Y. Lee, S. Jin, H.-Y. Kim, J.Y. Yoo, Prediction of sessile drop evaporation considering surface wettability, *Microelectronic Engineering* 88 (2011) 3249–3255.
- [22] B.H.-P. Cheong, T.W. Ng, Y. Yu, O.W. Liew, Using the meniscus in a capillary for small volume contact angle measurement in biochemical applications, *Langmuir* 27 (2011) 11925.
- [23] G. Debregeas, F. Brochard-Wyart, Spreading of viscous droplets on a non viscous liquid, *Journal of Colloid and Interface Science* 190 (1997) 134.
- [24] T.L. Cheng, W. Yu, Spontaneous formation of stable capillary bridges for firming compact colloidal microstructures in phase separating liquids: A computational study, *Langmuir* 28 (2012) 2696.
- [25] J. Qian, H. Gao, Scaling effects of wet adhesion in biological attachment systems, *Acta Biomaterialia* 2 (2006) 51.
- [26] W. Schwalb, T.W. Ng, J.K.K. Lye, O.W. Liew, B.H.-P. Cheong, Surface tension drawing of liquid from microplate capillary wells, *Journal of Colloid and Interface Science* 365 (2012) 314.
- [27] H.M. Princen, Capillary phenomena in assemblies of parallel cylinders III. Liquid columns between horizontal parallel cylinders, *Journal of Colloid and Interface Science* 31 (1970) 171.
- [28] S. Semenov, V.M. Starov, R.G. Rubio, H. Agogo, M.G. Velarde, Evaporation of sessile water droplets: Universal behaviour in presence of contact angle hysteresis, *Colloids and Surfaces A* 391 (2011) 135.
- [29] R.D. Deegan, O. Bakajin, T.F. Dupont, G. Huber, S.R. Nagel, T.A. Witten, Capillary flow as the cause of ring stains from dried liquid drops, *Nature* 389 (1997) 827.
- [30] H.M. Gorr, J.M. Zueger, D.R. McAdams, J.A. Barnard, Salt-induced pattern formation in evaporating droplets of lysozyme solutions, *Colloids and Surfaces B* 103 (2013) 59.
- [31] S. Dodds, M. Carvalho, S. Kumar, Stretching liquid bridges with moving contact lines: the role of inertia, *Physics of Fluids* 23 (2011) 092101.
- [32] J.W. Gibbs, On the equilibrium of heterogeneous substances, *Transactions Connecticut Academy* 2 (1876) 108.
- [33] L. Zargazadeh, J.A.W. Elliott, Comparative surface thermodynamic analysis of new fluid phase formation between a sphere and a flat plate, *Langmuir* 29 (2013) 3610.
- [34] W. Thomson, On the equilibrium of vapour at a curved surface of liquid, *Philosophical Magazine* 141 (1871) 448.
- [35] J. Liu, W. Zuo, Y. Mei, Droplet-induced anomalous deformation of a thin microplate, *Colloids and Surfaces A* 412 (2012) 108.
- [36] H. Gau, S. Herminghaus, P. Lenz, R. Lipowsky, Liquid morphologies on structured surfaces: From microchannels to microchips, *Science* 283 (1999) 46.

B.9 Scale-like cantilever cell traps



RSC Advances

PAPER

View Article Online
View Journal | View Issue

Scale-like cantilever cell traps†

Boyin Liu,^a Jing Fu,^a Anthony Somers,^b Murat Muradoglu^c and Tuck Wah Ng^{*ac}Cite this: *RSC Adv.*, 2014, 4, 2652Received 25th October 2013
Accepted 18th November 2013

DOI: 10.1039/c3ra46123h

www.rsc.org/advances

The micro-domain provides excellent conditions for performing biological experiments on small populations of cells and has given rise to the proliferation of so-called lab-on-a-chip devices. In order to fully utilize the benefits of cell assays, means of retaining cells at defined locations over time are required. Here, the creation of scale-like cantilevers, inspired by biomimetics, on chemically robust planar silicon nitride (Si₃N₄) film using focused ion beam machining is described. Using SEM and optical profilometry imaging, regular tilting of the cantilever with almost no warping of the cantilever was uncovered. With Monte Carlo simulation, it was found that the ion implantation in the film was limited to tens of nanometers, and SEM imaging confirmed that the ion beam milling edges were smooth. Finite element analysis showed that the scale-like cantilever was best at limiting stress concentration without difficulty in manufacture and having stresses more evenly distributed along the edge. It also had a major advantage in that the degree of deflection could be simply altered by changing the central angle. From a piling simulation conducted, it was found that a random delivery of simulated particles on to the scale-like obstacle should create a triangular collection. In the experimental trapping of polystyrene beads in suspension, the basic triangular piling structure was observed, but with extended tails and a fanning out around the obstacle. This was attributed to the aggregation tendency of polystyrene beads that acted on top of the piling behavior. In the experiment with bacterial cells, triangular pile up behind the cantilever was absent and the bacteria cells were able to slip inside the cantilever's opening despite the size of the bacteria being larger than the gap. Overall, the fabricated scale-like cantilever architectures offer a viable way to trap small populations of material in suspension.

1. Introduction

The properties of biological materials and surfaces result from a complex interplay between surface morphology and physical and chemical properties formed by adaptation over a long period of time. Biological hierarchical structures, with dimensions of features ranging from the macro-scale to the nano-scale, have provided vital lessons and guidance on how materials, devices and processes with useful outcomes can be developed. Some successful examples include drag reduction in fluid flow,¹ superhydrophobicity,² photoluminescence,³ reflection,⁴ coloration,⁵ and self-healing.⁶

Skins with scales (scutes) are a prominent feature in reptiles such as snakes. Various suggestions have been advanced to elucidate their function, including (i) a kind of zip-fastener supporting the molding process by holding old and new skin

together until the old skin is entirely shed,⁷ (ii) surface strengthening,⁸ (iii) anti-contamination,⁹ and (iv) anti-fouling.¹⁰ Recently, in an attempt to better understand how snakes are able to travel through narrow openings despite being restricted from using coiled motion propulsion, evidence of a concertina-type movement, aided by the directional frictional anchors provided by the ventral scales, had been confirmed by observing the locomotion of corn snakes (*Pantherophis guttatus*).¹¹

The *Azolla*, alternatively, is a genus of small aquatic ferns widely distributed around the world. Its branches and stems are covered with small, alternate, overlapping leaves which resemble scales under a cursory observation. Affixed to these leaves are populations of the cyanobacterium *Anabaena azollae* which the *Azolla* shares a symbiotic relationship with. Underwater, the shape of these leaves has long been suspected of helping to trap minerals such as phosphorus, which can be abundant in waterways during chemical runoffs. This then allows the cyanobacterium, which fixes atmospheric nitrogen, to feed the *Azolla*, allowing it to grow at great speeds.¹² This efficient trapping capacity also renders it ideal for phytoremediation, where heavy metals from polluted aquatic ecosystems can be removed, disposed, or recovered.¹³

The technology of handling small liquid volumes in biochemical analysis, commonly referred to as microfluidics, was initially based on continuous flow and closed architectures.¹⁴

^aDepartment of Mechanical and Aerospace Engineering, Monash University, Clayton, VIC 3800, Australia

^bInstitute for Frontier Materials (IFM) Deakin University, 221 Burwood Highway, Burwood, VIC 3125, Australia

^cLaboratory for Optics, Acoustics & Mechanics, Monash University, Clayton, VIC 3800, Australia

† Electronic supplementary information (ESI) available. See DOI: 10.1039/c3ra46123h

Paper

View Article Online
RSC Advances

Issues such as clogging (when particulates or cells are present), access impediments, and difficulties in integration and scaling due to the flow at any one location being dependent on the flow properties of the entire system, have resulted in increasing interest to apply discrete, open, and independently controllable sample volumes instead.^{15,16} This approach permits the microfluidic function to assume a set of basic repeated operations, whereby one unit of fluid can be moved over one unit of distance, thus facilitating the use of hierarchical and cell-based approaches for microfluidic biochip designs that offer flexible and scalable system architectures as well as high fault tolerance capabilities. Moreover, because the volumes can be controlled independently, such systems offer greater potential to be reconfigured whereby groups of unit cells in an array can be altered to change their functionality.

The micro-domain provides excellent conditions for performing biological experiments on small populations of cells and has given rise to the proliferation of so-called lab-on-a-chip devices. In order to fully utilize the benefits of cell assays, means of retaining cells at defined locations over time are required. This was first performed by localized surface modifications¹⁷ or chemical immobilization¹⁸ in microfluidic networks. More recently, hydrodynamic effects working in tandem with applied field gradients that induce forces on cells, such as electrical,¹⁹ optical,²⁰ magnetic,²¹ or acoustic²² fields, have been attempted. These methods generally require investment of time, resource, and expertise to develop. Most researchers conducting cell based assay investigations in the laboratory, however, frequently seek approaches that eschew these demands. Such an approach, which is inspired by the workings of biological scale-like structures that assist in directional frictional anchoring and trapping, is described here.

2. Materials and methods

Substrate and preparation

The substrate used was a typical submicron film supported on a silicon frame (Ted Pella Inc, Redding, CA, USA). The area to be worked on was fabricated from chemically robust, low-stress, planar silicon nitride (Si_3N_4) film and the area is supported by a rigid 3 mm silicon frame. The area of the thin film portion was 1.5 mm and its thickness was 200 nm. Focused ion beam milling was conducted using a FIB-SEM dual system (Helios Nanolab 600, FEI company, Hillsboro, USA). The ion beam voltage and current were kept at 30 kV and 0.28 nA respectively. The diameter of the scale-shape fabricated was 10 μm –20 μm in which the cutting angle was fixed at 315°. The dwell time for each ion beam burst was kept at 10⁵ ns in which 5 passes were made. In order to fashion each scale-like cantilever, the time taken was 2 minutes and 30 seconds. After the cantilever was shaped, bombarding its center with the ion beam of same accelerating voltage and ion current caused it to tilt downwards. One of the important advantages of using the ion-beam processing was that the structures could be directly visualized in the electron microscopy mode within the same equipment. This permitted each step of the fabrication process to be closely monitored.

Profilometry

As the structures generated were flexible, contacting methods were not suited to determine its 3D shape. For this, an optical profilometer (Bruker, GT-K1) was used. The profilometer was located on a pneumatic vibration-isolation table (Newport) fitted with active high attenuation isolation and calibrated using step height standards (Bruker, Veeco). The area surrounding the cantilever was taken as the zero height from which the depth was determined. Analysis was done on the Vision 64 (Ver. 5.10) software.

Numerical simulation of cantilever structure creation and use

For the FIB process leading to the creation of the cantilever structures, it is instructive to evaluate the interaction of ions with matter. To do this, we applied the computer programs associated with the Stopping and Range of Ions in Matter (SRIM). SRIM (available at <http://www.srim.org>) is based on a Monte Carlo simulation method, namely the binary collision approximation with a random selection of the impact parameter of the next colliding ion. As the input parameters, it needs the ion type and energy (in the range 10 eV–2 GeV) and the material of one or several target layers.

A natural question that comes to mind is whether there is any advantage in the structural creation of scale-like cantilevers. Using the mechanical design software Solidworks (Dassault Systèmes SolidWorks Corp., Waltham, Massachusetts, USA) and associated analysis packages, we modeled cantilevers that are rectangular and circular in shape with the finite element analysis (FEA) method. Four types of cantilever geometries were tested, including a rectangle of inverse aspect ratio (1.618 : 1) with the long edge fixed, a scale-like plate with 315° central angle fixed at the chord, a square cantilever, and a rectangle of aspect ratio (1 : 1.618) with the short edge fixed. Since the eventual goal was to accomplish cell trapping, the effective lengths were kept to the scale range matching that of cells. During FIB fabrication, we started with an effective length of 10 μm , followed by a scale down procedure to eventually fit the size of a single cell. In order to remain consistency between fabrication and FEA simulation, the lengths of the free ends of rectangular and square cantilevers, as well as the diameter of scale-like cantilever, were set to 10 μm . All the cantilevers were prepared on 25 μm × 25 μm , 200 nm thick membrane models in Solidworks. The width of the kerf is related to the ion beam size and was speculated by observing the kerf width of fabrication product, which was approximately 200 nm.

Numerical piling simulation

The manner in which particles accumulate at the cantilever can be modeled as a delivery of points in a spatially random manner in a plane. When the points make contact with the scale shape its ability to be retained or to move away can be related to the prescribed conditions imposed. This has some parallels with the way bulk granular materials, when poured onto a horizontal surface, form a conical pile.²³ The computer modeling should then essentially apply a cellular automata (CA) approach which

is an alternative to continuum and discrete element models for predicting the flow of granular materials.²⁴ With this, the flow field can be divided into cells that each possesses a finite number of states. The current state of each cell is a function of its state and those of its neighbors at the previous time-step. This function is governed by update rules that define the interactions that can occur between particles moving around a lattice connecting adjacent cell centers. The rules themselves can incorporate mass and momentum conservation albeit in a simple, discrete manner.

The simulations are based on a robust block cellular automata algorithm. It assumes a basic neighborhood interaction rule that is able to model basic piling and toppling of particles onto a surface. The particles are assumed to be uniform blocks of "mass" that can conserve momentum and pile in a lattice structure. In this model we assumed that there are no inter-particle or surface forces. The lattice of cells (used in computation) is divided into non-overlapping blocks and the transition rule applied to a whole block at a time rather than a single cell. Block cellular automata are useful for simulations of physical quantities, because it is straightforward to choose transition rules that obey physical constraints such as reversibility and conservation laws. A 2×2 block rule set known as the Margolus neighborhood,²⁵ written in Matlab, was used to propagate particles that randomly appear above the obstacle surface. We consider each cell to be of a rectangular shape where the cell's x and y dimensions dictate the repose angle. When run over a period of time, an equilibrium piling structure can be seen above the obstacle surface. This is then used as a basis to consider the piling behavior.

Trapping experimentation

The trapping experimentation on the substrate was conducted using $1 \mu\text{m}$ polystyrene microbeads in suspension and gram-negative bacterial cells (*Klebsiella pneumoniae*) solution after glutaraldehyde fixation. Before the experiments were conducted, the membrane surface was washed by absolute ethanol and dried in air. The polystyrene beads, originally in solution at 10%v/v in deionized water, was diluted 50 times before usage. The isolated bacteria *Klebsiella pneumoniae* was cultured and incubated until it reached approximately 10^8 CFU mL^{-1} (colony-forming units per milliliter). The samples were then fixed with 2.5% glutaraldehyde in phosphate-buffered saline (PBS) for 20 min and stored at 4°C based on safety protocols. Glutaraldehyde cross-links the proteins of cells and is the standard chemical used in fixation. Fixation is a chemical process by which biological cells are preserved from decay, thereby preventing autolysis or putrefaction. Fixation terminates any ongoing biochemical reactions, and may also increase the mechanical strength or stability of treated cells. Prior to conducting the experiments on the fabricated scale structure, the cells were washed two times with Milli-Q water and re-suspended in Milli-Q water to remove only the supernatants. Hence, the bacteria concentration remained at 10^8 CFU mL^{-1} during the tests. There are no salts existing in the solution that can be deposited. During the test a manual pipette was used to

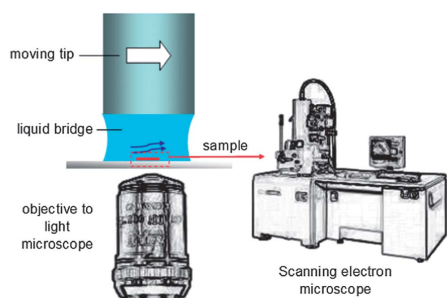


Fig. 1 Schematic description of the ability to use a moving tip to trap particles in a liquid bridge on a structured substrate. A light microscope is useable to observe the trapping of the particles as they are still in the liquid medium. For higher resolution imaging, the sample is dried and placed in an SEM.

dispense $100 \mu\text{L}$ of each solution onto the substrate as a drop. In the experiments, a tip was placed to contact the drop such that it created a liquid bridge (see Fig. 1). As the tip was moved, it could create a flow within the liquid bridge^{26,27} from which the fabricated shape on the substrate could trap the contents. Two imaging modes were used. In one, the substrate was allowed to completely dry before it was placed into a scanning electron microscope for imaging. In another mode, the substrate, whilst still in liquid medium, is imaged directly using an inverted optical microscope (Nikon Eclipse E200) with a $40\times$ objective.

3. Results and discussion

Fig. 2A shows the SEM image of a typical cantilever that has been manufactured correctly using the FIB. Due to the small ion beam size and translational precision, it was possible to shape the cantilever out with good definition. Nevertheless, it was necessary not to use a larger ion beam current (although it will speed up processing) as it can result in a warped shape of the cantilever (see Fig. 2B) due to locked-in induced stresses. The measured profile of the cantilever and of its surroundings is given in Fig. 3A. It can be seen that the surrounding surface was

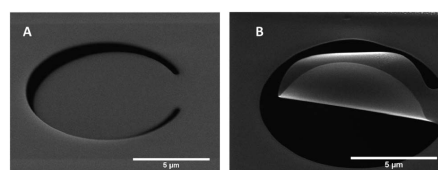


Fig. 2 Precision ion beam machining with the right parameters which creates a well structured scale-like cantilever in A. The use of a too large diameter ion beam can produce warping in the cantilever as shown in B.

Paper

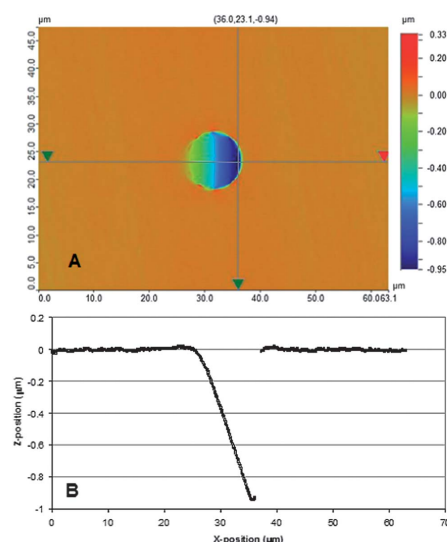


Fig. 3 Optical profilometry (A) map of the fabricated cantilever which shows good topographic control in the manufacture. Taking a (B) central horizontal section of the created cantilever shows a tilt angle of 6° .

maintained planar except for the machined-out shape. From a horizontal profile section measured (Fig. 3B), it can be seen that a regular tilting of the cantilever at 6 degrees could be achieved. We inspected the vertical profile sections and found almost no warping of the cantilever. This demonstrates that locked-in induced stresses were limited, making it possible to create good working shaped cantilevers.

1000 gallium (Ga) ions were simulated to impinge on a Si_3N_4 substrate using SRIM simulation to gain insight into the ion-structure interaction (see ESI, Fig. 1†). It was found that the range of interaction volume of the ion implantation on the material surface was limited to 30 nm. This is essentially the volume on the target surface that is affected by the energetic Ga ions. As the interaction volume in our preparation scheme was limited to 30 nm, it indicates that the ions bombarded only a small extent of the surface each time during the cut out process. A small interaction volume is often taken to indicate that the ion processing is highly localized and thus desirable. As a result, the edges where the ion beam milling terminated were also smooth despite the kerf size limited to 200 nm (see Fig. 2). The mechanical properties of silicon nitride based cantilevers, produced by low pressure chemical vapor deposition (LPCVD) technique, were analyzed using FEA modeling. In doing this, the geometries of the cantilevers were translated into discrete sub-domains using curvature based meshes. A 1 kPa normal pressure was applied to all the membrane surfaces with the cantilevers resting at the equilibrium position. Fig. 4 shows the stress distribution on the four types of cantilevers with

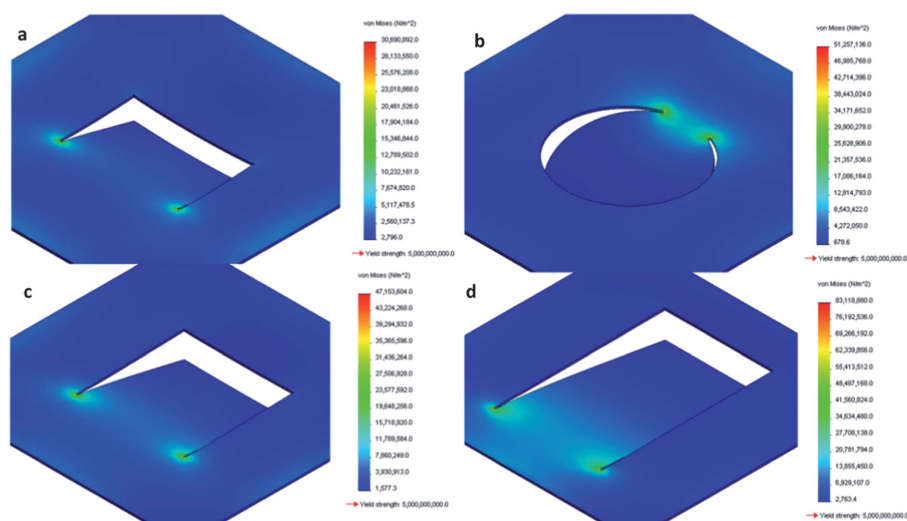


Fig. 4 FEA stress analysis results of (a) rectangular cantilever with inverse aspect ratio 1.618 : 1, (b) scale-like cantilever with 315° central angle, (c) square cantilever, (d) rectangular cantilever with aspect ratio 1 : 1.618. The effective lengths are kept at $10\ \mu\text{m}$ in all cases. The corners of the fixed end are clearly areas of high stress concentration from a similar force imposed on all nodes.

deformation results. In all cases, it can be seen that the corners of the fixed end experienced the highest levels of stress concentrations and the mode of deflection was regular. From the probability density function of the stress values shown in Fig. 5, all the four datasets conform to the log-normal distribution with a goodness of fit value (also often referred to as the p -value) of larger than 0.98. They indicate that the majority data of circular and square cantilever stress values range between 0 and 3 MPa. (Fig. 6A) gives the box-plots that depict the stress distribution at the edges when a 1 kPa normal pressure was applied. The box indicates data points that are between the first and third quartiles of the data set, while the asterisks denote values that are 1.5 times larger than the third quartile. Although most of stress data of the rectangular cantilever (1.618 : 1) also sit in the same region, the corresponding box-plots in (Fig. 6A) indicate a large amount of stress values that are over 50 MPa. The 2D mapping results in Fig. 4 indicate that these are located mostly near the region where cantilever and membrane are connected. Based on this we can surmise that the rectangular shaped cantilever with the short edge fixed is not suitable in the trapping application because it suffers from significantly larger stresses despite the same normal pressure applied. The thin and fragile membrane is thus prone to fracture under higher stresses and this has also been experimentally experienced from time to time during the handling of the membrane in solutions containing particles and bacteria. Although the rectangular cantilever fixed at the long edge exhibited the lowest amount of stress, this geometry is difficult to fabricate if the process were to be scaled down, in particular when the effective length of trapping for the cantilever needs to be reduced to about 1 μm . This is because manufacturing of the shorter sides in the sub-micron range will be especially challenging. The stress values of the scale-like and square cantilevers were close to each other. Nevertheless, the square cantilever has two more weak points located at right angles to the cut (~ 4 MPa). Furthermore the stresses along the edges of the scale-like cantilever were more evenly distributed. The box plots in (Fig. 6B) alternatively depict

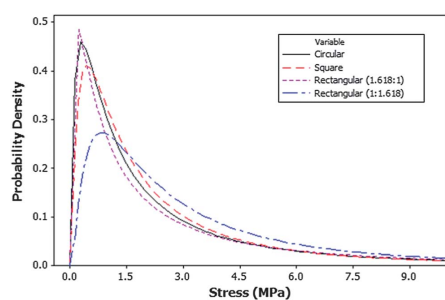


Fig. 5 The probability density function of stress distributions for the four different types of cantilevers modeled. These curves indicate a goodness of fit value (also often referred to as the p -value) of larger than 0.98. They indicate that the majority data of circular and square cantilever stress values range between 0 and 3 MPa.

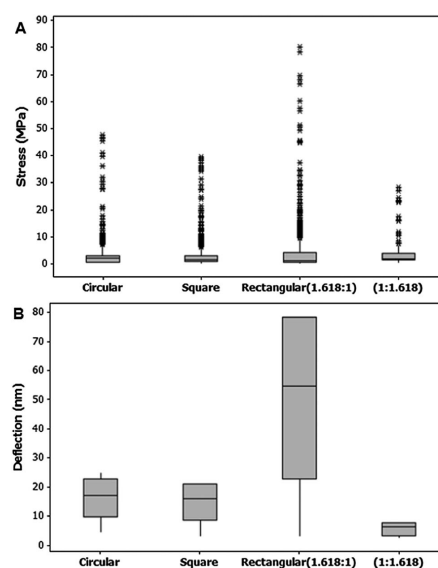


Fig. 6 (A) Box plots of the stress distribution for the edge of cuts with 1 kPa normal pressure for the four different types of cantilevers simulated. The box includes the data points between first quartile and third quartile of the data set, while the asterisks are values larger than 1.5 times of third quartile. With the (B) box plots of deflection of points around cantilever edges with 1 kPa normal pressure the number of data points larger than 1.5 times of third quartile was substantially lower.

the deflection of points at the edges when a 1 kPa normal pressure was applied. Here, it can be seen that despite the extreme stress of the rectangular cantilever (1 : 1.618) appearing to be the smallest, it only undergoes a limited deflection under the same pressure as shown in (Fig. 6B). Thus a higher pressure is required to produce the necessary deflection to trap cells.

Fig. 7 provides the maximum stress and tip deflection change with the central angle of circular cantilever under 1 kPa normal pressure. It can be inferred that there was a direct correlation between the membrane response in terms of maximum stress and deflection. This is an important result as it is typically desirable for the cantilever to deflect but not by too much when the forces are applied. Increasing the deflection will generally enable larger particles to be trapped by essentially creating a taller obstacle. This will entail changing the central angle should the effective length be held constant. A major advantage of the scale-like cantilever is that the degree of deflection can be simply altered by changing the central angle. Hence the performance of the cantilever can be manipulated easily without changing the length-scale of the cantilever too much. As a result, a scale-like cantilever is favored not only in a biomimetic context, but also in terms of limiting stress, attaining the right amount of deflection, and the ease of

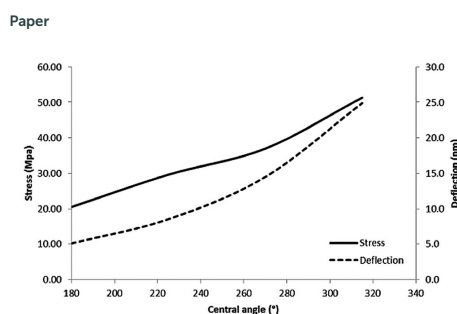


Fig. 7 Distributions of the maximum stress and tip deflection change with the central angle of the circular cantilever under 1 kPa normal pressure. The trends show that control of deflection through the right ion beam delivery should also be considered in relation to the maximum stress developed.

structural strength manipulation. It should be noted, however, that the maximum stress developed during fabrication is also increased, which increases the likelihood of fracture failure. Consequently, there are limits to trying to keep the effective length constant to trap larger particles. Fig. 7 also shows the relation between the normal pressure and opening angle of a same size cantilever predicted by FEA simulation in Solidworks. The opening angle of the cantilever increases with increase in the normal pressures. A 6 degrees cantilever deflection, for instance, can be achieved by applying approximately 45 kPa of normal pressure, which translates to the momentum of Ga ions accelerated by a voltage of 30 kV and ion current of 0.28 nA with 1 μ s exposure. It should be noted that this approximation is interpolated from the nominal mechanical properties of the membrane available in the literature. In practice, a portion of ion momentum could be dispersed during sputtering, resulting in the lock-in of stresses in the structure which could affect the measurement. It is plausible that the actual Young's modulus of the membrane could first be determined using AFM force spectroscopy. This may then provide a more empirical depiction of the cantilever's deflection from the ion beam bombardment. From an application perspective, the size of particles to be trapped will be proportional to the deflection of the cantilever. For a given effective length, this will dictate the central angle and the maximum stress during fabrication. These factors guide the effective length and thus size of the cantilever to be used.

At this stage, it is pertinent to mention that we assume that the process of machining the cantilever shapes out will result in small residual stresses since the interaction volume is limited to 30 nm. After the cantilever shape is cut out, a dose of Ga atoms bombards the cantilever to bend it. Hence, the momentum of the Ga atoms is taken to be responsible in generating the uniformly distributed normal pressure which causes the cantilever to deflect to the position that is useable for trapping. Admittedly, a certain degree of springback will occur. We however assume that this is negligible. We note that since a dose of ion beam was used to cause the cantilever to bend, the

amount of deflection could conceivably be adjusted by the beam strength. The level of control this way however will likely not be that good. We envisage that the additional positioning a physical block behind the cantilever may be a better way to limit the deflection and thus fix the central angle.

With a random delivery of simulated particles on to the scale-like obstacle, the piling was found to form a triangular collection (see Fig. 8 top). This was not surprising as this was essentially a conversion from a cone collection in the 3D case. The equilibrium triangular shape was dependent on the ability of each point to remain in relation to the slope condition that it has been programmed to withstand. This condition, also called the angle of repose, is the steepest angle of descent of the slope relative to the horizontal plane when piled material on the slope face is on the verge of sliding. This condition is imposed through the cellular automata algorithm to better represent the maximum piling height achieved on the circular surface for a given angle of repose. The plot given at the bottom of Fig. 8 shows the normalized parameter of height of the pile h against obstacle radius R , to observe an increasing trend with the repose angle θ .

The ability to trap is illustrated in Fig. 9 with typical examples using (A) polystyrene beads, and (B) the fixed *Klebsiella pneumoniae*. In the case of polystyrene beads, the basic triangular piling structure was observed as per simulation. However, an extended tail and a fanning out around the obstacle were also evident. We believe that this is attributed to the aggregation tendency of polystyrene beads that acts on top of the piling behavior. Some factors influencing aggregation are size and concentration, surface charge level, and the nature and concentration of ions in the suspending medium. While there may also be a possibility of surface sticking at play, the contribution of this is not likely to be significant as found in recent studies.²⁸ A different scenario is played out with the bacteria sample. Here, the triangular pile up before the cantilever is absent. It can be seen, however, that the bacteria cells were able to slip inside the cantilever's opening despite the size of the bacteria being larger than the gap. This leaves us to conclude that the cells, unlike the beads, were more pliable and thus able to accomplish this. Recent investigations have found that, due to the structural and compositional heterogeneity of bacterial cell surfaces, the softer outer layer tended to deform in order to concentrate the stress toward the more rigid, hard core.²⁹ Consequently, there is capacity for bacterial cells in general to flatten themselves out considerably while still avoiding structural damage. The squeezing into the gap was also likely the contributing factor for the absence of the triangular pile up. When the flow direction was reversed, there was significant decrease in the ability to trap the beads and bacteria (see C and D in Fig. 9). Hence the approach offers a directional trapping feature in relation to the flow and orientation of the cantilever. It should be noted that the samples in Fig. 9 were recorded using an SEM. As such the substrate surface appears opaque. In reality, the substrate is thin and will permit viewing of its underside with an optical microscope. Hence, while the bacteria may be able to squeeze into the gap of the cantilever, they can still be imaged, thus allowing biochemical analysis modes to be implemented.

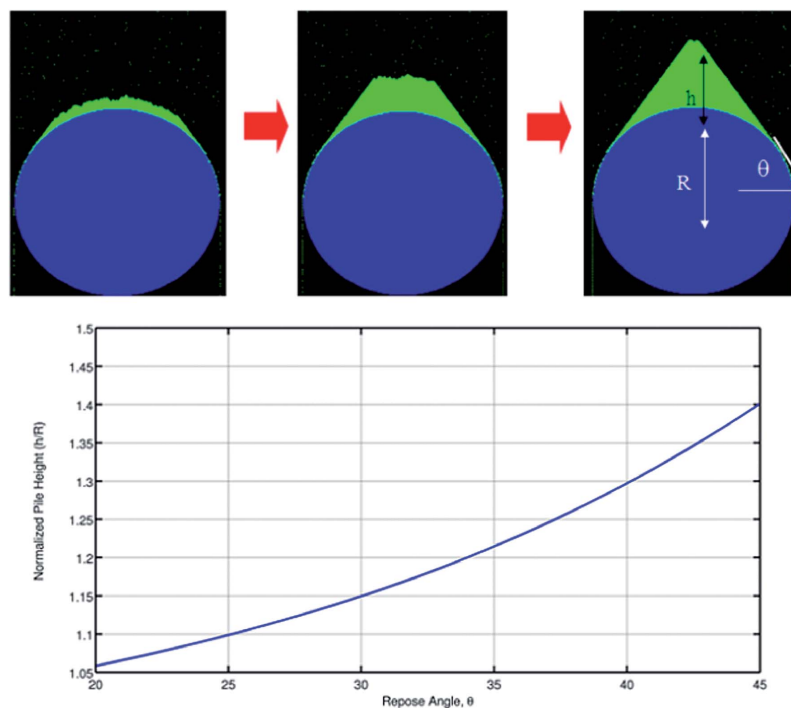


Fig. 8 Snapshots (top) of the simulation of the piling process in progress which leads to a triangular collection. The piling characteristic is described by the height of the pile h , in relation to the radius of the obstacle R , and the repose angle θ . The results from simulated piling indicate that the equilibrium triangular shape was dependent on the ability of each point to remain in relation to the slope condition that can be withstood. The plot (below) shows a normalized parameter of height of the pile h against obstacle radius R , to follow an increasing trend with the repose angle θ .

The degree of image sharpness is naturally lower using optical microscopy imaging (see Fig. 10A and B). Nevertheless, this mode of imaging permits the substrate to remain in the liquid media. We applied this in ascertaining the consistency of trapping. Fig. 10C presents data of the particles trapped by the cantilever for a series of ten runs conducted. In every run, the beads could be trapped, showing the consistency of the approach. Over the ten runs, the average number of particles trapped was 67 beads with a standard deviation of 17. The significant number of beads trapped infers feasibility in using this approach as a platform for developing biochemical analysis applications.

The ease with which the trapping could be done here using an open flow generation arguably offers an ability to create simpler cellular analysis devices. In doing so, it presents a different pathway to creating devices in applications such as the capture of circulating tumor cells, in which 3D-nanostructured substrate coated with cancer cell capture agents are

effective but typically applied within closed channel fluidic networks.³⁰ The recent ability to concentrate particles at the moving contact line even as a drop undergoes a squeeze flow from a sandwich^{31,32} coupled with nanostructures created at the scale-like interface are possible future developments for this trapping approach. This could also benefit from the feature of low sample loss when highly non-wetting elements are used to generate the squeeze flow.²⁷ Care, however, has to be exercised that when the three-phase contact line travels over the cantilever, so that surface tension does not cause the cantilevers to bend excessively and fracture. It is conceivable that any structures patterned on the surface that impede flow are also workable. However, the formation of these structures in the micron and nanometer scale will typically require a photolithographic process involving chemical etching. The approach here is simpler to execute and does not involve any wet processing steps which create effluents that harm the environment.

Paper

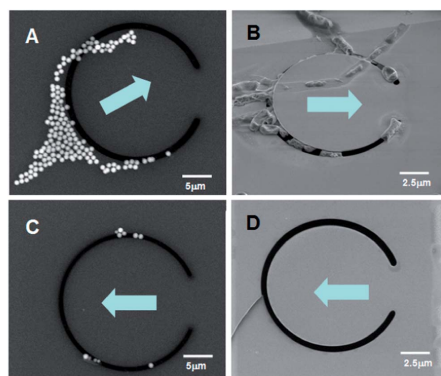
View Article Online
RSC Advances

Fig. 9 Experimental record of the trapping of 1 μm polystyrene beads using the scale-like cantilever in A which shows piling with particle aggregation. The trapping fixed bacterial cells in B shows capacity to slip into the gap of the cantilever despite the size of the bacterial being larger. The directions of the flow in all cases are indicated by the arrows. When the direction of flow was reversed with the 1 μm polystyrene beads (C) and bacterial cells (D), there was diminished trapping ability. This demonstrates a directional trapping capability.

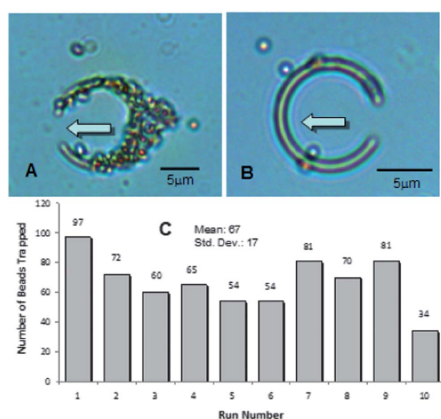


Fig. 10 Typical optical microscopy images recorded of the 1 μm polystyrene beads in liquid interacting with the scale-like cantilever where flow in one direction traps them (A) while flow in the opposite direction clears them off (B). For the flow causing the particles to be trapped, the distribution of the number of beads at each run, indicated in C, has an average of 67 beads trapped with standard deviation of 17.

4. Conclusions

The construction of a scale-like cantilever on chemically robust, low-stress, planar silicon nitride film supported by a rigid silicon frame using focused ion beam machining is described.

Through SEM and optical profilometry imaging, the approach was found to be able to create regular tilting of the cantilever with almost no warping of the cantilever. With Monte Carlo simulation based on SRIM, it was found that the interaction volume of the ions on the material surface was limited to tens of nanometers. This accounted for the ability for the edges of the ion beam milling termination to be smooth despite the kerf size limited to 200 nm. Finite element analysis showed stress concentrations to be located mostly near the regions where cantilever and membrane were connected. The scale-like cantilever was found to be the best architecture in terms of limiting stress concentration without difficulty in manufacture and having stresses more evenly distributed along the edge. It also had a major advantage in that the degree of deflection can be simply altered by changing the central angle. Hence the dynamic performance of the cantilever can be manipulated easily without varying the length-scale of the cantilever too much. From a piling simulation conducted, it was found that a random delivery of simulated particles on to the scale-like obstacle should create a triangular collection. In the experimental trapping of polystyrene beads in suspension, the basic triangular piling structure was observed, but with extended tail and a fanning out around the obstacle. This was attributed to the aggregation tendency of polystyrene beads that acts on top of the piling behavior. In the case with fixed bacterial cells, the triangular pile up behind the cantilever was absent and the bacteria cells were able to slip inside the cantilever's opening despite the size of the bacteria being larger than the gap. This meant that the cells, unlike the beads, were more pliable and thus able to accomplish this. In ascertaining the consistency of trapping over 10 runs, the average number of particles trapped was 67 beads with a standard deviation of 17. The significant number of beads trapped infers feasibility in using this approach as a platform for developing biochemical analysis applications. Overall, the scale-like cantilever, which is inspired biologically, has been found to offer a viable way to trap small populations of material in suspension in an open access manner.

Acknowledgements

Use of facilities at the Melbourne Centre of Nanofabrication is appreciated.

References

- 1 G. D. Bixler and B. Bhushan, *Soft Matter*, 2013, **9**, 1620.
- 2 X. F. Gao and L. Jiang, *Nature*, 2004, **432**, 36.
- 3 K. Yu, S. Lou, J. Ding, D. Zhang, Q. Guo and T. Fan, *Soft Matter*, 2013, **9**, 2614.
- 4 A. R. Parker, *Philos. Trans. R. Soc. London, Ser. A*, 2009, **367**, 1759.
- 5 K. Kertesz, Z. Balint, Z. Vertesy, G. I. Mark, V. Louse, J. P. Vigneron and L. P. Biro, *Curr. Appl. Phys.*, 2006, **6**, 252.
- 6 P. Fratzl, *Nat. Mater.*, 2008, **7**, 610.
- 7 P. F. A. Maderson, *J. Morphol.*, 1966, **116**, 39.
- 8 R. Ruibal and V. Ernst, *J. Morphol.*, 1965, **117**, 271.

View Article Online

RSC Advances

Paper

- 9 D. J. Gower, *J. Morphol.*, 2003, **258**, 249.
- 10 C. J. McCarthy, in *Proceedings of the fourth ordinary general meeting of the Societas Europaea Herpetologica*, ed. J. J. Van Gelder, H. Strijbosch and P. J. M. Bergers, Nijmegen, 1987, p. 279.
- 11 H. Marvi and D. L. Hu, *J. R. Soc. Interface*, 2012, **7**, 3067.
- 12 R. W. Holst and J. H. Yopp, *American Fern Journal*, 1979, **69**, 17.
- 13 L. J. Umali, J. R. Duncan and J. E. Burgess, *Biotechnol. Lett.*, 2006, **28**, 45.
- 14 D. J. Beebe, J. S. Moore, J. M. Bauer, Q. Yu, R. H. Liu, C. Devadoss and B.-H. Jo, *Nature*, 2000, **404**, 588.
- 15 A. R. Wheeler, *Science*, 2008, **322**, 539.
- 16 M. Abdelgawad and A. R. Wheeler, *Adv. Mater.*, 2009, **21**, 920.
- 17 R. S. Kane, S. Takayama, E. Ostuni, D. E. Ingber and G. M. Whitesides, *Biomaterials*, 1999, **20**, 2363.
- 18 R. Davidsson, B. Johansson, V. Passoth, M. Bengtsson, T. Laurell and J. Emneus, *Lab Chip*, 2004, **4**, 488.
- 19 M. P. Hughes and H. Morgan, *J. Phys. D: Appl. Phys.*, 1998, **31**, 2205.
- 20 M. Muradoglu, T. Le, C. Y. Lau, O. W. Liew and T. W. Ng, *Biomed. Opt. Express*, 2012, **3**, 2465.
- 21 A. H. B. de Vries, B. E. Krenn, R. van Driel and J. S. Kanger, *Biophys. J.*, 2005, **88**, 2137.
- 22 M. J. Ruedas-Rama, A. Dominguez-Vidal, S. Radel and B. Lendl, *Anal. Chem.*, 2007, **79**, 7853.
- 23 A. Mehta and G. C. Barker, *Rep. Prog. Phys.*, 1994, **57**, 383.
- 24 K. R. LaMarche, S. L. Conway, B. J. Glasser and T. Shinbrot, *Granular Matter*, 2007, **9**, 219.
- 25 N. Margolus, *Phys. D*, 1984, **10**, 81.
- 26 W. Schwalb, T. W. Ng, J. K. K. Lye, O. W. Liew and B. H.-P. Cheong, *J. Colloid Interface Sci.*, 2012, **365**, 314.
- 27 T. Vuong, B. H. P. Cheong, J. K. K. Lye, O. W. Liew and T. W. Ng, *Anal. Biochem.*, 2012, **430**, 53.
- 28 F. Shao, T. W. Ng, J. Efthimiadis, A. Somers and W. Schwalb, *J. Colloid Interface Sci.*, 2012, **377**, 421.
- 29 Y. Chen, W. Norde, H. C. van der Mei and H. J. Busscher, *mBio*, 2012, DOI: 10.1128/mBio.00378-12.
- 30 J. W. Costerton, P. S. Stewart and E. P. Greenberg, *Science*, 1999, **284**, 1318.
- 31 B. H.-P. Cheong, O. W. Liew and T. W. Ng, *Microsc. Res. Tech.*, 2013, **76**, 767.
- 32 B. H.-P. Cheong, O. W. Liew and T. W. Ng, *Anal. Biochem.*, 2014, **444**, 57.

B.10 Nanoscale environment sensing scheme with Brownian nanorod and plasmon resonator

Plasmonics
DOI 10.1007/s11468-013-9633-8

Nanoscale Environment Sensing Scheme with Brownian Nanorod and Plasmon Resonator

Murat Muradoglu · Chun Yat Lau · Ian Gralinski · Tuck Wah Ng

Received: 6 August 2013 / Accepted: 7 November 2013
© Springer Science+Business Media New York 2013

Abstract Tracking a Brownian particle's motion allows localized parameters at its immediate vicinity to be measured. In this, the introduction of a rod that is drawn by a tunable attractive force to a cylindrical pillar overcomes the problems of the particle drifting away from the venue of measurement as well as colliding with other particles. With nanoscale particles, fluorescence labeling suffers from photobleaching and erratic signal due to blinking, while monitoring the polarization of scattered light is limited by the accuracy of correlating the rotational state of the rod to intensity changes. Here, we advance having the cylindrical pillar operate as a surface plasmon-based optical resonator to sense the contacts of nanorods. Simulations with a one-dimensional summed difference expression developed to reduce the difficulty of analyzing a three-dimensional dataset comprising wavelength, rod orientation, and gap distance allowed us to confirm distinct changes in transmission at 600 nm across all orientation angles with contact to noncontact or vice versa. This allows application of a cutoff transmission threshold. The metric f , which defines the proportion of incidences when the nanorod moves freely under Brownian motion influence, showed reduction with normalized charge increase. Good linear sensitivity responses were found at specific ranges in the f versus normalized charge relationship, which when correlated with temperature T , showed df/dT to be maximal when the normalized charge product value was -200 . From an uncertainty estimation conducted, a restriction to 1 standard deviation variation necessitated only $O(10^{-2})$ seconds of sampling using standard photodetectors. This portends significant advantages when sensing environments that are changing temporally rapidly.

Keywords Brownian · Nanorod · Sensing · Plasmon · Resonator

Introduction

The notion of applying Brownian motion for sensing had been conceived for some time [1]. Arguably, the first experiment to physically demonstrate this was based on measuring the milli-Kelvin temperatures in electrical circuits [2]. Yet, deriving information of parameters such as temperature and viscosity from the liquid microenvironment is crucial for processes that involve electrochemistry and biology. Tracking a single Brownian particle's motion offers an attractive means of measuring the localized parameters at its immediate vicinity. The merits of such a sensor include its minimal disturbance to the evolution of the measured quantity around the localized environment and an absence of any input energy to drive the probe [3]. Some recent adaptations have been reported to ascertain parameters such as magnetic susceptibility and surface forces [4–6]. While fluctuations in the Brownian motion using freely translating particles should provide inexhaustible amounts of information, there is the problem of these particles drifting away from the venue of measurement as well as colliding with other particles. The former causes the problem of lapses in measurement continuity. This can be mitigated somewhat by use of external forces to restrict the particle to a specific location (e.g., optical traps) [7]. Nevertheless, this and the latter issue of collisions tend to introduce additional complexity in interpreting the underlying mechanics [8].

The interaction between rotational and translational Brownian diffusion in isotropic macromolecules is well known from the expositions of Einstein and Smulochowski [9, 10]. With anisotropic macromolecules, the differentiated diffusion constants parallel and perpendicular to the particle's long axis in the short term postulated by Perrin [11, 12] were

M. Muradoglu · C. Y. Lau · I. Gralinski · T. W. Ng (✉)
Laboratory for Optics and Applied Mechanics, Monash University,
Clayton, Melbourne, VIC 3800, Australia

later established experimentally [13]. Hydrodynamic or electrostatic interactions cause the diffusion constants to be significantly affected in the short term [14, 15]. An account of how Brownian rods are able to end-tether naturally to surfaces [16] underlines a rotational–translational coupling. While this tethering behavior may allow information on the microenvironment to be interrogated, it is hampered by opportunistic ventures of the free end towards the surface to cause the motion to cease altogether. A recent scheme has been reported to overcome these limitations wherein a Brownian rod is drawn in by a tunable attractive force from a cylindrical pillar [17] (see Fig. 1). This approach requires the rotational diffusion to be derived from image sequences of the rod’s movement, which is possible when the rod dimensions are diffraction resolvable optically but not when a nanorod is used. Considering that

$$D_a = \frac{k_B T [\ln(2r) - 0.5]}{2\pi\eta L}, D_b = \frac{k_B T [\ln(2r) + 0.5]}{4\pi\eta L}, \quad (1)$$

$$D_\theta = \frac{3k_B T [\ln(2r) - 0.5]}{\pi\eta L^3}$$

denote the respective diffusion coefficients for the long length translation, short length translation, and rotation of a Brownian rod—where k_B is Boltzmann’s constant, T the temperature in Kelvin, $r = L/d$ (L and d are the length and the diameter of the rod, respectively), and η the viscosity of the fluid at T —it is evident that the reduced length scales of a nanorod should imbue heightened diffusion and thus more sensitive interpretations of the environment. It also limits the influence of the probe on the environment due to influences such as viscous drag.

Fluorescence labeling offers a method of resolving nanoscale objects on an optical microscope. A major drawback of this is the limited observation time due to photobleaching (organic dyes) and the erratic signal due to blinking. Gold and silver nanoparticles show strong light scattering at the plasmon resonance wavelength due to the collective oscillation of their conduction electrons. By imaging only the scattered light from a sample [18], it has been claimed that

the detection of particles down to 20 nm in size is possible. That the scattered light is strongly polarized along the long axis makes gold nanorods in principle an ideal orientation probe. The use of a birefringent crystal to create twin images of a nanorod at orthogonal polarizations had been reported as a means to track its rotational and translation venture [19]. This approach is limited by the accuracy of correlating the rotational state of the rod to the intensity variations associated to the two polarization states in the image. In the context of the Brownian sensing scheme here, we contend that more robust information can be gleaned from interrogating the surface plasmon interaction instead.

Surface plasmon resonance (SPR) is well understood as the collective oscillation of electrons in a solid or liquid stimulated by incident light. The resonance condition is established when the frequency of light photons matches the natural frequency of surface electrons oscillating against the restoring force of positive nuclei. SPR is the basis of many standard tools for measuring adsorption of material onto planar metal surfaces, giving rise to the fundamental principle behind many biosensor applications and different lab-on-a-chip sensors [20]. Optical resonators, by virtue of their confinement properties, have been proposed to provide higher sensitivity measurements [21–23].

Method

In considering the effect of an attractive force drawing the nanorod to contact the pillar, it can be assumed that the force of attraction that acts through the center of the two bodies (i.e., the stationary pillar and Brownian rod) is similar to that in [17] as depicted in Fig. 1a. The combination of the attractive force and Brownian perturbation gives rise to two distinct states, one in which the rod is moving freely (state I) and the other in which the rod contacts the pillar surface and consequently the diffusion coefficients are diminished (state II). It is important to note that the residence of the rod in either state is not exclusive. Even when there is no attractive force applied, the rod may sojourn by pure Brownian perturbation to contact the pillar thus switching states. Its departure from the pillar causes

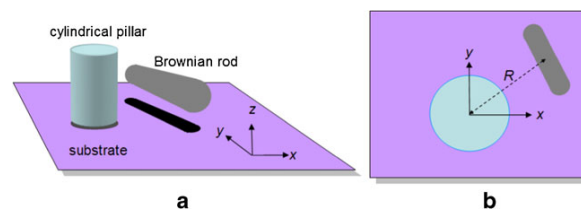


Fig. 1 Schematic of a microenvironment sensing scheme [17] in which a microscale rod is drawn to a cylindrical pillar using an attractive force as viewed three dimensionally (a) and from the top (b). If motion is

assumed to be exclusively in the x – y plane, the Brownian rod motion can be monitored by a camera placed in the z -axis

the opposite to occur. When an attractive force is applied, the proportion of time spent in each of the two states will be altered in accordance with the magnitude of the force. In view that the surface plasmon leakage provides a distinct intensity-based binary indication of residence in either states I or II, it should logically be possible then to deduce the conditions of the environment solely from this information. This will require a means to sensitively ascertain the state condition.

Figure 2 provides description of the nanoenvironment sensing scheme. Apart from a nanoscale rod being drawn to a cylindrical pillar using an attractive force, the cylindrical pillar serves as an optical plasmon resonator. Light is delivered through one distal end of the optical fiber and sensed at the other distal end. Despite having a small optical mode volume, optical resonators can possess ultra-high quality factors in water. The interaction between the resonator's evanescent field and its environment can shift the resonance frequency of the optical mode, such that when a nanoparticle attaches to the resonator surface it induces a wavelength shift that is dependant on the polarizability and position of the nanoparticle, the electric field of the resonator, and the optical volume [24]. This shift is normally used as indicator of nanoparticle attachment. If the nanoparticle is metallic, a localized surface plasmon resonance effect should result, potentially creating a larger effect on the resonator output. Metallic nanorods support both the longitudinal and transverse plasmon modes, with the plasmon resonances polarized along and orthogonal to the length axis of the nanorod. The proximity of the nanorod with the resonator can potentially create an even stronger effect on the resonator output.

In our scheme, these disruptions to the optical signals from the resonator, as a result of a Brownian rod contacting the cylinder, enables the states I and II to be determined temporally and more importantly sensitively. What is attractive is that no imaging is required. This circumvents the well-known difficulty of resolving nanoscale objects in real time. We also seek to harness the use of single wavelength tracking which circumvents to use of spectral signature.

Modeling

There are two parts to the modeling: one to establish the ability of nanorods to extinct the plasmon resonator signals such that it is appropriate for sensing, and the other to investigate if the state change conditions as a result of Brownian perturbation and attractive force are able to reveal information about the environment. For the former, we model the system shown in Fig. 2 using the Finite Difference Time Domain method, whereby the input beam is guided along an optical fiber that couples into the optical resonator. The optical resonator comprises a 40-nm inner dielectric core with a refractive index of $n_c=3.4$ and a 10-nm outer gold (Au) shell. We simulate using a Gaussian beam with a center wavelength of $\lambda_c=550$ nm having full width half maximum of 200 nm. Light inputs into the fiber at one distal end and we monitor the transmittance at the other distal end. The nanorod is orientated with a rotation of θ , such that $\theta=0^\circ$ and $\theta=90^\circ$ correspond to the vertical and horizontal alignments, respectively, as shown in Fig. 2. The gap d denotes the distance between the outer shell of the pillar and the nanorod so that $d=0$ is the contact situation. The dispersive property of gold is represented with the Drude-Lorentz oscillator model with coefficients given in [25].

The width of the tapered fiber is taken to be 200 nm. This is a typical subwavelength diameter optical fiber that can provide strong evanescent coupling [26, 27]. It should be noted that the drifting of single mode fibers in the range of micrometers can cause significant changes [28]. We assume that the means to limit these spurious movements are incorporated.

For any application of product of charges of magnitude of q_p , on the pillar and rod, this creates an attractive force

$$F = \frac{\epsilon q_p}{R^2} \tag{2}$$

that draws the nanorod towards the cylindrical pillar, with ϵ being the permittivity of the medium in which the rod resides, and R the centroid to centroid distance between the rod and

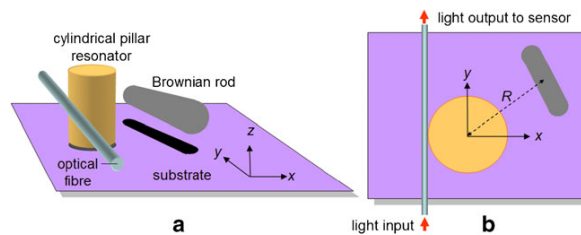


Fig. 2 Schematic of the proposed nanoenvironment sensing scheme in which a nanoscale rod is drawn to a cylindrical pillar using an attractive force as viewed three dimensionally (a) and from the top (b). The cylindrical pillar serves as a plasmonic optical resonator sensor with light

input and output through the optical fiber. The contact of the Brownian nanorod with the cylinder causes changes to the optical signal. Under this scheme, no imaging of the nanorod is required

pillar. The Brownian diffusion perturbations provide the random counteracting forces that oppose this. Equations (1) were used to calculate the diffusion coefficients of the rod when free and in order to obtain the values for the diffusion coefficients when the rod was tethered, the free diffusion coefficients were multiplied by scale factors of 0.0720, 0.6729, and 0.2838 for changes in the diffusion coefficients D_a , D_b , and D_θ , respectively, as previously observed. For the translational diffusion coefficients, this is based on the rod having a length of 60 nm and diameter of 25 nm and moving in deionized water. A 100-nm diameter cylindrical pillar was also applied. In the simulations, it was assumed that the attractive force did not affect the rotation of the rod. Collisions between the rod and the pillar were treated as inelastic, with the velocity of the rod becoming zero on contact with the pillar. A time step size of $\Delta t = 1/300$ s was found to be sufficient for simulations at a test temperature of 293 K. For consistency, the particle was always started from the same position with its centroid lying on the x -axis and its long axis parallel to the y -axis.

Results and Discussion

We first simulate for the horizontal and vertical orientations of the nanorod for three gap values $d = \{0, 2.5 \text{ nm}, 10 \text{ nm}\}$. The transmission distribution is shown in Fig. 3 for the two alignments $\theta = 0^\circ$ and $\theta = 90^\circ$. For all parameters, there is a noticeable resonance at $\lambda = 525$ nm. This corresponds to the primary mode of the plasmonic resonator. At this resonance wavelength, there appears to be very little dependence on the gap value d , and some small dependence on the orientation. Hence, contrary to intuition, tracking for changes at the resonance wavelength will be less sensitive. There is a noticeable dip in the spectral signatures at the vicinity of 600 nm. This is likely due to coupling effects of two different shapes (i.e., a cylinder with nanorod) which essentially creates a heterodimer. A recent study of the interaction of nanorods with

nanospheres can produce strong Fano resonance effects that lead to dramatic spectral changes [29].

We now investigate the absolute value of the transmission profiles for five different values of $d = \{0, 2.5, 5.0, 7.5, 10 \text{ nm}\}$ and for $0^\circ \leq \theta \leq 90^\circ$. For convenience, we symbolize the transmission data matrix as $S_{\lambda_n, \theta_m}^{d_p}$ where λ_n , θ_m , and d_p correspond to the n th wavelength, m th angle, and p th gap value, respectively. The surface plot of $(S_{\lambda_n, \theta_m}^{d_p})$ for the set of d values sampled is shown in Fig. 4.

We now define the difference between the contact transmission data matrix (i.e. $S_{\lambda_n, \theta_m}^{d_0}$) and the q th noncontact gap transmission data matrix $S_{\lambda_n, \theta_m}^{d_q}$ as

$$D_{\lambda_n, \theta_m}^{(0,q)} = \text{abs}(S_{\lambda_n, \theta_m}^{d_0} - S_{\lambda_n, \theta_m}^{d_q}) \text{ for } q = \{1, 2, 3, 4\} \quad (3)$$

With this, it is possible to define the aggregated difference in transmission as

$$W_n^{(0,q)} = \sum_m D_{\lambda_n, \theta_m}^{(0,q)} \quad (4)$$

This essentially reduces a three-dimensional dataset to a one-dimensional summed difference expression. The results for $W_n^{(0,q)}$ where $q = \{1, 2, 3, 4\}$ are shown in Fig. 5. They conclusively show that there is a distinct change in transmission at 600 nm across all angles of orientation when the gap changes from contact to noncontact or vice versa. This suggests that when operated at the wavelength of 600 nm, a noticeable transmission change occurs when there is contact regardless of the nanorod’s orientation. The use of a single wavelength tracking offers the advantage of obviating the use of spectrum readings, which are typically slower and impose greater demands on instrumentation. If we take any specific orientation angle, the transmission plots in Fig. 6 (also at 600 nm) show distinct perceptibility with the gap value $d =$

Fig. 3 Transmission spectra of a nanorod placed a distance, $d = 0$ (contact), $d = 2.5$ nm, and $d = 10$ nm, indicated by the blue, green, and red lines, respectively. The orientation of the particle is either vertical, $\theta = 0^\circ$, or horizontal $\theta = 90^\circ$ indicated by the non-marked and marked lines, respectively

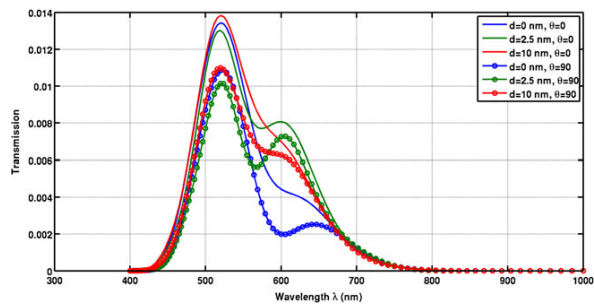
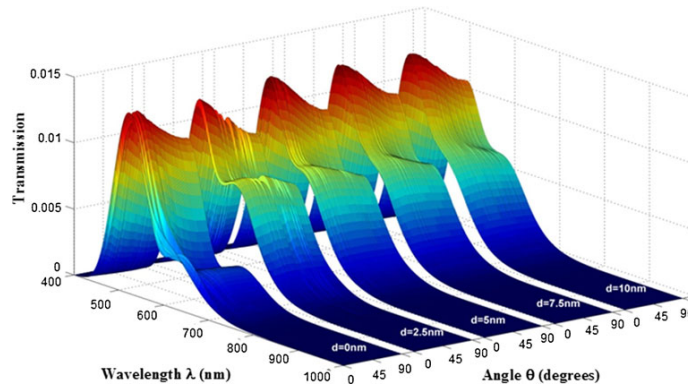


Fig. 4 Transmission spectra for gap values $d = \{0, 2.5, 5, 7.5, 10 \text{ nm}\}$ over a continuous range of angle from 0° to 90°



0. In fact, it can be seen that this perceptibility is distinct notwithstanding the orientation angle. Hence by using a cutoff transmission, it should be possible to confirm that the nanorod contacts the pillar. This is an important feature as in practice the nanorod is able to, due to Brownian motion, contact the pillar at various orientation angles.

It is possible to define two distinct states pertaining to the position of the nanorod in relation to the cylindrical pillar. One is with the rod is moving freely (state I) and the other with the rod contacting the cylinder surface (state II). In the erstwhile approach of interrogating the environment using translational and rotational trajectories of a particle [17], both a rod and a sphere can yield the required information when residence is in state I. When the probe resides in state II, only the rotational information can be used due to rotational and translational coupling. Since a sphere cannot yield the rotational information readily, only the use of a rod is feasible to provide the information necessary to determine the environment. By interrogating the proportion of time of the residence in states I and II as we propose here instead, there is no impediment to using a sphere. Nanorods however, as shown, cause improved extinction of the plasmon resonance signal in the rod. This in

turn offers improved accuracy in ascertaining whether the rod is under state I or II residence with the cylindrical pillar.

A convenient metric to use is f , the proportion of incidences when the rod is in state I, i.e., free [17]. With the efficient optical sensing system described previously, this can be determined to a high degree of accuracy. Figure 7 provides plots of f against the normalized charge product calculated from 18,000 samples at temperatures of 273, 323, and 373 K. As expected, increasing the magnitude of the charges such that the force is attractive reduces the proportion of time spent in state I. That there was shifting of the plots indicated sensitivity to temperature. Nevertheless, distinctive S-shape trends are observed, indicating that there are ranges in the normalized charge products in which relatively good sensitivity responses are possible. Figure 8 provides plots of f against temperature (in the range of 27 to 373 K) at various the normalized charge products. It can be seen that all the trends are highly linear in the cases, having Pearson product-moment correlation coefficients above 0.98. At different normalized charge products however, the slope values (i.e., of df/dT) are different. The significantly higher values of df/dT infer heightened detection sensitivity. Figure 9 furnishes a plot of the approximated values of df/dT against the normalized charge

Fig. 5 Aggregated differences of the transmission spectra over all angles between all contact and noncontact combinations, i.e., $W^{(0,q)}(\lambda)$ where $q = \{1, 2, 3, 4\}$. The plot shows that between contact and noncontact cases there is a distinguished difference of transmission at 600 nm. This feature allows for unique detection of contact between the nanorod and cylindrical pillar

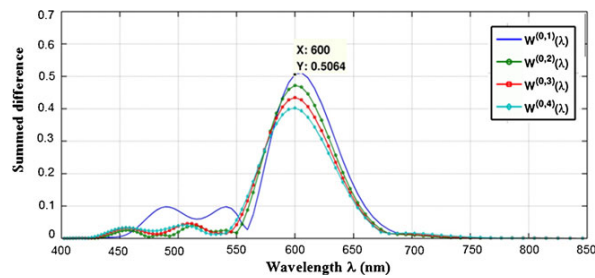
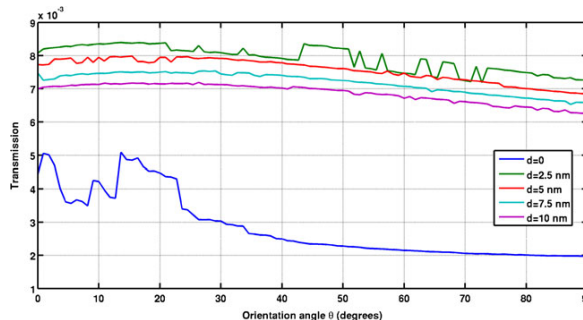


Fig. 6 Transmission readings at 600 nm showing distinct perceptibility when gap value $d=0$. The orientation angle does affect the distinct perceptibility



product. It can be seen that the d/dT is maximal when the normalized charge product value is -200 . This value is naturally only useable for the dimensions applied in the simulation.

It is important to note that uncertainty in the environment estimation diminishes by increasing the number of sample points in states I and II. This uncertainty can be determined by calculating the sample standard deviation of 100 diffusion coefficients at each value of N , which represents the number of samples. If we consider the application of temperature sensing, a restriction of the uncertainty to 1 standard deviation (which corresponds to 0.5 K) will require 744,344 and 657,492 sample points to be observed in states I and II, respectively. Based on camera recordings made at 50 fps, this will require monitoring the rod over 14,887 and 13,150 s in states I and II, respectively. However, considering that standard photodetectors with 50 MHz sampling rate are now readily available, the monitoring times with the current scheme should correspondingly be lowered to 0.015 and 0.013 s instead. This portends a significant advantage in the ability to sense environments that are temporally changing.

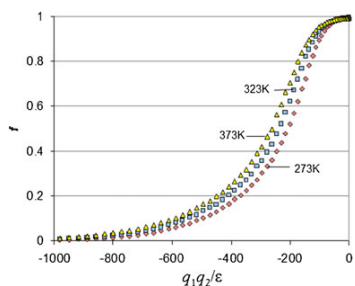


Fig. 7 Plots of f (the fraction of time in state I) against the normalized charge product calculated from 18,000 samples at 0, 25, and 100 °C. All simulations started with the rod touching the edge of the pillar. Increasing the magnitude of the charges such that the force is attractive reduces the proportion of time spent in state I

We have opted to depict the attractive force of the nanorod to the pillar using charges. Since optical plasmonic force schemes have been reported to be able to trap particles [30, 31], there is plausible scope to apply an all plasmon approach in the scheme. A challenge to do this, however, lies in the ability to introduce sufficient optical power for trapping (which is significantly higher than that needed for sensing). An added caution lies in the tendency of heat to be generated from strong plasmon fields [32, 33] which will affect the environment to be sensed. We also note that while optical fibers are widely reported to couple light into and out of resonators, and depicted here, recent waveguide coupling designs [34, 35] may offer the ability to improve the coupling efficiency and to aid in the creation of integrated devices.

Conclusions

This work investigated the use of a surface plasmon-based optical resonator to sense the nanoscale environment from the

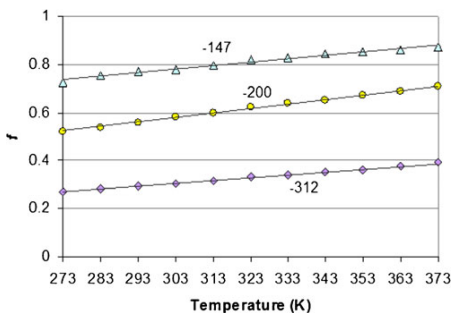


Fig. 8 Plots of f (the fraction of time in state I) against temperature calculated from 18,000 samples at various normalized charge products. All simulations started with the rod touching the edge of the pillar. It can be seen that all the trends are approximately linear

Plasmonics

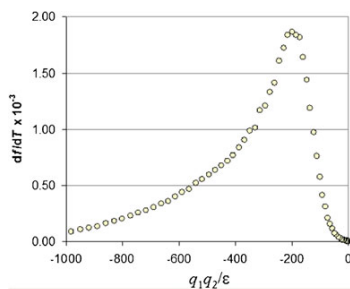


Fig. 9 Plot of the approximated values of df/dT (taken between 273 to 373 K) against the normalized charge product. Higher values of df/dT indicate higher sensitivity. A normalized charge of -200 gave a maximal value of df/dT

Brownian perturbations of nanorod drawn to a cylindrical pillar by attractive forces. Using simulations of an optical resonator that comprises a 40-nm inner dielectric refractive index of 3.4 core with a 10-nm outer gold shell, and driven by a Gaussian beam with center wavelength 550 nm, noticeable resonance was found at 525 nm. At this resonance wavelength, however, there was very little dependence on the gap value. Hence, tracking for changes at the resonance wavelength would be rather insensitive. A one-dimensional summed difference expression $W_p^{(0,sp)}$ was derived to reduce the difficulty of analyzing a three-dimensional dataset composed of λ_n , θ_m , and d_p . Using this expression, it was shown that there was a distinct change in transmission at 600 nm across all angles of orientation when the gap changes from contact to noncontact or vice versa. This meant that operation at this wavelength would produce a noticeable transmission change when there was contact regardless of nanorod orientation. The use of a single wavelength tracking offers the advantage of obviating the use of spectrum readings, which are typically slower and impose greater demands on instrumentation. With distinct perceptibility with zero gap value notwithstanding the orientation angle, it would be possible to apply a cutoff transmission threshold to confirm if the nanorod contacts the pillar. This feature is important as Brownian motion could cause the nanorod to contact the pillar at various orientation angles in practice. In analyzing the Brownian-driven movement, two distinct states that define the position of the nanorod in relation to the cylindrical pillar are when the nanorod was moving freely (state I) and when the nanorod was contacting the cylinder surface (state II). Using the metric f that defined the proportion of incidences when the nanorod was in state I, increase in the magnitude of the charges was found to reduce f . The distinctive S-shape trends of plots of f against normalized charge magnitude indicated that there were ranges in the normalized charge products in which relatively good linear sensitivity responses

were possible. At these regions, the Pearson product-moment correlation coefficients were found to be above 0.98. In correlating to the temperature T , df/dT was found to be maximal when the normalized charge product value was -200 . From an uncertainty estimation conducted, a restriction of the uncertainty to 1 standard deviation (which corresponds to 0.5 K) will require 744,344 and 657,492 sample points to be observed in states I and II, respectively. Based on camera recordings made at 50 fps, this will require monitoring the rod 14,887 and 13,150 s in states I and II, respectively, but with standard photodetectors with 50 MHz sampling rate, the monitoring times are lowered 0.015 and 0.013 s instead. The approach here offers a significant advantage in the ability to sense environments that are temporally changing.

Acknowledgments T.W. acknowledges funding from the Australian Research Council Discovery Project DP120100583.

References

1. Lawson AW, Long EA (1946) Further remarks on the possible use of Brownian motion in low temperature thermometry. *Phys Rev* 70: 977–978
2. Wheatley JC, Webb RA (1973) MilliKelvin temperatures measured with a noise thermometer. *Science* 182:220–307
3. Kurchan J (2005) In and out of equilibrium. *Nature* 433:222–225
4. van Ommering K, Lamers CCH, Nieuwenhuis JH, van Uzendoom LJ, Prins MWJ (2009) Analysis of individual magnetic particle motion near a chip surface. *J Appl Phys* 105:104905
5. Duggal R, Pasquali M (2006) Dynamics of individual single walled carbon nanotubes in water by realtime visualization. *Phys Rev Lett* 96:246104
6. Agayan RR, Smith RG, Kopelman R (2008) Slipping friction of an optically and magnetically manipulated microsphere rolling at a glass–water interface. *J Appl Phys* 104:054915
7. Neild A, Ng TW, Yui WMS (2009) Optical sorting of dielectric Rayleigh spherical particles with scattering and standing waves. *Opt Express* 17:5321–5329
8. Volpe G, Volpe G, Petrov D (2007) Brownian motion in a non-homogeneous force field and photonic force microscope. *Phys Rev E* 76:061118
9. Einstein A (1905) On the movement of small particles suspended in a stationary liquid demanded by the molecular kinetic theory of heat. *Ann Phys* 17:549–560
10. Smoluchowski MV (1916) Über Brownsche Molekularbewegung unter Einwirkung äußerer Kräfte und deren Zusammenhang mit der verallgemeinerten Diffusionsgleichung. *Ann Phys* 353:1103–1112
11. Perrin F (1934) Mouvement brownien d'un ellipsoïde - I. Dispersion diélectrique pour des molécules ellipsoïdales. *J Phys Radium* 5:497–511
12. Perrin F (1936) Mouvement Brownien d'un ellipsoïde (II). Rotation libre et dépolarisation des fluorescences. Translation et diffusion de molécules ellipsoïdales. *J Phys Radium* 7:1–11
13. Han Y, Alsayed AM, Nobili M, Zhang J, Lubensky TC, Yodh AG (2006) Brownian motion of an ellipsoid. *Science* 314: 626–630

14. Bhaduri B, Neild A, Ng TW (2008) Directional Brownian diffusion dynamics in carbon nanofibers. *Appl Phys Lett* 92:084105
15. Han Y, Ahsayed A, Nobili M, Yodh AG (2009) Quasi-two-dimensional diffusion of single ellipsoids: aspect ratio and confinement effects. *Phys Rev E* 80:011403
16. Neild A, Padding JT, Lu Y, Bhaduri B, Briels WJ, Ng TW (2010) Translational and rotational coupling in Brownian rods near a solid surface. *Phys Rev E* 82:041126
17. Gralinski I, Ng TW (2012) Brownian rod scheme in microenvironment sensing. *AIP Adv* 2:012180
18. Yasuda R, Noji H, Yoshida M, Kinoshita K, Itoh H (2001) Resolution of distinct rotational substeps by submillisecond kinetic analysis of F1-ATPase. *Nature* 410:898–904
19. Sonnichsen C, Alivisatos AP (2005) Gold nanorods as novel nonbleaching plasmon-based orientation sensors for polarized single-particle microscopy. *Nano Lett* 5:301–304
20. van Gent J, Lambeck PV, Kreuwel HJ, Gerritsma GJ, Sudhölter EJ, Reinhoudt DN, Popma TJ (1990) Optimization of a chemo-optical surface plasmon resonance based sensor. *Appl Opt* 29:2843–2849
21. Chen Y-H, Guo LJ (2013) High Q long-range surface plasmon polariton modes in sub-wavelength metallic microdisk cavity. *Plasmonics* 8:167–171
22. Chen J, Li Z, Zou Y, Deng Z, Xiao J, Gong Q (2013) Coupled-resonator-induced fano resonances for plasmonic sensing with ultra-high figure of merits. *Plasmonics*. doi:10.1007/s11468-013-9580-4
23. Lu Q, Chen D, Wu G, Peng B, Xu J (2012) A hybrid plasmonic microresonator with high quality factor and small mode volume. *J Opt* 14:125503
24. Arnold S, Khoshsima M, Teraoka I, Holler S, Vollmer F (2003) Shift of whispering-gallery modes in microspheres by protein adsorption. *Opt Lett* 28:272–274
25. Ung B, Sheng Y (2007) Interference of surface waves in a metallic nanoslit. *Opt Exp* 15:1182–1190
26. Cai M, Painter O, Vahala KJ (2000) Observation of critical coupling in a fiber taper to a silica-microsphere whispering-gallery mode system. *Phys Rev Lett* 85:74–77
27. Dong S, Ding H, Liu Y, Qi X (2012) Investigation of evanescent coupling between tapered fiber and a multimode slab waveguide. *Appl Opt* 51:C152–C157
28. Wang L, Li Y, Porcel MG, Vermeulen D, Han X, Wang J, Jian X, Baets R, Zhao M, Morthier G (2012) A polymer-based surface grating coupler with an embedded Si₃N₄ layer. *J Appl Phys* 111:114507
29. Shao L, Fang C, Chen H, Man YC, Wang J, Lin HQ (2012) Distinct plasmonic manifestation on gold nanorods induced by the spatial perturbation of small gold nanospheres. *Nano Lett* 14:1424–1430
30. Juan ML, Righini M, Quidant R (2011) Plasmon nano-optical tweezers. *Nat Photonics* 5:349–356
31. Muradoglu M, Ng TW, Neild A, Gralinski I (2011) Tailored leaky plasmon waves from a subwavelength aperture for optical particle trapping on a chip. *J Opt Soc Am B* 28:602–607
32. Ma H, Bendix PM, Oddershede LB (2012) Large-scale orientation dependent heating from a single irradiated gold nanorod. *Nano Lett* 12:3954–3960
33. Kang H, Jia B, Li J, Morrish D, Gu M (2010) Enhanced photothermal therapy assisted with gold nanorods using a radially polarized beam. *Appl Phys Lett* 96:063702
34. Liu H, Sun X, Yao F, Pei Y, Yuan H, Zhao H (2012) Controllable coupling of localized and propagating surface plasmons to Tamm plasmons. *Plasmonics* 7:749–754
35. Han X, Ji X, Wen H, Zhang J (2012) H-shaped resonant optical antennas with slot coupling. *Plasmonics* 7:7–11

Bibliography

- [1] P. N. Lebedev, “Experimental examination of light pressure,” *Ann. der Physik*, vol. 6, p. 433, 1901.
- [2] G. Hettner, “Zur theorie der photophorese,” *Zeitschrift für Physik*, vol. 37, no. 3, pp. 179–192, 1926.
- [3] A. Ashkin, “History of optical trapping and manipulation of small-neutral particle, atoms, and molecules,” *Selected Topics in Quantum Electronics, IEEE Journal of*, vol. 6, no. 6, pp. 841–856, 2000.
- [4] T. Iwaki, “Effect of internal flow on the photophoresis of a micron-sized liquid droplet,” *Phys. Rev. E*, vol. 81, p. 066315, 2010.
- [5] C. Y. Soong, W. K. Li, C. H. Liu, and P. Y. Tzeng, “Theoretical analysis for photophoresis of a microscale hydrophobic particle in liquids,” *Opt. Express*, vol. 18, pp. 2168–2182, Feb 2010.
- [6] M. Tamagawa, H. Monjushiro, and H. Watarai, “Microgravity laser-photophoresis of high density microparticles in water,” *Colloids and Surfaces A: Physicochemical and Engineering Aspects*, vol. 220, no. 13, pp. 279 – 284, 2003.
- [7] T. W. Ng, A. Neild, and P. Heeraman, “Continuous sorting of brownian particles using coupled photophoresis and asymmetric potential cycling,” *Opt. Lett.*, vol. 33, pp. 584–586, Mar 2008.
- [8] A. Vogel, V. Horneffer, K. Lorenz, N. Linz, G. Hüttmann, and A. Gebert, “Principles of laser microdissection and catapulting of histologic specimens and live cells,” in *Laser Manipulation of Cells and Tissues* (M. W. Berns and K. O. Greulich, eds.), vol. 82 of *Methods in Cell Biology*, pp. 153 – 205, Academic Press, 2007.
- [9] A. Siddiqi, T. W. Ng, and A. Neild, “Specific collection of adherent cells using laser release in a droplet-driven capillary cell,” *Journal of Biomedical Optics*, vol. 15, no. 6, pp. 065003–065003–6, 2010.

-
- [10] A. Ashkin, "Acceleration and trapping of particles by radiation pressure," *Phys. Rev. Lett.*, vol. 24, pp. 156–159, Jan 1970.
- [11] J. C. Maxwell, *Treatise on electricity and magnetism*. Oxford, UK: Clarendon Press, 1873.
- [12] A. Ashkin, J. M. Dziedzic, J. E. Bjorkholm, and S. Chu, "Observation of a single-beam gradient force optical trap for dielectric particles," *Opt. Lett.*, vol. 11, pp. 288–290, May 1986.
- [13] S. Chu, "Nobel lecture: The manipulation of neutral particles," *Rev. Mod. Phys.*, vol. 70, pp. 685–706, Jul 1998.
- [14] W. Ketterle, "Nobel lecture: When atoms behave as waves: Bose-einstein condensation and the atom laser," *Rev. Mod. Phys.*, vol. 74, pp. 1131–1151, Nov 2002.
- [15] S. M. Block, L. S. B. Goldstein, and B. J. Schnapp, "Bead movement by single kinesin molecules studied with optical tweezers," *Nature*, vol. 348, 1990.
- [16] M. Zahn and S. Seeger, "Optical tweezers in pharmacology," *Cell. Mol. Biol.*, vol. 44, 1998.
- [17] T. N. Buican, M. J. Smyth, H. A. Crissman, G. C. Salzman, C. C. Stewart, and J. C. Martin, "Automated single-cell manipulation and sorting by light trapping," *Appl. Opt.*, vol. 26, 1987.
- [18] C. Bustamante, Z. Bryant, and S. B. Smith, "Ten years of tension: single-molecule dna mechanics," *Nature*, vol. 421, 1987.
- [19] A. Ashkin and J. M. Dziedzic, "Optical trapping and manipulation of viruses and bacteria," *Science*, vol. 235, p. 1517, 1986.
- [20] K. Svoboda, P. P. Mitra, and S. M. Block, "Fluctuation analysis of motor protein movement and single enzyme-kinetics," *Proc. Natl. Acad. Sci.*, vol. 91, pp. 11782–11786, 1994.
- [21] C. Bustamante, S. B. Smith, J. Liphardt, and D. Smith, "Single-molecule studies of dna mechanics," *Curr. Opin. Struct. Biol.*, vol. 10, pp. 279–285, 2000.
- [22] D. Meirrow and J. Schenker, "The current status of sperm donation in assisted reproduction technology: Ethical and legal considerations," *Journal of Assisted Reproduction and Genetics*, vol. 14, no. 3, pp. 133–138, 1997.
- [23] K. König, H. Liang, M. W. Berns, and B. J. Tromberg, "Cell damage in near-infrared multimode optical traps as a result of multiphoton absorption," *Opt. Lett.*, vol. 21, pp. 1090–1092, Jul 1996.

- [24] H. Schneckenburger, A. Hendinger, R. Sailer, M. Bauer, K. Schütze, M. H. Gschwend, and W. S. L. Strauss, “Cell viability in optical tweezers: high power red laser diode versus nd:yag laser,” *Journal of Biomedical Optics*, vol. 5, no. 1, pp. 40–44, 2000.
- [25] U. Mirsaidov, W. Timp, K. Timp, M. Mir, P. Matsudaira, and G. Timp, “Optimal optical trap for bacterial viability,” *Phys. Rev. E*, vol. 78, p. 021910, Aug 2008.
- [26] K. Svoboda and S. M. Block, “Optical trapping of metallic rayleigh particles,” *Opt. Lett.*, vol. 19, pp. 930–932, Jul 1994.
- [27] P. Ke and M. Gu, “Characterization of trapping force on metallic mie particles,” *Applied Optics*, vol. 38, pp. 160–167, JAN 1 1999.
- [28] L. P. Ghislain, N. A. Switz, and W. W. Webb, “Measurement of small forces using an optical trap,” *Review of Scientific Instruments*, vol. 65, no. 9, pp. 2762–2768, 1994.
- [29] A. Rohrbach and E. H. K. Stelzer, “Trapping forces, force constants, and potential depths for dielectric spheres in the presence of spherical aberrations,” *Appl. Opt.*, vol. 41, pp. 2494–2507, May 2002.
- [30] R. I. Litvinov, H. Shuman, J. S. Bennett, and J. W. Weisel, “Binding strength and activation state of single fibrinogen-integrin pairs on living cells,” *Proceedings of the National Academy of Sciences*, vol. 99, no. 11, pp. 7426–7431, 2002.
- [31] F. Gittes and C. F. Schmidt, “Chapter 8 signals and noise in micromechanical measurements,” vol. 55 of *Methods in Cell Biology*, pp. 129 – 156, Academic Press, 1997.
- [32] F. Gittes and C. F. Schmidt, “Interference model for back-focal-plane displacement detection in optical tweezers,” *Opt. Lett.*, vol. 23, pp. 7–9, Jan 1998.
- [33] K. Sasaki, M. Koshioka, H. Misawa, N. Kitamura, and H. Masuhara, “Pattern formation and flow control of fine particles by laser-scanning micromanipulation,” *Opt. Lett.*, vol. 16, pp. 1463–1465, Oct 1991.
- [34] K. Sasaki, H. Fujiwara, and H. Masuhara, “Optical manipulation of a lasing microparticle and its application to near-field microspectroscopy,” *Journal of Vacuum Science Technology B: Microelectronics and Nanometer Structures*, vol. 15, no. 6, pp. 2786–2790, 1997.
- [35] C. Mio, T. Gong, A. Terray, and D. Marr, “Morphological control of mesoscale colloidal models,” *Fluid Phase Equilibria*, vol. 185, no. 12, pp. 157 – 163, 2001.

- [36] L. P. Faucheux, L. S. Bourdieu, P. D. Kaplan, and A. J. Libchaber, “Optical thermal ratchet,” *Phys. Rev. Lett.*, vol. 74, pp. 1504–1507, Feb 1995.
- [37] R. Verma, J. C. Crocker, T. C. Lubensky, and A. G. Yodh, “Entropic colloidal interactions in concentrated dna solutions,” *Phys. Rev. Lett.*, vol. 81, pp. 4004–4007, Nov 1998.
- [38] P. A. M. Neto and H. M. Nussenzveig, “Theory of optical tweezers,” *EPL (Europhysics Letters)*, vol. 50, no. 5, p. 702, 2000.
- [39] T. A. Nieminen, V. L. Y. Loke, A. B. Stilgoe, G. Knöner, A. M. Brańczyk, N. R. Heckenberg, and H. Rubinsztein-Dunlop, “Optical tweezers computational toolbox,” *Journal of Optics A: Pure and Applied Optics*, vol. 9, no. 8, p. S196, 2007.
- [40] M. J. Kendrick, D. H. McIntyre, and O. Ostroverkhova, “Wavelength dependence of optical tweezer trapping forces on dye-doped polystyrene microspheres,” *J. Opt. Soc. Am. B*, vol. 26, pp. 2189–2198, Nov 2009.
- [41] A. Ashkin, “Forces of a single-beam gradient laser trap on a dielectric sphere in the ray optics regime,” *Biophysical Journal*, vol. 61, no. 2, pp. 569 – 582, 1992.
- [42] H. C. van de Hulst, *Light scattering by small particles*. New York: Dover, 1981.
- [43] J. A. Lock, “Interpretation of extinction in gaussian-beam scattering,” *J. Opt. Soc. Am. A*, vol. 12, pp. 929–938, May 1995.
- [44] M. Berg, C. Sorensen, and A. Chakrabarti, “A new explanation of the extinction paradox,” *Journal of Quantitative Spectroscopy and Radiative Transfer*, vol. 112, no. 7, pp. 1170 – 1181, 2011.
- [45] G. Mie, “Beitrage zur optik triiber medien speziel kolloidaler metallosungen,” *Ann. Phys.*, vol. 330, p. 377, 1908.
- [46] P. C. Waterman, “Matrix formulation of electromagnetic scattering,” *Proceedings of the IEEE*, vol. 53, no. 8, pp. 805–812, 1965.
- [47] B. Peterson and S. Ström, “Matrix for electromagnetic scattering from an arbitrary number of scatterers and representations of $e(3)$,” *Phys. Rev. D*, vol. 8, pp. 3661–3678, Nov 1973.
- [48] G. Gouesbet, J. Lock, and G. Gréhan, “Generalized lorenz-mie theories and description of electromagnetic arbitrary shaped beams: Localized approximations and localized beam models, a review,” *Journal of Quantitative Spectroscopy and Radiative Transfer*, vol. 112, no. 1, pp. 1 – 27, 2011.

- [49] B. Sun and D. G. Grier, “The effect of mie resonances on trapping in optical tweezers: comment,” *Opt. Express*, vol. 17, pp. 2658–2660, Feb 2009.
- [50] P. Chýlek and J. Zhan, “Interference structure of the mie extinction cross section,” *J. Opt. Soc. Am. A*, vol. 6, pp. 1846–1851, Dec 1989.
- [51] A. B. Stilgoe, T. A. Nieminen, G. Knöener, N. R. Heckenberg, and H. Rubinsztein-Dunlop, “The effect of mie resonances on trapping in optical tweezers,” *Opt. Express*, vol. 16, pp. 15039–15051, Sep 2008.
- [52] M. L. Gorodetsky, A. A. Savchenkov, and V. S. Ilchenko, “Ultimate Q of optical microsphere resonators,” *Opt. Lett.*, vol. 21, pp. 453–455, Apr 1996.
- [53] E. Xifre-Perez, F. J. Garcia de Abajo, R. Fenollosa, and F. Meseguer, “Photonic binding in silicon-colloid microcavities,” *Phys. Rev. Lett.*, vol. 103, p. 103902, Sep 2009.
- [54] A. Rohrbach and E. H. K. Stelzer, “Three-dimensional position detection of optically trapped dielectric particles,” *Journal of Applied Physics*, vol. 91, no. 8, pp. 5474 – 5488, 2002.
- [55] G. A. Siviloglu, J. Broky, A. Dogariu, and D. N. Christodoulides, “Observation of accelerating airy beams,” *Phys. Rev. Lett.*, vol. 99, no. 21, p. 213901, 2007.
- [56] J. Durnin, J. J. Miceli, and J. H. Eberly, “Diffraction-free beams,” *Phys. Rev. Lett.*, vol. 58, 1987.
- [57] J. Baumgartl, M. Mazilu, and K. Dholakia, “Optically mediated particle cleaning using airy wavepackets,” *Nature*, vol. 2, pp. 675 – 678, 2008.
- [58] J. Arlt, V. Garces-Chavez, W. Sibbett, and K. Dholakia, “Optical micromanipulation using a bessel light beam,” *Opt. Commun.*, vol. 197, pp. 239–245, 2001.
- [59] T. Čižmár, V. Garces-Chavez, K. Dholakia, and P. Zemánek, “Optical conveyor belt for delivery of submicron objects,” *Appl. Phys. Lett.*, vol. 86, p. 174101, 2005.
- [60] W. Heisenberg, “Über den anschaulichen inhalt der quantentheoretischen kinematik und mechanik,” *Zeitschrift für Physik*, vol. 43, pp. 172–198, 1927.
- [61] M. Ohtsu and K. Kobayashi, *Optical Near Fields*. Berlin Heidelberg: Springer-Verlag, 2004.
- [62] A. H. Barnett, S. P. Smith, M. Olshanii, K. S. Johnson, A. W. Adams, and M. Pretiss, “Substrate-based atom waveguide using guided two-color evanescent light fields,” *Phys. Rev. A*, vol. 61, p. 023608, 2000.

- [63] F. L. Kien, V. I. Balykin, and K. Hakuta, “Atom trap and waveguide using a two-color evanescent light field around a subwavelength-diameter optical fiber,” *Phys. Rev. A*, vol. 70, p. 063403, 2004.
- [64] S. Kuriakose, D. Morrish, X. Gan, J. W. M. Chon, K. Dholakia, and M. Gu, “Near-field optical trapping with an ultrashort pulsed laser beam,” *Appl. Phys. Lett.*, vol. 92, p. 081108, 2008.
- [65] S. Kawata and T. Sugiura, “Movement of micrometer-sized particles in the evanescent field of a laser beam,” *Opt. Lett.*, vol. 17, pp. 772–774.
- [66] L. N. Ng, M. N. Zervas, J. S. Wilkinson, and B. J. Luff, “Manipulation of colloidal gold nanoparticles in the evanescent field of a channel waveguide,” *Appl. Phys. Lett.*, vol. 19, pp. 1439 – 1444, 2000.
- [67] S. A. Maier, *Plasmonics: Fundamentals and Applications*. New York: Springer Science, 2007.
- [68] H. J. Lezec, A. Degiron, E. Devaux, R. A. Linke, L. Martin-Moreno, F. J. García-Vidal, and T. W. Ebbensen, “Beaming light from a subwavelength aperture,” *Science*, vol. 297, pp. 820 – 822, 2002.
- [69] R. Mehfuz, M. W. Maqsood, and K. J. Chau, “Enhancing the efficiency of slit-coupling to surface-plasmon-polaritons via dispersion engineering,” *Optics Express*, vol. 18, no. 17, 2010.
- [70] T. c. v. Čižmár, M. Šiler, M. Šerý, P. Zemánek, V. Garcés-Chávez, and K. Dholakia, “Optical sorting and detection of submicrometer objects in a motional standing wave,” *Phys. Rev. B*, vol. 74, p. 035105, Jul 2006.
- [71] A. Neild, T. W. Ng, and W. M. S. Yip, “Optical sorting of dielectric rayleigh spherical particles with scattering and standing waves,” *Optics Express*, vol. 17, no. 6, p. 5321, 2009.
- [72] A. N. Grigorenko, N. W. Roberts, M. R. Dickinson, and Y. Zhang, “Nanometric optical tweezers based on nanostructured substrates,” *Nature Photonics*, vol. 2, pp. 365–370, 2008.
- [73] M. Righini, G. Volpe, C. Girard, D. Petrov, and R. Quidant, “Surface plasmon optical tweezers: Tunable optical manipulation in the femtonewton range,” *Phys. Rev. Lett.*, vol. 100, p. 186804, 2008.
- [74] Z. Fang, F. Lin, S. Huang, W. Song, and X. Zhu, “Focusing surface plasmon polariton trapping of colloidal particles,” *Appl. Phys. Lett.*, vol. 94, p. 063306, 2009.

- [75] W. L. Barnes, W. A. Murray, J. Dintinger, E. Devaux, and T. W. Ebbensen, “Surface plasmon polaritons and their role in the enhanced transmission of light through periodic arrays of subwavelength holes in a metal film,” *Phys. Rev. Lett.*, vol. 92, p. 107401, 2004.
- [76] J. A. Dionne, L. A. Sweatlock, H. A. Atwater, and A. Polman, “Plasmon slot waveguides: Towards chip-scale propagation with subwavelength-scale localization,” *Phys. Rev. B*, vol. 73, p. 035407, 2006.
- [77] D. R. Jackson, J. Chen, R. Qiang, F. Capolino, and A. A. Oliner, “The role of leaky plasmon waves in the directive beaming of light through a subwavelength aperture,” *Optics Express*, vol. 16, no. 26, pp. 21271–21281, 2008.
- [78] J. Arlt and K. Dholakia, “Generation of high-order bessel beams by use of an axicon,” *Opt. Comm.*, vol. 177, pp. 297 – 301, 2000.
- [79] J. J. Miret and C. J. Zapata-Rodriguez, “Diffraction-free propagation of subwavelength light beams in layered media,” *J. Opt. Soc. Am. B*, vol. 27, pp. 1435 – 1445, 2010.
- [80] Z. Zhang and S. C. Glotzer, “Self-assembly of patchy particles,” *Nano. Lett.*, vol. 4, pp. 1407 – 1413, 2004.
- [81] R. Brown, “A brief account of microscopical observations made in the months of june, july and august, 1827, on the particles contained in the pollen of plants; and on the general existence of active molecules in organic and inorganic bodies..” 1828.
- [82] A. Einstein, “Über die von der molekularkinetischen theorie der warme geforderte bewegung von in ruhenden flussigkeiten suspendierten teilchen,” *Annalen der Physik*, vol. 322, no. 8, pp. 549–560, 1905.
- [83] A. Einstein, “Zur theorie der brownschen bewegung,” *Annalen der Physik*, vol. 324, no. 2, pp. 371–381, 1906.
- [84] M. von Smoluchowski, “Zur kinetischen theorie der brownschen molekularbewegung und der suspensionen,” *Annalen der Physik*, vol. 326, no. 14, pp. 756–780, 1906.
- [85] P. S. Burada, P. Hanggi, F. Marchesoni, G. Schmid, and P. Talkner, “Diffusion in confined geometries,” *ChemPhysChem*, vol. 10, no. 1, pp. 45–54, 2009.
- [86] J. W. Swan and J. F. Brady, “Simulation of hydrodynamically interacting particles near a no-slip boundary,” *Physics of Fluids*, vol. 19, no. 11, pp. –, 2007.

- [87] J. W. Swan and J. F. Brady, “Particle motion between parallel walls: Hydrodynamics and simulation,” *Physics of Fluids (1994-present)*, vol. 22, no. 10, 2010.
- [88] F. Perrin, “Mouvement brownien d’un ellipsoïde - i. dispersion diélectrique pour des molécules ellipsoïdales,” *J. Phys. Radium*, vol. 5, no. 10, pp. 497–511, 1934.
- [89] F. Perrin, “Mouvement brownien d’un ellipsoïde (ii). rotation libre et dépolariation des fluorescences. translation et diffusion de molécules ellipsoïdales,” *J. Phys. Radium*, vol. 7, no. 1, pp. 1–11, 1936.
- [90] Y. Han, A. M. Alsayed, M. Nobili, J. Zhang, T. C. Lubensky, and A. G. Yodh, “Brownian motion of an ellipsoid,” *Science*, vol. 314, no. 5799, pp. 626–630, 2006.
- [91] B. Bhaduri, A. Neild, and T. W. Ng, “Directional brownian diffusion dynamics with variable magnitudes,” *Applied Physics Letters*, vol. 92, no. 8, pp. –, 2008.
- [92] S.-K. Son and S.-I. Chu, “Multielectron effects on the orientation dependence and photoelectron angular distribution of multiphoton ionization of CO₂ in strong laser fields,” *Phys. Rev. A*, vol. 80, p. 011403, Jul 2009.
- [93] J. Elgeti and G. Gompper, “Self-propelled rods near surfaces,” *EPL (Europhysics Letters)*, vol. 85, no. 3, p. 38002, 2009.
- [94] J. T. Padding and W. J. Briels, “Translational and rotational friction on a colloidal rod near a wall,” *The Journal of Chemical Physics*, vol. 132, no. 5, pp. –, 2010.
- [95] A. Neild, J. T. Padding, L. Yu, B. Bhaduri, W. J. Briels, and T. W. Ng, “Translational and rotational coupling in brownian rods near a solid surface,” *Phys. Rev. E*, vol. 82, p. 041126, Oct 2010.
- [96] I. Gralinski and T. W. Ng, “Brownian rod scheme in microenvironment sensing,” *AIP Advances*, vol. 2, no. 1, pp. –, 2012.
- [97] A. Neild, T. W. Ng, and W. M. S. Yip, “Optical sorting of dielectric rayleigh spherical particles with scattering and standing waves,” *Opt. Express*, vol. 17, pp. 5321–5329, Mar 2009.
- [98] M. O. Magnasco, “Forced thermal ratchets,” *Phys. Rev. Lett.*, vol. 71, pp. 1477–1481, Sep 1993.
- [99] C. R. Doering, W. Horsthemke, and J. Riordan, “Nonequilibrium fluctuation-induced transport,” *Phys. Rev. Lett.*, vol. 72, pp. 2984–2987, May 1994.
- [100] C. R. Doering, “Stochastic ratchets,” *Physica A: Statistical Mechanics and its Applications*, vol. 254, no. 12, pp. 1 – 6, 1998.

- [101] P. Bicchi, C. Marinelli, and R. A. Bernheim, “Hgin photoassociation, bound-bound transitions, and excimer emission,” *Phys. Rev. A*, vol. 56, pp. 2025–2031, Sep 1997.
- [102] A. A. Dubkov and B. Spagnolo, “Acceleration of diffusion in randomly switching potential with supersymmetry,” *Phys. Rev. E*, vol. 72, p. 041104, Oct 2005.
- [103] A. Haljas, R. Mankin, A. Sauga, and E. Reiter, “Anomalous mobility of brownian particles in a tilted symmetric sawtooth potential,” *Phys. Rev. E*, vol. 70, p. 041107, Oct 2004.
- [104] J. Rousselet, L. Salome, A. Ajdari, and J. Prost, “Directional motion of brownian particles induced by a periodic asymmetric potential,” *Nature*, vol. 370, no. 6489, pp. 446–448, 1994.
- [105] A. W. Lawson and E. A. Long, “Further remarks on the possible use of brownian motion in low temperature thermometry,” *Phys. Rev.*, vol. 70, pp. 977–978, Dec 1946.
- [106] J. C. Wheatley and R. A. Webb, “Millikelvin temperatures measured with a noise thermometer: Brownian motion in electrical circuits has been used to measure temperatures as low as 2 millikelvins,” *Science*, vol. 182, no. 4109, pp. 241–248, 1973.
- [107] J. Kurchan, “In and out of equilibrium,” *Nature*, vol. 433, no. 7023, pp. 222–225, 2005.
- [108] K. van Ommering, C. C. H. Lamers, J. H. Nieuwenhuis, L. J. van IJzendoorn, and M. W. J. Prins, “Analysis of individual magnetic particle motion near a chip surface,” *Journal of Applied Physics*, vol. 105, no. 10, pp. –, 2009.
- [109] R. Duggal and M. Pasquali, “Dynamics of individual single-walled carbon nanotubes in water by real-time visualization,” *Phys. Rev. Lett.*, vol. 96, p. 246104, Jun 2006.
- [110] R. R. Agayan, R. G. Smith, and R. Kopelman, “Slipping friction of an optically and magnetically manipulated microsphere rolling at a glass-water interface,” *Journal of Applied Physics*, vol. 104, no. 5, pp. –, 2008.
- [111] G. Volpe, G. Volpe, and D. Petrov, “Brownian motion in a nonhomogeneous force field and photonic force microscope,” *Phys. Rev. E*, vol. 76, p. 061118, Dec 2007.
- [112] R. Yasuda, H. Noji, M. Yoshida, K. Kinosita, and H. Itoh, “Resolution of distinct rotational substeps by submillisecond kinetic analysis of f1-atpase,” *Nature*, vol. 410, no. 6831, pp. 898–904, 2001.

- [113] C. Sonnichsen and A. P. Alivisatos, “Gold nanorods as novel nonbleaching plasmon-based orientation sensors for polarized single-particle microscopy,” *Nano Letters*, vol. 5, no. 2, pp. 301–304, 2005. PMID: 15794615.
- [114] J. van Gent, P. V. Lambeck, H. J. M. Kreuwel, G. J. Gerritsma, E. J. R. Sudhölter, D. N. Reinhoudt, and T. J. A. Popma, “Optimization of a chemooptical surface plasmon resonance based sensor,” *Appl. Opt.*, vol. 29, pp. 2843–2849, Jul 1990.
- [115] Y. Guo, L. Yan, W. Pan, B. Luo, K. Wen, Z. Guo, and X. Luo, “Characteristics of plasmonic filters with a notch located along rectangular resonators,” *Plasmonics*, vol. 8, no. 2, pp. 167–171, 2013.
- [116] J. Chen, Z. Li, Y. Zou, Z. Deng, J. Xiao, and Q. Gong, “Coupled-resonator-induced fano resonances for plasmonic sensing with ultra-high figure of merits,” *Plasmonics*, vol. 8, no. 4, pp. 1627–1631, 2013.
- [117] Q. Lu, D. Chen, G. Wu, B. Peng, and J. Xu, “A hybrid plasmonic microresonator with high quality factor and small mode volume,” *Journal of Optics*, vol. 14, no. 12, p. 125503, 2012.
- [118] M. G. Whitesides, “The origins and the future of microfluidics,” *Nature*, vol. 442, pp. 0028–0836, 2006.
- [119] T. M. Squires and S. R. Quake, “Microfluidics: Fluid physics at the nanoliter scale,” *Rev. Mod. Phys.*, vol. 77, pp. 977–1026, Oct 2005.
- [120] R. Pal, M. Yang, R. Lin, B. N. Johnson, N. Srivastava, S. Z. Razzacki, K. J. Chomistek, D. C. Heldsinger, R. M. Haque, V. M. Ugaz, P. K. Thwar, Z. Chen, K. Alfano, M. B. Yim, M. Krishnan, A. O. Fuller, R. G. Larson, D. T. Burke, and M. A. Burns, “An integrated microfluidic device for influenza and other genetic analyses,” *Lab Chip*, vol. 5, pp. 1024–1032, 2005.
- [121] S. Jakeway, A. de Mello, and E. Russell, “Miniaturized total analysis systems for biological analysis,” *Fresenius J Anal Chem.*, vol. 366(6-7), pp. 525–39, 2000.
- [122] M. Brivio, R. Fokkens, W. Verboom, D. Reinhoudt, N. Tas, M. Goedbloed, and A. van den Berg, “Integrated microfluidic system enabling (bio)chemical reactions with on-line maldi-tof mass spectrometry,” *Anal Chem.*, vol. 15;74(16), 2002.
- [123] T. H. Schulte, R. L. Bardell, and B. H. Weigl, “Microfluidic technologies in clinical diagnostics,” *Clinica Chimica Acta*, vol. 321, no. 12, pp. 1 – 10, 2002.
- [124] V. Srinivasan, V. K. Pamula, and R. B. Fair, “An integrated digital microfluidic lab-on-a-chip for clinical diagnostics on human physiological fluids,” *Lab Chip*, vol. 4, pp. 310–315, 2004.

- [125] A. J. deMello, "Control and detection of chemical reactions in microfluidic systems," *Nature*, vol. 442, pp. 0028–0836, 2006.
- [126] J. El-Ali, P. K. Sorger, and K. F. Jensen, "Cells on chips," *Nature*, vol. 442, 2006.
- [127] D. B. Weibel and G. M. Whitesides, "Applications of microfluidics in chemical biology," *Current Opinion in Chemical Biology*, vol. 10, no. 6, pp. 584 – 591, 2006.
- [128] A. E. Herr, A. V. Hatch, D. J. Throckmorton, H. M. Tran, J. S. Brennan, W. V. Giannobile, and A. K. Singh, "Microfluidic immunoassays as rapid saliva-based clinical diagnostics," *Proceedings of the National Academy of Sciences*, vol. 104, no. 13, pp. 5268–5273, 2007.
- [129] T. Thorsen, R. W. Roberts, F. H. Arnold, and S. R. Quake, "Dynamic pattern formation in a vesicle-generating microfluidic device," *Phys. Rev. Lett.*, vol. 86, pp. 4163–4166, Apr 2001.
- [130] D. T. Chiu and R. M. Lorenz, "Chemistry and biology in femtoliter and picoliter volume droplets," *Accounts of Chemical Research*, vol. 42, no. 5, pp. 649–658, 2009. PMID: 19260732.
- [131] B. T. Kelly, J.-C. Baret, V. Taly, and A. D. Griffiths, "Miniaturizing chemistry and biology in microdroplets," *Chem. Commun.*, pp. 1773–1788, 2007.
- [132] H. Song, D. L. Chen, and R. F. Ismagilov, "Reactions in droplets in microfluidic channels," *Angewandte Chemie International Edition*, vol. 45, no. 44, pp. 7336–7356, 2006.
- [133] L. Li and R. F. Ismagilov, "Protein crystallization using microfluidic technologies based on valves, droplets, and slipchip," *Annual review of biophysics*, vol. 39, pp. 139–158, 2010.
- [134] J. Leng and J.-B. Salmon, "Microfluidic crystallization," *Lab Chip*, vol. 9, pp. 24–34, 2009.
- [135] J. I. Park, A. Safari, S. Kumar, A. Gnther, and E. Kumacheva, "Microfluidic synthesis of polymer and inorganic particulate materials," *Annual Review of Materials Research*, vol. 40, no. 1, pp. 415–443, 2010.
- [136] R. N. Zare and S. Kim, "Microfluidic platforms for single-cell analysis," *Annual review of biomedical engineering*, vol. 12, pp. 187–201, 2010.
- [137] Y.-C. Tan, V. Cristini, and A. P. Lee, "Monodispersed microfluidic droplet generation by shear focusing microfluidic device," *Sensors and Actuators B: Chemical*, vol. 114, no. 1, pp. 350–356, 2006.

- [138] Y. Zhao and S. K. Cho, "Micro air bubble manipulation by electrowetting on dielectric (ewod): transporting, splitting, merging and eliminating of bubbles," *Lab on a Chip*, vol. 7, no. 2, pp. 273–280, 2007.
- [139] W. Barthlott and C. Neinhuis, "Purity of the sacred lotus, or escape from contamination in biological surfaces," *Planta*, vol. 202, no. 1, pp. 1–8, 1997.
- [140] X. Gao and L. Jiang, "Biophysics: Water-repellent legs of water striders," *Nature*, vol. 432, pp. 0028–0836, 2004.
- [141] L. Y. L. Wu, Q. Shao, X. C. Wang, H. Y. Zheng, and C. C. Wong, "Hierarchical structured sol-gel coating by laser textured template imprinting for surface superhydrophobicity," *Soft Matter*, vol. 8, pp. 6232–6238, 2012.
- [142] Y. Lai, X. Gao, H. Zhuang, J. Huang, C. Lin, and L. Jiang, "Designing superhydrophobic porous nanostructures with tunable water adhesion," *Advanced Materials*, vol. 21, no. 37, pp. 3799–3803, 2009.
- [143] H. Zhou, H. Wang, H. Niu, A. Gestos, X. Wang, and T. Lin, "Fluoroalkyl silane modified silicone rubber/nanoparticle composite: A super durable, robust superhydrophobic fabric coating," *Advanced Materials*, vol. 24, no. 18, pp. 2409–2412, 2012.
- [144] S. M. Kang, I. You, W. K. Cho, H. K. Shon, T. G. Lee, I. S. Choi, J. M. Karp, and H. Lee, "One-step modification of superhydrophobic surfaces by a mussel-inspired polymer coating," *Angewandte Chemie International Edition*, vol. 49, no. 49, pp. 9401–9404, 2010.
- [145] Y. Li, L. Li, and J. Sun, "Bioinspired self-healing superhydrophobic coatings," *Angewandte Chemie International Edition*, vol. 49, no. 35, pp. 6129–6133, 2010.
- [146] X. Li, Y. Liu, A. Zhu, Y. Luo, Z. Deng, and Y. Tian, "Real-time electrochemical monitoring of cellular H_2O_2 integrated with in situ selective cultivation of living cells based on dual functional protein microarrays at au-TiO₂ surfaces," *Analytical Chemistry*, vol. 82, no. 15, pp. 6512–6518, 2010.
- [147] A. I. Neto, C. A. Custodio, W. Song, and J. F. Mano, "High-throughput evaluation of interactions between biomaterials, proteins and cells using patterned superhydrophobic substrates," *Soft Matter*, vol. 7, pp. 4147–4151, 2011.
- [148] F. Shao, T. W. Ng, O. W. Liew, J. Fu, and T. Sridhar, "Evaporative preconcentration and cryopreservation of fluorescent analytes using superhydrophobic surfaces," *Soft Matter*, vol. 8, pp. 3563–3569, 2012.

- [149] J. Ballester-Beltran, P. Rico, D. Moratal, W. Song, J. F. Mano, and M. Salmeron-Sanchez, "Role of superhydrophobicity in the biological activity of fibronectin at the cell-material interface," *Soft Matter*, vol. 7, pp. 10803–10811, 2011.
- [150] T. Vuong, B. H.-P. Cheong, J. K. K. Lye, O. W. Liew, and T. W. Ng, "Microplate well coverage mixing using superhydrophobic contact," *Analytical Biochemistry*, vol. 430, no. 1, pp. 53 – 55, 2012.
- [151] F. Gentile, G. Das, M. Coluccio, F. Mecarini, A. Accardo, L. Tirinato, R. Tal-lerico, G. Cojoc, C. Liberale, P. Candeloro, P. Decuzzi, F. D. Angelis, and E. D. Fabrizio, "Ultra low concentrated molecular detection using super hydrophobic surface based biophotonic devices," *Microelectronic Engineering*, vol. 87, no. 58, pp. 798 – 801, 2010.
- [152] T. W. Ng and Y. Panduputra, "Dynamical force and imaging characterization of superhydrophobic surfaces," *Langmuir*, vol. 28, no. 1, pp. 453–458, 2012.
- [153] E. Carrilho, S. T. Phillips, S. J. Vella, A. W. Martinez, and G. M. Whitesides, "Paper microzone plates," *Analytical Chemistry*, vol. 81, no. 15, pp. 5990–5998, 2009. PMID: 19572563.
- [154] B. H.-P. Cheong, V. Diep, T. W. Ng, and O. W. Liew, "Transparency-based microplates for fluorescence quantification," *Analytical Biochemistry*, vol. 422, no. 1, pp. 39 – 45, 2012.
- [155] X. Y. Li, B. H.-P. Cheong, A. Somers, O. W. Liew, and T. W. Ng, "Surface-scribed transparency-based microplates," *Langmuir*, vol. 29, no. 2, pp. 849–855, 2013.
- [156] L. J. Kricka, K. Imai, and P. Fortina, "Analytical ancestry: Evolution of the array in analysis," *Clinical Chemistry*, vol. 56, no. 12, pp. 1797–1803, 2010.
- [157] A. Zarowna-Dabrowska, E. O. McKenna, M. E. Schutte, A. Glidle, L. Chen, C. Cuestas-Ayllon, D. Marshall, A. Pitt, M. D. Dawson, E. Gu, J. M. Cooper, and H. Yin, "Generation of primary hepatocyte microarrays by piezoelectric printing," *Colloids and Surfaces B: Biointerfaces*, vol. 89, no. 0, pp. 126 – 132, 2012.
- [158] H. Rhode, M. Schulze, S. Renard, P. Zimmermann, T. Moore, G. A. Cumme, and A. Horn, "An improved method for checking hts/uhts liquid-handling systems," *Journal of Biomolecular Screening*, vol. 9, no. 8, pp. 726–733, 2004.
- [159] H. Y. Tan, T. W. Ng, A. Neild, and O. W. Liew, "Capillary wells microplate with side optical access," *Journal of Biomolecular Screening*, vol. 15, no. 9, pp. 1160–1164, 2010.

- [160] G. Lu, H. Y. Tan, A. Neild, O. W. Liew, Y. Yu, and T. W. Ng, “Liquid filling in standard circular well microplates,” *Journal of Applied Physics*, vol. 108, no. 12, pp. –, 2010.
- [161] B. H.-P. Cheong, J. K. K. Lye, S. Backhaus, O. W. Liew, and T. W. Ng, “Microplates based on liquid bridges between glass rods,” *Journal of Colloid and Interface Science*, vol. 397, no. 0, pp. 177 – 184, 2013.
- [162] P. G. de Gennes, “Wetting: statics and dynamics,” *Rev. Mod. Phys.*, vol. 57, pp. 827–863, Jul 1985.
- [163] A. Marmur, “Equilibrium and spreading of liquids on solid surfaces,” *Advances in Colloid and Interface Science*, vol. 19, no. 12, pp. 75 – 102, 1983.
- [164] C. Ye, M. Li, J. Hu, Q. Cheng, L. Jiang, and Y. Song, “Highly reflective superhydrophobic white coating inspired by poplar leaf hairs toward an effective “cool roof”,” *Energy Environ. Sci.*, vol. 4, pp. 3364–3367, 2011.
- [165] J. S. Allen, “An analytical solution for determination of small contact angles from sessile drops of arbitrary size,” *Journal of Colloid and Interface Science*, vol. 261, no. 2, pp. 481 – 489, 2003.
- [166] N. M. Dingle and M. T. Harris, “A robust algorithm for the simultaneous parameter estimation of interfacial tension and contact angle from sessile drop profiles,” *Journal of Colloid and Interface Science*, vol. 286, no. 2, pp. 670 – 680, 2005.
- [167] Y.-L. Hung, Y.-Y. Chang, M.-J. Wang, and S.-Y. Lin, “A simple method for measuring the superhydrophobic contact angle with high accuracy,” *Review of Scientific Instruments*, vol. 81, no. 6, pp. –, 2010.
- [168] E. Rame, “The interpretation of dynamic contact angles measured by the wilhelmy plate method,” *Journal of Colloid and Interface Science*, vol. 185, no. 1, pp. 245 – 251, 1997.
- [169] F. Restagno, C. Poulard, C. Cohen, L. Vagharchakian, and L. Léger, “Contact angle and contact angle hysteresis measurements using the capillary bridge technique,” *Langmuir*, vol. 25, no. 18, pp. 11188–11196, 2009. PMID: 19735159.
- [170] R. Picknett and R. Bexon, “The evaporation of sessile or pendant drops in still air,” *Journal of Colloid and Interface Science*, vol. 61, no. 2, pp. 336 – 350, 1977.
- [171] C. Bourges-Monnier and M. E. R. Shanahan, “Influence of evaporation on contact angle,” *Langmuir*, vol. 11, no. 7, pp. 2820–2829, 1995.

- [172] H. Song, Y. Lee, S. Jin, H.-Y. Kim, and J. Y. Yoo, "Prediction of sessile drop evaporation considering surface wettability," *Microelectronic Engineering*, vol. 88, no. 11, pp. 3249 – 3255, 2011.
- [173] B. H.-P. Cheong, T. W. Ng, Y. Yu, and O. W. Liew, "Using the meniscus in a capillary for small volume contact angle measurement in biochemical applications," *Langmuir*, vol. 27, no. 19, pp. 11925–11929, 2011.
- [174] G. Debregeas and F. Brochard-Wyart, "Nucleation radius and growth of a liquid meniscus," *Journal of Colloid and Interface Science*, vol. 190, no. 1, pp. 134 – 141, 1997.
- [175] T.-L. Cheng and Y. U. Wang, "Spontaneous formation of stable capillary bridges for firming compact colloidal microstructures in phase separating liquids: A computational study," *Langmuir*, vol. 28, no. 5, pp. 2696–2703, 2012.
- [176] J. Qian and H. Gao, "Scaling effects of wet adhesion in biological attachment systems," *Acta Biomaterialia*, vol. 2, no. 1, pp. 51 – 58, 2006.
- [177] W. Schwalb, T. W. Ng, J. K. K. Lye, O. W. Liew, and B. H.-P. Cheong, "Surface tension drawing of liquid from microplate capillary wells," *Journal of Colloid and Interface Science*, vol. 365, no. 1, pp. 314 – 319, 2012.
- [178] H. Princen, "Capillary phenomena in assemblies of parallel cylinders: Iii. liquid columns between horizontal parallel cylinders," *Journal of Colloid and Interface Science*, vol. 34, no. 2, pp. 171 – 184, 1970.
- [179] B. C. Brock, "Using vector spherical harmonics to compute antenna mutual impedance from measured or computed fields," *Sandia Report SAND2000-2217-Revised*, 2001.
- [180] M. E. Rose, *Multipole Fields*. New York: Wiley, 1955.
- [181] L. Tsang, K.-H. Ding, and J. A. Kong, *Scattering of Electromagnetic Waves: theories and applications*. Newark, NJ: Wiley, 2000.
- [182] P. B. Bareil and Y. Sheng, "Modeling highly focused laser beam in optical tweezers with the vector gaussian beam in the t-matrix method," *J. Opt. Soc. Am. A*, vol. 30, pp. 1–6, Jan 2013.
- [183] J. H. Crichton and P. L. Marston, "The measurable distinction between the spin and orbital angular momenta of electromagnetic radiation," in *Electronic Journal of Differential Equations Conf*, vol. 4, pp. 37–50, 2000.

- [184] A. D. Rakic, A. B. Djurišić, J. M. Elazar, and M. L. Majewski, “Optical properties of metallic films for vertical-cavity optoelectronic devices,” *Appl. Opt.*, vol. 37, pp. 5271–5283, Aug 1998.
- [185] A. F. Oskooi, D. Roundy, M. Ibanescu, P. Bermel, J. D. Joannopoulos, and S. G. Johnson, “MEEP: A flexible free-software package for electromagnetic simulations by the FDTD method,” *Computer Physics Communications*, vol. 181, pp. 687–702, January 2010.
- [186] Y. Park, M. Diez-Silva, G. Popescu, G. Lykotrafitis, W. Choi, M. S. Feld, and S. Suresh, “Refractive index maps and membrane dynamics of human red blood cells parasitized by plasmodium falciparum,” *Proceedings of the National Academy of Sciences*, vol. 105, no. 37, pp. 13730–13735, 2008.
- [187] J. Chen, Z. Yu, L. Zhang, and G. Chen, “Microfluidic bioreactors for highly efficient proteolysis,” *Current Chemical Biology*, vol. 3, no. 3, pp. 291–301, 2009.
- [188] H. N. Vu, Y. Li, M. Casali, D. Irimia, Z. Megeed, and M. L. Yarmush, “A microfluidic bioreactor for increased active retrovirus output,” *Lab on a Chip*, vol. 8, no. 1, pp. 75–80, 2008.
- [189] E. Figallo, C. Cannizzaro, S. Gerecht, J. A. Burdick, R. Langer, N. Elvassore, and G. Vunjak-Novakovic, “Micro-bioreactor array for controlling cellular microenvironments,” *Lab on a Chip*, vol. 7, no. 6, pp. 710–719, 2007.
- [190] M. He, J. S. Edgar, G. D. Jeffries, R. M. Lorenz, J. P. Shelby, and D. T. Chiu, “Selective encapsulation of single cells and subcellular organelles into picoliter-and femtoliter-volume droplets,” *Analytical Chemistry*, vol. 77, no. 6, pp. 1539–1544, 2005.
- [191] S. Daniel, M. K. Chaudhury, and P.-G. De Gennes, “Vibration-actuated drop motion on surfaces for batch microfluidic processes,” *Langmuir*, vol. 21, no. 9, pp. 4240–4248, 2005.
- [192] H. Y. Tan, T. W. Ng, A. Neild, and O. W. Liew, “Point spread function effect in image-based fluorescent microplate detection,” *Analytical biochemistry*, vol. 397, no. 2, pp. 256–258, 2010.
- [193] J. Kok Keung Lye, T. Wah Ng, and W. Yeong Liang Ling, “Discrete microfluidics transfer across capillaries using liquid bridge stability,” *Journal of Applied Physics*, vol. 110, no. 10, pp. 104509–104509, 2011.
- [194] J.-J. Zhong, K. Fujiyama, T. Seki, and T. Yoshida, “A quantitative analysis of shear effects on cell suspension and cell culture of perilla frutescens in bioreactors,” *Biotechnology and bioengineering*, vol. 44, no. 5, pp. 649–654, 1994.

- [195] W. Y. Sim, S. W. Park, S. H. Park, B. H. Min, S. R. Park, and S. S. Yang, "A pneumatic micro cell chip for the differentiation of human mesenchymal stem cells under mechanical stimulation," *Lab on a chip*, vol. 7, no. 12, pp. 1775–1782, 2007.
- [196] H. Li, J. R. Friend, and L. Y. Yeo, "Microfluidic colloidal island formation and erasure induced by surface acoustic wave radiation," *Physical review letters*, vol. 101, no. 8, p. 084502, 2008.
- [197] J. Whitehill, A. Neild, T. W. Ng, and M. Stokes, "Collection of suspended particles in a drop using low frequency vibration," *Applied Physics Letters*, vol. 96, no. 5, pp. 053501–053501, 2010.
- [198] H. Xia, J. Wang, Y. Tian, Q.-D. Chen, X.-B. Du, Y.-L. Zhang, Y. He, and H.-B. Sun, "Ferrofluids for fabrication of remotely controllable micro-nanomachines by two-photon polymerization," *Advanced Materials*, vol. 22, no. 29, pp. 3204–3207, 2010.
- [199] B. Weiss, W. Hilber, R. Holly, P. Gittler, B. Jakoby, and K. Hingerl, "Dielectrophoretic particle dynamics in alternating-current electro-osmotic micropumps," *Applied Physics Letters*, vol. 92, no. 18, pp. –, 2008.
- [200] J. A. King and W. M. Miller, "Bioreactor development for stem cell expansion and controlled differentiation," *Current Opinion in Chemical Biology*, vol. 11, no. 4, pp. 394 – 398, 2007.
- [201] N. K. Inamdar, L. G. Griffith, and J. T. Borenstein, "Transport and shear in a microfluidic membrane bilayer device for cell culture," *Biomicrofluidics*, vol. 5, no. 2, pp. –, 2011.
- [202] C. M. Potter, M. H. Lundberg, L. S. Harrington, C. M. Warboys, T. D. Warner, R. E. Berson, A. V. Moshkov, J. Gorelik, P. D. Weinberg, and J. A. Mitchell, "Role of shear stress in endothelial cell morphology and expression of cyclooxygenase isoforms," *Arteriosclerosis, thrombosis, and vascular biology*, vol. 31, no. 2, pp. 384–391, 2011.
- [203] K. Yamamoto, T. Sokabe, T. Watabe, K. Miyazono, J. K. Yamashita, S. Obi, N. Ohura, A. Matsushita, A. Kamiya, and J. Ando, "Fluid shear stress induces differentiation of flk-1-positive embryonic stem cells into vascular endothelial cells in vitro," *American Journal of Physiology-Heart and Circulatory Physiology*, vol. 288, no. 4, pp. H1915–H1924, 2005.
- [204] J. R. Glossop and S. H. Cartmell, "Effect of fluid flow-induced shear stress on human mesenchymal stem cells: Differential gene expression of il1b and map3k8 in mapk signaling," *Gene Expression Patterns*, vol. 9, no. 5, pp. 381 – 388, 2009.

- [205] Z. Yang, W.-H. Xia, Y.-Y. Zhang, S.-Y. Xu, X. Liu, X.-Y. Zhang, B.-B. Yu, Y.-X. Qiu, and J. Tao, “Shear stress-induced activation of tie2-dependent signaling pathway enhances reendothelialization capacity of early endothelial progenitor cells,” *Journal of Molecular and Cellular Cardiology*, vol. 52, no. 5, pp. 1155 – 1163, 2012.
- [206] M. Morga-Ramírez, M. T. Collados-Larumbe, K. E. Johnson, M. J. Rivas-Arreola, L. M. Carrillo-Cocom, and M. M. Álvarez, “Hydrodynamic conditions induce changes in secretion level and glycosylation patterns of von willebrand factor (vwf) in endothelial cells,” *Journal of bioscience and bioengineering*, vol. 109, no. 4, pp. 400–406, 2010.
- [207] Y. Ban, Y. ying Wu, T. Yu, N. Geng, Y. yue Wang, X. guang Liu, and P. Gong, “Response of osteoblasts to low fluid shear stress is time dependent,” *Tissue and Cell*, vol. 43, no. 5, pp. 311 – 317, 2011.
- [208] M. Bier, I. Derényi, M. Kostur, and R. D. Astumian, “Intrawell relaxation of overdamped brownian particles,” *Physical Review E*, vol. 59, no. 6, p. 6422, 1999.
- [209] J.-P. Matas, J. F. Morris, and E. Guazzelli, “Inertial migration of rigid spherical particles in poiseuille flow,” *Journal of Fluid Mechanics*, vol. 515, no. 1, pp. 171–195, 2004.
- [210] D. Di Carlo, D. Irimia, R. G. Tompkins, and M. Toner, “Continuous inertial focusing, ordering, and separation of particles in microchannels,” *Proceedings of the National Academy of Sciences*, vol. 104, no. 48, pp. 18892–18897, 2007.
- [211] J. Koo and C. Kleinstreuer, “Liquid flow in microchannels: experimental observations and computational analyses of microfluidics effects,” *Journal of Micromechanics and Microengineering*, vol. 13, no. 5, p. 568, 2003.
- [212] Y. Zhang, Z. Liu, J. Yang, and L. Yuan, “A non-contact single optical fiber multi-optical tweezers probe: Design and fabrication,” *Optics Communications*, vol. 285, no. 20, pp. 4068 – 4071, 2012.
- [213] K. Dholakia, M. P. MacDonald, P. Zemánek, and T. Čižmár, “Cellular and colloidal separation using optical forces,” *Methods in cell biology*, vol. 82, pp. 467–495, 2007.
- [214] Y.-N. Dai, P. Li, J.-P. Zhang, A.-Q. Wang, and Q. Wei, “Swelling characteristics and drug delivery properties of nifedipine-loaded ph sensitive alginatechitosan hydrogel beads,” *Journal of Biomedical Materials Research Part B: Applied Biomaterials*, vol. 86B, no. 2, pp. 493–500, 2008.

- [215] M. Nieto-Vesperinas, P. Chaumet, A. Rahmani, *et al.*, “Near-field photonic forces,” *Philosophical transactions- Royal society of London series*.
- [216] J. Weiner, “The physics of light transmission through subwavelength apertures and aperture arrays,” *Reports on Progress in Physics*, vol. 72, no. 6, p. 064401, 2009.
- [217] J. J. Miret, C. J. Zapata-Rodríguez, *et al.*, “Diffraction-free propagation of sub-wavelength light beams in layered media,” *JOSA B*, vol. 27, no. 7, pp. 1435–1445, 2010.
- [218] Z. Zhang and S. C. Glotzer, “Self-assembly of patchy particles,” *Nano Letters*, vol. 4, no. 8, pp. 1407–1413, 2004.
- [219] H. Brenner, “Rheology of a dilute suspension of axisymmetric brownian particles,” *International Journal of Multiphase Flow*, vol. 1, no. 2, pp. 195 – 341, 1974.
- [220] A. Neild, T. W. Ng, and T. Woods, “Optimizing photophoresis and asymmetric force fields for grading of brownian particles,” *Appl. Opt.*, vol. 48, pp. 6820–6826, Dec 2009.
- [221] P. Zijlstra, J. W. Chon, and M. Gu, “Five-dimensional optical recording mediated by surface plasmons in gold nanorods,” *Nature*, vol. 459, no. 7245, pp. 410–413, 2009.
- [222] H. Kang, B. Jia, J. Li, D. Morrish, and M. Gu, “Enhanced photothermal therapy assisted with gold nanorods using a radially polarized beam,” *Applied physics letters*, vol. 96, no. 6, pp. 063702–063702, 2010.
- [223] Y. Zhang, J. Yu, D. J. Birch, and Y. Chen, “Gold nanorods for fluorescence lifetime imaging in biology,” *Journal of biomedical optics*, vol. 15, no. 2, pp. 020504–020504, 2010.
- [224] S. Guz and M. Sviridov, “Green noise in quasistationary stochastic systems,” *Chaos: An Interdisciplinary Journal of Nonlinear Science*, vol. 11, no. 3, pp. 605–610, 2001.
- [225] B. C. Bag and C.-K. Hu, “Current inversion induced by colored non-gaussian noise,” *Journal of Statistical Mechanics: Theory and Experiment*, vol. 2009, no. 02, p. P02003, 2009.
- [226] B. Spagnolo, A. A. Dubkov, and N. V. Agudov, “Escape times in fluctuating metastable potential and acceleration of diffusion in periodic fluctuating potentials,” *Physica A: Statistical Mechanics and its Applications*, vol. 340, no. 13, pp. 265 – 273, 2004. [News and Expectations in Thermostatistics](#).

- [227] B. Spagnolo and A. Dubkov, "Diffusion in flashing periodic potentials," *The European Physical Journal B-Condensed Matter and Complex Systems*, vol. 50, no. 1-2, pp. 299–303, 2006.
- [228] S. Arnold, M. Khoshsima, I. Teraoka, S. Holler, and F. Vollmer, "Shift of whispering-gallery modes in microspheres by protein adsorption," *Optics letters*, vol. 28, no. 4, pp. 272–274, 2003.
- [229] M. Cai, O. Painter, and K. J. Vahala, "Observation of critical coupling in a fiber taper to a silica-microsphere whispering-gallery mode system," *Physical Review Letters*, vol. 85, no. 1, p. 74, 2000.
- [230] S. Dong, H. Ding, Y. Liu, and X. Qi, "Investigation of evanescent coupling between tapered fiber and a multimode slab waveguide," *Applied optics*, vol. 51, no. 10, pp. C152–C157, 2012.
- [231] L. Wang, Y. Li, M. Garcia Porcel, D. Vermeulen, X. Han, J. Wang, X. Jian, R. Baets, M. Zhao, and G. Morthier, "A polymer-based surface grating coupler with an embedded Si_3N_4 layer," *Journal of Applied Physics*, vol. 111, no. 11, pp. 114507–114507, 2012.
- [232] L. Shao, C. Fang, H. Chen, Y. C. Man, J. Wang, and H.-Q. Lin, "Distinct plasmonic manifestation on gold nanorods induced by the spatial perturbation of small gold nanospheres," *Nano letters*, vol. 12, no. 3, pp. 1424–1430, 2012.
- [233] M. L. Juan, M. Righini, and R. Quidant, "Plasmon nano-optical tweezers," *Nature Photonics*, vol. 5, no. 6, pp. 349–356, 2011.
- [234] H. Ma, P. M. Bendix, and L. B. Oddershede, "Large-scale orientation dependent heating from a single irradiated gold nanorod," *Nano letters*, vol. 12, no. 8, pp. 3954–3960, 2012.
- [235] X. Han, X. Ji, H. Wen, and J. Zhang, "H-shaped resonant optical antennas with slot coupling," *Plasmonics*, vol. 7, no. 1, pp. 7–11, 2012.
- [236] A. Qi, L. Yeo, J. Friend, and J. Ho, "The extraction of liquid, protein molecules and yeast cells from paper through surface acoustic wave atomization," *Lab Chip*, vol. 10, pp. 470–476, 2010.
- [237] J. Friend and L. Y. Yeo, "Microscale acoustofluidics: Microfluidics driven via acoustics and ultrasonics," *Rev. Mod. Phys.*, vol. 83, pp. 647–704, Jun 2011.
- [238] A. Qi, L. Y. Yeo, and J. R. Friend, "Interfacial destabilization and atomization driven by surface acoustic waves," *Physics of Fluids*, vol. 20, no. 7, pp. –, 2008.

- [239] L. Y. Yeo and J. R. Friend, "Ultrafast microfluidics using surface acoustic waves," *Biomicrofluidics*, vol. 3, no. 1, pp. –, 2009.
- [240] G. O. Mallory and J. B. Hajdu, *Electroless plating: fundamentals and applications*. Access Online via Elsevier, 1990.
- [241] S. Warriar and R. Lin, "Silver coating on carbon and sic fibres," *Journal of Materials Science*, vol. 28, no. 18, pp. 4868–4877, 1993.
- [242] H. Chang, C. Pitt, and G. Alexander, "Electroless silver plating of oxide particles in aqueous solution," *Journal of Materials Science*, vol. 28, no. 19, pp. 5207–5210, 1993.
- [243] J. T. Han, D. H. Lee, C. Y. Ryu, and K. Cho, "Fabrication of superhydrophobic surface from a supramolecular organosilane with quadruple hydrogen bonding," *Journal of the American Chemical Society*, vol. 126, no. 15, pp. 4796–4797, 2004. PMID: 15080681.
- [244] A. Lafuma and D. Quéré, "Superhydrophobic states," *Nature materials*, vol. 2, no. 7, pp. 457–460, 2003.
- [245] D. Bartolo, F. Bouamrine, E. Verneuil, A. Buguin, P. Silberzan, and S. Moulinet, "Bouncing or sticky droplets: Impalement transitions on superhydrophobic micropatterned surfaces," *EPL (Europhysics Letters)*, vol. 74, no. 2, p. 299, 2006.
- [246] J. B. Boreyko and C.-H. Chen, "Restoring superhydrophobicity of lotus leaves with vibration-induced dewetting," *Phys. Rev. Lett.*, vol. 103, p. 174502, Oct 2009.
- [247] B. Mockenhaupt, H.-J. Ensikat, M. Spaeth, and W. Barthlott, "Superhydrophobicity of biological and technical surfaces under moisture condensation: Stability in relation to surface structure," *Langmuir*, vol. 24, no. 23, pp. 13591–13597, 2008.
- [248] Y.-T. Cheng and D. E. Rodak, "Is the lotus leaf superhydrophobic?," *Applied Physics Letters*, vol. 86, no. 14, pp. –, 2005.
- [249] J. W. Krumpfer, P. Bian, P. Zheng, L. Gao, and T. J. McCarthy, "Contact angle hysteresis on superhydrophobic surfaces: An ionic liquid probe fluid offers mechanistic insight," *Langmuir*, vol. 27, no. 6, pp. 2166–2169, 2011.
- [250] J. B. Lee, H. R. Gwon, S. H. Lee, and M. Cho, "Wetting transition characteristics on microstructured hydrophobic surfaces," *Materials Transactions*, vol. 51, no. 9, pp. 1709–1711, 2010.
- [251] M. Jin, X. Feng, L. Feng, T. Sun, J. Zhai, T. Li, and L. Jiang, "Superhydrophobic aligned polystyrene nanotube films with high adhesive force," *Advanced Materials*, vol. 17, no. 16, pp. 1977–1981, 2005.

- [252] H. Mertaniemi, R. Forchheimer, O. Ikkala, and R. H. A. Ras, “Rebounding droplet-droplet collisions on superhydrophobic surfaces: from the phenomenon to droplet logic,” *Advanced Materials*, vol. 24, no. 42, pp. 5738–5743, 2012.
- [253] H. Zuo, Q. Liu, J. Wang, L. Yang, and S. Luo, “Technique to improve the accuracy of the retrieval of aerosol size-distribution,” *Opt. Lett.*, vol. 35, pp. 1380–1382, May 2010.
- [254] Y. Wang, S. Fan, X. Feng, G. Yan, and Y. Guan, “Regularized inversion method for retrieval of aerosol particle size distribution function in $w(1,2)$ space,” *Appl. Opt.*, vol. 45, pp. 7456–7467, Oct 2006.
- [255] R. W. Boyd, “Radiometry and the detection of optical radiation,” *New York, John Wiley and Sons, 1983, 261 p.*, vol. 1, 1983.
- [256] S. Enoki, K. Saeki, K. Maki, and K. Kuwajima, “Acid denaturation and refolding of green fluorescent protein,” *Biochemistry*, vol. 43, no. 44, pp. 14238–14248, 2004. PMID: 15518574.
- [257] C. Zhang, X.-H. Xing, and K. Lou, “Rapid detection of a gfp-marked enterobacter aerogenes under anaerobic conditions by aerobic fluorescence recovery,” *FEMS Microbiology Letters*, vol. 249, no. 2, pp. 211–218, 2005.
- [258] C. Zhang, M.-S. Liu, and X.-H. Xing, “Temperature influence on fluorescence intensity and enzyme activity of the fusion protein of gfp and hyperthermophilic xylanase,” *Applied Microbiology and Biotechnology*, vol. 84, no. 3, pp. 511–517, 2009.
- [259] S. Semenov, V. Starov, R. Rubio, H. Agogo, and M. Velarde, “Evaporation of sessile water droplets: Universal behaviour in presence of contact angle hysteresis,” *Colloids and Surfaces A: Physicochemical and Engineering Aspects*, vol. 391, no. 1, pp. 135–144, 2011.
- [260] R. D. Deegan, O. Bakajin, T. F. Dupont, G. Huber, S. R. Nagel, and T. A. Witten, “Capillary flow as the cause of ring stains from dried liquid drops,” *Nature*, vol. 389, no. 6653, pp. 827–829, 1997.
- [261] H. M. Gorr, J. M. Zueger, D. R. McAdams, and J. A. Barnard, “Salt-induced pattern formation in evaporating droplets of lysozyme solutions,” *Colloids and Surfaces B: Biointerfaces*, 2012.
- [262] S. Dodds, M. Carvalho, and S. Kumar, “Stretching liquid bridges with moving contact lines: The role of inertia,” *Physics of Fluids*, vol. 23, no. 9, pp. 092101–092101, 2011.

- [263] J. W. Gibbs, "On the equilibrium of heterogeneous substances," *American Journal of Science*, no. 96, pp. 441–458, 1878.
- [264] L. Zargazadeh and J. A. Elliott, "Comparative surface thermodynamic analysis of new fluid phase formation between a sphere and a flat plate," *Langmuir*, vol. 29, no. 11, pp. 3610–3627, 2013.
- [265] W. Thomson, "Lx. on the equilibrium of vapour at a curved surface of liquid," *The London, Edinburgh, and Dublin Philosophical Magazine and Journal of Science*, vol. 42, no. 282, pp. 448–452, 1871.
- [266] J. Liu, W. Zuo, and Y. Mei, "Droplet-induced anomalous deformation of a thin micro-plate," *Colloids and Surfaces A: Physicochemical and Engineering Aspects*, 2012.
- [267] H. Gau, S. Herminghaus, P. Lenz, and R. Lipowsky, "Liquid morphologies on structured surfaces: from microchannels to microchips," *Science*, vol. 283, no. 5398, pp. 46–49, 1999.
- [268] P. Maderson, "Histological changes in the epidermis of the tokay (gekko gekko) during the sloughing cycle," *Journal of Morphology*, vol. 119, no. 1, pp. 39–50, 1966.
- [269] R. Ruibal and V. Ernst, "The structure of the digital setae of lizards," *Journal of Morphology*, vol. 117, no. 3, pp. 271–293, 1965.
- [270] D. J. Gower, "Scale microornamentation of uropeltid snakes," *Journal of Morphology*, vol. 258, no. 2, pp. 249–268, 2003.
- [271] H. Marvi and D. L. Hu, "Friction enhancement in concertina locomotion of snakes," *Journal of The Royal Society Interface*, vol. 9, no. 76, pp. 3067–3080, 2012.
- [272] R. W. Holst and J. H. Yopp, "Studies of the azolla-anabaena symbiosis using azolla mexicana. i. growth in nature and laboratory," *American fern journal*, 1979.
- [273] L. Umali, J. Duncan, and J. Burgess, "Performance of dead azolla filiculoides biomass in biosorption of au from wastewater," *Biotechnology letters*, vol. 28, no. 1, pp. 45–50, 2006.
- [274] A. Mehta and G. Barker, "The dynamics of sand," *Reports on Progress in Physics*, vol. 57, no. 4, p. 383, 1994.
- [275] K. R. LaMarche, S. L. Conway, B. J. Glasser, and T. Shinbrot, "Cellular automata model of gravity-driven granular flows," *Granular Matter*, vol. 9, no. 3-4, pp. 219–229, 2007.

-
- [276] N. Margolus, “Physics-like models of computation,” *Physica D: Nonlinear Phenomena*, vol. 10, no. 1, pp. 81–95, 1984.
- [277] Y. Chen, W. Norde, H. C. van der Mei, and H. J. Busscher, “Bacterial cell surface deformation under external loading,” *mBio*, vol. 3, no. 6, pp. e00378–12, 2012.
- [278] J. Costerton, P. S. Stewart, and E. Greenberg, “Bacterial biofilms: a common cause of persistent infections,” *Science*, vol. 284, no. 5418, pp. 1318–1322, 1999.
- [279] B. H.-P. Cheong, O. W. Liew, and N. Wah, “Mrt letter: Micro-to nanoscale sample collection for high throughput microscopy,” *Microscopy research and technique*, vol. 76, no. 8, pp. 767–773, 2013.
- [280] B. H.-P. Cheong, O. W. Liew, and T. W. Ng, “Squeezed flow preconcentration for probe tip biosensors,” *Analytical biochemistry*, vol. 444, pp. 57–59, 2014.